Technical Physics, Vol. 49, No. 6, 2004, pp. 661–668. Translated from Zhurnal Tekhnicheskoĭ Fiziki, Vol. 74, No. 6, 2004, pp. 1–7.

ATOMS, SPECTRA, RADIATION

Differential Cross Section Minima for Elastic Scattering of Electrons by Krypton Atoms in the Energy Range 0–500 eV

V. I. Kelemen

Institute of Electronic Physics, National Academy of Sciences of Ukraine, Uzhgorod, 88000 Ukraine
e-mail: kelemen@iep.uzhgorod.ua

Received June 17, 2003; in final form, October 29, 2003

Abstract—Elastic scattering of 0- to 500-eV electrons by krypton atoms is studied in terms of a model of phenomenological real potential with allowance for spin–orbit interaction. The energy dependences of the angular positions of differential cross section minima are calculated and compared with experimental data. The energies and angular positions of seven critical points where the differential cross sections reach minimal values are determined. The results obtained are in good agreement with the available experimental data. © *2004 MAIK "Nauka/Interperiodica".*

INTRODUCTION

By means of elastic scattering of electrons by argon atoms, it was demonstrated [1–3] that the angular position of the differential cross section (DCS) minimum may be viewed as a fundamental characteristic of scattering in a wide energy range. It turned out that the energy dependences of the positions of low-angle (<90°) and high-angle (>90°) DCS minima (measured and calculated with various techniques) agree with each other much better than the minimal values of the cross sections. In [1], such dependences are given for collision energies from 3 to 100 eV; in [2, 3], for energies of up to 500 eV (for low-angle minima, to 133 eV [3]).

For krypton atoms, this problem is of even greater interest. For energies above 70 eV, the third minimum begins to show in the angular dependences of the DCS [4]. This minimum is clearly seen in the angular range from 140° to 150° at energies up to 200 eV [5, 6]. Most techniques cannot measure DCSs at angles >150°. Hence, extrapolation of experimental results to high angles must rely on analytical information about these minima. In addition, while the highest critical energy for argon atoms is ≈130 eV [3, 5, 7], in the case of krypton it rises to ≈450 eV [5, 7]. Thus, the search for DCS critical minima must be extended up to 500 eV.

The positions of the minima found in this work are compared with experimental data [7–13], which are accurate to ±3°. In [7], the energies and angles of four critical minima were estimated with an accuracy of several tenths of an electron volt and several hundredths of a degree. In [8], the DCS absolute values were measured in the energy interval 20–400 eV and in the angular range 20°–150° (with an angular resolution of ±1.5° or higher). The angular dependences of DCSs are represented in the form of tables with an angular step of 10° (2° in the vicinity of the minima). In [9], the DCS relative values were measured at collision energies from 100 to 3000 eV in the 5°–55° angular range. The positions of low-angle minima at 100, 150, and 200 eV are given with an accuracy of several tenths of a degree. DCS absolute measurements (with an accuracy of 20%) at energies varying from 3 to 100 eV and at angles varying from 20° to 135° were reported in [10]. The positions of the minima are given accurate to ±2°. DCS absolute measurements with the same accuracy (20%) were also performed in [11] but for energies from 5 to 200 eV and angles from 10° to 125° (the angular resolution is ±2°). Finally, the DCS relative values were measured at energies between 20 and 80 eV and angles between 10° and 150° [12, 13]. The angular resolution was 2° at 12 eV and 0.8° at 80 eV. The DSC values were normalized using data from [10], because of which the accuracy of the absolute values was relatively low, ≈24%. The positions of the minima accurate to 1° were given in [13].

Elastic scattering of electrons by krypton atoms was theoretically studied [4–6, 14–18]. However, the angular positions of the DCS minima were calculated only in [4]. When using the data represented in the form of tables with an angular step within 5°, we evaluated the positions of the minima by the smoothing-out procedure.

In [4], elastic scattering of electrons by krypton atoms was comprehensively analyzed with the *R*-matrix method. The phase shifts (for $L = 0$–4) at energies from 0.1 to 15 eV, as well as the DCS values and angles of minima at energies from 1 to 120 eV, are given. In [18], the DCS values were calculated at energies from 0.8 to 150 eV in the relativistic approximation using a model polarization potential that takes into account both the dipole and quadrupole polarizabilities

1063-7842/04/4906-0661$26.00

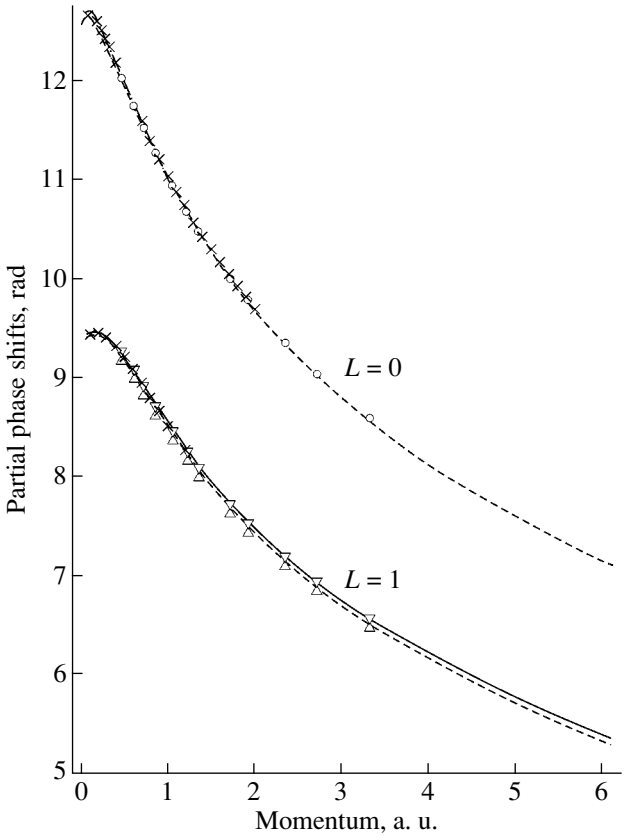

Fig. 1. *s*- and *p*-wave phase shifts vs. incident electron momentum. The dash-and-dot curve is taken from [4], (×) data taken from [16]. For $L = 0$: dashed curve, our calculation; (○) data from [26]. For $L = 1$: continuous and dashed curves, our calculation of δ_1^- and δ_1^+, respectively; (▽) and (△) data points for δ_1^- and δ_1^+ from [26].

of krypton atoms. In the relativistic approximation without allowance for polarization interaction (and also without allowance for exchange interaction at energies higher than 200 eV), Walker [5] determined the DCSs in a wide energy range (from 2 to 1500 eV) but the results were represented only graphically. Also, he tabulated the energies and angles of complete spin polarization of scattered electrons. We used these data to find the critical minima (thereafter, these minima are referred to as minima from [5]). In [6], the DCS values at energies from 20 to 3000 eV were calculated in terms of a local complex potential. The data for ten energy values from the interval 20–500 eV were tabulated. In [14], elastic scattering of electrons by krypton atoms at low energies (between 0.01 to 30 eV) was studied in the semirelativistic approach. When calculating the DCS minima, we used partial phase shifts given for $L = 0$–8 in [14] and asymptotic phase values (see, e.g., (8) in [3]) for $L \geq 9$. The authors of [15] evaluated the DCSs in the relativistic approximation in terms of a local potential at energies ranging from 10 to 50 eV. However, the results obtained in [15] are shown graphically only in a narrow angular range.

This process at low energies was thoroughly investigated in [16], where the calculations were carried out by treating exchange exactly and including only the dipole part of the polarization potential. The phase shifts are given for $L = 0$–6 at energies from 0 to 54.4 eV and the DCS values, for nine energies from the interval 3–50 eV. In [17], the data for elastic scattering of electrons by krypton atoms were refined by taking into account the dynamic distortion effects. However, only the energy dependences of the integral cross sections are tabulated in that work.

In this work, we calculate the energy dependences of the angular positions of DCS minima and find the critical minima of the DCSs of elastic electron scattering by krypton atoms at energies up to 500 eV.

CALCULATION METHOD AND DISCUSSION OF RESULTS

The scattering cross sections were calculated by the same theoretical approach as in [3]. As an electron–atom interaction potential, we took a phenomenological real potential $V(r)$ (see Eq. (5) in [3]). The parameters of the static potential $V_s(r)$ and the electron density $\rho(r)$ for a krypton atom were taken from [19], where they were calculated by the Hartree–Fock method: ${}^a\gamma_2 = -0.9534$ and ${}^a\gamma_1 = 1 - {}^a\gamma_2$ (dimensionless parameters); ${}^a\lambda_1 = 6.029$, ${}^a\lambda_2 = 52.84$, ${}^b\lambda_1 = 14.032$, ${}^b\lambda_2 = 38.138$, ${}^b\lambda_3 = 2.174$, ${}^b\gamma_1 = -16.23$, ${}^b\gamma_2 = -28.297$, and ${}^b\gamma_3 = 0.7832$ (these parameters are expressed in units of a_0^{-1}, where a_0 is the first Bohr radius of a hydrogen atom). The electron density and the ionization potential of a krypton atom, $I = 13.9997$ eV [20], are used to calculate the local exchange potential $V_e(r)$. The dipole polarizability of a krypton atom, $\alpha_d = 16.74 a_0^3$, which is necessary for calculation of the polarization potential

$$V_p(r) = -\frac{\alpha_d}{2r^4}\left\{1 - \exp\left[-\left(\frac{r}{R_c}\right)^6\right]\right\},$$

was taken from [21]. As in [3], the parameter R_c appearing in the expression for $V_p(r)$ was calculated from the condition for the well-known Ramsauer–Townsend minimum in the integral cross section of slow electron scattering by inert gas atoms (see, e.g., [22, 23] and references therein). For several values of R_c, the energy dependence of the low-energy *s*-wave phase shift δ_0 was evaluated with the variable phase method [24, 25]. It was found that, with $R_c = 3.2a_0$ (Fig. 1), the phase shift δ_0 first increases from 12.59 rad at a collision energy $E = 0.001$ eV to 12.64 rad at $E = 0.07$ eV and then drops to 12.57 rad $\approx 4\pi$ at $E = 0.41$ eV. Eventually, we observed a deep minimum of the *s*-wave partial

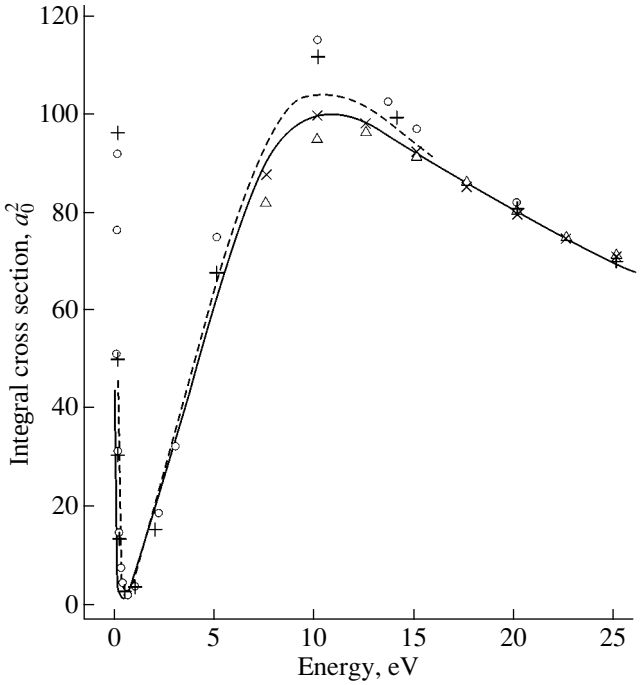

Fig. 2. Energy dependence of the integral cross section of electron scattering by krypton atoms. Data points (×) and (△) are taken from [27] and [28], respectively. The solid curve refers to our calculation; dashed line is taken from [4]; and symbols (+) and (○) are analytical values from [14] and [17], respectively.

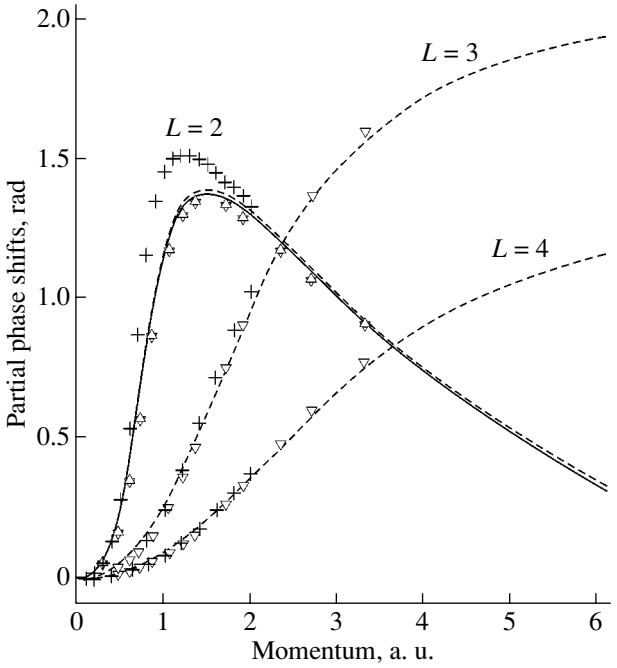

Fig. 3. *d*-, *f*-, and *g*-wave phase shifts vs. incident electron momentum (the *d* phase is given for $\delta_2 - \pi$). For all *L*, the dashed curve is our calculation of δ_L^-, (▽) δ_L^- from [26], the dash-and-dot curve is taken from [4], and (+) data from [16]. For $L = 2$: the solid curve is our calculation of δ_2^+ and (△) δ_2^+ from [26].

cross section, which gave rise to the Ramsauer–Townsend minimum at 0.42 eV of the integral cross section (Fig. 2). In [23], the minimum value of the experimental cross section was estimated as $(1.7 \pm 0.5)a_0^2$ at $E = 0.66 \pm 0.29$ eV. This value coincides with our value, $1.3a_0^2$ at 0.42 eV, within the measurement error in both energy and cross section.

Figure 1 shows that, starting from $k = 0.38$ a.u. (we use the atomic units, so that $e = m_e = \hbar = 1$), our energy dependences of the phase shifts δ_0 and δ_1 agree well with the calculations in [4, 16] and with the relativistic calculation [26]. For the orbital moments $L = 3$ and 4, the agreement with the cited works is also satisfactory (Fig. 3). For the *d*-wave phase shift, we obtained good agreement with the data of [26] (Fig. 3). It was noted [16] that the difference between the phase shifts found by various techniques is the greatest when $L = 2$ and the energy varies between 6 and 50 eV. The sharp (resonance-like) growth of the *d*-wave phase shift at energies between 1 and 20 eV causes a maximum at 10 eV in the integral cross section. As follows from Fig. 2, our calculation is in good agreement with the experiment [27]. The fact that the maximum of the cross section at 10 eV in [16, 17] is higher than the experimental value by more than 20% implies that the *d*-wave phase shift at this energy has a less steep slope than that reported in [16, 17]. In [4], the maximal scattering cross section is higher than the experimental value by only 5%. As follows from Fig. 3, the *d* phase calculated in [4] also has a less steep slope than in [16, 17].

Table 1 compares the partial phase shifts for $L = 0$–3 obtained in this paper with those obtained by nonrelativistic *R*-matrix [4], semirelativistic [14], and relativistic [26] calculations. In [14, 26], a krypton atom was described in terms of relativistic Hartree–Fock wave functions. In all the three works cited, exchange interaction was taken into account exactly. In [4, 14], polarization interaction was included via the dipole polarizability; in [26], via a model polarization potential with the dipole and quadrupole polarizabilities taken into consideration. As follows from Table 1, the *s* phases calculated in [4, 14, 26] are virtually coincident. Hence, the difference between the nonrelativistic and relativistic approaches to describing a krypton atom is insignificant.

For comparison with [4], Table 1 also lists the phase shift values evaluated without allowance for spin–orbit interaction. Our value of δ_0 is seen to deviate from that in [4] by no more than 0.09%. For δ_1, the difference is 0.5%; for δ_2, 0.03% at 5 eV and 1.3% at 10 eV. Thus, we may conclude that the parametrized $V_s(r)$ and $\rho(r)$, as well as local $V_e(r)$, used in this work, adequately

Table 1. Partial phase shifts δ_L (rad) of the waves for elastic scattering of electrons by krypton atoms

δ_L	E = 5 eV				E = 10 eV				E = 100 eV		E = 150 eV	
	[4]	[14]	[26]	our calculation	[4]	[14]	[26]	our calculation	[26]	our calculation	[26]	our calculation
δ_0	11.77	11.797	11.76	11.78	11.28	11.312	11.284	11.29	9.0420	9.011	8.5868	8.551
δ_1	9.013	–	–	9.043	8.661	–	–	8.701	–	6.902	–	6.523
δ_1^-	–	9.097	9.062	9.072	–	8.736	8.703	8.734	6.9126	6.935	6.537	6.556
δ_1^+	–	9.066	9.029	9.028	–	8.697	8.662	8.685	6.8638	6.886	6.488	6.507
$\Delta\delta_1$	–	0.031	0.033	0.044	–	0.039	0.041	0.049	0.0488	0.049	0.049	0.049
δ_2	3.564	–	–	3.565	4.155	–	–	4.104	–	4.237	–	4.064
δ_2^-	–	3.629	3.492	3.566	–	4.290	4.016	4.108	4.2110	4.244	4.053	4.071
δ_2^+	–	3.635	3.494	3.564	–	4.289	4.013	4.100	4.1988	4.232	4.040	4.059
$\Delta\delta_2$	–	–0.006	–0.002	0.002	–	0.001	0.003	0.008	0.0122	0.012	0.013	0.012
δ_3	0.07373	0.0692	–	0.07469	0.1371	0.1594	–	0.1801	–	1.349	–	1.559
δ_3^-	–	–	0.0657	0.07469	–	–	0.1532	0.1801	1.3633	1.350	1.5936	1.560
δ_3^+	–	–	0.0660	0.07469	–	–	0.1522	0.1801	1.3629	1.349	1.5936	1.559
$\Delta\delta_3$	–	–	–0.0003	0	–	–	0.001	0	0.004	0.001	0	0.001

Note: Spin–orbit split of the phase shift is $\Delta\delta_L = \delta_L^- - \delta_L^+$, where $\delta_L^\pm \equiv \delta_L^{L \pm 1/2}$.

describe static–exchange ($V_s + V_e$) electron–atom interaction.

Comparing our calculation of δ_0 with the relativistic calculation made in [26], we note that the difference is no more than 0.09% at low energies and no more than 0.42% at high energies. For *p*, *d*, and *f* waves, the difference between our calculations and those in [26] is, respectively, 0.35, 2.2, and 15.5% at 10 eV; for 150 eV, the respective differences are lower: 0.29, 0.47, and 2.2%. This leads us to conclude that the difference between our calculations and calculations [26] arises from using different model polarization potentials rather than from incomplete taking account of relativistic effects.

As follows from Table 1, our calculation, in general, agrees well with the calculation made in [14]. As applied to the *d* phase, the difference is 4.4% at 10 eV. Figure 2 shows that the maximal integral cross section obtained in [14] at 10 eV is 10% higher than the experimental value obtained in [27]. As was already noted, the *d* phase in [27] grew faster than in [4, 26] and in our work at this energy.

From the expression for the spin-flip scattering amplitude $g(\theta)$ (see, e.g., expression (3) in [3]), it follows that this amplitude depends on the spin–orbit split $\Delta\delta_L$ of the phase shifts. Table 1 demonstrates that *p* and *d* waves make a major contribution to this amplitude and that $\Delta\delta_{1,2}$ obtained in this work at 100 and 150 eV are the same as those obtained in [26].

Thus, the phase shifts of the other waves (other than the *d* wave) obtained by us with the local potential $V(r)$ (involving the parameter R_c found from the above requirements for the low-energy behavior of the *s* wave phase shift) also agree well with those obtained with the *R*-matrix approach [4] and calculations [14, 16, 26], which were made in various approximations, over a wide energy range.

Since the values of the phase shifts found in [16, 26] for $L \geq 7$ were asymptotic, we compared the energy dependences of δ_7 that were derived from the phase equation and from formula (8) in [3]. The discrepancy between the curves becomes tangible even at 50 eV. Starting from 120 eV, this discrepancy increases with energy, and, at 500 eV, the asymptotic value of δ_7 exceeds the calculation by about 30%. Clearly, for $L >$

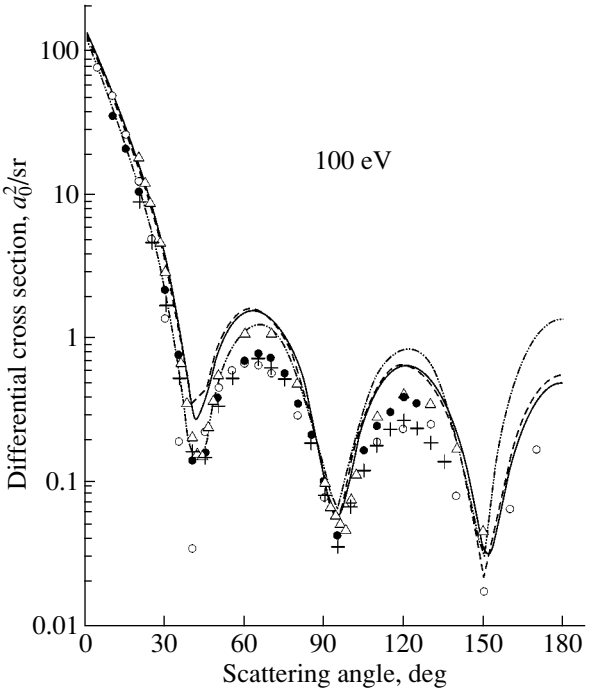

Fig. 4. Angular dependence of the DCS of electron scattering by krypton atoms at 100 eV. Data points (△), (+), and (●) are taken from [8], [10], and [11], respectively. The solid curve refers to our calculation, the dash-and-dot line is taken from [4], the dashed curve is from [18], and symbols (○) are analytical values from [6].

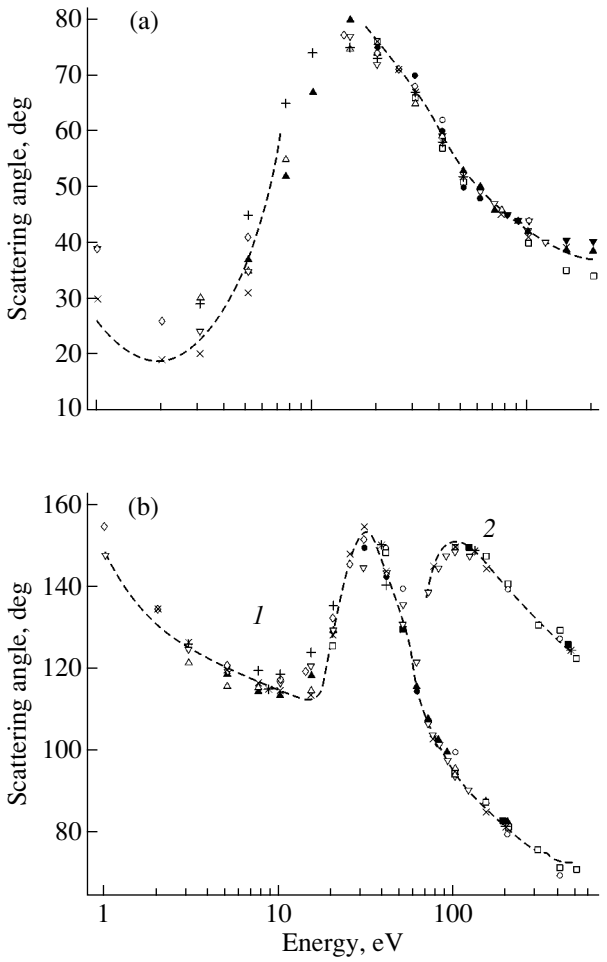

Fig. 5. Energy dependences of the angular positions of the (a) low-angle and (b) high-angle DCS minima for elastic scattering of electrons by krypton atoms. Data points: (■) [7], (○) [8], (▼) [9], (△) [10], (▲) [11], and (●) [13]. Analytical values: (▽) [4], (×) [18], (∗) [5], (□) [6], (◇) [14], and (+) [16]. The dashed line is our calculation.

7, this discrepancy will also become noticeable at a certain energy.

The number of partial waves that is calculated with the phase equation depends on the incident electron energy. For 1 eV, the number of waves is six; for 500 eV, 32 waves arise. Therefore, for 500 eV, we used the asymptotic phases only from $L = 32$ (versus $L = 20$ for 150 eV). A total of 300 partial phase shifts were used in DCS calculation.

As was mentioned in the Introduction, the DCS of electron scattering by a krypton atom may have three minima at a certain energy. For 100 eV, this is illustrated in Fig. 4. As is seen, theoretical and experimental angular positions of the minima are is good agreement. The minimum at angles ≤80° will be called the low-angle minimum (minimum 1); two others, high-angle minima (minima 2 and 3). Figure 5 shows the energy dependences of the angular positions of the corresponding minima.

Comparing the positions of minimum 1 (Fig. 5a) found experimentally [6, 8–11, 13] and theoretically [4, 14, 16, 18], we may infer that our calculation follows the general run of these dependences. The exception is the energy range from 7.5 to 15 eV, where minimum 1 calculated by us and in [4, 14, 18] is smoother than in [10, 11, 16]. Note that, at these energies, the DCS varies smoothly in the angular range 60°–80° and the discrepancy between our calculation and experimental values [10, 11] is within the experimental error. From 20 eV on, minimum 1 again becomes distinct in both experimental and theoretical cross sections, the discrepancy between the positions of the minimum being is as small as 4°. Such a small discrepancy persists up to 100 eV. Figure 5a shows the angular positions of the minimum to 200 eV. At still higher energies, the low-angle minimum flattens and disappears in the experiment [8], calculations [5, 6], and in our calculation (starting from 194 eV).

As follows from Fig. 5b, the angular position of minimum 2 (curve *1*) changes from 148.8° at 1 eV to 112.8° at 15 eV. Then, the angle of the minimum increases to 153.5° at 30 eV and decreases again to 73.1° at 500 eV.

From 69 eV, minimum 3 appears in the angular dependence of the DCS. Its angular position changes from 138.2° at 69 eV to 151.6° at 100 eV and reaches 123.9° at 500 eV (curve *2*). The DCSs calculated in [4–

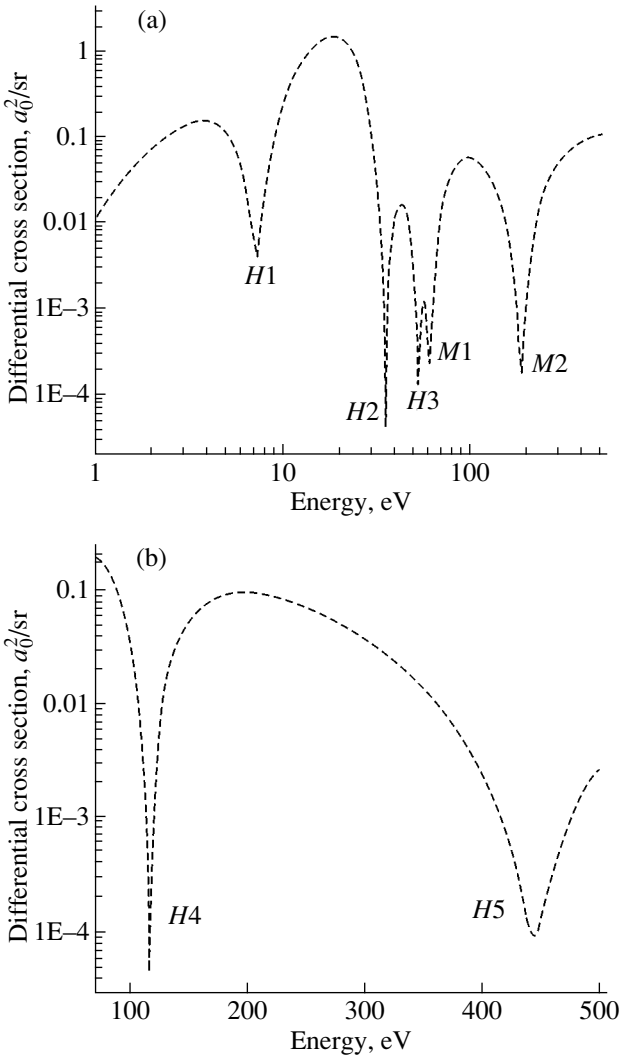

Fig. 6. Energy dependences of the high-angle DCS minima for elastic scattering of electrons by krypton atoms. The angular positions of the minima correspond to (a) curve *1* and (b) curve *2* in Fig. 5b. *H*1 (7.4 eV, 117.15°), *H*2 (35.9 eV, 149.70°), *H*3 (53.6 eV, 128.15°), *M*1 (61.4 eV, 114.14°), *M*2 (187 eV, 82.46°), *H*4 (116.5 eV, 150.71°), and *H*5 (444.2 eV, 125.86°) are critical points.

6, 18] for energies between 70 and 200 eV also have three minima. In [10], the experimental DCS values are given for angles to 135°; in [8, 12, 13], to 150°. At energies of 75 eV in [10], 80 eV in [13], and 100 eV in [8, 10, 11], the DCS show high-angle maxima at 120°–130° and then drop at 125° in [11], 135° in [10], and 150° in [10, 13]. As the energy increases, the position of minimum 3 shifts toward lower angles. In [8], this minimum is distinctly seen even at 140 and 130° for 200 and 400 eV, respectively. Finally, Fig. 5b demonstrates the experimental [7] and analytical [5] positions of the critical minima. It is noteworthy that the position of minimum 3 found by us (curve *2*) is in good agreement with the positions of the minima found in [5, 7]. As follows from Fig. 5b, the experimental and analytical positions of minima 2 and 3 are in excellent agreement over the energy range 50–500 eV.

Calculation shows that minimum 2 flattens and disappears, starting from 640 eV. In the energy interval 500–630 eV, the DCS value in minimum 2 remains practically unchanged, $\sim 0.11 a_0^2/sr$. Within this energy interval, the angle of minimum 2 varies from 73° to 78°. As for minimum 3, our calculation shows that its angular position changes from 124° to 115° at energies between 500 and 800 eV. At these energies, the DCS value gradually increases from 0.0026 to $0.03 a_0^2/sr$.

The high-angle minima turned out to be the deepest (see, e.g., Fig. 4). Figure 6 demonstrates the energy dependence of the DCS values in minima 2 and 3 (the angular positions of these minima are given by curves *1* and *2*, respectively, in Fig. 5b). Seven least values of the DCS thus found are referred to as critical minima of the DCS of electron scattering by krypton atoms. The critical values of energies, E_C, and angles, θ_C, are compared with experimental data currently available [7]. As we noted above, the points of complete spin polarization of electrons elastically scattered by krypton atoms were reported in [5]. At these points, the Sherman function $S(E, \theta) = \pm 1$. Since these points are arranged symmetrically about a critical minimum (cf., e.g., Tables 1 and 2 in [3]), we tried to estimate the values of E_C and θ_C that could be obtained in [5]. These estimates are listed in Table 2, from which is follows that the angular positions of the minima *H*2 and *H*4, as well as the energy positions of *M*2 and *H*5, are in good agreement with the experiment [7]. The position of the minimum *H*1 agrees well with the position of the high-angle minimum at 7.5 eV, which was observed at 116° and 115° in experiments [10] and [11], respectively, and also at 117° and 120° in theoretical works [18] and [16], respectively.

Note that the values of all E_C in [5] exceed those found in this work. Possibly, this is because polarization interaction in [5] was disregarded.

Jansen and de Heer [9] referred to the private communication by Walker (1974), where he performed calculations including a polarization potential similar to that used in this work. They compared their results with the results of Walker, which take into account both exchange and polarization interactions, and with his results including only exchange interaction (given in parentheses below). For the former case, the DCS ratio at 100 eV equals 0.96 (1.99) at 5° and 0.89 (1.32) at 10°. Evidently, inclusion of the polarization potential brings the theoretical and experimental results closer together. We compared our calculations with the results of [9] and found that, at 100 eV, the associated ratios equal 0.93 at 5° and 0.84 at 10°; that is, they are almost the same as in Walker's communication. Note that the value of the parameter R_c (appearing in the expression for the polarization potential) used by Walker ($R_c = 3a_0$)

Table 2. Energy, E_C, and angular, θ_C, positions of the critical minima

Critical minima	Our calculation		Other results		
	E_C, eV	θ_C, deg	E_C, eV	θ_C, deg	refs.
*H*1	7.4	117.15	8.6	115.4	[5]
*H*2	35.9	149.70	38.7 ± 0.6	149.70 ± 0.01	[7]
			37.9	150.7	[5]
*H*3	53.6	128.15	–	–	–
*M*1	61.4	114.14	–	–	–
*H*4	116.5	150.71	121.6 ± 0.8	149.98 ± 0.05	[7]
			128.5	149.3	[5]
*M*2	187	82.46	188.0 ± 0.9	83.2 ± 0.3	[7]
			195	81.9	[5]
*H*5	444.2	125.86	444.2 ± 1.4	126.6 ± 0.20	[7]
			459	125.2	[5]

was also calculated from the energy of the Ramsauer–Townsend minimum. Since the polarization potentials $V_p(r)$ in our work and in Walker's communication are virtually the same, it may be argued that the absence of $V_p(r)$ in [5] causes a slower growth (compared with our results; see Fig. 3) of the phase shifts for $L \geq 2$ (primarily, the phase shift of the *d* wave), which cannot help affecting the energy positions of the critical minima in [5]. Note that, in our calculation (e.g., for $E = 7.4$ eV), the contribution of the *d* wave partial cross section to the integral section amounts to 57% (for the effect of the polarization potential on the energy dependence of the phase shifts, see, e.g., [29]).

We did not report here the energy dependences of the DCS low-angle minima, since these minima exceed $0.01 a_0^2/sr$ at $E \geq 1$ eV (see Fig. 6). For example, at $E = 1$ eV, the low-angle minimum is observed at 25.7°. At this point, the direct scattering amplitude magnitude squared is $|f|^2 = 1.2 \times 10^{-2} a_0^2/sr$ and the exchange amplitude magnitude squared is $|g|^2 = 7.7 \times 10^{-4} a_0^2/sr$. Note that, at the deepest high-angle minimum *H*1, $|f|^2 = 7.5 \times 10^{-6} a_0^2/sr$ and $|g|^2 = 4.2 \times 10^{-3} a_0^2/sr$; that is, $|g|^2$ is almost three orders of magnitude higher than $|f|^2$. For all the critical minima found in this work, the condition $|g|^2 \geq |f|^2$ is fulfilled in the neighborhood of the critical angles θ_C. This means (see, e.g., [3]) that complete spin polarization of scattered electrons may be found in the energy and angular vicinity of these minima.

REFERENCES

1. R. Panajotović, D. Filipović, B. Marinković, *et al.*, J. Phys. B **30**, 5877 (1997).
2. D. Filipović and B. Marinković, in *Proceedings of the 20th International Conference on Physical Electronic and Atomic Collisions, Vienna, 1997*, p. TH005.
3. V. I. Kelemen, Zh. Tekh. Fiz. **72** (9), 13 (2002) [Tech. Phys. **47**, 1083 (2002)].
4. W. C. Fon, K. A. Berrington, and A. Hibbert, J. Phys. B **17**, 3279 (1984).
5. D. W. Walker, Adv. Phys. **20**, 257 (1971).
6. I. E. McCarthy, C. J. Noble, B. A. Phillips, and A. D. Turnbull, Phys. Rev. A **15**, 2173 (1977).
7. J. Kessler, J. Liedtke, and C. B. Lukas, in *Proceedings of the International Summer School and Symposium on the Physics of Ionized Gases, Dubrovnik, 1976*, Ed. by B. Navinšek (J. Stefan Inst., Ljubljana, 1976), p. 61.
8. J. F. Williams and A. Crowe, J. Phys. B **8**, 2233 (1975).
9. R. H. J. Jansen and F. J. de Heer, J. Phys. B **9**, 213 (1976).
10. S. K. Srivastava, H. Tanaka, A. Chutjian, *et al.*, Phys. Rev. A **23**, 2156 (1981).
11. A. Danjo, J. Phys. B **21**, 3759 (1988).
12. D. Filipović, S. Kazakov, B. Marinković, *et al.*, in *Contributed Papers of the International Conference on Physics of Ionized Gases, Sibenik, 1986*, pp. 3–6.
13. S. M. Kazakov, Doctoral Dissertation in Mathematics and Physics (Minsk, 1991).
14. L. T. Sin Fai Lam, J. Phys. B **15**, 119 (1982).
15. F. Kemper, B. Awe, F. Rosicky, and R. Feder, J. Phys. B **16**, 1819 (1983).
16. R. P. McEachran and A. D. Stauffer, J. Phys. B **17**, 2507 (1984).
17. D. J. R. Mimnagh, R. P. McEachran, and A. D. Stauffer, J. Phys. B **26**, 1727 (1993).

18. J. E. Sienkiewicz and W. E. Baylis, J. Phys. B **25**, 2081 (1992).
19. T. G. Strand and R. A. Bonham, J. Chem. Phys. **40**, 1686 (1964).
20. A. A. Radtsig and B. M. Smirnov, *Reference Data on Atoms, Molecules, and Ions* (Énergoatomizdat, Moscow, 1986; Springer-Verlag, Berlin, 1985).
21. T. M. Miller and B. Bederson, in *Advances in Atomic and Molecular Physics*, Ed. by D. R. Bates and B. Bederson (Academic, New York, 1977), Vol. 13, pp. 1–55.
22. L. S. Frost and A. V. Phelps, Phys. Rev. A **136**, 1538 (1964).
23. Yu. K. Gus'kov, R. V. Savvov, and V. A. Slobodyanyuk, Zh. Tekh. Fiz. **48**, 277 (1978) [Sov. Phys. Tech. Phys. **23**, 167 (1978)].
24. F. Calogero, *Variable Phase Approach to Potential Scattering* (Academic, New York, 1967; Mir, Moscow, 1972).
25. V. V. Babikov, *The Variable Phase Method in Quantum Mechanics* (Nauka, Moscow, 1988) [in Russian].
26. J. E. Sienkiewicz and W. E. Baylis, J. Phys. B **24**, 1739 (1991).
27. K. Jost, P. G. F. Bisling, F. Eschen, *et al.*, in *Proceedings of the 13th International Conference on Physics of Electronic and Atomic Collisions, Berlin, 1983*, p. 91.
28. M. S. Dababneh, Y. F. Hsieh, W. E. Kauppila, *et al.*, Phys. Rev. A **26**, 1252 (1982).
29. H. A. Kurtz and K. D. Jordan, J. Phys. B **14**, 4361 (1981).

Translated by V. Isaakyan

Technical Physics, Vol. 49, No. 6, 2004, pp. 669–676. Translated from Zhurnal Tekhnicheskoĭ Fiziki, Vol. 74, No. 6, 2004, pp. 8–15.

GASES AND LIQUIDS

Capillary Disintegration of a Configuration Formed by Two Viscous Ferrofluids Surrounding a Current-Carrying Conductor and Having a Cylindrical Interface

V. M. Korovin

Research Institute of Mechanics, Moscow State University, Vorob'evy Gory, Moscow, 119992 Russia
e-mail: korovin@imec.msu.ru

Received February 26, 2003; in final form, December 2, 2003

Abstract—The effect is studied of a magnetic field with circular lines of force on the capillary instability of the cylindrical interface between two immiscible ferrofluids with different magnetic susceptibilities but equal densities and viscosities. A dispersion relation is obtained using a modified equation of motion, and the limiting conditions for instability development (high Ohnesorge numbers) are analyzed. © *2004 MAIK "Nauka/Interperiodica".*

INTRODUCTION

Capillary disintegration of a cylindrical sheath that consists of an air-surrounded high-viscosity fluid covering a thin filament has long been the subject of extensive investigation [1, 2]. A natural example of such an object is an as-spun web [1].

The ferrohydrodynamic analogue [3–6] of the classical experiments [1] clearly demonstrates the efficiency of a magnetic field in controlling the capillary disintegration of a cylindrical layer of a magnetic fluid covering a long circular current-carrying conductor. Unlike a nonmagnetic fluid used in the experiments [1, 2], a ferromagnetic fluid experiences the action of bulk magnetic forces, which are directed to the axis of symmetry and confine the layer to the conductor surface. In the experiments [3, 4], the outer interface was kept strictly cylindrical by eliminating the effect of the gravitational force on the ferrofluid. To this end, the conductor with the overlayer was immersed in a high-viscosity nonmagnetic fluid having the same density as the ferrofluid of the layer to produce the effect of hydrodynamic weightlessness. In these modifications of the classical experiments, the ferrofluid layer is several orders of magnitude thicker than the air-surrounded sheath of a nonmagnetic fluid around the filament.

The stabilizing effect of a magnetic field (induced by the current passing through the conductor) on the capillary disintegration of a cylindrical configuration formed by viscous magnetic and nonmagnetic fluids is the most convenient to treat in terms of a model that considers a cylindrical layer of a nonviscous ferrofluid surrounded by a gas of negligible density [4–6]. The use of such a simplification in experiments with two viscous fluids has made it possible to evaluate the critical magnetic Bond number Bo_m (which was found to be equal to unity), which separates the stable, $\mathrm{Bo}_\mathrm{m} > 1$, and unstable, $\mathrm{Bo}_\mathrm{m} < 1$, configurations. It has been concluded that the wavelength λ_* of the most rapidly growing harmonic (this harmonic defines the typical size of drops upon the disintegration of the continuous layer) is almost independent of the thickness of the layer. It should be noted in this context that a more complex model that includes the viscosity of the ferrofluid, which produces the cylindrical layer, and a finite density of the surrounding nonviscous fluid exhibits an appreciable dependence of the parameter λ_* on the thickness of the layer [7].

In this work, we study capillary instability of a two-fluid system formed by immiscible ferrofluids separated by a cylindrical interface at the zero time. It is assumed that they have the same densities and viscosities but the magnetic susceptibility of the inner fluid is higher. The effect of a magnetic field and the thickness of the layer on λ_* is considered in the limiting case of capillary instability development when the contribution of inertial forces is negligible compared with that of viscous forces (high Ohnesorge numbers).

PROBLEM DEFINITION

We are dealing with a continuous layer of a quiescent ferrofluid with a constant thickness d covering a straight cylindrical conductor of radius c that carries a time-invariable current I inducing a magnetic field $\mathbf{H}$. The layer is surrounded by a immiscible ferrofluid that fills a cuvette. The walls of the cuvette and the free surface of the ferrofluid in the cuvette are far away from the lateral surface of the layer. It is assumed the both liquids are Newtonian and have equal dynamic viscosity coefficient η and density ρ. At the same time, their absolute magnetic susceptibilities (μ_1 and μ_2 for the inner and outer fluids, respectively) differ from each

1063-7842/04/4906-0669$26.00

other and depend only on the magnetic field magnitude, with $\mu_1(H) > \mu_2(H)$.

Let us introduce the cylindrical coordinate system (r, ϑ, z) such that the z axis as aligned with the conductor axis. Vectors $\mathbf{e}_r$, $\mathbf{e}_\vartheta$, and $\mathbf{e}_z$ are the unit vectors along the coordinates r, ϑ, and z. In this coordinate system, the interface between the fluids (which are in hydrostatic equilibrium) is described by the equation $r = a$, where $a = c + d$, and the magnetic field is azimuthal: $\mathbf{H}(r) = \mathbf{H}e_\vartheta$; so, in the domain occupied by the fluids, $r > c$, we have $H = I/(2\pi r)$. Next, the magnetic susceptibility $\chi_0(H)$, the magnetization $\mathbf{M}_0$, and the bulk magnetic force density $\mathbf{f}_0$ in this two-fluid system are given by

$$\chi_0 = \chi_1(H)[1 - \theta(z - a)] + \chi_2(H)\theta(r - a),$$
$$\mathbf{M}_0 = \chi_0\mathbf{H}, \quad \mathbf{f}_0 = \mu_0 M_0 \operatorname{grad} H = -\frac{\mu_0\chi_0 I^2}{4\pi^2 r^3}\mathbf{e}_r, \tag{1}$$

where $\chi_j(H) = \mu_j/\mu_0 - 1$ are the magnetic susceptibilities of the inner ($j = 1$) and outer ($j = 2$) fluids; $\mu_0 = 4\pi \times 10^{-7}$ H/m is the magnetic constant; and $\theta(r - a)$ is the Heaviside function:

$$\theta(r - a) = \begin{cases} 0 & \text{for} \quad r < a \\ 1 & \text{for} \quad r > a. \end{cases}$$

Obviously, the magnetic force is a potential in hydrostatic equilibrium.

It is known [3–6] that, in experiments, the static configuration under consideration can be implemented only if the magnetic Bond number $\mathrm{Bo}_\mathrm{m} = \mu_0(4\pi^2\alpha a)^{-1}I^2(\chi_1 - \chi_2)|_{H = H(a)} > 1$ (hereafter, a is the surface tension coefficient). For Bond numbers smaller than unity (the Bond number decreases with decreasing the current I), the cylindrical interface becomes unstable and the continuous cylindrical layer of the inner fluid disintegrates into drops, which are strung on the conductor like beads.

Consider the case where surface tension forces give rise to joint axisymmetric motion of immiscible fluids when the interface between them is a cylindrical surface weakly distorted in the longitudinal direction that is described by the equation $r = r_s(z, t)$ (t is the time). Let $r_s(z, t) = a + \zeta(z, t)$, where $\zeta(z, t)$ describes a small perturbation ($|\zeta(z, t)/a| \ll 1$) of the initial radius of the cylindrical interface. The function $\zeta(z, t)$ is *a priori* unknown and is to be found during the solution of the problem.

For the axisymmetric motion of the fluids, a distortion of the initially cylindrical interface between media with different magnetic susceptibilities does not disturb the initial magnetic field, since circular lines of force do not intersect the disturbed interface. In this case, however, the magnetic fluids are redistributed, because fluid particles with different susceptibilities cross the imaginary geometrical surface $r = a$, which coincides with the initial shape of the interface. Then, the magnetic susceptibility $\chi(H)$, the magnetization $\mathbf{M}$, and the bulk magnetic force density $\mathbf{f}$ in the motion-disturbed two-fluid system are given by expressions other than (1):

$$\chi = \chi_1(H)[1 - \theta(rr - r_s)] + \chi_2(H)\theta(r - r_s),$$
$$\mathbf{M} = \chi\mathbf{H}, \quad \mathbf{f} = -\frac{\mu_0\chi I^2}{4\pi^2 r^3}\mathbf{e}_r. \tag{2}$$

It is easy to check that

$$\operatorname{curl}\mathbf{f} = \Gamma\delta(r - r_s)\mathbf{e}_\vartheta, \quad \Gamma = \frac{\mu_0(\chi_2 - \chi_1)I^2}{4\pi^2 r^3}\frac{\partial\zeta}{\partial z}, \tag{3}$$

where $\delta(r - r_s)$ is the Dirac function.

Thus, a distortion of the initial cylindrical surface (because of which $\partial\zeta/\partial z \neq 0$) due to capillary forces leads to magnetic force vorticity ($\operatorname{curl}\mathbf{f}$) at the interface, while beyond the interface, the magnetic force remains potential.

Since the fluids are incompressible, the velocity field $\mathbf{u}(r, z, t) = (u_r, 0, u_z)$ are solenoidal:

$$\operatorname{div}\mathbf{u} = 0. \tag{4}$$

The features of the situation under study is the constant density of the medium, the constant dynamic viscosity coefficient throughout the two-fluid system, and the absence [8] of pairs of lumped external forces [9] on the interface $r = r_s(z, t)$. Because of this, we may depart from the standard linear problem of hydrodynamic stability of two immiscible fluids with a cylindrical interface [7]. Recall that this problem requires that differentiable solutions to the hydrodynamic equations be found separately in either of the domains occupied by the fluids with the subsequent joining of these solutions by means of kinematic and dynamic conditions at the interface.

In terms of the linear theory, these conditions are set on the undisturbed interface given by $r = a$. Analysis shows [10] that, in our case, the derivatives $\partial u_r/\partial r$, $\partial u_r/\partial z$, $\partial u_z/\partial r$, and $\partial u_z/\partial z$ are continuous at the interface. In this case, the dynamic condition on the interface between the ferrofluids that reflect the balance of normal forces (stresses) acting on the opposite sides of the interface does not involve viscous forces [6]. As a result, we arrive at the situation typical of nonviscous fluids: a pressure shock at the interface depends on the surface tension coefficient α and mean curvature K of the interface and does not depend on the velocity field:

$$p_2(a, z, t) - p_1(a, z, t) = -2\alpha K,$$
$$K = \frac{1}{2}\left(\frac{1}{a} - \frac{\zeta}{a^2} - \frac{\partial^2\zeta}{\partial z^2}\right) > 0, \tag{5}$$

where $p_1(r, z, t)$ and $p_2(r, z, t)$ are the pressures in the inner ($c < r < a$) and outer ($a < r < \infty$) ferrofluids, respectively.

In our approximation, the deflection of the normal to the interface from the radial direction is ignored; therefore, the stress $\mathbf{f}_c$ due to capillary forces acting on the interface from the outer ferrofluid can be written, in view of (5), as $\mathbf{f}_c(z, t) = -2\alpha K\mathbf{e}_r$.

In contrast to the standard statement of the problem [7], we consider the two-fluid system as a unified medium. For such a medium, the pressure can be written as

$$p(r, z, t) = \begin{cases} p_1(r, z, t) & \text{for} \quad r < a \\ p_2(r, z, t) & \text{for} \quad r > a. \end{cases}$$

As in [11], capillary forces will appear directly in the equation of motion. To do this in the framework of the linear theory implies [10] that the modified differential equation of motion must contain the stress $\mathbf{f}_c$ localized at the interface $r = a$. Neglecting the terms quadratic in velocity, one can write the equation of motion for the medium considered in the form

$$\rho\frac{\partial \mathbf{u}}{\partial t} = -\text{grad}\, p + \eta\Delta\mathbf{u} + \mathbf{f} + \rho\mathbf{g} + \mathbf{F}_c, \qquad (6)$$

$$\mathbf{F}_c = \mathbf{f}_c\delta(r - a), \quad \mathbf{f}_c = -2\alpha K\mathbf{e}_r. \qquad (7)$$

Here, $\mathbf{g} = (g_r, g_\vartheta, g_z)$ is the free-fall acceleration, $\mathbf{F}_c$ is the density of bulk forces due to the capillary effect, and Δ is the Laplacian. In view of (6), it is easy to show that condition (5) is fulfilled automatically for a solution $(\mathbf{u}, p)$ to the set of equations (4) and (6) provided that the velocity field is continuous. Thus, if modified equation of motion (6) is used, the need for dynamic condition (5) is eliminated.

On the surface of the conductor, the impermeability and attachment conditions must be met:

$$u_r(c, z, t) = 0, \quad u_z(c, z, t) = 0. \qquad (8)$$

The linearized kinematic condition at the interface ($r = a$) has the form

$$\frac{\partial\zeta}{\partial t} = u_r(a, z, t). \qquad (9)$$

Physically, equality (9) means that the interface consists of the same fluid particles. Note also that $\mathbf{u} \longrightarrow 0$ at $r \longrightarrow \infty$, which follows from the physical essence of the problem.

Let us exclude the pressure from (6) to simplify the mathematics. Applying the curl operator to (6) and taking into account (7) yields

$$\frac{\partial\boldsymbol{\omega}_\nu}{\partial t} - \nu\Delta\boldsymbol{\omega}_\nu = \frac{1}{2\rho}(\text{curl}\mathbf{f} + \text{curl}\mathbf{F}_c), \quad \nu = \frac{\xi}{\rho}, \qquad (10)$$

$$\text{curl}\mathbf{F}_c = \alpha\left(\frac{1}{a^2}\frac{\partial\zeta}{\partial z} + \frac{\partial^3\zeta}{\partial z^3}\right)\delta(r - a)\mathbf{e}_\vartheta, \qquad (11)$$

where $\boldsymbol{\omega}_\nu = \frac{1}{2}\text{curl}\mathbf{u}$ is the velocity vortex vector.

Equation (10) describes diffusion of vorticity in a moving two-fluid system. Vorticity arises when the fluid is attached to the solid conductor and also when there exist vorticity sources, such as magnetic and capillary force vorticities (Eqs. (3) and (11), respectively), which appear on the right of (10).

Introducing the Stokes stream function $r\psi(r, z, t)$ into Eq. (4) yields

$$u_r = \frac{\partial\psi}{\partial z}, \quad u_z = -\frac{1}{r}\frac{\partial(r\psi)}{\partial r},$$

then, one readily finds that

$$\boldsymbol{\omega}_\nu = \frac{1}{2}\mathbf{e}_\vartheta L\psi, \quad \Delta\boldsymbol{\omega}_\nu = \frac{1}{2}\mathbf{e}_\vartheta LL\psi,$$

where

$$L = \frac{\partial^2}{\partial r^2} + \frac{1}{r}\frac{\partial}{\partial r} - \frac{1}{r^2} + \frac{\partial^2}{\partial z^2}.$$

With regard to these expressions, Eq. (10) in scalar form can be recast as

$$\left(L - \frac{1}{\nu}\frac{\partial}{\partial t}\right)L\psi = \frac{\alpha}{\eta a^2}\left\{\text{Bo}_m\left(\frac{a}{r}\right)^3\frac{\partial\zeta}{\partial z}\delta[r - a - \zeta(z, t)]\right.$$
$$\left. - \left(\frac{\partial\zeta}{\partial z} + a^2\frac{\partial^3\zeta}{\partial z^3}\right)\delta(r - a)\right\}. \qquad (12)$$

With regard to the stream function, kinematic condition (9) at the interface and condition (8) on the conductor surface take the form

$$\left.\frac{\partial\zeta}{\partial t} - \frac{\partial\psi}{\partial z}\right|_{r = a} = 0, \qquad (13)$$

$$\left.\frac{\partial\psi}{\partial z}\right|_{r = c} = 0, \quad \left.\frac{\partial\psi}{\partial r}\right|_{r = c} + \frac{\psi(c, z, t)}{c} = 0. \qquad (14)$$

Now, we turn to the set of differential equations (12) and (13) and study the time variation of its solution that satisfies boundary-value condition (14).

DISPERSION RELATION

Since the problem is axisymmetric, the operator method based on Hankel transformation [12] seems to be the most appropriate for finding a solution to Eq. (12). It is known that, for a piecewise continuous function $w(r)$ satisfying the general limitedness conditions [12], the Hankel inversion formulas of order n =

0, 1, 2, … are valid:

$$\mathcal{H}_n\{w(r)\} = \int_0^\infty w(r)J_n(sr)r\,dr \equiv W_n(s),$$
$$\mathcal{H}_n^{-1}\{W(s)\} = \int_0^\infty W_n(s)J_n(sr)s\,ds \equiv w(r), \quad (15)$$

where $J_n(sr)$ is the nth-order Bessel function.

The following equality is valid [12]:

$$\mathcal{H}_1\left\{\frac{d^2w}{dr^2} + \frac{1}{r}\frac{dw}{dr} - \frac{w}{r^2}\right\} = -s^2W_1(s). \quad (16)$$

We extend the definition of the function $\psi(r, z, t)$, setting it equal to $\psi(c, z, t)$ for $0 \le r \le c$, and introduce the designation

$$\mathcal{H}_1\{\psi(r, z, t)\} = \Sigma(s, z, t).$$

Applying the first-order Hankel transformation to Eq. (12) and taking into account (16), we get

$$\left(\frac{\partial^2}{\partial z^2} - \frac{1}{\nu}\frac{\partial}{\partial t} - s^2\right)\left(\frac{\partial^2}{\partial z^2} - s^2\right)\Sigma = \frac{\alpha J_1(sa)}{\eta a}\left\{\frac{\partial\zeta}{\partial z}\left[\frac{a^3\mathrm{Bo_m}}{(a+\zeta)^3} - 1\right] - a^2\frac{\partial^3\zeta}{\partial z^3}\right\}. \quad (17)$$

Neglecting quantities on the order of $|\zeta/a|$ and higher (i.e., quantities much smaller than unity), we arrive at a linear equation that describes the early stage of instability development, where the difference between the actual (time-varying) shape of the interface $r = r_s(z, t)$ and the initial static shape $r = a$ is as yet small:

$$\left(\frac{\partial^2}{\partial z^2} - \frac{1}{\nu}\frac{\partial}{\partial t} - s^2\right)\left(\frac{\partial^2}{\partial z^2} - s^2\right)\Sigma = \frac{\alpha J_1(sa)}{\eta a}\left[\frac{\partial\zeta}{\partial z}(\mathrm{Bo_m} - 1) - a^2\frac{\partial^3\zeta}{\partial z^3}\right]. \quad (18)$$

Physically, the transition from Eq. (17) to Eq. (18) means that the distribution of magnetic sources

$$\frac{1}{2\rho}\Gamma\delta(r - r_s)\mathbf{e}_\vartheta,$$

which are localized at the interface $r = r_s(z, t)$ and are a factor responsible for the velocity field vorticity, may be transferred from the surface $r = r_s(z, t)$ to the surface $r = a$ in terms of the linear the ory.

The coefficients of linear equations (13) and (18) do not depend on time; therefore, one may apply the Fourier transformation to study the behavior of a solution to linearized problem (12)–(14) [13]. In this case, using the inverse Fourier transformation, one constructs a solution as a superposition of partial solutions (normal modes) in which space variables and time are separated and the time dependence is specified by the factor $\exp(-i\omega t)$:

$$\zeta_k\exp[i(kz - \omega t)], \quad \Psi_k(r)\exp[i(kz - \omega t)], \quad \Sigma_k(s)\exp[i(kz - \omega t)], \quad i = \sqrt{-1}. \quad (19)$$

Here, ζ_k is the constant (the Fourier transform of the desired function $\zeta(z, t)$ at the zero time $t = 0$), k is the real parameter (wavenumber), and the function $\omega = \omega(k)$ is to be found during the solution of the problem.

After finding the function $\Sigma_k(s)$ by using the inverse Hankel transformation, the amplitude function $\Psi_p(r)$ is determined as a frequency solution to linearized inhomogeneous equation (12):

$$\Psi_p(r)\exp[i(kz - \omega t)], \quad \Psi_p(r) = \mathcal{H}_1^{-1}\{\Sigma_k(s)\}. \quad (20)$$

Substituting expressions (19) into Eqs. (13) and (18) and into boundary-value conditions (14) yields

$$\zeta_k\omega + k\Psi_k(a) = 0, \quad (21)$$

$$(s^2 + k^2)(s^2 + m^2)\Sigma_k(s) = \frac{i\alpha\kappa\zeta_k}{\eta a^2}QJ_1(sa), \quad (22)$$

$$\Psi_k(c) = 0, \quad \left.\frac{d\Psi_k}{dr}\right|_{r=c} + \frac{\Psi_k(c)}{c} = 0, \quad (23)$$

where

$$Q = \mathrm{Bo}_m - 1 + \kappa^2, \quad \kappa = ka,$$
$$m = \sqrt{k^2 - i\frac{\omega}{\nu}}, \quad \mathrm{Re}\,m > 0.$$

Using the expansion of the rational fraction

$$\frac{1}{(s^2 + k^2)(s^2 + m^2)} = \frac{1}{m^2 - k^2}\left(\frac{1}{s^2 + k^2} - \frac{1}{s^2 + m^2}\right)$$

we obtain from equality (22)

$$\Sigma_k(s) = \frac{i\alpha Q}{\eta a^2}\frac{\kappa\zeta_k}{m^2 - k^2}\left[\frac{J_1(sa)}{s^2 + k^2} - \frac{J_1(sa)}{s^2 + m^2}\right].$$

Then, turning to (20) and using the definite integrals of cylindrical functions [14, formulas (6.535) and (6.541)], we find

$$\Psi_p(r) = \frac{i\alpha}{\eta a^2}\frac{\kappa\zeta_k}{m^2 - k^2}QR(r), \quad (24)$$

where

$$R(r) = K_1(\kappa)I_1(kr) - K_1(ma)I_1(mr) \quad \text{for} \quad r \le a,$$
$$R(r) = I_1(\kappa)K_1(kr) - I_1(ma)K_1(mr) \quad \text{for} \quad r \ge a.$$

It is easy to check that solution (24) at the point $r = a$ has continuous first- and second-order derivatives.

Since solution (24) does not satisfy conditions (21) and (23), it is necessary to invoke solutions of type (19), which are solutions to the homogeneous equation

$$\left(L-\frac{1}{\nu}\frac{\partial}{\partial t}\right)L\psi = 0. \tag{25}$$

This equation corresponds to inhomogeneous equation (12). Substituting the second expression in (19) into (25) yields

$$\left[\frac{d^2}{dr^2}+\frac{1}{r}\frac{d}{dr}-\left(\frac{1}{r^2}+m^2\right)\right]$$

$$\times\left[\frac{d^2}{dr^2}+\frac{1}{r}\frac{d}{dr}-\left(\frac{1}{r^2}+k^2\right)\right]\Psi_k = 0.$$

The fundamental set of this equation is readily expressed through the modified Bessel functions of the first and second kind [15]:

$$\Psi_k^{(1)} = I_1(kr), \quad \Psi_k^{(2)} = K_1(kr),$$

$$\Psi_k^{(3)} = I_1(mr), \quad \Psi_k^{(4)} = K_1(mr).$$

The next step is to construct, in view of (24), a general solution like

$$\Psi_k(r) = CK_1(kr) + DK_1(mr) + \Psi_p(r), \tag{26}$$

which is limited at $r \longrightarrow \infty$ and contains arbitrary constants C and D.

We now substitute (26) into (21) and (23), using the recurrence relations [15] for the Bessel functions, to arrive at a set of linear homogeneous algebraic equations for C, D, and ζ_k:

$$C\kappa K_1(\kappa) + D\kappa K_1(q) + \zeta_k$$

$$\times\left\{\omega a - \frac{\alpha\kappa^2}{\rho a^2\omega}Q[I(\kappa)K_1(\kappa) - I_1(q)K_1(q)]\right\} = 0,$$

$$CK_1(\kappa_1) + DK_1(q_1) + \zeta_k\frac{\alpha\kappa}{\rho a^2\omega}$$

$$\times Q[I_1(q_1)K_1(q) - I_1(\kappa_1)K_1(\kappa)] = 0,$$

$$C\kappa_1 K_0(\kappa_1) + Dq_1 K_0(q_1) + \zeta_k\frac{\alpha\kappa}{\rho a^2\omega}$$

$$\times Q[\kappa_1 I_0(\kappa_1)K_1(\kappa) - q_1 I_0(q_1)K_1(q)] = 0,$$

where

$$\kappa_1 = kc = \kappa(1-\sigma), \quad q = ma,$$

$$q_1 = mc = q(1-\sigma) \quad \sigma = d/a < 1.$$

The existence condition for a nontrivial solution to this set is found by equating its determinant to zero:

$$\begin{vmatrix} \kappa K_1(\kappa) & \kappa K_1(q) & \omega a - \dfrac{\alpha\kappa^2}{\rho a^2\omega}Q[I_1(\kappa)K_1(\kappa) - I_1(q)K_1(q)] \\ K_1(\kappa_1) & K_1(q_1) & \dfrac{\alpha\kappa^2}{\rho a^2\omega}Q[I_1(q_1)K_1(q) - I_1(\kappa_1)K_1(\kappa)] \\ \kappa_1 K_0(\kappa_1) & q_1 K_0(q_1) & \dfrac{\alpha\kappa^2}{\rho a^2\omega}Q[\kappa_1 I_0(\kappa_1)K_1(\kappa) - q_1 I_0(q_1)K_1(q)] \end{vmatrix} = 0. \tag{27}$$

This condition is a dispersion relation from which the desired function $\omega = \omega(k)$ can be found. Calculating determinant (27) in view of expressions [15] for the Wronskians $W\{K_0(\kappa_1), I_0(\kappa_1)\}$ and $W\{K_0(q_1), I_0(q_1)\}$ gives

$$\omega^2 = \frac{\alpha\kappa^2}{\rho a^3}(\mathrm{Bo_m} - 1 + \kappa^2)\{I_1(\kappa)K_1(\kappa) - I_1(q)K_1(q)$$

$$+ [\kappa_1 K_0(\kappa_1)K_1(q_1) - q_1 K_0(q_1)K_1(\kappa_1)]^{-1}$$

$$\times\{K_1^2(\kappa)[\kappa_1 I_0(\kappa_1)K_1(q_1) + q_1 I_1(\kappa_1)K_0(q_1)]$$

$$- 2K_1(\kappa)K_1(q)$$

$$+ K_1^2(q)[\kappa_1 I_1(q_1)K_0(\kappa_1) + q_1 I_0(q_1)K_1(\kappa_1)]\}\}. \tag{28}$$

In the limit $\nu \longrightarrow 0$, dispersion relation (28) takes the form

$$\omega^2 = \frac{\alpha}{\rho a^3}\frac{\kappa^2 K_1(\kappa)}{K_1(\kappa_1)}(\mathrm{Bo_m} - 1 + \kappa^2)$$

$$\times[I_1(\kappa)K_1(\kappa_1) - I_1(\kappa_1)K_1(\kappa)],$$

which coincides, up to notation, with the dispersion relation obtained in the standard statement of the stability problem for nonviscous magnetic fluids [7, expression (30)]. Since the effects of capillary and viscous forces are mutually independent, this is evidence for the validity of applying modified linearized equation of motion (6), where the density of bulk forces due to the capillary effect is calculated by (7).

VISCOUS REGIME OF CAPILLARY INSTABILITY

Disintegration (when $\mathrm{Bo}_m < 1$) of the initially cylindrical configuration formed by magnetic fluids is a complex process with the participation of capillary, inertial, magnetic, and viscous forces. Consider the development of instability for the case when the effect of inertial forces is negligible compared with the effect of viscous forces. Such a situation is observed at high Ohnesorge numbers, $Z = \eta(\rho\alpha d)^{-\frac{1}{2}} \gg 1$. In this case, the linear stage of instability development is characterized by the time scale $\tau_v = \eta a/(\alpha\sigma)$ [7].

Dispersion relation (27) can be written in dimensionless form

$$\begin{vmatrix} \kappa K_1(\kappa) & \kappa K_1(q) & \varepsilon\sigma\Omega^2 - \kappa^2 Q[I_1(\kappa)K_1(\kappa) - I_1(q)K_1(q)] \\ K_1(\kappa_1) & K_1(q_1) & \kappa Q[I_1(q_1)K_1(q) - I_1(\kappa_1)K_1(\kappa)] \\ \kappa_1 K_0(\kappa_1) & q_1 K_0(q_1) & \kappa Q[\kappa_1 I_0(\kappa_1)K_1(\kappa) - q_1 I_0(q_1)K_1(q)] \end{vmatrix} = 0, \tag{29}$$

where $\Omega = \omega\tau_v$, $q = \sqrt{\kappa^2 - i\varepsilon\Omega}$, and $\varepsilon = Z^{-2}$.

Let the determinant on left of (29) be designated by $F(\Omega, \kappa; \varepsilon, \sigma, \mathrm{Bo}_m)$. It is easy to see that, for $\Omega = 0$, the first column of the determinant equals the second column and all the elements of the third column vanish, so that $F(0, \kappa; \varepsilon, \sigma, \mathrm{Bo}_m) \equiv 0$. It follows that dispersion relation (29) has the second-tuple trivial root $\Omega = 0$, which, certainly, is of no interest.

Similar considerations show that $F(\Omega, \kappa; 0, \sigma, \mathrm{Bo}_m) = 0$ for any Ω, κ, σ, and Bo_m. Differentiating the left of (29) with respect to ε yields

$$\begin{aligned} F'_\varepsilon = &\begin{vmatrix} \kappa K_1(\kappa) & \kappa \dfrac{d}{d\varepsilon}K_1(q) & \varepsilon\sigma\Omega^2 - \kappa^2 Q[I_1(\kappa)K_1(\kappa) - I_1(q)K_1(q)] \\ K_1(\kappa_1) & \dfrac{d}{d\varepsilon}K_1(q_1) & \kappa Q[I_1(q_1)K_1(q) - I_1(\kappa)_1)K_1(\kappa)] \\ \kappa_1 K_0(\kappa_1) & \dfrac{d}{d\varepsilon}[q_1 K_0(q_1)] & \kappa Q[\kappa_1 I_0(\kappa_1)K_1(\kappa) - q_1 I_0(q_1)K_1(q)] \end{vmatrix} \\ &+ \begin{vmatrix} \kappa K_1(\kappa) & \kappa K_1(q) & \sigma\Omega^2 + \kappa^2 Q\dfrac{d}{d\varepsilon}[I_1(q)K_1(q)] \\ K_1(\kappa_1) & K_1(q_1) & \kappa Q\dfrac{d}{d\varepsilon}[I_1(q_1)K_1(q)] \\ \kappa_1 K_0(\kappa_1) & q_1 K_0(q_1) & -\kappa Q\dfrac{d}{d\varepsilon}[q_1 I_0(q_1)K_1(q)] \end{vmatrix}. \end{aligned} \tag{30}$$

From (30), we find that $F'_\varepsilon(\Omega, \kappa; 0, \sigma, \mathrm{Bo}_m) \equiv 0$, since the last column in the first determinant on the right of (30) consists of zeros and the first two columns in the second determinant are the same if $\varepsilon = 0$. Similarly, one can show that $F''_{\varepsilon\varepsilon}(\Omega, \kappa; 0, \sigma, \mathrm{Bo}_m) \neq 0$ in the general case. Therefore, the expansion of the function $F(\Omega, \kappa; \varepsilon, \sigma, \mathrm{Bo}_m)$ in a power of the small parameter $\varepsilon \ll 1$ starts with the quadratic term. Thus, for high Ohnesorge numbers, dispersion relation (29) in a first approximation takes the form

$$F''_{\varepsilon\varepsilon}(\Omega, \kappa; 0, \sigma, \mathrm{Bo}_m) = 0. \tag{31}$$

Using the properties of determinants known from higher algebra, one can find from (31) a root Ω corresponding to the viscous regime of capillary instability development for the configuration of magnetic fluids. In dimensional form, this root appears as

$$\begin{aligned} \omega &= \frac{i\alpha}{2\eta a}\kappa\varphi(\kappa, \sigma)(1 - \mathrm{Bo}_m - \kappa^2), \\ \varphi(\kappa, \sigma) &= \frac{\det\|c_{ij}\|}{c_{21}c_{32} - c_{22}c_{31}}, \end{aligned} \tag{32}$$

where $\|c_{ij}\|$ is the 3×3 matrix

$$\begin{Vmatrix} K_1(\kappa) & K_0(\kappa) + K_2(\kappa) & c_{13} \\ K_1(\kappa_1) & (1-\sigma)[K_0(\kappa_1) + K_2(\kappa_1)] & c_{23} \\ \kappa K_0(\kappa_1) & 2[\kappa_1 K_1(\kappa_1) - K_0(\kappa_1)] & c_{33} \end{Vmatrix}$$

with

$$c_{13} = I_1(\kappa)K_0(\kappa) - I_2(\kappa)K_1(\kappa),$$

$$c_{23} = \frac{1}{2}\{I_1(\kappa_1)[K_0(\kappa) + K_2(\kappa)]$$

$$-(1-\sigma)K_1(\kappa)[I_0(\kappa_1) + I_2(\kappa_1)]\},$$

$$c_{33} = I_0(\kappa_1)K_1(\kappa) + \kappa_1 I_1(\kappa_1)K_1(\kappa)$$

$$-\frac{\kappa}{2}I_0(\kappa_1)[K_0(\kappa) + K_2(\kappa)].$$

The function $\varphi(\kappa, \sigma)$ is defined for any $\kappa > 0$ and $0 < \sigma < 1$, with $\varphi(\kappa, \sigma) > 0$ and $\lim_{\kappa \to 0} \varphi(\kappa, \sigma) = 0$. Then, the sign of $\mathrm{Im}\,\omega$ coincides with that of the factor $1 - \mathrm{Bo_m} - \kappa^2$. Accordingly, in the plane $(\mathrm{Bo_m}, \kappa)$, the curve of neutral stability (along which $\mathrm{Im}\,\omega = 0$), which separates the stability ($\mathrm{Im}\,\omega < 0$) and instability ($\mathrm{Im}\,\omega > 0$) domains, is described by the equation $\kappa = \sqrt{1 - \mathrm{Bo_m}}$ at $0 \le \mathrm{Bo_m} \le 1$.

In Fig. 1, the stability domain is represented by the first quadrant, exclusive of the hatched part (instability domain). It is seen that the threshold dimensionless wavenumber $\kappa_{th} = \sqrt{1 - \mathrm{Bo_m}}$ decreases (the range of unstable harmonics shrinks) as the magnetic field grows. If $\mathrm{Bo_m}$ is initially larger than unity ($\mathrm{Bo_m} > 1$), the configuration of immiscible magnetic fluids with the cylindrical interface is stable. Obviously, this conclusion agrees with the results of study of capillary instability in terms of the nonviscous fluid model [3–6].

For $Z \gg 1$ and given $\mathrm{Bo_m}$ ($0 \le \mathrm{Bo_m} \le 1$) and σ ($0 < \sigma < 1$), the wavenumber $\kappa_* = 2\pi a/\lambda_*$ of the most rapidly growing harmonic, which specifies the typical size of drops due to the capillary disintegration of the initial two-fluid configuration, is a point where the function $\mathrm{Im}\,\omega(\kappa)$ reaches a maximum. From (32), the equation for κ_* is written as follows:

$$(1 - \mathrm{Bo_m} - \kappa_*^2)[\varphi(\kappa_*, \sigma) + \kappa_* \varphi'_\kappa(\kappa_*, \sigma)]$$
$$-2\kappa_*^2 \varphi(\kappa_*, \sigma) = 0. \quad (33)$$

Note that a similar analysis was also performed for nonviscous ferrofluids. The capillary instability of the limiting cases of a gas-surrounded cylindrical layer (namely, a thin liquid sheath covering a cylindrical current-carrying conductor and a continuous liquid cylinder placed in a magnetic field with circular lines of force) was investigated. It was found that [4, 6] that the difference between the wavelengths λ_*^0 of the most rapidly growing harmonics is less than 2% throughout the range $0 \le \mathrm{Bo_m} \le 1$. For the thin layer,

$$\lambda_*^0 = 2\pi a \sqrt{\frac{2}{1 - \mathrm{Bo_m}}}. \quad (34)$$

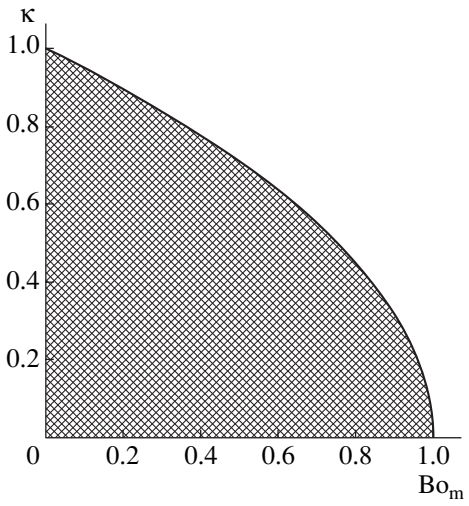

Fig. 1. Instability domain (hatched).

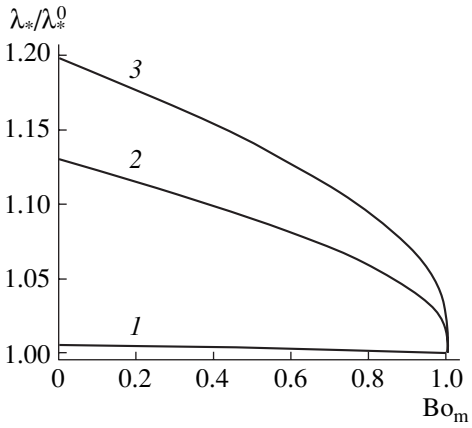

Fig. 2. Normalized wavelength of the most rapidly growing harmonic vs. magnetic Bond number for δ = (*1*) 0.05, (*2*) 0.8, and (*3*) 0.99.

Figure 2 plots the normalized wavelength λ_*/λ_*^0 versus the magnetic Bond number for different σ. The curves were constructed using formula (34) after solution of Eq. (33). It is seen that drops produced by the capillary disintegration of the layer in the case of contacting immiscible fluids of the same viscosity surrounding a current-carrying conductor of radius *c* are coarser than in the case of a gas-surrounded nonviscous fluid for the same $\mathrm{Bo_m}$ and *c*. The difference between the size of the drops is the most pronounced at small $\mathrm{Bo_m}$ and increases with increasing relative thickness of the layer.

Comparison of the curves in Fig. 2 with those constructed for the case when a viscous ferrofluid is in contact with a nonviscous fluid of the same density [7] indicates that the dependence of the size of the drops on the layer thickness is governed primarily by attachment

condition (8) for fluid particles on the conductor surface. Shear stresses at the interface are of minor importance.

CONCLUSIONS

The axisymmetric problem of capillary instability of an initially cylindrical configuration formed by two ferrofluids of different magnetic susceptibilities that surround a current-carrying conductor is stated. The problem is solved by using a modified equation of motion that includes in explicit form capillary forces localized on the weakly distorted cylindrical interface. A dispersion relation is derived, and its root corresponding to a limiting regime of instability (the effect of inertial forces is negligible compared with viscous forces in the general balance of inertial, viscous, capillary, and magnetic forces) is found.

An equation for the neutral stability curve is derived, and the range of stability on the plane (Bo_m, κ) is revealed (Bo_m is the magnetic Bond number, and κ is the dimensionless wavenumber). It is shown that, at small Bo_m, the thickness of the initially cylindrical layer of the ferrofluid between the conductor surface and interface has a significant effect on the size of drops produced by the capillary disintegration of the layer. In this case, the drops are coarser than in the case of the capillary disintegration of a gas-surrounded nonviscous ferrofluid layer covering a current-carrying conductor.

ACKNOWLEDGMENTS

This work was supported by the Russian Foundation for Basic Research (project no. 02-01-00694).

REFERENCES

1. Ch. V. Boy, *Bulles de savon* (Gauthier-Villars, Izd. L. F. Panteleeva, St. Petersburg, 1894).
2. S. L. Goren, J. Fluid Mech. **12**, 309 (1962).
3. V. I. Arkhipenko, Yu. D. Barkov, V. G. Bashtovoĭ, *et al.*, Dokl. Akad. Nauk BSSR **23**, 341 (1979).
4. V. I. Arkhipenko, Yu. D. Barkov, V. G. Bashtovoĭ, *et al.*, Izv. Akad. Nauk SSSR, Mekh. Zhidk. Gaza, No. 4, 3 (1980).
5. R. Rosensweig, *Ferrohydrodynamics* (Cambridge Univ. Press, Cambridge, 1985; Mir, Moscow, 1989).
6. B. M. Berkovsky, V. F. Medvedev, and M. S. Krakov, *Magnetic Fluids*: *Engineering Applications* (Oxford Univ. Press, Oxford, 1993; Khimiya, Moscow, 1989) [in Russian].
7. V. M. Korovin, Zh. Tekh. Fiz. **71** (12), 16 (2001) [Tech. Phys. **46**, 1504 (2001)].
8. G. I. Barenblatt and G. G. Chernyĭ, Prikl. Mat. Mekh. **27**, 784 (1963).
9. L. I. Sedov, *A Course in Continuum Mechanics* (Wolters-Noordhoff, Groningen, 1971; Nauka, Moscow, 1983), Vol. 1.
10. V. M. Korovin, Zh. Tekh. Fiz. **72** (10), 22 (2002) [Tech. Phys. **47**, 1226 (2002)].
11. H. A. Stone and M. P. Brenner, J. Fluid Mech. **318**, 373 (1996).
12. M. A. Lavrent'ev and B. V. Shabat, *Methods of the Theory of Functions of Complex Variable* (Nauka, Moscow, 1973; Springer-Verlag, Berlin, 1959).
13. M. J. Ablowitz and H. Segur, *Solitons and the Inverse Scattering Transform* (SIAM, Philadelphia, 1981; Mir, Moscow, 1987).
14. I. S. Gradshteyn and I. M. Ryzhik, *Table of Integrals, Series, and Products* (Nauka, Moscow, 1971; Academic, New York, 1980).
15. M. Abramovitz and I. A. Stegun, *Handbook of Mathematical Functions* (Dover, New York, 1972; Mir, Moscow, 1979).

Translated by V. Isaakyan

Technical Physics, Vol. 49, No. 6, 2004, pp. 677–680. Translated from Zhurnal Tekhnicheskoĭ Fiziki, Vol. 74, No. 6, 2004, pp. 16–19.

GASES AND LIQUIDS

Mathematical Model of a Fluid Flowmeter

É. I. Chaplygin, Yu. V. Zemskov, and V. V. Korzin

Volgograd State Technical University (Volzhskiĭ Branch), Volzhskiĭ, Volgograd oblast, 404121 Russia

e-mail: george@vlink.ru

Received May 16, 2003; in final form, November 10, 2003

Abstract—A mathematical model of operation of a fluid (jet) device measuring the liquid or gas flow rate is suggested. The model takes into account the effect of deep negative feedback produced by connecting the control channels of the bistable jet element. © *2004 MAIK "Nauka/Interperiodica".*

Fluid flowmeters the sensitive element of which is a liquid or gas jet flowing out of the feed channel of the jet device and producing pressure pulses with a frequency proportional to the velocity of the flow of the working medium have appeared quite recently and have not yet found wide application [1, 2]. At the present time, exhaustive experimental data and a comprehensive theoretical description concerning the principle of operation of such transducers are lacking. This is one of the reasons why these flowmeters are of limited use. However, the advantages of such a measuring technique (the simple design and reliability of the transducer, the absence of moving parts, the frequency-modulated pickup signal, the possibility of measuring the flow rate in corrosive and cryogenic environments, the weak dependence of the performance characteristics of the flowmeters on external factors and fluid properties, quick response, the possibility of measuring the flow rate of pulsating flows with a good accuracy, a high radiation resistance of the transducer, explosion and fire safety, and stability against electromagnetic fields) make it very promising for industrial applications.

Let us consider the process in the chamber of a discrete jet device [3] without ventiducts. Its operation is based on the effect of attraction of the jet to the wall. External feedback is provided by connecting the two control channels to each other (Fig. 1).

Feed channel *1* (usually of a rectangular cross section) produces a jet to be measured. The deviation of the jet from the axis of working chamber *4* depends on the pressure difference in control channels *2* and *3*. Even a slight deflection of the jet, for example, downward (Fig. 1), results in the formation of a low-pressure region near the lower wall of the working chamber due to the ejecting effect of the jet. This favors a further deflection of the jet toward this wall, causing the near-wall region to shrink and the pressure in it to drop. Eventually, the transverse pressure drop acting on the jet rises and the jet bends further (the Coanda effect [3]). Thus, in jet devices with closed working chambers (without ventiducts), internal positive feedback due to the Coanda effect arises: a deflection of the main jet from the device axis in any direction results in an avalanche-like process, which is completed when the jet touches the nearest wall of the working chamber.

Connection of the control channels of the device to each other provides external negative feedback. When the jet is deflected downward, the pressure in lower control channel *3* becomes lower than that in upper control channel *2* (because of the ejecting effect) and the working medium starts moving along feedback loop *7* toward the lower control channel. Outflow of the working medium from the upper part of the chamber and inflow to the lower part make the main jet move upward. Accordingly, the pressure difference between the control channels decreases, but the medium goes on moving in the feedback loop owing to the inertia of the medium. At the time when the deflection of the main jet becomes equal to zero (hence, the pressures in the control channels become equal to each other), the velocity of the medium in the feedback loop and the angular velocity of the main jet reach maximal values. The medium moving by inertia continues to push the main jet upward. Now, the pressure decreases in the upper control channel, which slows down the velocity of the medium in the feedback loop (which is as yet directed toward the lower control channel) and, hence, the angular velocity of the main jet. Finally, the jet touches the

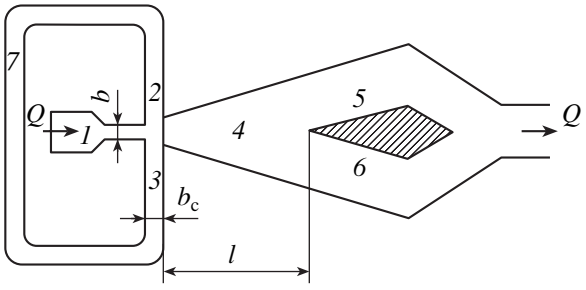

Fig. 1. Flow-rate jet transducer with aerohydrodynamic feedback: (*1*) feed channel, (*2*, *3*) control channels, (*4*) working chamber, (*5*, *6*) outlet ducts, and (*7*) feedback loop.

1063-7842/04/4906-0677$26.00 © 2004 MAIK "Nauka/Interperiodica"

upper wall, the pressure difference in the control channels reaches a maximum, and the velocity of the medium in the feedback loop drops to zero and then changes sense. The medium again starts moving in the feedback loop under the action of pressure difference in the control channels but now toward the upper control channel. Then, the process reverses symmetrically.

Earlier, when considering oscillations in jet self-excited generators, the researchers ran into difficulties associated with quantitative description of the mechanism of main jet switching. It was argued, for example, that the flowmeter under consideration generates relaxation oscillations [1]. In [4], the jet switching mechanism was considered under the assumption that the departure of the main jet from the chamber wall is caused only by inflow from the control channel. However, experimental data showed that pressure oscillations in the control channels are near-sinusoidal, while flow visualization in transparent models [5] did not support the relaxation behavior of oscillations.

In this paper, we (as in [4]) consider the motion of the main jet in the chamber of a jet generator as harmonic vibrations of a string. Such a behavior of the jet is untypical of standard operating regimes of pneumonic discrete devices based on the effect of jet attraction to the wall. However, with the dimensions of the control channels and feedback loop chosen appropriately, the working point of a discrete device falls into the linear portion of the performance characteristic.

Based on the above assumption, we will consider switching in a jet self-excited generator. For a given volume of the fluid (Fig. 2), the angular momentum conservation law [6] yields

$$\frac{d}{dt}\iiint_V \mathbf{r}\times\rho\mathbf{u}\,dV = \iiint_V \mathbf{r}\times\rho\mathbf{F}\,dV - \oiint_S \mathbf{r}\times\rho\,d\mathbf{S} + \oiint_S \mathbf{r}\times(T_\mu\,d\mathbf{S}).$$

Here, p and ρ are the pressure and density of the working medium, respectively; F are the volume forces (per unit mass); S is the surface bounding the volume V considered; and T_μ is the stress tensor.

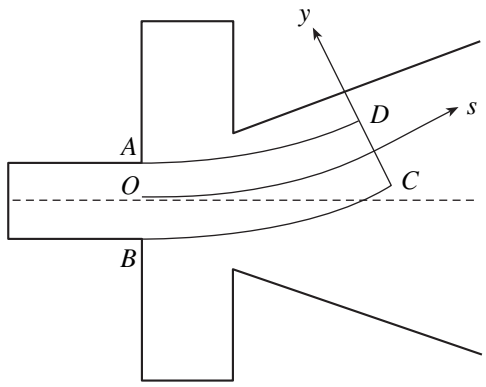

Fig. 2. On derivation of the jet vibration equation in the chamber of a discrete device.

Neglecting the volume forces and assuming the medium to be incompressible, we obtain for the two-dimensional case

$$\iint_\sigma \rho(\dot u + u^2/R)s\,ds\,dy - \iint_\sigma \rho(\dot u - uv/R)y\,ds\,dy = m_1 + m_2.$$

Here, the overcircles indicate time derivatives; σ is the surface area of the two-dimensional domain under consideration (*AOBCD* in Fig. 2]); u and v are the axial and radial velocity components, respectively; R is the radius of curvature of the jet axial line; s is the curvilinear coordinate measured along the jet axis; y is the coordinate running normally to the jet axis;

$$m_1 = \int_0^s (p_1 - p_2)s\,ds; \quad m_2 = -sb\mu\,d\theta/dt$$

(the moments m_1 and m_2 are taken relative to the center of the feed channel outlet section); θ is the deflection of the jet axial line from the feed channel axis; and p_1 and p_2 are the pressures in the control channels.

Considering the motion of the main jet as string vibrations, i.e., assuming that

$$v = sd\theta/dt; \quad u = u_0 - yd\theta/dt,$$

where u_0 is the axial velocity of the jet, we come to

$$\iint_\sigma \rho\dot v s\,ds\,dy \approx \rho\iint_\sigma s^2\ddot\theta\,ds\,dy = \rho bs^3\ddot\theta/3,$$

$$\iint_\sigma (\rho u^2 s/R)\,ds\,dy \approx \rho u_0^2 bs^2/2R,$$

$$-\iint_\sigma \rho\dot u y\,ds\,dy \approx \rho\iint_\sigma y^2\ddot\theta\,ds\,dy = \rho b^3 s\ddot\theta/12.$$

If the conditions

$$y \ll s, \quad v \ll u, \quad \rho uvy \ll \rho u_0^2 s,$$

are satisfied, we have

$$\iint_\sigma \frac{\rho uv}{R} y\,ds\,dy \ll \iint_\sigma \frac{\rho u^2 s}{R}\,ds\,dy.$$

Putting $s = b_c$, where b_c is the width of the control

channels, we obtain the differential equation

$$\ddot{\theta} + \frac{12\nu}{b^2 + 4b_c^2}\dot{\theta} + \frac{6u_0^2}{b^2 + 4b_c^2}\theta = \frac{6b_c p_c}{\rho b(b^2 + 4b_c^2)}, \quad (1)$$

where the angle θ is taken at $s = b_c$, $p_c = p_2 - p_1$, and ν is the kinematic viscosity.

If $u_0 \gg 2\nu\omega$, where $\omega = 2\pi f$ and f is the vibration frequency, the second term in Eq. (1) can be neglected; if $6u_0^2/(b^2 + 4b_y^2) \gg \omega^2$, the first one can also be neglected. Then, the solution to Eq. (1) has the form

$$\theta/p_c = b_c/\rho b u_0^2. \quad (2)$$

If the jet shifts by an angle $d\theta$, it displaces the volume

$$dV = \frac{hl}{2}dy = \frac{hl^2}{2}d\theta = \frac{hl^2 b_c}{2\rho b u_0^2}dp_c$$

in one of the control channels. Taking into account that

$$dV/dt = -S_f v_f \equiv -q_f,$$

where S_f is the cross-sectional area of the feedback loop, v_f is the flow-rate-averaged velocity of the medium in the feedback loop, and h is the height of the chamber, we arrive at

$$-\frac{hl^2 b_c}{2S_f \rho b u_0^2}\frac{dp_c}{dt} = u_f \quad (3)$$

(the minus sign takes into account that, when the jet shifts towards the lower control pressure, the working medium moves toward the higher pressure).

The d'Alembert equation for the feedback loop has the form

$$p_c(t) = R_f q_f(t) + L_f \frac{dq_f}{dt},$$

where $R_f = 8\chi_a \rho \nu l_f/\pi r_f^4$ is the resistance; $L_f = \chi_r \beta \rho l_f/\pi r_f^2$ is the inductance; and l_f and r_f are the length and radius of the feedback loop; respectively. The correctives χ_a and $\chi_r\beta$ take into account that the flow of the medium is unsteady [7].

The experiments performed with our transducers showed that the corrective $\chi_r\beta$ may be set equal to unity in a first approximation and the corrective χ_a can be calculated by the formula

$$\chi_a = \frac{1}{2}\sqrt{\frac{r_f^2\omega}{8\nu}} + 0.4.$$

Eventually, we get the differential equation

$$\ddot{p}_c + \frac{32\chi_a \nu}{d_f^2}\dot{p}_c + \frac{\pi d_f^2 b u_0^2}{2hb_c l^2 l_f}p_c = 0 \quad (4)$$

(where $d_f = 2r_f$ is the diameter of the feedback loop cross section), which describes vibrations with the frequency

$$f = \frac{1}{2\pi}\sqrt{\frac{\pi d_f^2 b u_0^2}{2hb_c l^2 l_f} - \frac{256\chi_a^2 \nu^3}{d_j^4}}. \quad (5)$$

If the condition

$$\frac{\pi d_f^6 Q^2}{512\chi_a^2 \nu^2 h^3 b b_c l^2 l_f} \gg 1 \quad (6)$$

(where $Q = u_0 hb$ is the volumetric flow rate of the medium) is satisfied, the viscosity of the medium can be neglected. Then, the vibration frequency is proportional to the volumetric flow rate of working medium:

$$f = \frac{u_0 d_f \sqrt{b}}{2l\sqrt{2\pi h b_c l_f}} = \frac{Q d_f}{2l\sqrt{2\pi h^3 b b_c l_f}}. \quad (7)$$

Formula (7) describes the effect of the volumetric flow rate of the working medium and geometric dimensions of a jet generator on its generator frequency. Condition (6) estimates the lower limit Q_{min} of the flow rate at which the generator frequency is proportional to the flow rate and is independent of the viscosity.

Equation (4) and formula (7) were obtained using the d'Alembert approximate formula. If the equations of fluid dynamics for the case of an incompressible liquid subjected to a harmonic action are solved exactly, we express the exact solution through the modified Bessel functions, expand them into series, and leave only two first terms to get an expression for the amplitude of the volumetric flow rate Q_f in the feedback loop and the amplitude of the pressure difference P_c in the control channels (tedious calculations are omitted):

$$Q_f = \frac{P_c d_f^2}{8\rho l_f f\sqrt{1 - \frac{4\sqrt{\nu/\pi f}}{d_f} - \ldots}}. \quad (8)$$

From (8), we obtain the equation for the vibration frequency

$$f = Qd_f\left(1 - \sqrt{\frac{\nu}{\pi f d_f^2}}\right)\frac{1}{2l\sqrt{2\pi h^3 b b_c l_f}}. \quad (9)$$

Note that, for $f \gg \nu/\pi d_f^2$, Eq. (9) yields the linear dependence of the frequency f on the flow rate Q with the same proportionality coefficient as in Eq. (7).

Experimental results

l, mm	l_f, mm	b_c, mm	d_f, mm	Experiment		Equation (9)		Error f/Q, %
				f, Hz	f/Q, m^{-3}	f, Hz	f/Q, m^{-3}	
36.2	630	9.9	8	5.4	2680	5.6	2800	5
36.2	630	9.9	10	7.1	3560	7.1	3540	1
36.2	705	8.1	8	5.8	2900	5.9	2940	2
36.2	705	8.1	10	7.3	3620	7.5	3705	3
26.2	630	8.1	8	6.1	4100	6.4	4300	6
26.2	630	8.1	10	10.6	5290	10.8	5410	3
26.2	630	9.9	8	–	3730	–	3700	1
26.2	705	9.9	10	6.5	4300	6.9	4610	7

If the feedback loop has a rectangular cross section $h_f \times b_f$, instead of Eq. (9), we have

$$f = Q\frac{\sqrt{h_f b_f}}{\pi l\sqrt{2h^3 b b_c l_f}}\left(1 - \frac{h_f + b_f}{h_f b_f}\sqrt{\frac{\nu}{4\pi f}}\right).$$

Setting a maximal permissible deviation δ of the transducer characteristic $f = f(Q)$ from the linear dependence,

$$\delta = \frac{h_f + b_f}{h_f b_f}\sqrt{\frac{\nu}{4\pi f}},$$

we obtain an expression for the minimal measurable flow rate:

$$Q_{min} = \frac{(h_f + b_f)^2 \nu l}{4\delta^2}\sqrt{\frac{2h^3 b b_f l_f}{h_f^5 b_f^5}}.$$

For $h_f = h$, we find that the minimal measurable value Q_{min} is reached when the width b_f of the feedback loop equals the height of the device: $b_f = h_f = h$.

To verify the mathematical model developed, we performed the experiment described in [4]. The results are listed in the table (the experimental and calculated values of the vibration frequency are given for $Q = 2 \times 10^{-3}$ m^3/s). In the experiment, we used a bistable jet element with the following geometric dimensions: b = 4.7 mm, h = 20.2 mm, l = 26.2 and 36.2 mm, l_f = 630 and 705 mm, b_c = 8.1 and 9.9 mm, and d_f = 8 and 10 mm.

Thus, one can design a fluid flowmeter, simulating its performance characteristic $f(Q)$ with our mathematical model. Also, the model helps in estimating the range of measurable flow rates Q where the deviation of the characteristic from the linear dependence does not exceed a given value.

REFERENCES

1. P. P. Kremlevskiĭ, *Flowmeters and Quantity Meters: A Handbook* (Mashinostroenie, Leningrad, 1989) [in Russian].
2. S. L. Treskunov, P. A. Aristov, and N. A. Barykin, Prib. Sist. Upravleniya, No. 11, 24 (1990).
3. L. A. Zalmanzon, *Theory of Pneumonic Devices* (Nauka, Moscow, 1989) [in Russian].
4. S.-G. Wu, H.-N. Su, and L.-J. Wang, in *Proceedings of the 20th Anniversary Fluidic Symposium, ASME Winter Annual Meeting, 1980*, pp. 49–54.
5. Yu. V. Zemskov and É. I. Chaplygin, in *Proceedings of All-Russia Conference on Pneumatic Hydroautomatics, Moscow, 1999*, pp. 177–178.
6. D. G. Loytsyansky, *Fluid Mechanics* (Nauka, Moscow, 1987) [in Russian].
7. D. N. Popov, *Hydraulic and Pneumatic Systems: Dynamics and Control* (Mashinostroenie, Moscow, 1976) [in Russian].

Translated by M. Astrov

Technical Physics, Vol. 49, No. 6, 2004, pp. 681–685. Translated from Zhurnal Tekhnicheskoĭ Fiziki, Vol. 74, No. 6, 2004, pp. 20–24.

GASES AND LIQUIDS

Numerical Simulation of the Translational Nonequilibrium Zone behind a Shock-Wave Front

A. Yu. Sazonov and N. V. Shut'

Moscow Institute of Physics and Technology, Zhukovskiĭ, Moscow oblast, 140180 Russia

e-mail: wtdiv@tsagi.rssi.ru

Received October 2, 2002; in final form, November 18, 2003

Abstract—The translational nonequilibrium zone in a shock wave is considered for a gas consisting of light particles and a small addition of heavy particles. The gas is taken to be two-dimensional, and long-range forces are assumed to be absent. In the framework of this approximation, a program for molecular dynamics simulation of the gas is developed. It is applied to calculate a particle distribution function in the shock wave, to analyze the time evolution of the distribution function, and to study its dependence on the gas composition. *© 2004 MAIK "Nauka/Interperiodica".*

INTRODUCTION

A plane shock wave (SW) in a gas is known to be divided into several characteristic zones. In the first zone (so-called translational nonequilibrium zone), a molecule velocity distribution function is transformed. Then, the zones of the excitation of rotational and vibrational degrees of freedom, the dissociation zones, and the zones of chemical reactions and ionization are present. Finally, thermodynamic equilibrium is established. In this work, prominence is given to the first zone, since all following processes nucleate in the translational nonequilibrium zone and strongly depend on it. High-energy particles appearing in the translational nonequilibrium zone can substantially change the following processes in the shock wave. It was experimentally found in [1, 2] that chemical and nuclear reactions can occur in shock waves; however, the threshold energies of the reactions significantly exceed the characteristic energies in the corresponding equilibrium states. In [1], the effect of the translational nonequilibrium zone behind a shock front was studied using a light gas with 0.1–3.0% iodine molecules. The authors detected short-lived peaks of nonequilibrium emission that were many times greater than the values characteristic of the equilibrium translational temperature. There are cases of undesirable effect of high-energy particles on physical processes, such as heat transfer during supersonic flight of an airplane in clouds or the processes that occur in supersonic and hypersonic wind channels when clusters or motes that are grown in a nozzle change the interparticle interaction in a shock wave before a body. Thus, the appearance of high-energy particles in a mixture of light and heavy gases should be studied in detail. The current experimental methods for studying nonequilibrium effects behind a shock front are mainly based on determining a spectrum and measuring the emission intensity of exciting gas molecules and do not give information on the processes preceding the appearance of the emitting states [1]. However, with numerical simulation, one can generate a nonequilibrium molecule velocity distribution function (DF) and track its evolution.

The purpose of this work is to simulate the mechanisms of the appearance of translational nonequilibrium behind a shock front in an ideal gas with heavy-atom additions (e.g., K or Cs additions used in magnetohydrodynamic (MHD) systems with a light working gas (He)). As a result of the simulation, we confirm the presence of high-energy collisions in the translational nonequilibrium zone in a shock wave and demonstrate the dynamics of establishing thermodynamic equilibrium.

FORMULATION OF THE PROBLEM

The simulation of the structure of a shock wave is based on considering the deceleration of a high-speed gaseous flow in a compression shock. The initial flow velocity corresponded to Mach numbers M = 8–10, which are realized in most modern hypersonic wind channels. In this case, the gas flow velocity exceeds the molecule thermal velocity by a factor of eight to ten. The gas is taken to be ideal; that is, there are no dissociation, long-range intermolecular forces, and rotational and vibrational degrees of freedom. This assumption seems to be grounded at a distance of about several mean free paths behind the SW front, where a new DF is formed, since vibrational, rotational, and electronic levels have not been excited. In the context of this approach, a certain qualitative description of the DF can be obtained far from the SW front, since translational degrees of freedom still affects it. The effects related to the translational nonequilibrium should be most pronounced in a gasdynamic flow containing

1063-7842/04/4906-0681$26.00

impurities whose mass differs substantially from the base gas. Then, during the deceleration (acceleration) of the flow, the kinetic energy is redistributed between the heavy and light components, and the DF remains substantially nonequilibrium for a certain time. In our numerical experiments, the concentration of such heavy atoms (e.g., cesium additions) is varied from 0.3 to 3%, which corresponds to the concentrations in MHD facilities. The mass ratio of the light to heavy component was varied from 1/34(He + Cs) to 1/127(H_2 + I_2). It should be noted that a difference in the masses by two or more orders of magnitude can be realized in wind channels with an arc heater, when metal vapor and clusters consisting of 100 or more atoms that form during electrode erosion enter into a flow.

SIMULATION ALGORITHM

To study the nonequilibrium distribution, we developed a program to simulate the elastic collisions of particle fluxes. The particle thermal motion in the fluxes and the interaction zone were calculated in the approximation of an ideal gas consisting of absolutely smooth and elastic balls of a certain radius. Although this model is rather simple and cannot describe many events occurring in a high-temperature gas, it is beyond reason to think that it cannot reveal the qualitative picture of the process. When performing preliminary checking calculations, we experimentally found the equilibrium molecule velocity distribution function and the basic equation of the molecular-kinetic theory of gases (Clapeyron–Mendeleev equation). However, upon these calculations, the motion of the balls–molecules was described by Newton's laws and was not related to any statistical laws.

The current program describes an ideal gas whose particles move on a plane in the X and Y coordinates. This restriction is not fundamental, and we are going to apply a more realistic three-dimensional program in the near future.

The motion of particles forming the ideal gas can be reduced to their translational motion and collisions; each particle is described with continuously varying coordinates X and Y and velocity components V_x and V_y. Moreover, each particle has a mass m and a radius R. Unlike a real gas, any molecule in the computer model can be marked (by assigning a serial number n).

The displacement of a particle in time Δt is described by the known formulas of mechanics

$$x_n = x_{n0} + V_x \Delta t,$$

$$y_n = y_{n0} + V_y \Delta t.$$

The most complex case for calculation is the case of two colliding atoms with different masses; nevertheless, it can also be solved with the laws of conservation of energy and momentum. When particles n and m collide, the new velocities are determined from the formulas

$$\Delta V = \frac{(x_m - x_n)(U_m - U_n) - (y_m - y_n)(V_m - V_n)}{4(r_m + r_n)^2},$$

$$U_n' = U_n + \frac{2m_m}{m_m + m_n}\Delta V(x_m - x_n),$$

$$U_m' = U_m + \frac{2m_n}{m_m + m_n}\Delta V(x_m - x_n),$$

$$V_n' = V_n + \frac{2m_m}{m_m + m_n}\Delta V(y_m - y_n),$$

$$V_m' = V_m + \frac{2m_n}{m_m + m_n}\Delta V(y_m - y_n).$$

The algorithm also contains collisions with walls, which are natural protection against an unlimited increase in the coordinates of some particles. When a particle interacts with a vertical or horizontal wall, the corresponding velocity projections simply change their sign (mirror reflection).

On the whole, the calculation procedure is Vilenkin's algorithm [3] optimized for solving this problem. The program based on this algorithm allows numerical experiments on 10^5 particles, thus calculating, on average, 1000 pair collisions per second on a computer with a Pentium II processor.

SIMULATION RESULTS

The effects related to the appearance of high-energy particles are likely to be most pronounced when two counter fluxes collide with each other. To simulate the interaction of the two particle fluxes, we apply the program for calculating an ideal gas that was described above. The initial positions of particles were set so that they form two areas with uniform filling. The particle velocities in the areas had the same moduli and opposed directions. Then, the particles were subjected to a 10% perturbation, which corresponds to the equilibrium distribution. Thus, we have two particle fluxes with Maxwell distributions that fly toward each other at velocities corresponding to hypersound with $M \sim 10$, which is typical of modern hypersonic wind channels. In some experiments, the masses and dimensions of certain particles (0.1–3.0% of their total number) were set different from the other values, which corresponded to the introduction of heavy-atom additions into the fluxes.

In the region of interaction of counter fluxes having particles with different masses, the velocity of the light particles can increase several times as a result of their reflection from the heavy particles. In other words, the heavy atoms can play the role of a high-speed piston

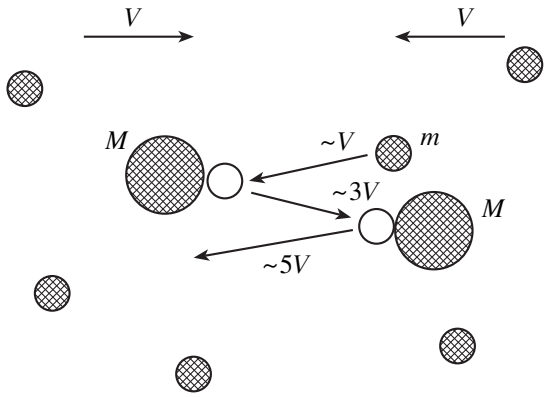

Fig. 1. Schematic diagram for the interaction of the counter fluxes.

that compresses layers of the light atoms and transfers its kinetic energy to them (Fig. 1).

To support this assumption, we performed two experiments. In the first, we determined a particle velocity distribution function in the region of interaction of the counter fluxes (Figs. 2, 3). In the second experiment, we also determined a DF, but to the fluxes were added 2% of particles whose mass was 34 times greater than that of the other particles. The flux velocities in the second case were decreased correspondingly for the kinetic energy to be equal to that of the first experiment (Figs. 4, 5). The distributions of the number of particles N over their velocities relative to the flux V/V_0 (Figs. 3, 5) can arbitrarily be divided into several characteristic ranges: (1) A particle velocity distribution in the undisturbed flux (before colliding with the opposing flux). The flux velocity in the second case is about 16% smaller for the total kinetic energy of the flux to be the same. The DF corresponds to a Maxwell distribution with a mean thermal velocity of about $0.1V_0$, where V_0 is the initial flux velocity. (2) A particle distribution in the region of interaction of the counter fluxes; characteristic maximum, which is caused by the collisions of the light particles flying toward each other, is clearly visible at about double the flux velocity. (3) This zone is present only in Fig. 5. It is caused by the collisions of the heavy and light atoms and, hence, is characterized by velocities of $(3–4)V_0$. This case corresponds to a fourfold increase in the particle velocities with respect to the flux velocity, and the scatter of the velocities results from the particle thermal motion in the fluxes and from the fact that not all collisions are frontal.

Obviously, to produce a large number of high-energy particles in MHD accelerators and similar facilities, it is advantageous to increase the content of heavy elements rather than to increase the flux velocity; the more so as it is difficult to increase the flux velocity in real practice.

To determine the optimum number of heavy particles, we simulated the situation where a mass ratio of the particles in a flux was the same and the number of heavy particles and the flux velocity were varied so that the total flux energy was constant. The number of the heavy particles was varied from 0 to 5.0% (Fig. 6).

Figure 6 shows the evolution of the light-particle distribution function with the number of the heavy particles; for convenience, only the lower parts of the DF are given. The X axis is the velocity, Y is the number of the heavy particles in percent, and Z is the total number of particles with a given velocity. Numerous peaks in Fig. 6 are caused by a small number of the particles in the experimental gas. As is seen from the curves, the number of fast particles in the light gas is maximum when the number of the heavy particles is 1.0–1.5%. It should be noted that the number of ultrafast particles (which appear because of the multiple reflection of the

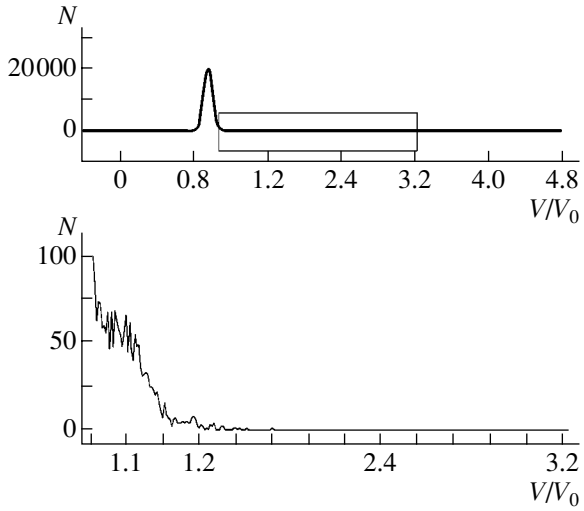

Fig. 2. Dependence of the number of the light particles on their absolute velocity.

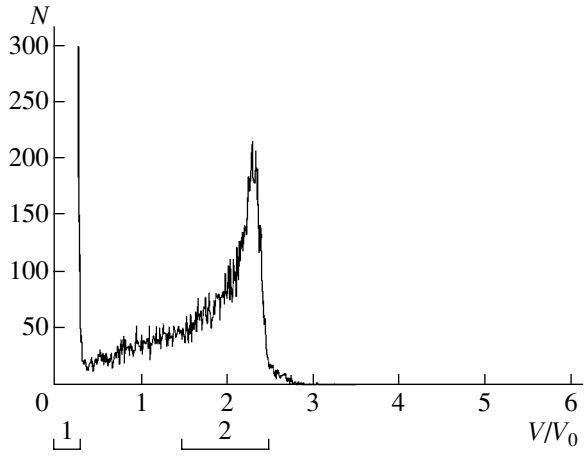

Fig. 3. Dependence of the number of the light particles on their velocity with respect to the flux.

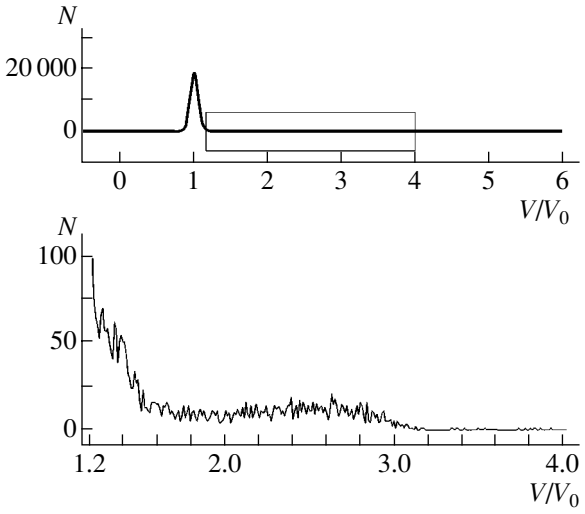

Fig. 4. Dependence of the number of the light particles on their absolute velocity in the presence of a 2% addition of heavy atoms.

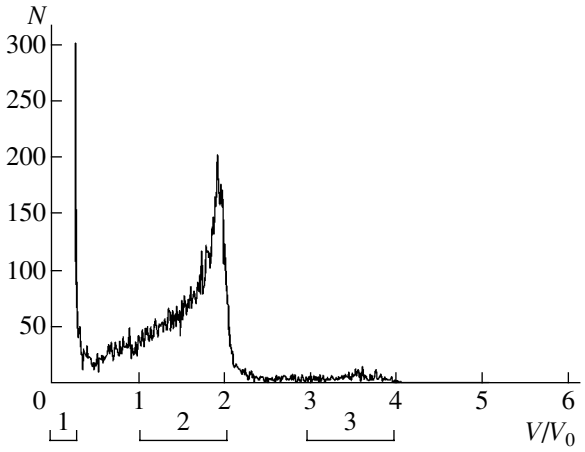

Fig. 5. Dependence of the number of the light particles on their relative velocity in the presence of a 2% addition of heavy atoms.

light particles from the heavy ones) increases in the range 3.0–4.5%. An increase in the total number of the particles (in this experiment, 3×10^5 particles were used) is assumed to increase the number of the ultrafast particles. In this case, the choice between these regions is specified by the problem to be solved.

When we perform the same experiment by varying the mass of the heavy particles and retaining their number unchanged, the results obtained are difficult to analyze. To make the analysis easier, we carried out a similar calculation; however, an increase in the mass was not compensated by the corresponding decrease in the velocity, and the total energy was varied proportionally to the change in the mass. In this experiment, the number of fast nonequilibrium particles increases slightly and the maximum velocity first slightly increases and then levels off (Fig. 7). The Z axis is the mass ratio of the heavy to light particles M/m, where M is the mass of the heavy particle and m is the mass of the light particle.

It is also of interest to follow the time evolution of the DF and the time dependence of the number of high-energy particles. To this end, we conducted a numerical experiment that is similar to the experiments described above. Two 150 000-particle short-lived fluxes consisting of a two-dimensional ideal gas having different masses move toward each other at the velocities that correspond to the Mach number $M = 10$. We determine the number of high-energy particles of the light gas from the beginning of the interaction of the gas fluxes, which was determined from changes in their DFs, to their stopping, when they transform into a fuzzy cloud of a high-temperature gas. High-energy particles were considered to be particles having an energy that is ten times greater than the mean kinetic energy of a particle. Figure 8 shows the results of this experiment depending on the concentration of the heavy atoms.

If the fluxes have heavy particles, a pronounced peak, which corresponds to an increase in the number of high-energy light particles, forms in the initial stage of the flux collision. The number of such particles first sharply increases as a result of countercollisions with

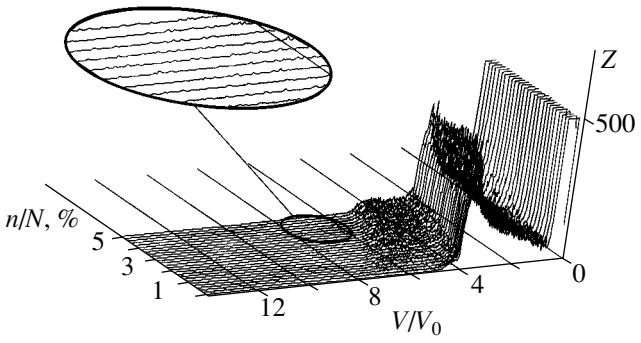

Fig. 6. Effect of the weight concentration of the heavy particles on the light-particle distribution function.

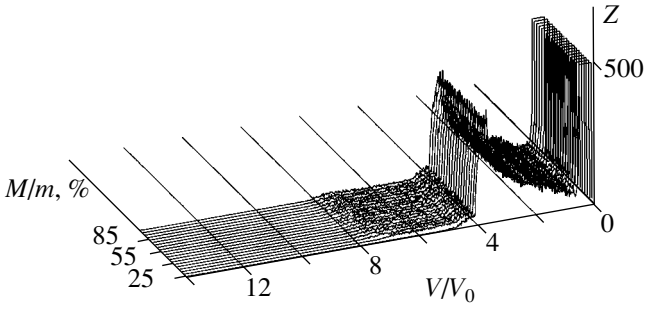

Fig. 7. Effect of the mass of the heavy particles on the light-particle distribution function.

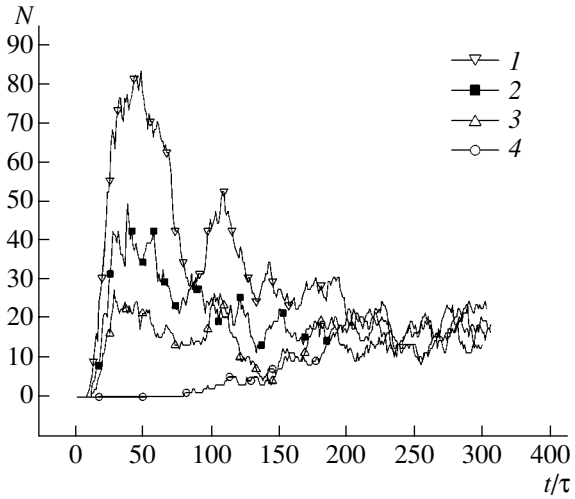

Fig. 8. Time variation of the number of high-energy particles. The mass ratio is 34; the relative concentration of the heavy particles is (*1*) 2, (*2*) 1, (*3*) 0.5, and (*4*) 0%.

the heavy atoms and then, in the time of about four to five mean free times τ_0 in the undisturbed flux, decreases because of establishing thermal equilibrium. In a time of about $(10–12)\tau_0$, a quasi-equilibrium state is established in the interaction zone, and the number of high-energy particles ceases to decrease and levels off.

In the absence of the heavy atoms, the initial peak is undetected and the number of high-energy particles increases gradually to the level that corresponds to thermal equilibrium (10–20 particles). The number of particles whose energy is ten times greater than the mean kinetic energy—which is calculated by the equilibrium-distribution formula

$$N = \frac{N_0}{\bar{w}} \int_{10\bar{w}}^{\infty} \exp\left(-\frac{w}{\bar{w}}\right) dw,$$

where w and $\bar{w}$ are the kinetic energy and the mean kinetic energy, respectively—is equal to 14. Thus, the maximum number of high-energy particles is detected at the maximum concentration of the heavy atoms (2%) and is five times greater than the corresponding parameter in the equilibrium state.

CONCLUSIONS

(1) Numerical simulation of the shock wave ($M \sim 10$) in a mixture of light and heavy gases revealed the appearance and dynamics of high-energy particles whose energies are ten or more times greater than the values characteristic of the equilibrium translational temperature.

(2) As the concentration of heavy particles increases, the number of high-energy particles increases in the range where the impact velocity exceeds the flux velocity by a factor of three to four. When the number of the heavy particles further increases, particles appear whose velocities are four to five times higher than those characteristic of the equilibrium translational temperature.

(3) As the mass of the heavy particles increases, the number of fast nonequilibrium particles increases only slightly and the maximum velocity first slightly increases and then levels off.

(4) When two fluxes consisting of a mixture of light and heavy gases collide with each other, a short-lived peak of high-energy particles appears in the early stage; then, it decreases due to establishing thermal equilibrium (Fig. 8).

(5) The presence of the zone with high-energy particles in the shock wave can be used to realize chemical and, possibly, nuclear reactions in gas flows having energies significantly lower than those required for their initiation.

ACKNOWLEDGMENTS

We are grateful to V.I. Alferov for his assistance in performing the simulation and preparing the manuscript.

REFERENCES

1. V. Yu. Velikodnyĭ, A. V. Emel'yanov, and A. V. Eremin, Zh. Tekh. Fiz. **69** (10), 23 (1999) [Tech. Phys. **44**, 1150 (1999)].
2. R. J. Beuhler, G. Friedlander, and L. Friedman, Phys. Rev. Lett. **63**, 1292 (1989).
3. A. N. Vilenkin and G. L. Kotkin, Kvant **6**, 3 (1989).

Translated by K. Shakhlevich

Technical Physics, Vol. 49, No. 6, 2004, pp. 686–690. Translated from Zhurnal Tekhnicheskoĭ Fiziki, Vol. 74, No. 6, 2004, pp. 25–28.

GAS DISCHARGES, PLASMA

Low-Power RF Plasma Sources for Technological Applications: II. Plasma Sources under Anomalous Skin Effect Conditions

K. V. Vavilin*, V. Yu. Plaksin*, Kh. M. Ri*, and A. A. Rukhadze**

** Moscow State University, Vorob'evy Gory, Moscow, 119899 Russia*

*** Prokhorov Institute of General Physics, Russian Academy of Sciences, ul. Vavilova 38, Moscow, 119991 Russia*

Received September 10, 2003

Abstract—A theory of a planar disk-shaped RF plasma source under anomalous skin effect conditions is developed. In the absence of an external magnetic field, such conditions are satisfied for transverse electromagnetic waves with phase velocities below the electron thermal velocity, and, in the presence of this field, they are satisfied for electron cyclotron waves with frequencies corresponding to the resonant absorption line. For each of these cases, the RF field power deposited in a plasma with given parameters is determined and the equivalent plasma resistance is calculated. © *2004 MAIK "Nauka/Interperiodica".*

1. INTRODUCTION

RF plasma sources operating with an external magnetic field under nonresonance conditions (at frequencies below the electron cyclotron frequency) and under resonance conditions (at frequencies close to the electron cyclotron frequency) have received a quite thorough investigation (see recent collections of papers [1, 2] and review [3] and also the literature cited therein). As for an RF plasma source operating without an external magnetic field, it was considered, to the best of our knowledge, only in our recent work [4]. As far as we know, however, plasma sources operating with an external magnetic field and without it were studied either with no allowance for the spatial dispersion or under the assumption that the spatial dispersion is weak. The operation of RF plasma sources under conditions of strong spatial dispersion has not yet been studied.

In the absence of an external magnetic field, the conditions of strong spatial dispersion are satisfied for transverse electromagnetic waves with frequencies corresponding to the anomalous skin effect [5]:

$$\nu_e \ll \omega \ll kV_{Te} \approx \left(\sqrt{\frac{\pi}{2}}\frac{\omega_{Le}^2\omega}{c^2V_{Te}}\right)^{\frac{1}{3}}V_{Te}. \qquad (1.1)$$

Here, the quantity

$$\lambda_{sk} \approx k^{-1} \equiv \left(\sqrt{\frac{\pi}{2}}\frac{\omega_{Le}^2\omega}{c^2V_{Te}}\right)^{-\frac{1}{3}}$$

is known as the anomalous skin depth. Note that conditixn (1.1) can be rewritten in the form

$$\nu_e^2 \ll \omega^2 \ll \omega_{Le}^2\frac{V_{Te}^2}{c^2}, \qquad (1.2)$$

which explicitly determines the frequency range of the anomalous skin effect.

On the other hand, in the presence of an external magnetic field, the conditions of strong spatial dispersion are satisfied for electron cyclotron waves with frequencies corresponding to the resonant absorption line [5]:

$$\nu_e|\omega - \Omega_e| \ll kV_{Te} \approx \left(\sqrt{\frac{\pi}{2}}\frac{\omega_{Le}^2\omega}{c^2V_{Te}}\right)^{\frac{1}{3}}V_{Te}. \qquad (1.3)$$

Here, as before, the quantity

$$\lambda_{sk} \approx k^{-1} \equiv \left(\sqrt{\frac{\pi}{2}}\frac{\omega_{Le}^2\omega}{c^2V_{Te}}\right)^{-\frac{1}{3}}$$

has the meaning of the anomalous skin depth, i.e., the depth to which the resonant ($\omega = \Omega_e$) cyclotron wave penetrates into the plasma.

Our objective here is to investigate a planar disk-shaped plasma source having a diameter $2R$ much greater than its length L (Fig. 1) under conditions (1.1)–(1.3) and also under the condition $L \gg \lambda_{sk}$, i.e.,

$$2R \gg \lambda_{sk} \approx k^{-1} \equiv \left(\sqrt{\frac{\pi}{2}}\frac{\omega_{Le}^2\omega}{c^2V_{Te}}\right)^{-\frac{1}{3}}. \qquad (1.4)$$

Such a source is equipped with an antenna that is positioned at its upper surface at $z = 0$ and has the form of a very tight Archimedes spiral with a current density

$$j_\varphi = \frac{\mu}{R(1 - J_0(\mu))}\delta(z)J_1\left(\mu\frac{r}{R}\right)e^{-i\omega t}I_0, \qquad (1.5)$$

where I_0 is the net antenna current, $J_0(x)$ and $J_1(x)$ are zero- and first-order Bessel functions, and $J_1(\mu) = 0$ (so that $\mu \approx 3.8$). The antenna excites an RF field, which heats the plasma and maintains the source operation (see [3] for details).

The numerical results presented below were obtained for the following set of prescribed parameter values: the neutral gas pressure was $P_0 \le 10^{-3}$ torr, the electron temperature was $T_e = 5$ eV (i.e., $V_{Te} = \sqrt{T_e/m} = 9.5 \times 10^7$ cm/s), the electron plasma density[1] was $n_e \sim 3 \times 10^{11}$–$5 \times 10^{12}$ cm^{-3}, and the RF field frequency was $\omega = 2\pi f = 8.52 \times 10^7$ s^{-1} (i.e., $f = 13.56$ MHz). However, all the formulas derived here are also valid for other parameter values satisfying conditions (1.1)–(1.3), the corresponding recalculation being easily performed. In our study, we also determine the RF field power deposited in a plasma and the effective resistance of the plasma in the source.

2. A PLASMA SOURCE OPERATING WITHOUT AN EXTERNAL MAGNETIC FIELD

In the absence of an external magnetic field, the electromagnetic fields described by axisymmetric solutions to Maxwell's equations have three nonzero components:

$$E_\varphi(z, r) = E_\varphi(z)J_1\left(\mu\frac{r}{R}\right), \quad B_r(z, r) = B_r(z)J_1\left(\mu\frac{r}{R}\right),$$

$$B_z(z, r) = B_z(z)J_0\left(\mu\frac{r}{R}\right).$$

For a source with the above geometry, these components satisfy the following set of Maxwell's equations:

$$\begin{gathered} -ic\frac{\partial E_\varphi}{\partial z} + \omega B_r = 0, \quad \frac{c\mu}{R}E_\varphi - i\omega B_z = 0, \\ \frac{\partial B_r}{\partial z} - \frac{\mu}{R}B_z + i\frac{\omega}{c}D_\varphi = \frac{4\pi}{c}j_\varphi(z), \end{gathered} \qquad (2.1)$$

where we have differentiated the components with allowance for their radial dependence. The azimuthal component of the electric induction, $D_\varphi(z)$, is assumed to be related to the electric field component $E_\varphi(z)$ by an integral relationship, which is derived from the kinetic theory of a bounded plasma. Under anomalous skin effect conditions, in which we are interested here, we can use inequalities (1.4) to pass over to the limit of a plasma that is semi-infinite in the z direction ($L \longrightarrow \infty$). If we adopt a model in which the electrons are specularly reflected from the surface $z = 0$, then we obtain (see [5], Sections 17, 18)

$$D_\varphi(z) = \int_{-\infty}^{\infty} dz'\hat{\varepsilon}^{\mathrm{tr}}(z - z', \omega)E_\varphi(z'), \qquad (2.2)$$

where $\hat{\varepsilon}^{\mathrm{tr}}(z - z', \omega)$ is the influence function, the Fourier transform of which,

$$\varepsilon^{\mathrm{tr}}(\omega, k) = \int dz\hat{\varepsilon}^{\mathrm{tr}}(z, \omega)e^{-ikz} \qquad (2.3)$$

is the transverse dielectric function of an isotropic collisional electron plasma [6],

$$\begin{aligned} \varepsilon^{\mathrm{tr}}(\omega, k) &= 1 - \frac{\omega_{Le}^2}{\omega(\omega + i\nu_e)}J_+\left(\frac{\omega + i\nu_e}{kV_{Te}}\right) \\ &\approx i\sqrt{\frac{\pi}{2}}\frac{\omega_{Le}^2}{\omega|k|V_{Te}}. \end{aligned} \qquad (2.4)$$

The last of these expressions refers to the validity limit of the anomalous skin effect approximation.

Equations (2.1) can readily be reduced to one equation for the electric field component $E_\varphi(z)$ in the plasma region ($z \ge 0$):

$$\frac{\partial^2 E_\varphi}{\partial z^2} - \frac{\mu^2}{R^2}E_\varphi + \frac{\omega^2}{c^2}D_\varphi = -\frac{4\pi i\omega}{c^2}j_\varphi(z), \qquad (2.5)$$

where the current density $j_\varphi(z)$ is given by expression (1.5) without the factor $J_1\left(\mu\frac{r}{R}\right)e^{-i\omega t}$. We solve this equation by the method described in [5], Sections 17 and 18. Specifically, we continue the function $E_\varphi(z)$ into the region $z < 0$ in such a way that the resulting function is even. To do this, we take into account the following boundary conditions, which are a consequence of

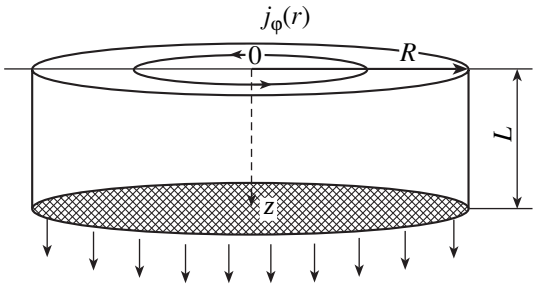

Fig. 1.

[1] For a cyclotron resonance–based plasma source, there is no need to impose a lower limit on the plasma density. The upper limit on the density stems from purely technical factors: high plasma densities cause overheating of the substrate in the source.

Eqs. (2.1) themselves:

$$\{E_\varphi(z)\}_{z=0} = 0, \quad \left\{\frac{\partial E_\varphi}{\partial z}(z)\right\}_{z=0} = \frac{\alpha}{R} I_0, \qquad (2.6)$$

where

$$\alpha = \frac{4\pi i\omega}{c^2}\frac{\mu}{1 - J_0(\mu)}.$$

Without going into the details of the technique for solving the problem at hand, we present the final expression for the field component $E_\varphi(z)$ in the plasma of the source:

$$E_\varphi(z) = -\frac{E'_\varphi(0)}{\pi}\int_{-\infty}^{\infty} dk e^{ikz}\left(k^2 - \frac{\omega^2}{c^2}\varepsilon^{tr}(\omega, k)\right)^{-1}, \quad (2.7)$$

where

$$E'_\varphi(0) = \frac{-\frac{\alpha}{R} I_0}{1 + \frac{k_0}{\pi}\int_{-\infty}^{\infty} dk\left(k^2 - \frac{\omega^2}{c^2}\varepsilon^{tr}(\omega, k)\right)^{-1}}, \qquad (2.8)$$

with

$$k_0 = \sqrt{\frac{\mu^2}{R^2} - \frac{\omega^2}{c^2}} \approx \frac{\mu}{R}$$

(which refers to the operating frequency $\omega = 8.52 \times 10^7\ s^{-1}$ of the RF plasma source under consideration).

In the frequency range corresponding to weak spatial dispersion, when the inequalities opposite to inequalities (1.2) are satisfied, expression (2.7) becomes

$$E_\varphi(z) = \frac{\frac{\alpha}{R} I_0}{k_1 + k_0} e^{-k_1 z}. \qquad (2.9)$$

Here,

$$k_1 = \sqrt{\frac{\mu^2}{R^2} - \frac{\omega^2}{c^2}\varepsilon(\omega)},$$

where $\varepsilon(\omega)$ is given by expression (2.4) from our earlier paper [4].

In this case, of course, solution (2.9) coincides with the solution obtained in [4] in the limit $L \longrightarrow \infty$.

As for the limit of strong spatial dispersion under discussion here, i.e., when conditions (1.2) hold and the anomalous skin effect takes place, formulas (2.7) and (2.8) should be used with the last of expressions (2.4). As a result, formulas (2.7) and (2.8) for the field within the plasma ($z > 0$) reduce to

$$E_\varphi(z) = \frac{\frac{\alpha}{R} I_0}{k_1 + k_0} e^{\frac{(i\sqrt{3}-1)}{2} k_1 z}, \qquad (2.10)$$

where we have introduced the notation

$$k_0 = \sqrt{\frac{\mu^2}{R^2} - \frac{\omega^2}{c^2}} \approx \frac{\mu}{R}, \quad k_1 = \left(\sqrt{\frac{\pi}{2}}\frac{\omega_{Le}^2 \omega}{c^2 V_{Te}}\right)^{\frac{1}{3}}. \qquad (2.11)$$

We can now calculate the RF field power deposited in the plasma of the source and to determine the effective plasma resistance. To do this, we begin with general expression (2.7), which is valid under the conditions of both weak and strong spatial dispersion, and also take into account the radial dependence of the electric field in the plasma. In this way, we arrive at the following general formula:

$$P_W = \frac{2\omega}{\pi}|E'_\varphi(0)|^2 \int_0^R r dr J_1^2\left(\mu\frac{r}{R}\right) \times \int_{-\infty}^{\infty} \mathrm{Im}\,\varepsilon^{tr}(\omega, k)\frac{dk}{\left(k^2 - \frac{\omega^2}{c^2}\varepsilon^{tr}\right)\left(k^2 - \frac{\omega^2}{c^2}\varepsilon^{tr*}\right)} \qquad (2.12)$$

$$= \alpha^2 I_0^2 \frac{\omega}{2\pi} J_0^2(\mu)\frac{\int_{-\infty}^{\infty} \mathrm{Im}\,\varepsilon^{tr}(\omega, k)\left|k^2 - \frac{\omega^2}{c^2}\varepsilon^{tr}\right|^{-2} dk}{\left|1 + \frac{k_0}{\pi}\int_{-\infty}^{\infty} dk\left(k^2 - \frac{\omega^2}{c^2}\varepsilon^{tr}\right)^{-1}\right|^2} = R_{\mathrm{eff}} I_0^2.$$

Ignoring the effects of spatial dispersion in the expression for the dielectric function, we see that formula (2.12) reduces to expression (3.12) from [4]. Under conditions of strong spatial dispersion (i.e., in the frequency range of the anomalous skin effect), formula (2.12) should be used with the last of expressions (2.4). As a result, we obtain

$$P_W = \frac{1}{3\sqrt{3}}\alpha^2 I_0^2 \frac{c^2}{\omega} J_0^2(\mu)\frac{k_1}{k_1^2 + \frac{4}{27}k_0^2} = R_{\mathrm{eff}} I_0^2. \quad (2.13)$$

From this expression, we can see that the deposited power P_W depends weakly on the source radius R and, as the plasma density increases, it decreases gradually according to the law $n_e^{-1/3}$. On the other hand, in the range of low plasma densities, when the inequalities opposite to inequalities (1.2) are satisfied and the spatial dispersion is negligible, the deposited power P_W increases gradually with n_e according to the same law [4].

For $n_e \sim 3 \times 10^{12}\ \mathrm{cm}^{-3}$ and for the above values of the source parameters, expression (2.13) yields $R_{\mathrm{eff}} \sim 1\ \Omega$.

Figure 2 illustrates how the effective plasma resistance R_{eff} depends on the plasma density n_e in the range $5 \times 10^{11} < n_e < 10^{13}$ cm^{-3} for sources of different radii R. The curves shown in the figure were calculated from exact formula (2.12) and from approximate formula (2.13). We can see that the exact and approximate formulas agree well with one another in the density range in which the latter is valid (i.e., for $n_e > 10^{12}$ cm^{-3}). The figure also shows the dependence of R_{eff} on the plasma density in the range of its low values, $n_e < 10^{11}$ cm^{-3}, in which the approximation used in [4] is valid. Here again, approximate formula (2.13) is seen to agree fairly well with exact formula (2.12) in the range $n_e < 3 \times 10^{10}$ cm^{-3}. On the whole, the optimistic conclusion of [4] is not confirmed by exact formula (2.12): even for optimum conditions such that $\omega \sim (V_{Te}/c)\omega_{Le}$, which, in accordance with Fig. 2, corresponds to $R \geq 20$ cm and $n_e \sim 5 \times 10^{11}$ cm^{-3}, the effective plasma resistance is no higher than 1.5 Ω.

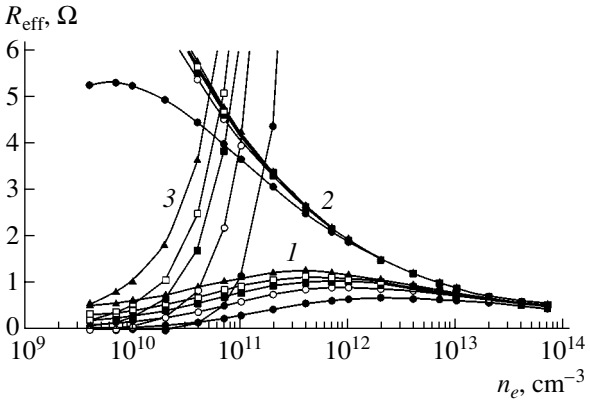

Fig. 2. Numerical results obtained for sources of different radii: $R = 5$ cm (closed circles), 10 cm (open circles), 15 cm (closed squares), 20 cm (open squares), and 30 cm (triangles). Curves *1* were calculated from formula (2.12), ascending curves *2* were calculated from formula (2.13), and descending curves *3* were calculated from formula (3.12) of [4].

3. CYCLOTRON PLASMA SOURCE

The analysis carried out in the previous section is equally valid for an electron cyclotron resonance–based plasma source operating at frequencies corresponding to the resonant absorption line, i.e., under conditions (1.3) (which refer to the anomalous skin effect approximation). The reason is that, under such circumstances, the absorption is strong, which allows us to treat the cyclotron wave in a plasma as if it were propagating in a quasi-longitudinal direction. In this case, the electromagnetic wave field has the same nonzero components as the field considered in the previous section. The only difference is in the expression for the effective dielectric function [6],

$$\varepsilon_{\text{eff}}(\omega, k_z) = 1 - \frac{\omega_{Le}^2}{\omega(\omega + i\nu_e - \Omega_e)} J_+\left(\frac{\omega + i\nu_e - \Omega_e}{k_z V_{Te}}\right) \approx i\sqrt{\frac{\pi}{2}}\frac{\omega_{Le}^2}{\omega|k_z|V_{Te}}. \quad (3.1)$$

However, in the limit of interest to us, i.e., under conditions (1.3), expression (3.1) coincides with the last of expressions (2.4). Obviously, expression (2.13) and the estimates obtained above for a resonant magnetic field of $B_0 \approx 5$ G apply equally to a cyclotron source operating under anomalous skin effect conditions. Moreover, the results of all the calculations that are illustrated in Fig. 2 and refer to the anomalous skin effect approximation also turn out to be valid for this resonant value of the magnetic field, in which case it is necessary to keep in mind that the anomalous skin effect occurs in the frequency range

$$(\omega - \Omega_e)^2 \ll \left(\frac{V_{Te}^2}{c^2}\omega_{Le}^2\Omega_e\right)^{\frac{2}{3}} \ll \Omega_e^2. \quad (3.2)$$

In the opposite limit, i.e., outside the cyclotron resonance frequency range, cyclotron sources should be analyzed in a manner different from that employed for sources operating without an external magnetic field. In this limit, the absorption of cyclotron waves excited in a plasma at frequencies differing from the resonant frequency Ω_e is important and thus should be taken into account. In order to calculate the effective plasma resistance in a mathematically rigorous way, we used formula (2.12), which is valid in the case at hand and in which we replaced $\varepsilon^{\text{tr}}(\omega, k)$ with $\varepsilon_{\text{eff}}(\omega, k_z)$ and changed from integration over k to integration over k_z. The results of calculations of $R_{\text{eff}}(n_e)$ for different values of B_0 are illustrated in Fig. 3. We can see that the effective resistance R_{eff}, as a function of plasma density, has a broad peak, which is displaced toward stronger magnetic fields as the density increases. This is a consequence of the collective nature of cyclotron waves: the higher the plasma density, the larger the amount by which the frequency of these waves deviates from Ω_e [6],

$$\omega_{\text{res}} = \Omega_e - \left(\sqrt{\frac{2}{\pi}}\frac{\omega_{Le}^2\omega V_{Te}^2}{c^2}\right)^{\frac{1}{3}}. \quad (3.3)$$

Expression (3.3) implies that the resonant frequency is close to the electron gyrofrequency but remains somewhat less than the latter. Consequently, at a given operating frequency of the source, resonance is achieved only in the range $\Omega_e > \omega$ (i.e., only for $B_0 >$

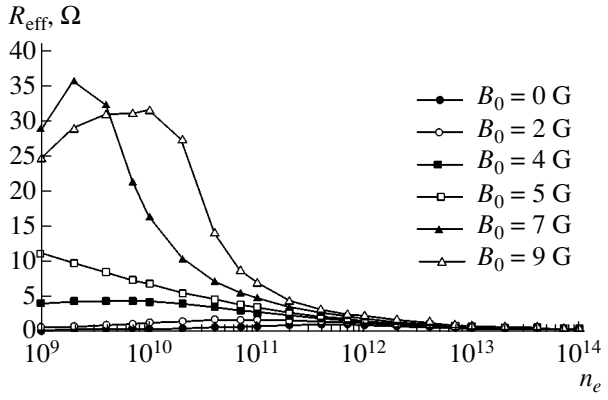

Fig. 3.

5 G). At weaker magnetic fields, resonance does not occur, as can be seen from Fig. 3. Note also that expression (3.1) and the results obtained in this section are valid for quasi-uniform cyclotron waves, i.e., under the conditions

$$\frac{\mu^2}{R^2} \ll \frac{\omega_{Le}^2}{c^2}, \quad \frac{\mu^2}{R^2} \ll \frac{\omega_{Le}^2}{c^2}\frac{\omega}{|\omega - \Omega_e|}, \tag{3.4}$$

which impose a lower limit on the plasma density and an upper limit on the external magnetic field. For the source parameters corresponding to Fig. 3, they are satisfied with a sufficient margin.

It is important to emphasize that, according to Fig. 3, the effective plasma resistance is high ($R_{\text{eff}} > 20\ \Omega$) in the plasma density range $n_e \sim 1\text{–}5 \times 10^{10}$ cm^{-3}. This indicates that RF cyclotron sources hold great promise for plasma technology.

In conclusion, note that the formulas derived here can also be used to describe cyclotron plasma sources operating at higher frequencies such that the vacuum wavelength is greater than the source radius, $2\pi c/\omega > R$, in which case the RF field that is excited by the antenna and maintains the plasma in the source can be described by the above approach. Progress to higher frequencies and, accordingly, to stronger magnetic fields will make it possible to work with gases at higher pressures, to produce plasmas with higher densities n_e, and to increase the allowable nonuniformity of the magnetic field B_0. In this way, it seems expedient to raise both the frequency ω and magnetic field B_0 by approximately one order of magnitude (i.e., $f \sim 50\text{–}100$ MHz and $B_0 \geq 100$ G), to utilize gases at pressures of $P_0 \sim 10^{-2}\text{–}10^{-1}$ torr, and thereby to achieve high operating efficiencies at plasma densities of $n_e \sim 10^{12}\text{–}10^{13}$ cm^{-3}.

REFERENCES

1. *High Density Plasma Sources*, Ed. by O. A. Popov (Neyes, New Jersey, 1995).
2. *Electron Cyclotron Emission and Electron Heating*, Ed. by G. Girrizzi (World Sci., Paris, 2002).
3. K. P. Shamray *et al.*, J. Phys. III **10** (Suppl.), C4365 (1997); in *Proceedings of the 23rd International Conference on Phenomena in Ionized Gases ICPIG-23, Touluse, 1997*.
4. K. V. Vavilin, A. A. Rukhadze, Kh. M. Ri, and V. Yu. Plaksin, Zh. Tekh. Fiz. **74** (5), 44 (2004) [Tech. Phys. **49**, 565 (2004)].
5. V. P. Silin and A. A. Rukhadze, *Electromagnetic Properties of Plasma and Plasmalike Media* (Atomizdat, Moscow, 1961) [in Russian].
6. A. F. Alexandrov, L. S. Bogdankevich, and A. A. Rukhadze, *Principles of Plasma Electrodynamics* (Vysshaya Shkola, Moscow, 1988; Springer-Verlag, Berlin, 1984).

Translated by O. Khadin

Technical Physics, Vol. 49, No. 6, 2004, pp. 691–697. Translated from Zhurnal Tekhnicheskoĭ Fiziki, Vol. 74, No. 6, 2004, pp. 29–34.

GAS DISCHARGES, PLASMA

Low-Power RF Plasma Sources for Technological Applications: III. Helicon Plasma Sources

K. V. Vavilin*, A. A. Rukhadze, Kh. M. Ri*, and V. Yu. Plaksin***

** Moscow State University, Vorob'evy Gory, Moscow, 119899 Russia*

*** Prokhorov Institute of General Physics, Russian Academy of Sciences, ul. Vavilova 38, Moscow, 119991 Russia*

Received September 10, 2003

Abstract—The third part of the paper is devoted to an investigation of the so-called helicon plasma sources. These are RF devices operating with a relatively weak external magnetic field, which is, at the same time, strong enough for the resonant electron gyrofrequency to be much higher than the industrial frequency ($\omega = 8.52 \times 10^7$ s^{-1}). As in [1, 2], a study is made of elongated cylindrical plasma sources in a longitudinal (directed along the cylinder axis) magnetic field and planar disk-shaped plasma sources in a transverse (perpendicular to the plane of the disk) magnetic field. A comparison of the present results with the results that were obtained in [3] without using the helicon approximation leads to the conclusion that elongated helicon sources hold great promise for plasma technologies. © *2004 MAIK "Nauka/Interperiodica".*

1. INTRODUCTION

In this paper, which is a continuation of [1, 2], we develop an analytic theory of RF plasma sources in a relatively weak external magnetic field. In the literature, such sources are known as helicon sources. The helicon plasma source was first proposed by Boswell [4] and its theory was first developed by Chen [5]. However, experimental investigations carried out by Alexandrov *et al.* [6] failed to provide much support for Chen's theory, as was pointed out in a review by Shamray *et al.* [7] (review articles on plasma sources can be found in a collection of papers [8], which contains a detailed bibliography on the subject). A correct theory of helicon plasma sources was constructed in [9–11]. Here, we will follow those papers in general terms.

We consider plasma sources having the same geometric configurations as those treated in [1] (see Fig. 1) and operating with a constant external magnetic field $\mathbf{B}_0$ parallel to the $0Z$ axis (i.e., $\mathbf{B}_0 \parallel 0Z$). The frequencies are assumed to satisfy the conditions

$$\nu_e \ll \omega \ll \Omega_e \ll \omega_{Le}, \tag{1.1}$$

where ω is the RF field frequency, $\omega_{Le} = \sqrt{4\pi e^2 n_e/m_e}$ is the electron Langmuir frequency, $\Omega_e = eB_0/mc$ is the electron gyrofrequency, and ν_e is the electron collision frequency. The quantities L, R, and P_0 have been introduced in [1]. Conditions (1.1) impose lower and upper limits on the magnetic field strength $\mathbf{B}_0$ (for $n_e \le 10^{13}$ cm^{-3}):

$$20 \text{ G} \ll \mathbf{B}_0 \ll 10^4 \text{ G}. \tag{1.2}$$

As in [1], the plasma parameters are assumed to satisfy the conditions

$$\omega \gg \nu_e, k_z V_{Te}; \quad \Omega_e \gg k_\perp V_{Te}, \tag{1.3}$$

where $k_z = \pi n/L$ ($n = 1, 2, 3, \ldots$) is the longitudinal component of the wave vector and $k_\perp = \mu_n/R$ is its transverse component, with μ_n being the roots of the Bessel function or of its derivative.

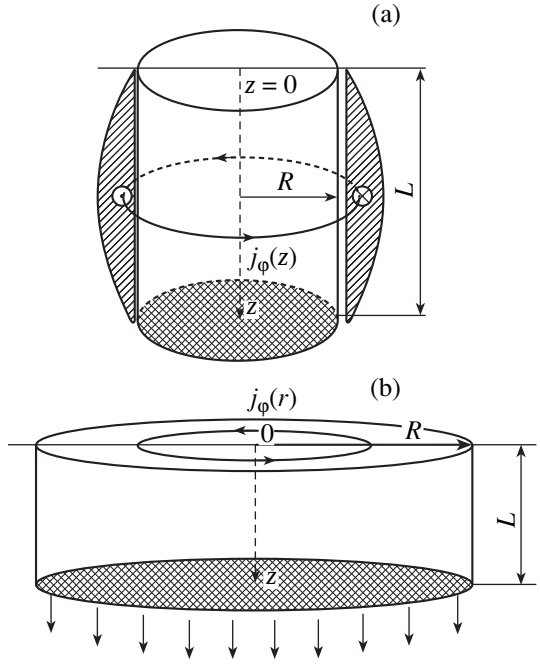

Fig. 1.

1063-7842/04/4906-0691$26.00

Under these conditions, we can describe the plasma by the dielectric tensor [2]

$$\varepsilon_{ij} = \begin{pmatrix} \varepsilon_\perp & ig & 0 \\ -ig & \varepsilon_\perp & 0 \\ 0 & 0 & \varepsilon_\parallel \end{pmatrix}, \quad (1.4)$$

with the elements

$$\varepsilon_\parallel = 1 - \frac{\omega_{Le}^2}{\omega^2}\left(1 - i\frac{\nu_e}{\omega}\right) + i\sqrt{\frac{\pi}{2}}\frac{\omega_{Le}^2\omega}{|k_z|^3 V_{Te}^3}\exp\left(-\frac{\omega^2}{2k_z^2 V_{Te}^2}\right),$$

$$\varepsilon_\perp = 1 + \frac{\omega_{Le}^2}{\Omega_e^2}\left(1 + i\frac{\nu_e}{\omega}\right), \quad (1.5)$$

$$g = \frac{\omega_{Le}^2}{\omega\Omega_e}\left(1 + 2i\frac{\omega\nu_e}{\Omega_e^2}\right).$$

The ranges and values of the plasma source parameters are the same as those in [1, 2], namely, $n_e = 10^{11}$–10^{13} cm^{-3}, $T_e = 5$ eV, $p_0 \le 10^{-3}$ torr, $R \ge 5$ cm, and $L \ge 10$ cm. It is easy to see that these parameters satisfy conditions (1.1) and (1.3).

2. ELONGATED HELICON PLASMA SOURCE ($L > 2R$)

In cylindrical coordinates, the components of an axisymmetric low-frequency electromagnetic field in a magnetized plasma can be described by the dependence $f(r, z)\exp(-i\omega t)$, in which case they obey the following Maxwell's equations:

$$-ic\frac{\partial E_\varphi}{\partial z} + \omega B_z = 0, \quad -ic\frac{\partial E_z}{\partial z} + ic\frac{\partial E_z}{\partial r} - \omega B_r = 0,$$

$$-ic\frac{\partial E_z}{\partial z} - \omega(\varepsilon_\perp E_r + igE_\varphi) = 0,$$

$$\frac{1}{r}\frac{\partial}{\partial r}rB_\varphi + i\omega\varepsilon_\parallel E_z = 0, \quad (2.1)$$

$$\frac{c}{r}\frac{\partial}{\partial r}rE_\varphi - i\omega B_z = 0,$$

$$-ic\frac{\partial B_r}{\partial z} + ic\frac{\partial B_z}{\partial r} - \omega(igE_z - \varepsilon_\perp E_\varphi) = -4\pi i j_\varphi.$$

The current density j_φ in an antenna positioned at the side surface of the source (Fig. 1a) can be represented as

$$j_\varphi = I_0\frac{k_z}{2}\delta(r - R)e^{-i\omega t}\sin k_z z, \quad (2.2)$$

where $k_z = \pi/L$ is the longitudinal wavenumber and I_0 is the net antenna current.

In the general case, Eqs. (2.1) are very difficult to solve because they describe two coupled waves—the so-called E and H waves. It is only in a spatially infinite plasma that these waves are decoupled and are eigenmodes of the oscillations of a magnetized plasma. For a cylindrical source, Eqs. (2.1) can be analyzed only numerically. However, in a first approximation, we can use the following relationships:

$$E_z^h = \frac{ic}{r\omega\varepsilon_\parallel}\frac{\partial}{\partial r}rB_\varphi \longrightarrow 0, \quad E_r^h = i\frac{g\omega^2}{c^2k_z^2}E_\varphi^h, \quad (2.3)$$

which are valid in the so-called helicon limit (i.e., in the case of sufficiently high plasma density). The conditions of applicability of these expressions are given by the inequalities

$$\frac{c^2k^2}{\omega_{Le}^2} \ll 1, \quad \frac{\omega}{\Omega_e} < \frac{\omega^2}{c^2k_z^2}\varepsilon_\perp \approx \frac{\omega_{Le}^2\omega^2}{\Omega_e^2c^2k_z^2} \ll 1 \quad (2.4)$$

($k^2 = k_z^2 + k_\perp^2$), which are known as the applicability conditions for the helicon approximation. Note that the right-hand part of the second of inequalities (2.4) is the condition for the plasma to be transparent to the helicon field.

Using inequalities (2.4), we can reduce Eqs. (2.1) to the following equation for the helicon field component E_φ^h:

$$\frac{\partial}{\partial r}\frac{1}{r}\frac{\partial}{\partial r}rE_\varphi^h - \left(\tilde{k}_z^2 - \frac{\omega^4g^2}{c^4\tilde{k}_z^2}\right)E_\varphi^h = -\frac{4\pi i\omega}{c^2}j_\varphi. \quad (2.5)$$

It is this equation that will be solved analytically below. Note that the quantity

$$\tilde{k}_z^2 = k_z^2 - \frac{\omega^2}{c^2}\varepsilon_\perp$$

contains a small (second) term, which correctly describes the absorption of a helicon field in a plasma because Img is negligibly small.

Hence, in the helicon approximation, we deal with the following situation. An antenna with an azimuthal current of density j_φ excites a purely helicon field (an H wave) in a magnetized dense plasma. This wave then generates a low-frequency potential E wave (an oblique Langmuir wave, or a Trivelpiece–Gould mode). In contrast to the helicon wave, which, under the conditions adopted here, is weakly absorbed by the plasma (because of the smallness of Img), the E-wave field is generally dissipated fairly efficiently and thereby heats the plasma.

We solve Eq. (2.5) separately for the region outside the plasma ($r > R$, $j_\varphi = 0$) and for the plasma region ($r < R$, $j_\varphi = 0$). We then match the solutions at the plasma surface with the help of the boundary conditions that can be obtained from Eqs. (2.1) by integrating them

across an infinitely thin layer around the side surface of the source:

$$\{E_\varphi^h\}_{r=R} = 0, \quad \left\{\frac{\partial E_\varphi^h}{\partial r}\right\}_{r=R} = \frac{4\pi\omega}{c^2}\frac{k_z}{2}I_0. \qquad (2.6)$$

These conditions were derived by using explicit expression (2.2) for the antenna current density at the side surface.

The general solution to Eq. (2.5) inside and outside the plasma region has the form

$$E_\varphi = \begin{cases} C_1 J_1(k_1 r), & r \le R \\ C_2 K_1(k_z r), & r \ge R, \end{cases} \qquad (2.7)$$

where

$$k_1^2 = \frac{\omega^4 g^2}{c^4 \tilde{k}_z^2} - \tilde{k}_z^2. \qquad (2.8)$$

The equations for the coefficients C_1 and C_2 follow from boundary conditions (2.6):

$$\begin{aligned} C_1 J_1(k_1 R) - C_2 K_1(k_z R) &= 0, \\ C_1 k_1 J_1'(k_1 R) - C_2 k_z K_1(k_z R) &= -\frac{2\pi\omega}{c^2} I_0. \end{aligned} \qquad (2.9)$$

Resolving these equations, we readily obtain the following expressions for C_1 and C_2:

$$C_1 = -\frac{2\pi\omega k_z}{c^2} I_0 \times \frac{K_1(k_z R)}{k_1 J_1'(k_1 R) K_1(k_z R) - k_z J_1(k_1 R) K_1'(k_z R)}, \qquad (2.10)$$

$$C_2 = -\frac{2\pi\omega k_z}{c^2} I_0 \times \frac{J_1(k_1 R)}{k_1 J_1'(k_1 R) K_1(k_z R) - k_z J_1(k_1 R) K_1'(k_z R)}. \qquad (2.11)$$

Unlike in plasma sources operating without an external magnetic field, in the plasma sources under consideration, this field can excite internal waves within the plasma. The waves so generated are described by the dispersion relation

$$k_1 J_1'(k_1 R) K_1(k_z R) - k_z J_1(k_1 R) K_1'(k_z R) = 0 \qquad (2.12)$$

which corresponds to the limit $C_{1,2} \longrightarrow \infty$. These are internal helicon waves satisfying the condition $k_1^2 > 0$. For an elongated plasma source (such that $L \ge 10$ cm, $R \le 5$ cm), this condition enables us to rewrite dispersion relation (2.12) in the form

$$\frac{J_1'(k_1 R)}{J_1(k_1 R)} = \frac{k_z}{k_1}\frac{K_1'(k_z R)}{K_1(k_z R)} \approx -\frac{0.6 k_z}{k_1} \ll 1. \qquad (2.13)$$

To a good accuracy, the solutions to dispersion relation (2.13) can be represented as

$$k_1^2 R^2 \approx \pi^2 (n + 1/2)^2, \qquad (2.14)$$

where $n = 1, 2, 3, \ldots$.

Using these solutions, we obtain the following formula for determining the resonant values of the magnetic field (or of the plasma density):

$$\frac{\omega^2 \omega_{Le}^2 R^2}{\Omega_e^2 c^2 k_z^2} \approx \frac{\pi^2 R^2}{L^2} + \pi^2 (n + 1/2)^2. \qquad (2.15)$$

Based on inequalities (2.4), we can write the applicability conditions for the helicon approximation in an explicit form:

$$\frac{3\times 10^{12}}{L^2}\left(1 + \frac{L^2}{R^2}\right) \ll n_e \ll 10^{11}\frac{B_0^2}{L^2}, \quad n_e > \frac{5\times 10^{11} B_0}{L^2}. \qquad (2.4')$$

In the case of a source with $L = 15$ cm and $R = 5$ cm, these conditions can be satisfied only for sufficiently dense plasmas ($n_e \gg 10^{11}$ cm^{-3}) and sufficiently strong magnetic fields ($B_0 \gg 10$ G). It is also obvious that condition (2.15) for the existence of an internal helicon wave should not go beyond the limits imposed by conditions (2.4'). For the above parameter values, this is in fact the case when $n_e > 7\times 10^{11} B_0/RL \ge 4\times 10^{11}$ cm^{-3}.

Thus, under conditions (2.12)–(2.15), i.e., when internal helicon waves can be excited, we arrive at the following expressions for the field components in the plasma region $r \le R$:

$$E_\varphi^h = C_1 J_1(k_1 r), \quad E_r^h = \frac{ig\omega^2}{c^2 k_z^2} E_\varphi^h, \qquad (2.16)$$

where C_1 is given by formula (2.10).

During the excitation of internal helicon waves in an elongated plasma source, the field components E_φ^h and E_z^h at resonance become fairly large because of the weak dissipation of the helicon field energy in the plasma. As a result, the helicon field (in particular, its component E_φ^h begins to excite a low-frequency potential E wave (a Trivelpiece–Gould mode). The potential of the E wave is determined by Poisson's equation with a source term:

$$\frac{1}{r}\frac{\partial}{\partial r} r\varepsilon_\perp \frac{\partial \Phi}{\partial r} - k_z^2 \varepsilon_\parallel \Phi = \frac{ig}{r}\frac{\partial}{\partial r}(r - E_\varphi^h). \qquad (2.17)$$

The right-hand side of this equation is assumed to be prescribed, so that we are dealing with a differential equation for oscillations subjected to a driving force. In

fact, substituting the field component E_φ^h given by the first of expressions (2.16) into Poisson's equation (2.17) yields the equation

$$\frac{\partial^2\Phi}{\partial r^2} + \frac{1}{r}\frac{\partial\Phi}{\partial r} - k_z^2\frac{\varepsilon_\parallel}{\varepsilon_\perp}\Phi = \frac{ig}{\varepsilon_\perp}k_1C_1J_0(k_1r). \qquad (2.18)$$

Solving this equation, we obtain the forced solution

$$\Phi(r) = -\frac{ig}{k_1^2\varepsilon_\perp + k_z^2\varepsilon_\parallel}C_1J_0(k_1r). \qquad (2.19)$$

The field components E_z^L and E_r^L of the potential Trivelpiece–Gould mode excited by a helicon wave have the form

$$E_z^L = -\frac{\partial\Phi}{\partial z} = \frac{-gk_1k_z}{k_1^2\varepsilon_\perp + k_z^2\varepsilon_\parallel}C_1J_0(k_1r) \approx \frac{k_1\omega}{k_z\Omega_e}C_1J_0(k_1r),$$

$$E_r^L = -\frac{\partial\Phi}{\partial r} = \frac{igk_1^2}{k_1^2\varepsilon_\perp + k_z^2\varepsilon_\parallel}C_1J_1(k_1r) \qquad (2.20)$$

$$\approx -i\left(\frac{k_1\omega}{k_z\Omega_e}\right)^2C_1J_1(k_1r).$$

These expressions show that, along with the helicon resonance described by dispersion relation (2.12), the Trivelpiece–Gould resonance can, in principle, exist, provided that the following condition is satisfied:

$$k_1^2\varepsilon_\perp + k_z^2\varepsilon_\parallel = 0. \qquad (2.21)$$

This is the condition under which a helicon wave can excite internal potential E waves. Under resonance condition (2.21), the field component E_z^L increases substantially; consequently, the maximum operating efficiency of a plasma source will obviously be achieved under the double resonance condition, i.e., when helicon resonance condition (2.12) and condition (2.21) for the resonant excitation of a potential Trivelpiece–Gould mode are satisfied simultaneously. It should be noted, however, that for an elongated helicon plasma source for which inequalities (2.4) are satisfied, the second term in condition (2.21) is much larger than the first term. In other words, in the helicon approximation, the Trivelpiece–Gould resonance is impossible, so that in such a source, the double resonance cannot occur.

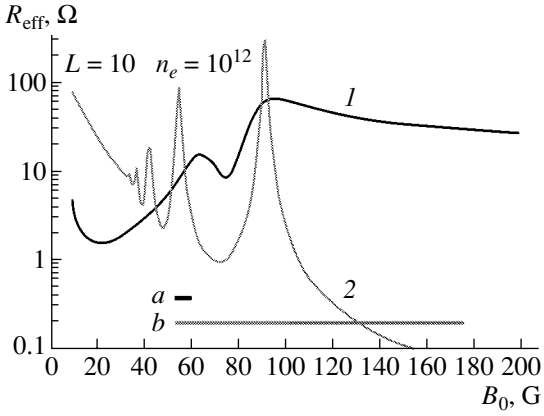

Fig. 2. Numerical results (*1*) obtained in [3] and (*2*) calculated from formula (2.24): (curve *a*) plasma region transparent to the helicon field and (curve *b*) region of applicability of the helicon approximation.

In any case, the total field in the plasma is the sum of the helicon and potential fields:

$$E_z = E_z^L, \quad E_r^L = E_r^h + E_r^L \approx E_r^h, \quad E_\varphi = E_\varphi^h. \qquad (2.22)$$

To conclude this section, we briefly discuss the question of the amount of RF field power absorbed by the plasma of the source,

$$\mathcal{P}_W = \frac{\omega}{4\pi}\int_0^R d\mathbf{r}\{\operatorname{Im}\varepsilon_\parallel|E_z|^2 + \operatorname{Im}\varepsilon_\perp|E_r|^2 + \operatorname{Im}g(E_zE_\varphi^* - E_\varphi E_z^*)\}. \qquad (2.23)$$

The last term in braces in this expression can be ignored because of the smallness of Im*g*.

Substituting the explicit expressions for the field components E_z and E_r into formula (2.23) and performing integration in the resulting formula, we finally obtain

$$\mathcal{P}_W = \frac{4\pi^2\omega^2k_z^2I_0^2}{8c^4} \times \frac{\omega R^2LK_1^2(k_zR)}{\left|k_1J_1'(k_1R)K_1(k_zR) - k_zJ_1(k_1R)K_1'(k_zR)\right|^2} \times \left\{\left(\frac{k_1\omega}{k_z\Omega_e}\right)^2\operatorname{Im}\varepsilon_\parallel(J_0^2(k_1R) + J_1^2(k_1R)) + \operatorname{Im}\varepsilon_\perp\left(1 + \frac{g^2\omega^4}{c^4k_z^2}\right)(J_1^2 + J_2^2 - 2J_0^2J_1^2/k_1R)\right\} \equiv R_{\text{eff}}I_0, \qquad (2.24)$$

where R_{eff} is the equivalent ohmic resistance of the plasma in the source.

Figures 2–7 show the dependence of the resistance R_{eff} on the magnetic field B_0 for $R = 5$ cm and for different values of L and n_e. In these figures, curves *1* are the corresponding curves from [3] and curves *2* were calculated from formula (2.24). We can see that, near helicon resonances defined by approximate condition (2.14), ohmic resistance increases abruptly by more than one order of magnitude. Moreover, the field components that are absorbed most efficiently are the E_r^h field component of the helicon wave and the E_z^L component of

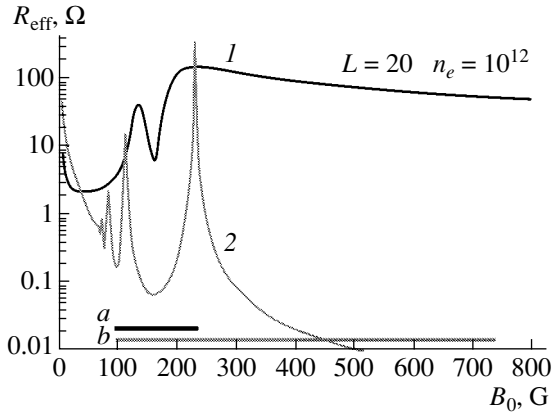

Fig. 3. The same as in Fig. 2.

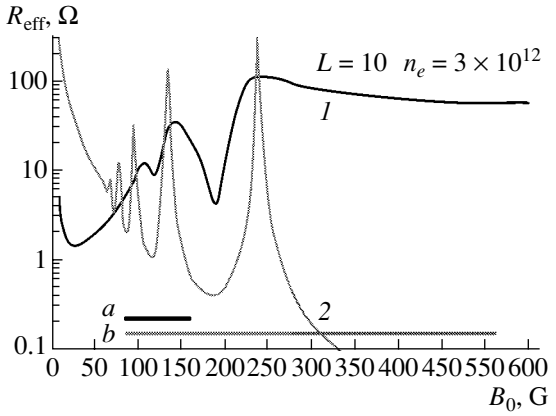

Fig. 4. The same as in Fig. 2.

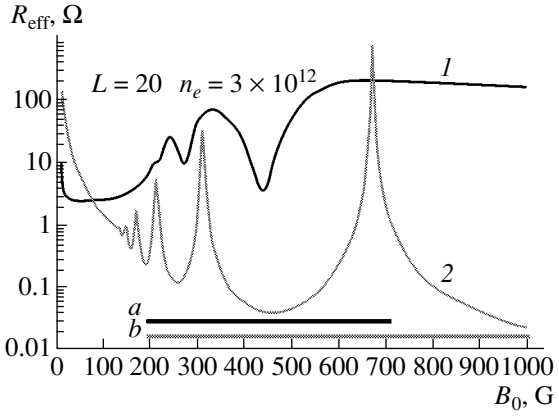

Fig. 5. The same as in Fig. 2.

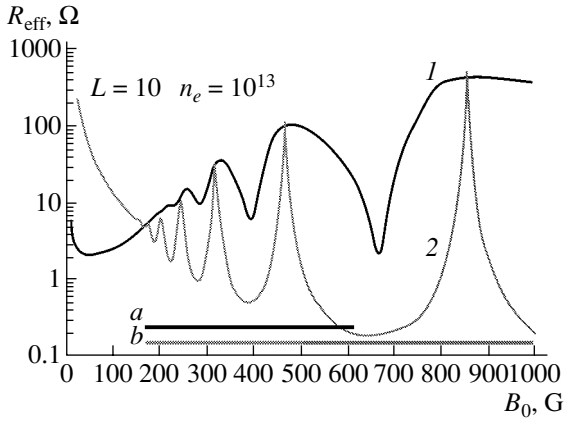

Fig. 6. The same as in Fig. 2.

the potential field of the Trivelpiece–Gould mode. Note also that the curves calculated in the helicon limit agree qualitatively with those calculated exactly for a plasma transparent to the helicon field. This qualitative agreement concerns the positions of resonances and the magnitudes of resistance at them. The plasma region transparent to the helicon field and the region of applicability of the helicon approximation are shown, respectively, by lines *a* and *b* at the bottom of each of Figs. 2–7. It should be stressed, however, that the curves obtained from the exact solution are smoother than those calculated from the helicon solution.

3. PLANAR DISK-SHAPED HELICON PLASMA SOURCE ($2R > L$)

As in [1, 2], we consider an antenna carrying a purely azimuthal current with the density

$$j_\varphi = \frac{I_0 \mu \delta(z)}{R[1 - J_0(\mu)]} J_1\left(\mu \frac{r}{R}\right) e^{-i\omega t} = \frac{I_0}{R} q \delta(z) J_1\left(\mu \frac{r}{R}\right) e^{-i\omega t}, \quad (3.1)$$

where $J_0(x)$ is a Bessel function, $J_1(\mu) = 0$ (i.e., $\mu \approx 3.8$), and $q = \mu/(1 - J_0(\mu)) \approx 2.7$. We assume that the antenna is positioned at the top surface of the cylinder[1] (Fig. 1b) and that the side surface of the cylinder and its bottom surface are metallic. Under inequalities (2.4) (i.e., in the helicon approximation), we take into account expression (3.1) and reduce the equation for the field component

$$E_\varphi^h = \tilde{E}_\varphi^h(z) J_1\left(\mu \frac{r}{R}\right)$$

in a planar disk-shaped source with $2R \gg L$ to the form

$$\frac{\partial^2 \tilde{E}_\varphi^h}{\partial z^2} - \frac{\mu^2}{R^2} \tilde{E}_\varphi^h + \frac{\omega^2}{c^2} \varepsilon_{\text{eff}}(\omega) \tilde{E}_\varphi^h = 0, \quad (3.2)$$

where $\varepsilon_{\text{eff}} = \varepsilon_\perp + g$ is given by formulas (1.5). Note that, since $\text{Im}\varepsilon_\perp \ll \text{Im}g$, the small term $\varepsilon_\perp \ll g$ is retained in order to provide a correct description of the absorption

[1] To the best of our knowledge, a systematic theoretical analysis of plasma sources with a geometry of this kind and with such an antenna has not yet been carried out in the literature.

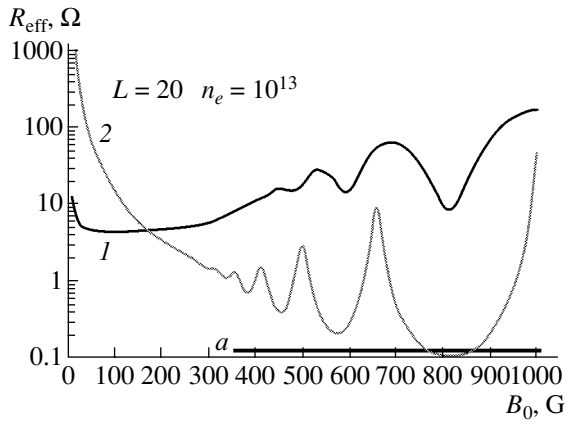

Fig. 7. The same as in Fig. 2.

of the helicon field in the plasma. Under the conditions in question, the radial component of the helicon field is equal to $E_r^h(z, r) = iE_\varphi^h(r, z)$. Equation (3.2) is valid both inside ($0 \le z \le L$) and outside ($z < 0$) the plasma. Accordingly, we solve Eq. (3.2) separately for these regions and then match the solutions at the plasma surface with the help of the boundary conditions

$$\{\tilde{E}_\varphi^h\}_{z=R} = 0,$$
$$\left\{\frac{\partial \tilde{E}_\varphi^h}{\partial z}\right\}_{z=0} = -\frac{4\pi i\omega}{c^2 R} q I_0 \{\tilde{E}_\varphi^h\}_{z=0} = 0. \tag{3.3}$$

As a result, we arrive at the following general solution to Eq. (3.2):

$$\tilde{E}_\varphi^h(z) = \begin{cases} C_1 e^{k_0 z}, & z < 0 \\ C_2 e^{ik_z z} + C_3 e^{-ik_z z}, & 0 \le z \le L, \end{cases} \tag{3.4}$$

where we have introduced the notation

$$k_z^2 = -\frac{\mu^2}{R^2} + \frac{\omega^2}{c^2}\varepsilon_{\text{eff}}, \quad k_0^2 = \frac{\mu^2}{R^2} - \frac{\omega^2}{c^2} \approx \frac{\mu^2}{R^2}. \tag{3.5}$$

We insert solution (3.4) into boundary conditions (3.3) to determine the coefficients C_1, C_2, and C_3:

$$C_1 = C_2(1 - e^{2ik_1 L}), \quad C_3 = -C_2 e^{2ik_1 L},$$
$$C_2 = -\frac{4\pi i\omega q I_0}{Rc^2(k_0 - ik_z - (k_0 + ik_z)e^{2ik_z L})}. \tag{3.6}$$

Thus, the helicon electric field in the source plasma is described by the formulas

$$\tilde{E}_\varphi^h = 2iC_2 e^{ik_z L}\sin[k_z(z - L)],$$
$$\tilde{E}_r^h(z) = i\tilde{E}_\varphi^h(z), \tag{3.7}$$

where the amplitude C_2 is given by the last of expressions (3.6).

Knowing the helicon field, we can repeat the above procedure for determining the potential of the electric field generated in the plasma. This procedure leads to the equation [cf. Eq. (2.17)]

$$\frac{\mu^2}{R^2}\varepsilon_\perp \tilde{\Phi} + \varepsilon_\parallel \frac{\partial^2 \tilde{\Phi}}{\partial z^2} = \frac{ig\mu}{R}\tilde{E}_\varphi(z), \tag{3.8}$$

where

$$\Phi = \tilde{\Phi}(z) J_0\left(\mu \frac{r}{R}\right).$$

From expressions (3.7) and Eq. (3.8), we obtain the following expressions for the longitudinal components of the potential electric field:

$$E_z^L = \tilde{E}_z^L(z) J_0\left(\mu \frac{r}{R}\right),$$
$$\tilde{E}_z^L(z) = \frac{2ik_z C_2 e^{ik_z L}}{k_z^2\varepsilon_\parallel + \frac{\mu^2}{R^2}\varepsilon_\perp}\cos[k_z(z - L)],$$
$$E_r^L = \tilde{E}_e^L(z) J_0\left(\mu \frac{r}{R}\right), \tag{3.9}$$
$$\tilde{E}_r^L(z) = \frac{2i\frac{\mu}{R} C_2 e^{ik_z L}}{k_z^2\varepsilon_\parallel + \frac{\mu^2}{R^2}\varepsilon_\perp}\sin[k_z(z - L)].$$

We can now calculate the RF power deposited in the plasma of a planar disk-shaped source. To do this, we turn to general formula (2.24), in which the last term in the integrand can be neglected as before. Substituting expressions (3.7) and Eq. (3.8) into this formula gives

$$\mathcal{P}_W = \frac{\omega}{4\pi}\int_0^R d\mathbf{r}\{\operatorname{Im}\varepsilon_\parallel |E_z^L|^2 + 2\operatorname{Im}\varepsilon_\perp |E_r^h|^2\}$$
$$= \frac{2\omega R^2 L}{R^2 c^4}\frac{16\pi^2\omega^2 q^2 J_0^2(\mu) \times 4I_0^2}{k_0^2 \sin^2 k_z L + k_z^2 \cos^2 k_z L} \tag{3.10}$$
$$\times\left\{\operatorname{Im}\varepsilon_\parallel \frac{q^2\mu^2}{k_z^2|\varepsilon_\parallel|^2} + 2\operatorname{Im}\varepsilon_\parallel\right\} = R_{\text{eff}} I_0^2.$$

The above analysis of a planar disk-shaped plasma source in the helicon approximation, first of all, leads to the conclusion that, as in an elongated source, internal helicon waves that can be excited in the plasma should satisfy the condition

$$k_0^2 \sin^2 k_z L + k_z^2 \cos^2 k_z L = 0, \tag{3.11}$$

where k_0 and k_z are given by formulas (3.5).

Since $k_0^2 \ll k_z$, the roots of Eq. (3.11) coincide to a good accuracy with the roots of the function $\cos^2 k_z L$; i.e., we arrive at the solutions [cf. Eq. (2.14)]

$$k_z^2 L^2 = \frac{L^2 \omega^2}{c^2} g^2 \approx \pi^2 (n + 1/2)^2. \quad (3.12)$$

The quantity k_z should be calculated with allowance for the second of conditions (1.3), namely, $\omega \gg k_z V_{Te}$, so that we have $L \geq 10$ cm. The helicon field is such that $E_e^h = E_\varphi^h \gg E_r^L$; consequently, neither the longitudinal resonance, which corresponds to the vanishing of the denominators in expressions (3.9), nor the double resonance can occur. As for the field component E_z^L, it contributes substantially to the plasma resistance. However, we did not analyze this case numerically because we do not know whether experimental measurements have been carried out in plasma sources with a geometry of this kind.

For L = 10 cm, R = 10 cm, B_0 = 50 G, and n_e = 10^{12} cm^{-3} (far from resonance), the plasma resistance is equal in order of magnitude to $R_{\text{eff}} \approx 1\ \Omega$. At resonance, the resistance R_{eff} is higher by more than one order of magnitude, as in the case of an elongated source.

The general conclusion of our study can be formulated as follows. The above investigation of analytic solutions for a helicon plasma source in different limiting cases has confirmed the correctness of the exact general numerical solution to the problem that was obtained in [3], according to which planar disk-shaped plasma sources are capable of operating efficiently both near the resonances and far from them.

REFERENCES

1. K. V. Vavilin, V. Yu. Plaksin, Kh. M. Ri, and A. A. Rukhadze, Zh. Tekh. Fiz. **74** (5), 44 (2004) [Tech. Phys. **49**, 565 (2004)].
2. K. V. Vavilin, V. Yu. Plaksin, Kh. M. Ri, and A. A. Rukhadze, Zh. Tekh. Fiz. **74** (6), 25 (2004) [Tech. Phys. **49**, 686 (2004)].
3. A. F. Alexandrov, G. E. Bugrov, E. A. Kralkina, *et al.*, J. Russ. Laser Res. **24**, 301 (2003).
4. R. W. Boswell, Plasma Phys. Controlled Fusion **26**, 1147 (1984).
5. F. F. Chen, Plasma Phys. Controlled Fusion **33**, 339 (1991); F. F. Chen and G. Chelavier, J. Vac. Sci. Technol. A **10**, 1389 (1992).
6. A. F. Alexandrov *et al.*, in *Proceedings of the 22nd International Conference on Phenomena in Ionized Gases (ICPIG-22), New Jersey, 1995*, Vol. 4, p. 153; in *Proceedings of the 25th International Conference on Phenomena in Ionized Gases (ICPIG-25), Nagoya, 2002*, Vol. 3, p. 33.
7. K. P. Shamray, A. F. Alexandrov, E. A. Kralkina, *et al.*, J. Phys. IV (France), Colloq. C4, Suppl. J. Phys. III, No. 10, C4-365 (1997).
8. *High Density Plasma Sources*, Ed. by O. A. Popov (Noyes, New Jersey, 1995).
9. N. F. Vorob'ev and A. A. Rukhadze, Fiz. Plazmy **20**, 1065 (1994) [Plasma Phys. Rep. **20**, 955 (1994)].
10. A. F. Aleksandrov, N. F. Vorob'ev, E. A. Kralkina, *et al.*, Zh. Tekh. Fiz. **64** (11), 53 (1994) [Tech. Phys. **39**, 1118 (1994)].
11. A. F. Aleksandrov, G. E. Bugrov, E. A. Kralkina, *et al.*, Prikl. Fiz., No. 1, 5 (1995).

Translated by O. Khadin

Technical Physics, Vol. 49, No. 6, 2004, pp. 698–706. Translated from Zhurnal Tekhnicheskoĭ Fiziki, Vol. 74, No. 6, 2004, pp. 35–42.

GAS DISCHARGES, PLASMA

The Influence of Metastable Atoms and the Effect of the Nonlocal Character of the Electron Distribution on the Characteristics of the Positive Column in an Argon Discharge

E. A. Bogdanov*, A. A. Kudryavtsev*, L. D. Tsendin, R. R. Arslanbekov***, V. I. Kolobov***, and V. V. Kudryavtsev******

** St. Petersburg State University, St. Petersburg, 198504 Russia*
e-mail: akud@ak2138.spb.edu
*** St. Petersburg State Polytechnic University, St. Petersburg, 195251 Russia*
e-mail: tsendin@phtf.stu.neva.ru
**** CFDRC, 215 Wynn Drive, Huntsville, AL, USA*
e-mail: vik@cfdrc.com
***** CFD-Canada, 45 English Ivyway, Toronto*
e-mail: vvk@cfdcanada.com
Received November 3, 2003

Abstract—Commercial CFDRC software (http://www.cfdrc.com/~cfdplasma) is used to self-consistently simulate the plasma of the positive column (PC) of a dc discharge in argon. The software allows simulations in an arbitrary 3D geometry by using Poisson's equation for the electric potential and fluid equations for the heavy components and by solving a nonlocal kinetic equation for electrons. It is shown that, in calculating the electron distribution function, the local approximation is almost always inapplicable under real conditions of a diffuse PC usually met in practice (pR < (5–10) cm Torr). The influence of metastable atoms, which can substantially affect the parameters of the PC plasma, is considered. It is shown that superelasic collisions play an important role in enriching the fast component of the electron distribution function and that the Penning ionization can result in an ascending volt–ampere characteristic of the positive column. *© 2004 MAIK "Nauka/Interperiodica".*

A fluid model (see, e.g., [1–5]) based on the assumption that the plasma electrons obey a Maxwellian distribution is still widely used to simulate gas-discharge plasma. However, it has long been known (see, e.g., [6]) that the electron distribution differs markedly from Maxwellian (perhaps, except for the case of Langmuir's paradox in the free-fall regime, when the electron distribution function (EDF) is fairly close to Maxwellian [7]). As a rule, at moderate degrees of ionization ($n_e/N < 10^{-3}$), the EDF is highly nonequilibrium and is depleted in the inelastic energy range $\varepsilon > \varepsilon^*$. For a real nonequilibrium EDF, calculations of the reaction constants under the assumption of a Maxwellian distribution have no physical sense, so it is difficult to estimate (even qualitatively) the errors introduced by this assumption.

Nevertheless, in practice, a number of the main plasma parameters are often consistent with calculations by the fluid model. This rather surprising result was attributed in [8, 9] to the fact that, in gas discharges, both the electron energy balance, governed by inelastic excitation processes, and the electron density balance, governed by ionization, are usually determined by the tail of the EDF, i.e., by collisions with a high energy threshold (or, in other words, by the temperature of the fast electrons, T_{et}). Therefore, the fluid model is actually dealing with the temperature of the fast electron component ($T_{et} < T_e$), rather than with the mean electron temperature T_e (the temperature averaged over the entire EDF). It is this circumstance that allows one to determine the ionization and excitation rates with a sufficiently high accuracy.

To take into account the non-Maxwellian character of the electron distribution and to determine the corresponding constants for reactions with the participation of electrons, the kinetic equation is usually solved in the local approximation, e.g., with the help of the Bolsig package [10] or the Lookup Tables technique [11]. For this approach to be applicable, it is necessary that the characteristic diffusion length Λ (e.g., for a cylinder, $\Lambda = R/2$) exceed the electron energy relaxation length λ_ε ($\Lambda \gg \lambda_\varepsilon$) [12]. For $\lambda_\varepsilon > \Lambda$, the results of calculations with the use of a local EDF are physically unjustified [12] and, as was shown in [13, 20], lead to crude errors in determining the parameters of the positive column (PC) of a glow discharge. An analysis of the transport properties [14] also shows that, for a weakly ionized plasma with a nonequilibrium EDF, a closed set of

fluid transport equations in the case of rare electron–electron collisions can be constructed only for the local regime, $\Lambda > \lambda_\varepsilon$. Hence, to determine the PC parameters using conventional methods, it is necessary to thoroughly analyze whether the local approximation for calculating the EDF is applicable.

When determining the EDF by solving the kinetic equation, it is necessary to know the longitudinal electric field E/p, which imparts energy to electrons. For this reason, when analyzing the EDF in plasma (see, e.g., [15]) and when creating a software for computing the EDF (see, e.g., [10]), the EDF is usually calculated in a given field. However, in plasma physics problems, neither the fields nor the particle motion can usually be considered given, because the fields are governed not only by the external conditions, but also by the charged particle motion, which in turn is governed by the fields. Therefore, all such problems should be solved self-consistently: only the fields needed to maintain a steady-state plasma are allowed by the plasma to penetrate into the discharge volume. The ionization rate is determined by the shape of the EDF that is formed by fields in the plasma. On the other hand, it is necessary that the production of charged particles by ionization compensate for their diffusion loss ($\nu_i\tau_a = 1$), which depends primarily on the discharge geometry and pressure $p\Lambda$. Therefore, the heating field E/p (in contrast to the discharge current) is also determined by the parameter $p\Lambda$ [8, 9]; i.e., for a given geometry, it cannot be specified arbitrarily.

Hence, the use of non-self-consistent models can lead to uncontrollable errors in determining the parameters of a gas-discharge plasma. In turn, the accuracy of self-consistent models is restricted by a "bottleneck," i.e., by the most uncertain element of the model. Therefore, even if the most advanced and reliable methods are used in some computational blocks of a code, whereas other its elements are known poorly (or insufficiently), the use of these methods does not improve the accuracy of the results obtained. In other words, in practice, it is desirable to use computational elements that are known with equal accuracy. Let us illustrate this with some typical examples.

It is usually believed (see, e.g., [16]) that the descending volt–ampere characteristic (VAC) of a discharge is associated with volume processes, for instance, with a transition from direct to step ionization or with an increase in the effect of electron–electron collisions on the formation of a Maxwellian EDF. However, in low-current (especially, capillary) discharges, the descending VAC can also be caused by an increase in the lifetime of charged particles due to a decrease in the thickness of the space-charge sheath with increasing current [17, 18]. Therefore, ignoring the finite thickness of the wall sheath (i.e., the extrapolation of the quasineutral plasma approximation up to the chamber wall) can result in significant errors at low discharge currents. The possibility of a descending (due to a change in the sheath thickness) VAC was also demonstrated in [19], in which direct ionization was only taken into account because step ionization can be ignored at low currents. However, at a relatively high density of metastable atoms, the Penning ionization of these atoms can predominate over direct ionization (see, e.g., [20]). This, in turn, can result in an ascending VAC [21]. In other words, a PC can possess both descending and ascending VACs. It is also well known that impacts of the second kind in collisions of slow electrons with metastable atoms can substantially enrich the high-energy part of the EDF and can thus substantially increase the direct-ionization constants and the excitation constants for high-lying levels [22]. Although the important role of the processes with the participation of metastable atoms has long been known, their influence on the characteristics of the PC plasma is usually considered within non-self-consistent models.

In this paper, the role of these processes is considered within a comprehensive self-consistent model. As a subject of studies, we have chosen the PC of a dc discharge in argon, which has received the most study in the literature.

The discharge parameters were simulated using a commercial software developed in the CFD Research Corporation, Huntsville, AL, USA [11, 23]. A detailed description of the self-consistent model of a discharge plasma, the iteration numerical scheme, and the methods for solving the set of equations is given in [11, 23]. In simulations, the main input parameters may be the geometry of the discharge volume, the pressure and composition of the working gas, and the specific power W deposited in plasma. A dc discharge is an exclusive case where the simple relation $W = jE$ allows one to specify the discharge current instead of W. The self-consistent electric field was found from Poisson's equation. Heavy particles were described in the fluid model. The parameters of the electron gas could be found by solving either the nonlocal or local kinetic equation for the EDF.

Some of the most detailed calculations of the formation of the EDF in a PC are presented in a series of studies [24–26] for an Ar-like gas with the same set of model cross sections for elastic and inelastic processes of the excitation and direct ionization and with allowance for the escape of electrons onto the wall. The density of charged particles was calculated taking into account direct ionization only; i.e., the density of metastable atoms and the processes with their participation were not considered. To test the code, we compared our results to the calculations performed in [24–26] for $NR \geq 10^{15}$ cm^{-3} (the tube radius was $R = 1$ cm) with the use of the same set of volume processes. The results obtained are in good agreement with data of [24–26] on the values of the EDF, E/p (the VAC), the wall potential Φ_w, the mean electron energy T_e, the electron density n_e, etc. Some of these results are presented in Table 1. It can be seen that the data obtained with the CFDRC

Table 1. Comparison of the employed CFDRC code with the results from [24–26]

(N_0R, I)	E_z, V/cm		Φ_w, V		$T_e(r = 0)$, eV		$n_e(r = 0)$, cm^{-3}	
10^{15} cm^{-2}, 10 mA	2.3	2.8	20.5	22.4	6	6.2	3.5×10^9	1.8×10^9
10^{16} cm^{-2}, 1 mA		6.2		20.5	5.3	4.6	–	7.6×10^8
10^{16} cm^{-2}, 10 mA	6.50	6.1	17	19.9	5.2	4.6	1.1×10^9	6.7×10^9

Note: The left columns for each parameter show the results from [24–26], and the right columns show the results of our study.

code are in good agreement with the data of test calculations. Below, we will consider the influence of a number of the above effects on the results of simulations of a PC in an argon discharge.

As was noted above, almost all of the available methods for calculating the parameters of a PC use a solution of the kinetic equation for electrons in the local approximation. This means that the EDF is factorized as follows:

$$f_0(w, r) = n_e(r) f_0^0(w, E/p); \quad (1)$$

i.e., it is assumed that the distribution over the kinetic energy w at a fixed point r depends on the local value of the reduced longitudinal field E/p and on other parameters (the gas temperature, the density of excited particles, etc.). This method is applicable when the characteristic diffusion length of the discharge exceeds the electron-energy relaxation length: $\Lambda \gg \lambda_\varepsilon$ [12]. If the energy balance is determined by elastic collisions, then for atomic gases in the energy range $\varepsilon < \varepsilon^*$, in which most electrons are concentrated, this length is

$$\lambda_\varepsilon \approx \lambda/\sqrt{\delta} \simeq 100\lambda \quad (2)$$

and the inequality $\lambda_\varepsilon > \Lambda$ holds up to relatively high pressures, $pR \le$ 5–10 cm Torr (here, ε^* is the threshold energy for inelastic processes and $\delta = 2m/M$). Therefore, under actual PC conditions, the local approximation for atomic gases (as well as the methods using this approximation to calculate the EDF) is almost always inapplicable. This is illustrated by Fig. 1, which shows that, even at relatively high values of pR (pR = 5.4 cm Torr), the EDF cannot be factorized in form (1), because the normalized EDFs plotted as functions of kinetic energy are different for different radii r. The EDF of this kind is of nonlocal nature; i.e., it depends on the values of the physical parameters (primarily on the field strength) in the region determined by the inequality $\lambda_\varepsilon \gg \lambda$ (where λ is the electron mean free path), rather than on their values at a given point. Since at $\lambda_\varepsilon \gg \Lambda$, the energy of an electron during its single pass across the tube changes only slightly, the integral of motion of such electrons is the total energy

$$\varepsilon = w + e\varphi(r) = mV^2/2 + e\varphi(r) \quad (3)$$

(the kinetic energy plus the potential energy) [12]. Therefore, from the physical standpoint, the most appropriate arguments for describing a nonlocal EDF are the variables ε and r. The behavior of the trapped ($\varepsilon \le e\Phi_w$) and transit ($\varepsilon > e\Phi_w$) electrons in the nonlocal regime is quite different (here, Φ_w is the potential difference between the discharge axis and the tube wall). For ($\varepsilon \le e\Phi_w$), after averaging the Boltzmann equation over the volume accessible to electrons possessing a given total energy, we find that the functions $f_0(\varepsilon)$ coincide without any shift that could be caused by the space potential and normalization [12]. This substantially simplifies the analysis of the formation of the EDF. The fact that the EDF of the trapped electrons $f_0(\varepsilon)$ does not depend on radius is used in practice to detect the nonlocal features of the EDF (Fig. 2). For transit electrons that can overcome the transverse potential drop and escape onto the wall, the nonlocal EDF in the collisional regime can depend on both ε and r [12]. It is also necessary to take into account that the relation between the volume processes and the escape of electrons onto the wall can be different for different energy ranges. Thus, as the pressure increases, the nonlocal EDF $f_0(\varepsilon)$ for trapped electrons in the inelastic energy range also becomes dependent on radius. The reason is that, for $\varepsilon > \varepsilon^*$, the corresponding electron relaxation length

$$\lambda_\varepsilon^* = \sqrt{\lambda\lambda^*} \quad (4)$$

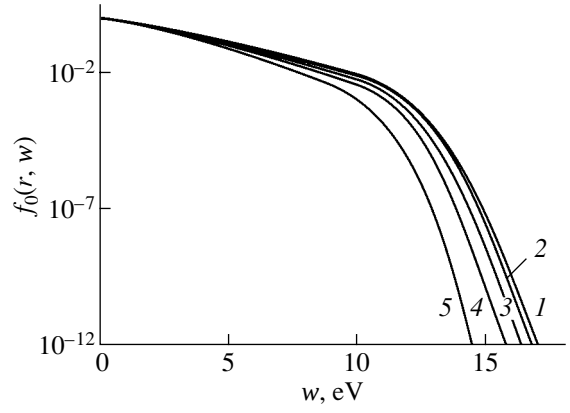

Fig. 1. Normalized EDFs for pR = 5.4 cm Torr as functions of kinetic energy: r = (*1*) 0, (*2*) 0.2R, (*3*) 0.4R, (*4*) 0.6R, and (*5*) 0.8R.

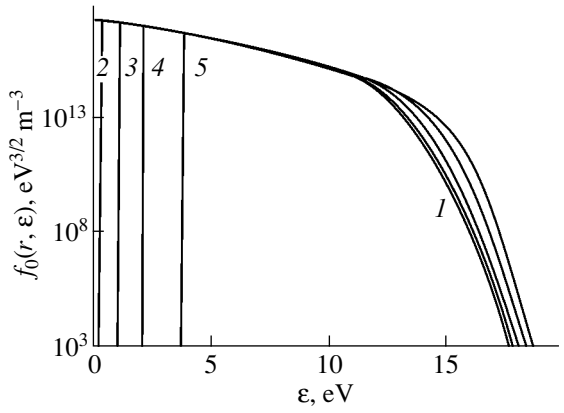

Fig. 2. EDFs over the total energy for pR = 5.4 cm Torr. Curves *1–5* correspond to the same radii as in Fig. 1.

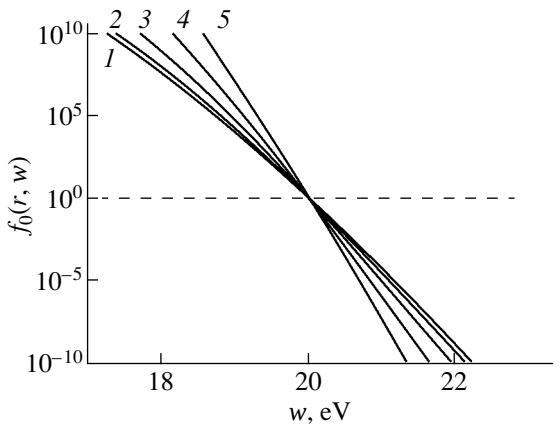

Fig. 3. Fast components of the EDFs over kinetic energy, joint at w_0 = 20 eV, for pR = 5.4 cm Torr. Curves *1–5* correspond to the same radii as in Fig. 1.

is much shorter than that given by Eq. (2) (here, λ^* is the electron mean free path related to inelastic processes), so the inequalities $\lambda_\varepsilon > \Lambda > \lambda_\varepsilon^*$ may hold at higher pressures. At first glance, it would seem that, in this situation, the EDF consists of a nonlocal component at $\varepsilon < \varepsilon^*$ and a local component at $\varepsilon > \varepsilon^*$ (a small local "tail" is attached to the nonlocal "body"). However, this is not the case because the fast component at $\varepsilon > \varepsilon^*$ is not factorized in form (1). When being normalized at some point at $w > \varepsilon^*$ (at w = 20 eV in Fig. 3) and recalculated as functions of kinetic energy, the tails $f_0^0(w)$ turn out to be different for different radii r (Fig. 3). As was noted above, the use of the local approximation for determining the EDF is restricted to the case where this function is factorized in form (1). We prefer to consider the EDF to be nonlocal when the terms with spatial gradients in the kinetic equation cannot be omitted. Depending on total energy (3), the components of this nonlocal EDF may be either dependent on or independent of the radius (see, e.g., [24], where the concept of a nonlocal EDF was considered in a narrower sense and by nonlocal functions were meant only the functions $f_0(\varepsilon, r)$ that were independent of the radius).

In [24–26], a number of effects influencing the VAC of a discharge (in particular, a change in the thickness of the wall sheath and the dependence of the ion mobility on the field strength $b_i(E)$) were pointed out. As an illustration of these effects, Fig. 4 shows a relative (with respect to calculations by the fluid model) change in the VAC of a discharge at a pressure of p = 100 mtorr and a tube radius of R = 1 cm; the VACs were calculated with (curve *1*) and without (curve *2*) allowance for variations in $b_i(E)$. The set of plasmochemical reactions was chosen according to [24–26], and the ion mobility was calculated by the formula by Frost. As was noted above, the fluid model gives a temperature $T_{et} < T_e$, so the field strength in the fluid model is lower than that in kinetic simulations. Taking into account the dependence $b_i(E)$, which leads to an increase in the time during which electrons escape onto the wall, also decreases the longitudinal heating field (Fig. 4). In the case at hand, we took into consideration the ionization mechanism alone; consequently, the calculated VAC that descends at low currents can be attributed to a narrower wall sheath. This effect should be taken into account in simulations of low-current (especially, capillary) discharges. As the current increases and the sheath thickness becomes sufficiently small, the VAC becomes saturated and the field depends only slightly on the current. The VACs similar to those presented in Fig. 4 were also computed both with and without taking into account electron–electron collisions in calculating the EDF. The calculations showed that, in the case under

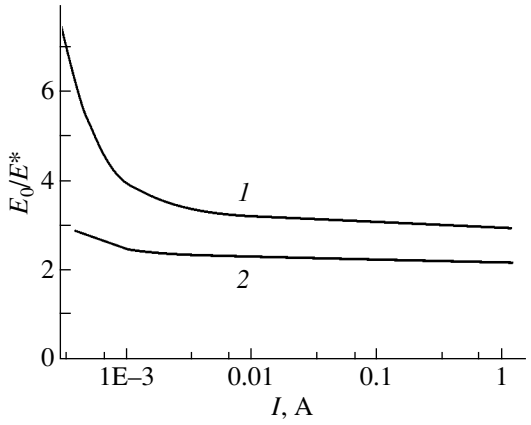

Fig. 4. VACs calculated for the set of reactions from [24–26] for p = 100 mtorr and R = 1 cm and normalized to E^* (the electric field calculated in the fluid model under the same conditions at a current of I = 1 A): (*1*) without and (*2*) with allowance for the dependence $b_i(E)$ by the Frost formula.

Table 2. The set of reactions for the three-level scheme of terms of an argon atom

No.	Reaction	ε, eV	Constant	Comment
1	$e + \mathrm{Ar} \longrightarrow e + \mathrm{Ar}$	–	Cross section [27]	Elastic scattering (momentum transfer)
2	$e + \mathrm{Ar} \rightleftharpoons e + \mathrm{Ar}_m^*$	11.55	Cross section [28]	Excitation and deexcitation of the metastable level
3	$e + \mathrm{Ar} \longrightarrow 2e + \mathrm{Ar}^+$	15.9	Cross section [27]	Direct ionization from the ground state
4	$e + \mathrm{Ar}_m^* \longrightarrow 2e + \mathrm{Ar}^+$	4.35	Cross section [28]	Step ionization from the metastable level
5	$e + \mathrm{Ar}_m^* \longrightarrow e + \mathrm{Ar}_r^*$	0.07	$k_q = 2 \times 10^{-13}$ m^3 s^{-1} [29]	Quenching of the metastable level via the transition to a resonant level (11.67 eV)
6	$e + \mathrm{Ar} \longrightarrow e + \mathrm{Ar}$	11.55	Cross section [28]	Total excitation by electron impact
7	$\mathrm{Ar}_r^* \longrightarrow \mathrm{Ar} + \hbar\nu$	–	$A_R = 10^6$ s^{-1}	Resonant emission with allowance for self-absorption (λ = 106.4 nm)
8	$2\mathrm{Ar}_m^* \longrightarrow \begin{cases} e + \mathrm{Ar}^+ + \mathrm{Ar} \\ e + \mathrm{Ar}_2^+ + \mathrm{Ar} \end{cases}$	–	$k_p = 6.2 \times 10^{-16}$ m^3 s^{-1} [29]	Penning ionization

study, electron–electron collisions play an important role only at high currents (>1 A). Since, under such conditions, the gas is heated and a transition to an arc can occur, the corresponding curves are not presented in Fig. 4. It should also be noted that, because of the high values of E/p at low pressures, the EDF was far from Maxwellian up to the degree of ionization $n_e/N \leq 10^{-2}$.

As in the test calculations [24–26], the above simulations were performed with allowance for direct ionization only. It is well know, however, that the parameters of a PC in noble gases are significantly affected by the processes with the participation of long-lived metastable states, whose densities n_m can be fairly high and usually exceed the electron density n_e. For this reason, we performed simulations with the use of the tree-level model of an argon atom with allowance for eight reactions listed in Table 2. The constants of the processes with the participation of electrons were calculated by convoluting the corresponding cross sections with the calculated EDF. As was expected, the use in [24–26] of the three-level scheme with allowance for direct ionization only restricts the applicability of the results to a low-pressure range $N_0R < 3 \times 10^{15}$ cm Torr, i.e., to the free-fall regime ($\lambda \geq R$). Table 3 presents the results of some our simulations of a PC in argon with allowance for three and eight reactions (with and without account taken of the processes with the participation of the metastable level). The results obtained show that, as the pressure increases (at $N_0R > 3 \times 10^{15}$ cm Torr), the step ionization and Penning ionization become dominant. As a result, the field decreases, while the electron density increases; this leads to a change in the other parameter sensitive to the density n_m. We note that the electron density profiles in the nonlocal case decrease almost linearly with radius, in contrast to the conventional (Bessel) profiles obtained in the fluid model (Fig. 5). The reason is the competition of two effects. First, ionization occurs predominantly near the tube axis, resulting in a narrower profile of n_e [12, 13]. Second, the dependence $b_i(E) \sim E^{-1/2}$ results in a smoother density profile in comparison to a Bessel profile.

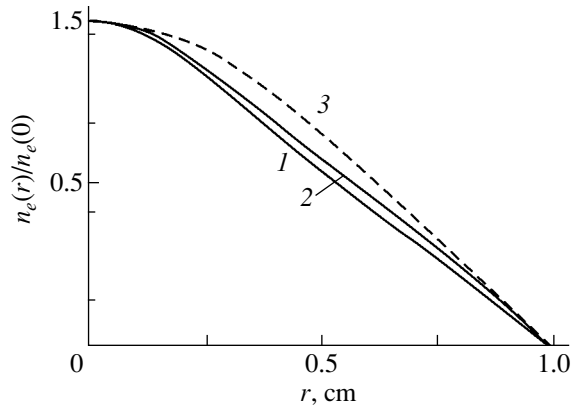

Fig. 5. Normalized electron density profiles for a gas density of $N_0 = 3 \times 10^{15}$ cm^{-3}: (*1*) without and (*2*) with allowance for the dependence of the ion mobility on the radial field (the Frost formula). The dashed line shows the Bessel function $J_0(2.4r/R)$.

At the same time, a number of the parameters, such as the temperature T_e (the electron energy averaged over the entire EDF), the wall potential Φ_w, etc., vary slightly. An insignificant change in T_e is explained by the fact that, in the case where the energy balance is governed by inelastic processes, the shape of the body of the EDF in the energy range $\varepsilon < \varepsilon^*$, where most of the electrons are concentrated, depends slightly on the field [9, 12]. These electrons, gaining the energy from the field in the range (0, ε^*), merely transfer the required energy flux to the tail of the EDF [9, 12]. At

Table 3. Comparison of the results of simulation of a PC in argon with three (3*R*) and eight (8*R*) volume reactions

No.	Parameters (N_0R, I)	E_z, V/cm		Φ_w, V		$T_e(r=0)$, eV		$n_e(r=0)$, 10^9 cm^{-3}	
		3*R*	8*R*	3*R*	8*R*	3*R*	8*R*	3*R*	8*R*
1	3×10^{15} cm^{-2}, 1 mA	3.5	3.7	20.7	21.6	5.1	5.2	0.44	0.43
2	3×10^{15} cm^{-2}, 10 mA	3.2	3.3	19.9	20.6	5.1	5.2	4.0	4.0
3	3×10^{15} cm^{-2}, 100 mA	3.2	3.1	19.5	19.9	5.1	5.1	36.7	37.4
4	3×10^{16} cm^{-2}, 1 mA	16.6	6.2	21.8	19.8	4.0	3.9	0.7	1.6
5	3×10^{16} cm^{-2}, 10 mA	16.4	3.8	20.4	17.6	4.0	3.8	5.9	21.6
6	5.76×10^{16} cm^{-2}, 10 mA	30.4	3.3	21.3	17.5	3.9	3.5	5.5	47.6
7	10^{17} cm^{-2}, 1 mA	55.4	4.0	25.5	18.2	3.8	3.6	0.6	6.9
8	10^{17} cm^{-2}, 10 mA	52.3	3.47	22.8	17.6	3.8	3.4	5.2	73

$\varepsilon < \varepsilon^*$, the EDF acts merely as a peculiar kind of a "pipeline" from a source in the low-energy region to a sink in the tail region ($\varepsilon > \varepsilon^*$), so that the electrons with $\varepsilon < \varepsilon^*$ make an insignificant contribution to the total energy balance of the electron gas. The electron distribution along this pipeline is determined by the condition that the energy flux inflowing near the zero energy is equal to the energy flux outflowing at the threshold energy ε^*, no energy is lost on the way, and the energy flux does not depend on the "fall."

The fast component of the EDF, f_{0t}, is determined by the total frequency ν^* of inelastic collisions involving the excitation of all atomic states. The function f_{0t} is fitted well by the exponential dependence [9]

$$f_{0t}(\varepsilon) = c_m e^{-\frac{\varepsilon}{T_{et}}} \tag{5}$$

with the temperature

$$T_{et} = \sqrt{\nu^*/D_E}, \tag{6}$$

where $D_E = 2(eE\lambda)^2\nu/3$ is the coefficient of diffusion over energy in the electric field (see, e.g., [9, 12] for details). It can be seen from Eq. (6) that T_{et} depends substantially on the choice of the excitation cross sections.

Our simulations revealed an interesting (but little-known) effect consisting in the replication of the shape of the body of the EDF in its fast component due to impacts of the second kind in collisions of slow electrons with metastable atoms. Figure 6 shows the EDFs calculated for $p = 1$ Torr, $R = 1$ cm, and $I = 10$ mA with (curve *1*) and without (curve *2*) allowance for impacts of the second kind. One can see that a gently sloping pedestal f_{0h}, replicating the shape of the slow component (the body) of the EDF is added to the usual EDF f_{0t} (5), which is sharply decreasing above the threshold excitation energy ($\varepsilon^* \simeq 11.55$ eV for argon). As a result, the fast component of the EDF can be represented as the sum $f_0 = f_{0t} + f_{0h}$. This shape of the EDF can be explained by the fact that the kinetic equation includes the source of fast electrons that is associated with impacts of the second kind and is proportional to the low-energy component (body) of the EDF, $f(w - \varepsilon^*)$. Roughly speaking, a partial solution taking into account inhomogeneity is added to the rapidly decaying solution of the homogeneous kinetic equation f_{0t} derived without allowance for this source (Fig. 6, curve *2*). At high metastable densities, the approximate expression for f_{0h} can be found by setting to zero the integral of inelastic collisions:

$$\nu^*(\varepsilon - e\varphi(r))\sqrt{\varepsilon - e\varphi(r)} \times\left(f_0(\varepsilon) - \frac{n_m g_a}{N_0 g_m} f_0(\varepsilon - \varepsilon^*)\right). \tag{7}$$

Thus, an additional fast component f_{0h} replicating the shape of the body of the EDF has the form

$$f_{0h}(\varepsilon) \simeq \frac{n_m g_a}{N_0 g_m} f_0(\varepsilon - \varepsilon^*). \tag{8}$$

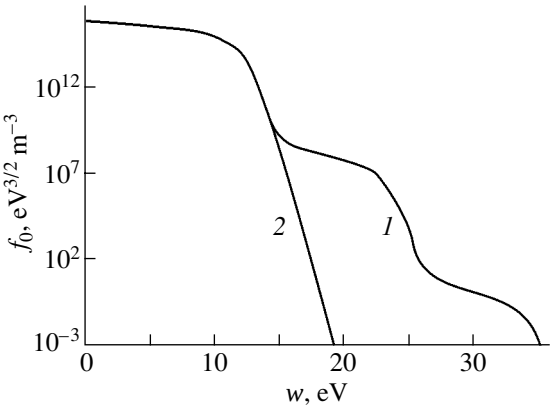

Fig. 6. EDFs at the axis of a discharge ($r = 0$), calculated (*1*) with and (*2*) without allowance for impacts of the second kind for $p = 1$ Torr, $R = 1$ cm, and $I = 10$ mA.

Table 4. Ratios of the excitation and direct-ionization constants calculated with an EDF calculated with and without allowance for impacts of the second kind for $N_0 = 10^{17}$ cm^{-3}, $R = 1$ cm, and $I = 10$ mA

No.	Level	ε, eV	Ratio of the excitation constants
1	$3d_3^{7/2}$	14.01	1.5
2	$3d_2^{5/2}$, $5s_2^{3/2}$	14.06	1.7
3	$3d_3^{5/2}$, $5s_1^{3/2}$	14.09	1.9
4	$3d_1^{3/2}$	14.15	2.1
5	$3d_2'^{5/2}$	14.21	2.3
6	$3d_2'^{5/2}$, $3d_2'^{5/2}$, $5s_0'^{1/2}$, $3s_1'^{5/2}$	14.23	2.4
7	$3d_1'^{3/2}$,	14.30	2.7
8	$3d_1^{1/2}$	14.71	19
9	$6p_1'^{1/2}$, $6p_1'^{3/2}$, $6p_2'^{3/2}$	15.20	109
10	Ar^+	15.76	2670

Although the amplitude (absolute value) of the additional fast component is lower by a factor of $\sim n_m/N_0$ than the low-energy component of the EDF at $\varepsilon \le \varepsilon^*$, it exceeds f_{0h} at energies of several electronvolts above the threshold energy ε*. This is because the value of T_{et} (6) is small and f_{0h} (5) sharply decreases with increasing energy. Since $f_0(\varepsilon - \varepsilon^*)$ near the threshold energy ε* varies slightly and is fitted well by the linear dependence [9]

$$f_0(\varepsilon) = c_n\left(1 - \frac{\varepsilon}{\varepsilon_1 + T_{et}}\right)$$

the high-energy component of the EDF increases substantially as a result of the replication of the body of the EDF into this energy range. In turn, this results in a change in the constants for direct ionization and the excitation for high-lying levels. Knowledge of the populations of these states is of interest for mass spectrometry and optical emission spectroscopy sources [30]. As an illustration, Table 4 show the relative change in the constants for direct ionization and the excitation of high-lying excited states when the EDF is calculated with and without allowance for impacts of the second kind of slow electrons with metastable atoms for $N_0 = 10^{17}$ cm^{-3}, $R = 1$ cm, and $I = 10$ mA. It can be seen from the table that the results differ markedly; hence, this effect should be taken into account in calculating high-lying excited states in gases that have long-lived metastable states.

The results of calculations also show (see Table 3) that the contribution from the Penning ionization to the production of electrons can be substantial at low currents. As was noted above, such an interesting and unusual phenomenon as an ascending VAC of a PC can be observed in this case. Recall that, in actual practice, the VACs are usually descending [16]. For this reason, to maintain a stable PC, it is necessary to use load resistors consuming an additional electric power. Obviously, the search for operating conditions with an ascending VAC, which make it possible to exclude energy loss in ballast resistors, is of importance for applications. Physical reasons for the ascending VAC can be elucidated by separating out the dominant terms in the particle balance equation [21]. The density of metastable atoms n_m in the PC at moderate pressures (when the diffusion loss of these atoms on the wall can be ignored) is determined by the two processes: their production by the excitation from the ground state (the constant k^*) and the quenching via a transition to a neighboring resonant level (the constant k_q):

$$n_m \simeq N_0 k^*/k_q. \quad (9)$$

Accordingly, if the dominant ionization mechanism is the Penning ionization with the constant k_p, then for the electron density we have

$$n_e \simeq k_p n_m^2 \tau_a \simeq k_p \tau_a (N_0 k^*)^2/k_q^2, \quad (10)$$

where τ_a is the ambipolar lifetime.

It can be seen from Eq. (10) that, for the electron density to increase with current, the constant k^* should increase; i.e., the field should somewhat increase (all of the other coefficients in Eq. (10) depend slightly on the field). Since such regimes are of great practical interest, we carried out special model calculations. These calcu-

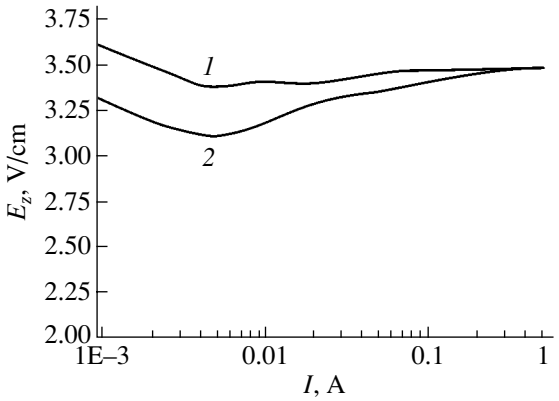

Fig. 7. Calculated VACs of the PC of a discharge in argon for $p = 1$ Torr, $R = 1$ cm, and the two values of the Penning ionization constant: k_p = (*1*) 6.2×10^{-16} and (*2*) 1.2×10^{-15} m^3 s^{-1}.

lations showed that, for $pR > 1$–3 cm Torr and currents of $I = 1$–100 mA, conditions exist at which the contribution of the Penning ionization is significant. Figure 7 shows the calculated VACs for $p = 1$ Torr and $R = 1$ cm. A decrease in the field at low currents is attributed to the above decrease in the thickness of the wall sheath. For the chosen set of reactions from Table 2 (curve *1*), a slight increase in the VAC is observed beginning from currents of about 5 mA. A comparison of the terms in the balance equation for n_e shows that this effect is due to the dominant contribution from the Penning ionization. An analysis of the literature data shows that the value of the Penning ionization constant $k_p = 6.2 \times 10^{-10}$ cm^3 s^{-1} from [31], which was used in our calculations (Table 2), is half as high as that corresponding to the literature data: $k_p = 1.2 \times 10^{-9}$ cm^3 s^{-1} (see, e.g., [32]). If we use this value of k_p, then the increase in the field at currents of 5–50 mA is more pronounced in the calculated VACs. At higher currents, the VAC levels out; this is attributed to an increased contribution of step ionization. Indeed, if the dominant ionization mechanism is step ionization with the constant k_{st}, then substituting Eq. (9) into the electron density balance equation, by analogy with Eq. (10) we have

$$n_e \simeq k_{st} n_m n_e \tau_a \simeq n_e k_{st} \tau_a N_0 k^*/k_q. \qquad (11)$$

The right- and left-hand sides of this equation show the same dependences on the electron density. Therefore, it follows from (11) that the current is independent of the field; i.e., the VAC is a horizontal line (Fig. 7). Unfortunately, the results are sensitive to the choice of the constants of the step ionization and Penning ionization, so that it is now difficult to make certain conclusions for each specific situation. In particular, it is necessary to estimate the contribution of step ionization [32]; for this purpose, it is necessary to solve the set of balance equations for a great many excited states. Therefore, to unambiguously answer the question as to the possibility of the formation of an ascending VAC in a PC (which is also of practical importance), it is necessary to carry out additional numerical and laboratory experiments.

In summary, self-consistent simulations of the PC of a dc discharge in argon have been carried out. It is shown that the local approximation for calculating the EDF is almost always inapplicable under real conditions of a diffuse PC. Consideration has been given to a number of important effects with the participation of metastable atoms; these effects can substantially influence the parameters of the PC plasma. In particular, the values of the direct-excitation constants of high-lying levels increase substantially because the population of the fast component of the EDF increases due to impacts of the second kind. It is shown that, at low currents, a decrease in the thickness of the wall sheath results in a descending VAC, whereas the Penning ionization can lead to an ascending VAC.

ACKNOWLEDGMENTS

This work was supported in part by the CRDF NSTM (grant no. RP-1-567-ST-03). L.D. Tsendin is grateful to a support from the Russian Foundation for Basic Research (project no. 01-02-16874) and NATO SfP (grant no. 974 354).

REFERENCES

1. M. Lieberman and A. Lichtenberg, *Principles of Plasma Discharges and Materials Processing* (Wiley, New York, 1994).
2. I. G. Kouznetsov, A. J. Lichtenberg, and M. A. Lieberman, Plasma Sources Sci. Technol. **5**, 662 (1996).
3. J. D. Bukowski, D. B. Graves, and P. Vitello, J. Appl. Phys. **80**, 2614 (1996).
4. M. W. Kiehlbauch and D. B. Graves, J. Appl. Phys. **91**, 3539 (2002).
5. J. T. Gudmindsson, I. G. Kouznetsov, K. K. Patel, and M. A. Liebermann, J. Phys. D **34**, 1100 (2002).
6. I. P. Shkarovsky, T. W. Johnson, and M. P. Bachinski, *The Particle Kinetics of Plasmas* (Addison-Wesley, Reading, 1966).
7. A. A. Kudryavtsev and L. D. Tsendin, Zh. Tekh. Fiz. **69** (11), 34 (1999) [Tech. Phys. **44**, 1290 (1999)].
8. A. A. Kudryavtsev and L. D. Tsendin, Pis'ma Zh. Tekh. Fiz. **28** (20), 7 (2002) [Tech. Phys. Lett. **28**, 841 (2002)].
9. E. A. Bogdanov, A. A. Kudryavtsev, L. D. Tsendin, *et al.*, Zh. Tekh. Fiz. **73** (8), 45 (2003) [Tech. Phys. **48**, 983 (2003)].
10. E. A. Bogdanov, A. A. Kudryavtsev, and L. D. Tsendin, Zh. Tekh. Fiz. **73** (8), 45 (2003) [Tech. Phys. **48**, 983 (2003)].
11. http://www.siglo-kinema.com/BOLSIG. Boltzmann Solver for the SIGLO-Series, CPA Tolouse&Kinema Software; http://www.cfdrc.com/~cfdplasma.
12. L. D. Tsendin, Plasma Sources Sci. Technol. **4**, 200 (1995).
13. J. Behnke, Yu. Golubovsky, S. U. Nisimov, and I. A. Porokhova, Contrib. Plasma Phys. **36**, 75 (1996).
14. A. V. Rozhansky and L. D. Tsendin, *Transport Phenomena in Partially Ionized Plasma* (Taylor & Francis, London, 2001).
15. V. L. Ginsburg and A. V. Gurevich, Usp. Fiz. Nauk **70**, 201 (1960) [Sov. Phys. Usp. **3**, 115 (1960)].
16. Yu. P. Raizer, *Gas Discharge Physics* (Nauka, Moscow, 1992; Springer-Verlag, Berlin, 1991).
17. V. E. Privalov, Kvantovaya Élektron. (Moscow) **4**, 2085 (1977).
18. D. A. Morozov, V. A. Stepanov, and M. V. Chirkin, Fiz. Plazmy **24**, 656 (1998) [Plasma Phys. Rep. **24**, 606 (1998)].
19. J. E. Lawler and U. Kortshagen, J. Phys. D **32**, 3188 (1999).
20. Yu. Golubovskii, I. A. Porokhova, J. Benke, and J. P. Bende, J. Phys. D **32**, 456 (1999).
21. T. J. Sommerer, J. Phys. D **29**, 769 (1996).

22. J. Bretagne, M. Capitelli, C. Gorse, and V. Puech, Europhys. Lett. **3**, 1179 (1987).
23. *CFD–PLASMA: User Manual* (CFD, Huntsville, 1999–2002).
24. U. Kortshagen, G. I. Parker, and J. E. Lawler, Phys. Rev. E **54**, 6746 (1996).
25. U. Kortshagen and J. E. Lawler, J. Phys. D **32**, 2737 (1999).
26. E. Kawamura and J. H. Ingold, J. Phys. D **34**, 3150 (2001).
27. A. V. Phelps, JILA Report No. 28, 1985, ftp://jila.colorado.edu/collision data/electronneutral.
28. M. Hayashi, *Ar cross section set*, ftp://jila.colorado.edu/collision data/hayashi.txt.
29. A. Bogaerts and R. Gijbels, Phys. Rev. A **52**, 3743 (1995).
30. A. Bogaerts, R. Gijbels, and J. Vlcek, J. Appl. Phys. **84**, 121 (1998).
31. N. B. Kolokolov, A. A. Kudryavtsev, and A. B. Blagoev, Phys. Scr. **50**, 371 (1994).
32. L. M. Biberman, V. S. Vorob'ev, and I. T. Yakubov, *Kinetics of Nonequilibrium Low-Temperature Plasmas* (Nauka, Moscow, 1982; Consultants Bureau, New York, 1987).

Translated by N. Larionova

Technical Physics, Vol. 49, No. 6, 2004, pp. 707–710. Translated from Zhurnal Tekhnicheskoĭ Fiziki, Vol. 74, No. 6, 2004, pp. 43–46.

SOLIDS

Amplitude Dependence of the Internal Friction in a Pb–62% Sn Alloy

V. M. Arzhavitin

Kharkov Institute of Physics and Technology, National Scientific Center, Akademicheskaya ul. 1, Kharkov, 61108 Ukraine

e-mail: vasil@kipt.kharkov.ua(TO:AR)

Received July 23, 2003

Abstract—The method of forced flexural vibrations is used to obtain the amplitude dependence of the internal friction ($Q^{-1}(\varepsilon_0)$) in the Pb–62% Sn alloy, which exhibits superplasticity at room temperature. A phenomenological model of the internal friction, in which the plasticity of alloys is considered as a hybrid relaxation–hysteresis process, is proposed. The numerical values of the cyclic-strain-hardening exponent n of the Pb–62% Sn alloy are determined in the microplastic and superplastic states, and the nature of the experimentally detected asymmetric maximum in $Q^{-1}(\varepsilon_0)$ is discussed. © *2004 MAIK "Nauka/Interperiodica".*

INTRODUCTION

Deformation in the bulk of polycrystals is almost always nonuniform and inhomogeneous. The only exclusion is superplastic deformation, since it occurs along grain boundaries. However, all grains are uniformly involved in the deformation process (without any statistical distribution of stresses in them), which partly causes the limiting plasticity of materials. Nevertheless, superplasticity mechanisms are still poorly understood [1]: composites [2] and even ceramics [3], including superconducting ceramics [4, 5], exhibit all characteristic features of a superplastic flow under certain temperature–rate loading conditions.

Materials having superplastic properties are mainly studied using the only particular type of loading—uniaxial tension. The internal friction method is rarely applied. From the experimental standpoint, the case of an alternating stress is more complex, which results in more complex behavior of the material to be studied. However, with this technique, one can imitate the superplasticity conditions (temperature, load, and loading rate) in materials and simultaneously (*in situ*) record their elastic and inelastic properties during a plastic flow. Therefore, the application of this technique for studying internal friction in superplastic materials can give new specific information on the superplasticity mechanisms.

EXPERIMENTAL

The eutectic Pb–62% Sn alloy, which has superplastic properties at room temperature, was melted from pure components in a laboratory furnace and then cast onto a massive copper base. After long-term (up to two years) aging in air, the ingots were subjected to ≈75% reduction on a hydraulic press. The workpieces were then used to cut samples in the form of a $2 \times 2 \times 20$-mm rectangular prism. The dependences of the internal friction on the resonance amplitude ε_0 of the flexural vibrations of a cantilever sample ($Q^{-1}(\varepsilon_0)$) were obtained at room temperature across the amplitude–frequency displacement peak [6]. The amplitude strain was recorded with an inductive sensor, which was calibrated visually using a remote microscope with an eyepiece micrometer. The error of measuring the amplitude strain was ±5%. The strain ε_0 was varied in the range $(0.53–3.75) \times 10^{-4}$. These values of ε_0 provided the range of stresses applied to a sample that certainly included the stresses inducing the superelastic behavior of the sample. The static Young modulus of the alloy is $E \approx 25$ GPa [8]. At this value, an optimum stress to produce superplasticity ($\sigma = E\varepsilon_0 \approx 7$ MPa [7]) is obtained at a strain $\varepsilon_0 \approx 2.8 \times 10^{-4}$. The dynamic Young modulus of the alloy is connected with the resonance frequency of sample vibrations f_0 by the quadratic relation $E \sim f_0^2$.

RESULTS AND DISCUSSION

The experimental $Q^{-1}(\varepsilon_0)$ dependence of the internal friction for the Pb–62% Sn alloy has a maximum at a strain amplitude $\varepsilon_0 \approx 2.2 \times 10^{-4}$ (Fig. 1). The classic Granato–Lücke mechanism of the breakaway of dislocations from pinning atoms does not produce a maximum in the $Q^{-1}(\varepsilon_0)$ curve. However, its modification can predict such an extremum. For example, in the Rodgers mechanism of the athermal breakaway of different-type dislocations from impurities, an asymmetric maximum in $Q^{-1}(\varepsilon_0)$ corresponds to the case when all highly mobile dislocations have broken away; then, the amplitude internal friction decreases. The following increase in the internal friction is related to the break-

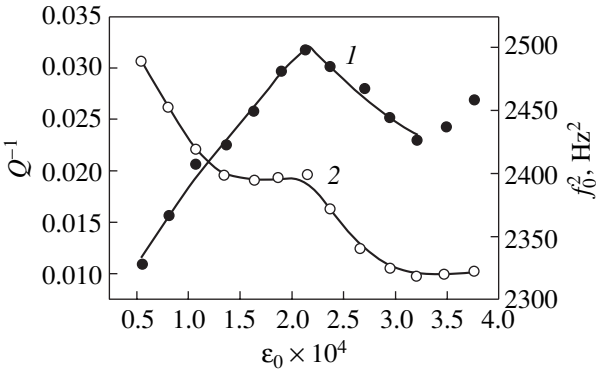

Fig. 1. Amplitude dependences of the internal friction and Young's modulus of the Pb–62% Sn alloy at room temperature: (*1*) approximated curve of the internal friction Q^{-1} and (*2*) Young's modulus E (in terms of the squared resonance vibration frequency f_0^2).

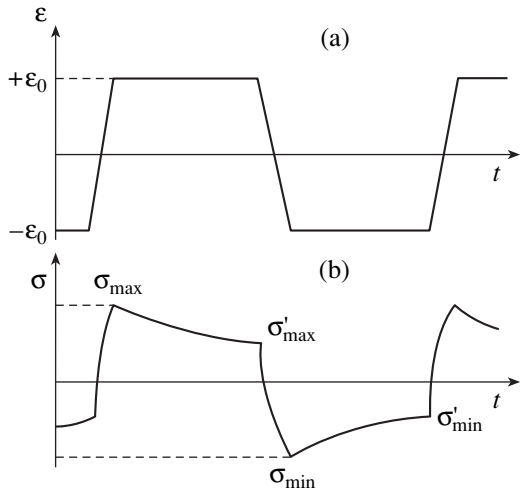

Fig. 2. Time variation (scaleless) of the normal components of (a) the strain (ε(*t*)) and (b) the stress (σ(*t*)) in the near-surface layer of a vibrating sample.

away of dislocations of another type [9]. The microscopic models of internal friction that imply breakaway of dislocations from pinning impurities can be applied to relatively pure materials in a limited range of applied stresses. At higher stresses, dislocations multiply in each loading cycle, break away from all barriers, and travel substantial distances within a grain. Then, the effect of internal friction can be caused by the interaction of dislocations with any obstacles to their motion that are located in their slip plane. For single dislocations to overcome different-type barriers at low temperatures, it is necessary to apply a stress σ that is higher than the dry-friction stress σ_f ($\sigma > \sigma_f$) [6, 10, 11]. The stress σ_f acquires a certain physical meaning, depending on the type of a barrier to be overcome by dislocations. The effect of the dry-friction stress on internal friction in materials can be taken into account using a phenomenological dislocation-free approach; it reflects more general dependences of microdeformation and hysteresis.

As the mathematical model for the behavior of materials under quasi-static loading, we choose the empirical equation of state [12], which is widely applied in engineering calculations. In this equation, the flow stress is sensitive to both the degree of strain (strain-hardening exponent n) and the strain rate (rate-hardening exponent m):

$$\sigma = \eta(e + \varepsilon)^n \dot{\varepsilon}^m, \qquad (1)$$

where η is the effective viscosity of the material, $\dot{\varepsilon}$ is the plastic-strain rate, and e is a material constant reflecting the fact that the plastic strain ε begins only after exceeding a certain critical stress.

At $n = 0$, Eq. (1) describes a viscous flow in materials, including a superplastic flow [1, 12, 13].

For metals deformed under quasi-static conditions, the strain-hardening exponent n is always smaller than unity; that is, the stress σ increases not directly proportional to the strain.

Let a hysteresis loop σ(ε) be described by the equation

$$\sigma = E\varepsilon \pm \eta(|e| + |\varepsilon|)^n |\dot{\varepsilon}|^m, \qquad (2)$$

in which the nonlinear correction to Hooke's law (1) specifies the shape of a hysteresis loop. Here, $|e|$, $|\varepsilon|$, and $|\dot{\varepsilon}|$ are the absolute values of the preliminary strain, the time-independent current strain, and the plastic-strain rate, respectively (Fig. 2). Curve (2) of cyclic loading describes the behavior of metals upon steady-state cyclic deformation after several early vibration cycles. Then, the parameters of loop (2) can be called the coefficient η and exponent n of cyclic strain hardening [14]. Quantitatively, they differ from the corresponding parameters of quasi-static loading. In particular, the exponent n of the relative strain ε in Eq. (2) can exceed unity [15].

Loop (2) is shown in Fig. 3. Hysteresis loop (2) differs from that proposed in [15] mainly in the factor $\dot{\varepsilon}^m$. The algebraic dependence of the stress on the strain is a discontinuous function at $\varepsilon = \varepsilon_0$. The hysteresis loop can be discontinuous (broken) only at $\sigma > \sigma_f$ [6]. For example, at room temperature, the loop σ(ε) with a break at the point $\varepsilon_0 \approx 5 \times 10^{-5}$ is experimentally observed in the Cu–38% Zn polycrystalline alloy [16].

In the general case, the stress and strain make up a second-rank tensor. Upon cyclic bending of the thin ($2 \times 2 \times 20$-mm) rods, the state of stress can be characterized only by the normal tensor component, since the other components are negligible. Therefore, the stress and strain can be taken as scalar quantities, without considering their tensor character.

The amplitude dependence of the internal friction can be calculated by the general formula [6]

$$Q^{-1} = \frac{\Delta W}{2\pi W} = \frac{\Delta W}{\pi E \varepsilon_0^2},$$

where $\Delta W = \oint \sigma d\varepsilon$ is the area of the hysteresis loop in the coordinates σ–ε. Then, we have

$$Q^{-1} = \frac{1}{\pi E \varepsilon_0^2}\oint \sigma d\varepsilon = \frac{4}{\pi E \varepsilon_0^2}\int_0^{\varepsilon_0} \eta (e+\varepsilon)^n \dot{\varepsilon}^m d\varepsilon = \frac{4\eta[(e+\varepsilon_0)^{n+1} - e^{n+1}]\dot{\varepsilon}^m}{\pi(n+1)E\varepsilon_0^2}. \quad (3)$$

Relation (3) describes internal friction of the hysteresis (amplitude-dependent) and relaxation (frequency-dependent) types at the same time, since it depends on both the strain amplitude ε_0 and the rate $\dot{\varepsilon}$ The latter depends somewhat on the frequency f_0 of cyclic deformation (Fig. 2). Then, we have a hybrid of relaxation and hysteresis [17] when the difference between them becomes insignificant.

It is necessary to distinguish the true and average values of the parameters of the hysteresis loop. Their true values are recorded upon testing under the conditions of a uniform state of stress (bending or torsion of hollow samples or longitudinal vibrations of solid samples). Otherwise, ΔW [6, 14] and, apparently, the index n [14] are averaged over the nonuniformly stressed volume of a sample. They are weight-average properties of a material for a certain test type.

Taking into account that the yield strength of the Pb–62% Sn alloy is low, we can assume that its plastic flow starts from the very beginning of deformation, at an arbitrary small strain. In this approximation, the preliminary strain is $e = 0$ and Eq. (3) can be simplified to the form

$$Q^{-1} = \frac{4\eta\varepsilon_0^n\dot{\varepsilon}^m}{\pi(n+1)E}. \quad (4)$$

At $n = 0$, we have from (4)

$$Q^{-1} = \frac{4\eta\dot{\varepsilon}^m}{\pi E\varepsilon_0};$$

that is, the internal friction can decrease with increasing strain amplitude ε_0. A similar amplitude dependence of the internal friction ($Q^{-1} \sim \dot{\varepsilon}/\varepsilon_0$, where $\dot{\varepsilon}$ is the tensile strain rate) was detected in a certain amplitude segment during creep [18].

From the standpoint of internal friction, a superplastic flow is often considered as a relaxation process [12, 19–22]. However, relaxation phenomena are usually observed at small applied loads, which do not cause plastic deformation in samples. This contradiction can be resolved if we assume, as above, that relaxation and hysteresis processes occur simultaneously.

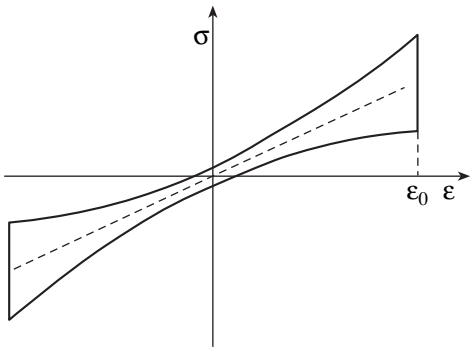

Fig. 3. Leonov–Bezpal'ko hysteresis loop σ(ε).

Of course, strain hardening is absent ($n = 0$) or extremely small during a superplastic flow. Upon uniaxial loading, the whole volume of a material is in a superplastic state, whereas, upon bending, stresses are distributed over the thickness of a vibrating rod and are maximum near its surface. Then, superplasticity is localized in the near-surface layer of the material at the instants of amplitude strains. The sample retains its stiffness and can withstand increasing alternating loads upon testing because of a quasi-elastic "core." Since the amplitude-dependent internal friction $Q^{-1}(\varepsilon_0)$ is a volume-averaged dissipative quantity, its contributions from the quasi-elastic core and the near-surface layer (superplasticity) cannot be distinguished. This apparatus specific feature made us choose the hysteresis loop σ(ε) in its general shape (2). Then, Eqs. (3) and (4) have to describe the total internal friction, which allows us to compare the results of calculation by Eqs. (3) and (4) with the experimental data.

As applied to the Pb–62% Sn alloy, the cyclic-strain-hardening exponent n is calculated by Eq. (4) using the ascending and descending branches of the experimental dependence of the internal friction on the amplitude (Fig. 1). When approximating (fitting) the ascending branch of $Q^{-1}(\varepsilon_0)$, we obtained $n = 1.75 \pm 0.03$. Therefore, the ascending branch of the internal friction is approximated by an almost linear dependence $Q^{-1} \sim \varepsilon_0^{0.75}$ (Fig. 1, curve *1*). The stage of a linear increase in the internal friction with ε_0 in alloys is caused by microstrains inside grains, when the mechanism of strain transfer from grain to grain has not been operative [10]. The procedure of approximating the descending branch of $Q^{-1}(\varepsilon_0)$ gives $n = 0.19 \pm 0.05$, which is close to zero. Therefore, the cyclic deformation of the Pb–62% Sn alloy proceeds in stages: in the first stage ($n \approx 1.75$), the internal friction increases due to microplastic strains in grains [10], whereas, in the second stage ($n \approx 0.19$), a superplastic state is actualized in the near-surface layer of the sample. In this case, the hardening stages are clearly pronounced, since a

transition from one stage to another is accompanied by a jump in the value of n. Thus, the cyclic-strain-hardening exponent n plays a specific role as an indicator of the deformation stages. A change in the mechanisms of plastic deformation at the maximum of the $Q^{-1}(\varepsilon_0)$ dependence is also accompanied by a stepwise decrease in the elastic modulus with increasing vibration amplitude (Fig. 1, curve *2*).

According to (4), the $Q^{-1}(\varepsilon_0)$ dependences in polycrystalline materials always have the shape of an asymmetric maximum when the rheological parameter $n > 1$ sharply changes into $0 \le n < 1$ upon changing hardening stages. In these cases, an asymmetric peak in $Q^{-1}(\varepsilon_0)$ can also be detected in alloys without superplastic properties.

CONCLUSIONS

(1) The amplitude dependence of the internal friction in the Pb–62% Sn alloy has a maximum in the relative-strain-amplitude range $(0.53–3.75) \times 10^{-4}$, which includes the strains at which this alloy exhibits superplastic behavior.

(2) A phenomenological model of the internal friction, in which the plasticity of polycrystalline alloys is considered as a hybrid relaxation–hysteresis process, is proposed. This model has been used to show that, in the strain range under study, the plastic deformation of the Pb–62% Sn alloy is a two-stage process. When going from the first stage of microplastic deformation of grains to the stage of superplastic behavior in the near-surface layer of the material, the strain-hardening exponent n decreases sharply from $n \approx 1.75$ to $n \approx 0.19$.

REFERENCES

1. R. A. Vasin, F. U. Enikeev, M. I. Mazurskiĭ, and O. S. Munirova, Probl. Prochn., No. 2, 6 (2000).
2. V. N. Perevezentsev and Yu. V. Svirina, Zh. Tekh. Fiz. **68** (12), 38 (1998) [Tech. Phys. **43**, 1436 (1998)].
3. N. G. Zaripov, Fiz. Tverd. Tela (St. Petersburg) **42**, 1621 (2000) [Phys. Solid State **42**, 1668 (2000)].
4. V. M. Arzhavitin, A. I. Verdyan, V. N. Golovin, *et al.*, Sverkhprovodimost: Fiz. Khim. Tekh. **3**, 2050 (1990).
5. Y. T. Chen, J. Yun, M. P. Harmer, *et al.*, Appl. Superplasticity **5**, 1452 (1995).
6. S. A. Golovin, A. Pushkar, and D. M. Levin, *Elastic and Inelastic Properties of Structural Metallic Materials* (Metallurgiya, Moscow, 1987) [in Russian].
7. V. F. Korshak, R. I. Kuznetsova, and I. G. Ivanov, Fiz. Met. Metalloved. **84**, 123 (1997).
8. B. M. Drapkin and V. K. Kononenko, Izv. Akad. Nauk SSSR, Met., No. 2, 162 (1987).
9. D. H. Rogers, J. Appl. Phys. **33**, 781 (1962).
10. Yu. Kon-Syu and L. M. Butkevich, Izv. Vyssh. Uchebn. Zaved. Fiz., No. 8, 33 (1968).
11. L. A. Solov'ev, *Internal Friction of Metallic Materials* (Nauka, Moscow, 1970) [in Russian], pp. 94–99.
12. M. W. Grabski, *Structural Superplasticity of Metals* (Slcedillaask, Katowice, 1972; Metallurgiya, Moscow, 1975) [Translated from Polish].
13. F. U. Enikeev, M. I. Mazurskiĭ, and O. S. Munirova, Zavod. Lab. Diagnostika Mater. **67** (4), 42 (2001).
14. V. T. Troshchenko, L. A. Khamaza, V. V. Pokrovskiĭ, *et al.*, *Cyclic Deformations and Fatigue of Metals*, Vol. 1: *Low-Cycle and High-Cycle Fatigue of Metals* (Naukova Dumka, Kiev, 1985) [in Russian].
15. L. F. Kochneva, *Internal Friction in Solids During Vibration* (Nauka, Moscow, 1979) [in Russian].
16. L. A. Solov'ev, L. M. Butkevich, and M. B. Makogon, Fiz. Met. Metalloved. **25**, 183 (1968).
17. S. I. Meshkov, V. S. Postnikov, and M. A. Rudis, *Relaxation Phenomena in Solids* (Metallurgiya, Moscow, 1968) [in Russian], pp. 153–156.
18. S. I. Meshkov, *Viscoelastic Behavior of Metals* (Metallurgiya, Moscow, 1974) [in Russian].
19. A. S. Tikhonov, *Superplasticity in Metals and Alloys* (Nauka, Moscow, 1978) [in Russian].
20. V. A. Piterimova, G. K. Mal'tseva, V. S. Novoselov, and N. B. Dyad'kova, *Internal Friction in Metals and Inorganic Materials* (Nauka, Moscow, 1982) [in Russian], pp. 88–92.
21. Y. Torisaka and S. Kojima, Acta Metall. Mater. **39**, 947 (1991).
22. A. Lakki and R. Schaller, J. Phys. IV (France) **6**, C8-331 (1996).

Translated by K. Shakhlevich

Technical Physics, Vol. 49, No. 6, 2004, pp. 711–714. Translated from Zhurnal Tekhnicheskoĭ Fiziki, Vol. 74, No. 6, 2004, pp. 47–50.

SOLIDS

Effect of Electron Irradiation on the Physicochemical Processes in $YBa_2Cu_3O_{6+x}$ High-Temperature Ceramics

E. S. Andasbaev, F. F. Komarov, A. I. Kupchishin, A. D. Muradov, and T. V. Pozdeeva

Sevchenko Research Institute of Applied Physical Problems, Belarussian State University, Minsk, 220064 Belarus

e-mail: KomarovF@bsu.by

Received October 1, 2003

Abstract—The influence of irradiation by 2-MeV electrons at integral doses of 0.1, 0.3, 1.5, and 3.0 MGy on the physicochemical processes in $YBa_2Cu_3O_{6+x}$ polycrystalline samples is investigated. At different stages of irradiation, processes occurring in the samples exert an opposing effect on the matrix and near-surface regions of the material. Irradiation with doses $D < 1.5$ MGy strengthens bonds in the intergranular spacer, which weaken because of a reduction in the potential surface barrier for oxygen migration to vacant sites. This results in ordering of the oxygen sublattice in near-surface regions. Irradiation with doses $D > 1.5$ MGy causes damage on the grain surface, which enhances oxygen diffusion from the bulk and, thus, leads to material degradation.

INTRODUCTION

Radiation-induced defects in high-temperature superconductors have been studied in many works. In [1–3], it has been shown that irradiation greatly modifies the properties of high-temperature superconductors. In particular, irradiation of $YBa_2Cu_3O_{6+x}$ (YBCO) ceramics stimulates physicochemical processes with the participation of volatile compounds, which may be either introduced into or released from this material. These volatiles, some of which are present in ambient air, affect the electrophysical and superconducting properties of the ceramics. Therefore, investigation into the influence of these substances (in combination with irradiation) on the properties of HTSC materials is of importance for protecting such materials from deleterious effects.

EXPERIMENTAL

In this study, physicochemical processes in YBCO ceramics that are induced by irradiation with 2-MeV electrons at integral doses of 0.1, 0.3, 1.5, and 3.0 MGy are investigated by the methods of IR, Raman, and thermal desorption spectroscopy.

The material studied was KIB-1commercial polycrystalline YBCO ceramics with a density of 5.2 g/cm^3. The samples were virtually one-phase (98%). Pellets measuring $2 \times 2 \times 0.5$ cm were cut into four parts. One of them was used as a reference, and the others were irradiated by electrons with different doses. 2-MeV electrons have a "soft" yet tangible effect on the ceramics, causing small displacements of oxygen atoms and atoms of other constituent elements from their sites in the lattice. The samples were placed in special holders and irradiated with an ÉLU-6 electron accelerator (5-μs-wide current pulses with a repetition rate of 200 Hz) in air at 393 K.

Introduction and evolution of volatiles were initially studied by thermal desorption. This method is widely applied for energy characterization of surface processes, as well as for studying the kinetics of sorption–desorption processes occurring on solid surfaces. In [4], gas evolution from YBCO samples after they had been heated in a vacuum was investigated by thermal desorption spectrometry. The same method was used in this work to study gas evolution from irradiated YBCO ceramic samples into a vacuum. Further, the intensities of several peaks from the mass spectra recorded at a certain temperature for different irradiation doses were digitized. Next, the data obtained were interpolated by using a cubic spline and, thus, the intensities of each of the peaks at a given time were found. In this way, we estimated the rates of evolution of gases from the sample into a vacuum vs. the irradiation dose at a given temperature.

DISCUSSION

We experimented with as-prepared YBCO ceramic samples and samples irradiated by 2-MeV electrons at integral doses of 0.1, 0.3, 1.5, and 3.0 MGy. For the as-

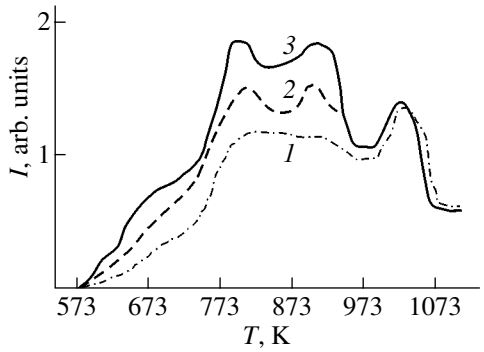

Fig. 1. Thermal desorption spectra of oxygen (*1*) in the as-prepared $YBa_2Cu_3O_{6+x}$ sample and in the $YBa_2Cu_3O_{6+x}$ samples irradiated by 2-MeV electrons at doses D = (*2*) 0.3 and (*3*) 3.0 MGy.

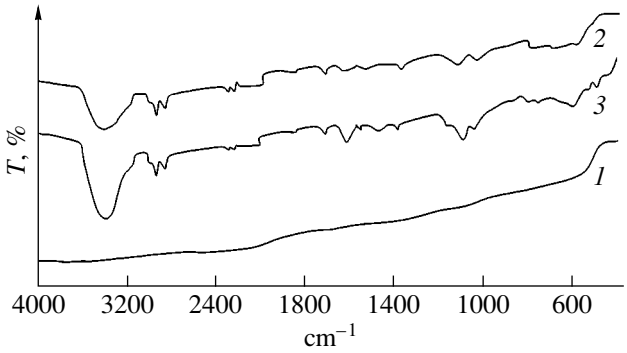

Fig. 2. IR absorption spectra taken from the (*1*) as-prepared yttrium-based ceramic and from the ceramic irradiated by 2-MeV electrons at doses of (*2*) 0.3 and (*3*) 1.5 MGy.

prepared samples with the orthorhombic phase, thermal desorption spectra of oxygen were recorded when the temperature was linearly varied in the interval 283–1200 K and the heating rate was varied between 0.1 and 0.5 K/s. As is seen from Fig. 1, oxygen evolution becomes appreciable at temperatures above 650 K. For all the samples, the oxygen evolution is the most intense in the temperature range 770–1000 K. For the samples irradiated with doses increasing from 0.1 to 3.0 MGy, the spectra exhibit two extra peaks in the temperature range 773–950 K. The intensities of both peaks grow with increasing irradiation dose.

It should be noted that, as the irradiation dose increases, the intensity of the high-temperature peak at T_{max} = 1025 K remains nearly unchanged, while the intensities of the two most intense peaks with T_{max} in the temperature range 773–950 K grow. The thermal desorption peak lying in the range T = 1000–1070 K was also observed in [5].

The samples irradiated by an integral dose of 3.0 MGy undergo the orthorhombic-to-tetragonal phase transition. Irradiation of the sample containing some amount of CuO causes this impurity to decompose by the reaction $2CuO \longrightarrow Cu_2O + 1/2O_2$, so that an additional amount of oxygen is released. Decomposition of CuO is responsible for the thermal desorption peak at T_{max} = 1025 K. The variation of the thermal desorption spectra for oxygen leads us to conclude that oxygen from the orthorhombic phase diffuses through oxygen vacancies in the basal plane *ab*. During irradiation, the oxygen leaves Cu–O chains located along the crystallographic *b* axis. The oxygen in the Cu–O chains has an increased mobility, which causes ordering of vacancies in the 60° superconducting phase and the orthorhombic-to-tetragonal phase transition during irradiation of YBCO ceramics. The rate of oxygen release from the YBCO structure is limited by the rate of its diffusion.

Subsequent investigation of oxygen diffusion [6, 7] revealed asymmetry of the diffusion process: the data on the electric conductivity suggest that oxygen evolution proceeds more slowly than oxygen absorption. The authors of [6, 7] explain this asymmetry by the presence of an energy barrier on the surfaces of individual grains. Overcoming of this barrier is the limiting stage of the process of oxygen release from the ceramic sample.

As follows from Fig. 2, the IR spectrum of the as-prepared samples does not contain absorption bands. However, upon irradiation by 2-MeV electrons at integral doses of 0.1 and 1.5 MGy, peaks at 470, 520, 780, 1080, 1630, 2900, and 3420 cm^{-1} appear. In this spectral range, the absorption bands are due to the vibrations of Cu–O bonds. The peak at 470 cm^{-1} is related to deformation vibrations in Cu–O chains and the peak at 520 cm^{-1}, to antisymmetric axial valence vibrations of Cu–O chains in the planes of the tetragonal structure. The peaks at 780 and 1080 cm^{-1} correspond to barium and copper carbonates; at 1630 cm^{-1}, to H_2O; and at 2900 cm^{-1}, to CH. Finally, the wide band covering the interval 3300–3500 cm^{-1} is related to Cu, Y, and Ba crystalline hydrates. The absorption bands of hydroxyl groups are absent because of a high coverage of the molecule surface [8].

These absorption bands are related to the oxygen evolving from the lattice and to ordering of oxygen vacancies in the Cu(1)–O(1) chains along the *b* axis in the Cu(2) planes. The latter effect is usually observed after irradiation by gamma rays and neutrons [9, 10]. Electron irradiation damages the ceramic layer and modifies the complex composition of the sample. By the method of IR spectroscopy, it was established that the modified composition cannot be identified as a mere mixture of the tetragonal and "green" phases. The maximum observed at 620 cm^{-1} is likely to be associated with atmospheric water molecules incorporated into crystallographic voids with the formation of Cu–O(H_2)

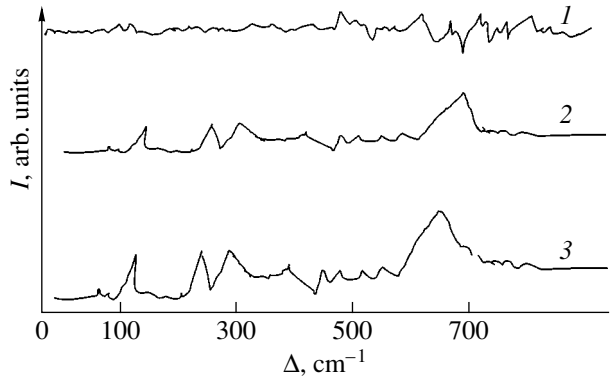

Fig. 3. Raman spectra taken from the (*1*) as-prepared $YBa_2Cu_3O_{6+x}$ ceramic and from the ceramic irradiated by 2-MeV electrons at doses of (*2*) 0.1 and (*3*) 3.0 MGy.

complexes. Such absorption bands were observed and discussed in [11].

In [9], where $YBa_2Cu_3O_{6+x}$ samples were irradiated by gamma-ray photons in air, the conclusion was drawn that copper radicals interact mainly with nitrogen oxides to form copper nitrates. From our IR spectra of yttrium-based ceramics, it follows that irradiation of the YBCO ceramics in air produces largely copper carbonates.

Such modifications in the YBCO structure suggest that electron irradiation generates active centers that interact with ambient air. The Raman spectra (Fig. 3) make it possible to establish the nature of defect-induced bands observed in the $YBa_2Cu_3O_{6+x}$ crystals. Electron irradiation partially breaks the initial structure of the sample, causing irreversible changes in the Raman spectra. As a result, the Raman spectrum in the range 200–400 cm^{-1} becomes similar to the spectrum of *c*-polarized vibrations of the O(2) and O(3) sublattices. O(1) vacancies arising in this case are responsible for the band at 220 cm^{-1} in the Raman spectrum of the electron-irradiated crystals. In the Raman spectra of the samples irradiated at integral doses of 0.1 and 1.5 MGy, other additional bands appear. The band at 223 cm^{-1} may be explained by disordering of the oxygen sublattice, which results in the formation of uncorrelated "glowing" defects. The second defect-induced peak with a maximum at 270 cm^{-1} is related to IR vibrations with a large wavevector. The intensity of these bands grows with increasing irradiation dose; therefore, they may be assigned to scattering by oxygen vacancies. Electron irradiation induces irreversible changes in the Raman spectra: the intensities of the defect-induced bands do not decay to the initial values. The weak band at 600 cm^{-1} is related to active IR stretching vibrations of Cu(1)–O(1) bonds in one-dimensional CuO chains. By virtue of the exclusion principle, this vibration mode in Raman processes is forbidden as applied to the ordered orthorhombic phase. However, it becomes Raman-active if lattice periodicity is disturbed by oxygen vacancies present in CuO chains [12]. Therefore, the intensity of the mode at 600 cm^{-1} may serve as a measure of the concentration of these vacancies.

CONCLUSIONS

Our results indicate that fast electrons and YBCO ceramics interact in air in a complex manner. At different stages of irradiation, processes that have an opposite effect on the matrix and near-surface regions of yttrium-based compounds occur simultaneously.

It is established that oxygen absorption and oxygen release in polycrystalline YBCO samples proceed asymmetrically. Absorption takes place in the entire volume of the material and is accompanied by surface diffusion, dissociation of molecules at specific surface centers, and diffusion of oxygen atoms into the lattice. At the same time, oxygen evolution from the sample is limited by a potential surface barrier on the grain surfaces.

At low irradiation doses ($D < 1.5$ MGy), weak bonds in intergranular spacers strengthen, because the potential surface barrier for oxygen migration to vacant sites decreases. In addition, the oxygen sublattice in near-surface regions becomes ordered.

High-dose ($D > 1.5$ MGy) irradiation damages the surface layers of the grains. Accordingly, oxygen diffusion from the bulk is enhanced and, thus, the ceramic material degrades. Grain boundaries become enriched by copper carbonate, which adversely affects the conductivity of intergranular spacers, decreases the critical current. Eventually, the material loses its superconducting properties.

IR spectroscopy data, as well as thermal desorption spectra and Raman spectra taken from electron-irradiated polycrystalline YBCO samples, indicate that the degradation of the ceramics is related to oxygen diffusion from the crystal lattice. The diffusion process is accompanied by ortho-I $\longrightarrow$ ortho-2 $\longrightarrow$ tetra phase transitions, as well as by incorporation of atmospheric moisture into crystallographic voids with the formation of Cu–O(H_2) complexes.

REFERENCES

1. H. Stormier, A. Levi, K. Baldwin, *et al.*, Phys. Rev. B **38**, 2472 (1988).
2. J. Mannhart, P. Chaudhari, D. Dimos, *et al.*, Phys. Rev. Lett. **61**, 2476 (1988).
3. J. H. Allen, P. R. Broussard, J. H. Claasen, *et al.*, Appl. Phys. Lett. **53**, 1338 (1988).
4. V. V. Semin, A. V. Nazarenko, and S. É. Khabarov, in *Proceedings of the 1st All-Russian Conference on High-Temperature Superconductivity, Moscow, 1988*.

5. N. Miura, H. Suzuta, V. Teraoka, *et al.*, Jpn. J. Appl. Phys. **27**, L337 (1988).
6. K. N. Tu, C. C. Tsuei, S. I. Park, *et al.*, Phys. Rev. B **38**, 772 (1988).
7. K. N. Tu, N. C. Yeh, S. I. Park, *et al.*, Phys. Rev. B **38**, 5118 (1988).
8. A. I. Kupchishin, A. D. Muradov, and E. S. Andasbaev, Vestn. Kaz. Gos. Univ., No. 2 (11), 135 (2001).
9. N. N. Degtyarenko, V. F. Elesin, and V. L. Melnikov, in *Proceedings of the International Workshop "Effects of Strong Disordering in HTSC," Zarechny, 1990*, pp. 433–436.
10. V. S. Chashchin and R. F. Konopleva, Fiz. Tverd. Tela (St. Petersburg) **39**, 977 (1997) [Phys. Solid State **39**, 877 (1997)].
11. J. P. Locquet *et al.*, Europhys. Lett. **7**, 469 (1988).
12. B. A. Aleksatin, I. F. Berger, S. V. Verkhovskiĭ, *et al.*, Preprint URO AN SSSR (Ural Division, Academy of Sciences of USSR, Sverdlovsk, 1988).

Translated by Yu. Vishnyakov

Technical Physics, Vol. 49, No. 6, 2004, pp. 715–719. Translated from Zhurnal Tekhnicheskoĭ Fiziki, Vol. 74, No. 6, 2004, pp. 51–56.

SOLID-STATE ELECTRONICS

Impulse Response of a Heterojunction MSM Photodiode

S. V. Averine

Institute of Radio Engineering and Electronics (Fryazino Branch), Russian Academy of Sciences, pl. Vvedenskogo 1, Fryazino, Moscow oblast, 141190 Russia

e-mail: sva278@ire216.msk.su

Received July 14, 2003

Abstract—A two-dimensional model is used to simulate drift of photogenerated carriers in the active region of high-speed photodiodes (metal–semiconductor–metal (MSM) rectifying contacts) that are made as a conventional planar structure and a structure with a heterojunction. These two types of photodiode structures are compared in terms of the impulse response and quantum efficiency. Variation of the planar MSM diode response with decreasing size of the interdigitated contact system is analyzed. The possibility of improving the speed of response of the MSM diode is discussed. It is shown that the structure with an InP/GaInAs heterojunction considerably modifies the transport of photogenerated carriers and remarkably improves the response speed.

INTRODUCTION

Photodiodes based on rectifying MSM contacts have recently become the subject of extensive scientific and applied research [1–7]. The structure of such diodes is quite simple: interdigitated contacts (fingers) are formed by photolithography means on the surface of an active semiconductor layer grown on a semi-insulating substrate. Light incident on the MSM diode surface generates electron–hole pairs within the absorption depth, which are separated by the internal electric field, inducing a photocurrent in the external circuit. A decrease in the spacing between the interdigitated contacts, along with thinning of the diode active layer, is viewed as the primary way of improving the speed of an MSM detector [1–5]. Owing to advances in fabrication technology, the contact spacing in MSM diodes has shrunk to the submicrometer or even nanometer scale. Recently [4], an MSM detector with the smallest contact sizes reported to date (the finger width and finger spacing are as small as 25 nm) was fabricated using electron-beam lithography. In order to achieve a tradeoff between the effect of carrier transit time and that of the capacitance in an MSM diode with a finger spacing of 25 nm, the size of the active region was reduced to 1×1 μm. Such a fine geometry poses the stubborn problem of focusing incident radiation when such structures are used in real experiments. The impulse response of such a diode has not been measured, and simulation by the Monte Carlo method using a one-dimensional model gives a bandwidth of 400 GHz (–3 dB) and a FWHM value of 0.25 ps. Using a two-dimensional model, we shall show that mere scaling down of the dimensions to improve the speed of the detector should be applied with care. The impulse response of a planar MSM diode will be studied with emphasis on limitations associated with the reduction of the interdigitated contact array. Unlike other models (see, e.g. [3–5]), our simulations take into account nonuniformity of the 2D electric field distribution in the active region of the detector. The simulation program has recently been successively used for simulating the impulse response of photodetectors based on GaInAs/GaAs superlattices [6] and GaInAs MSM photodiodes [7]. Here, this model is extended for electron–hole transport processes in heterojunction MSM structures. We show that the presence of the heterojunction in the light-absorbing region considerably influences the transport of photogenerated carriers and improves the speed of the InP/GaInAs MSM photodiode.

SIMULATION OF THE IMPULSE RESPONSE OF AN MSM DETECTOR

The response of an MSM detector to a short optical pulse is studied by simulating transport of photogenerated carriers in the active region of the diode. The spacing between adjacent contact fingers and the penetration depth of incident radiation specify the active region of the diode.

In general, as the finger spacing shrinks, carrier transit time decreases. However, the transit time depends essentially on the drift velocity of carriers and, thus, on the electric field strength in the active region of the diode. In order to achieve a high response speed, the active region of the diode must be completely depleted of carriers and the electric field in it must be high enough to provide near-saturation drift velocities [1, 8]. In this case, a time of carrier drift to corresponding interdigitated contacts is given by [9]

$$\tau_{dr} = \frac{t\chi}{2V}, \quad (1)$$

1063-7842/04/4906-0715$26.00

where

$$\frac{1}{V^4} = \frac{1}{2}\left(\frac{1}{V_e^4} + \frac{1}{V_h^4}\right), \quad (2)$$

t is the finger spacing; χ is a correcting factor; V is the average drift velocity; and V_e and V_h are the saturation drift velocities of electrons and holes, respectively.

Such a 1D approach to carrier transport analysis is valid only if the finger spacing in the MSM diode structure is large (on the order of several micrometers). This is due to the fact that the penetration depth of radiation into GaAs at a wavelength of 750 nm is approximately 1 μm. Simulation shows that, if the finger spacing exceeds the penetration depth of incident radiation, the electric field in the active region of a planar MSM diode is uniform and its strength is high enough to ensure drift at near-saturation velocities for the majority of photogenerated carriers. However, such an approach fails if the finger spacing is less than ≈1 μm. In this case, near-saturation drift velocities for most photogenerated carriers are difficult to achieve; therefore, a 2D approach to analyzing the electric field distribution and transport of carriers is necessary for such structures. Our model was described in detail in [6, 7]. Simulation is two-dimensional in the sense that the distributions of photogenerated carriers, potential, and electric field are considered along the X and Y coordinates of a unit cell of the active region of an MSM diode. The effect of the heterojunction is taken into account via the field induced by the potential difference between two semiconductor layers. At each simulation step, the heterojunction field is added to the internal field due to the potential difference between interdigitated contacts, as well as by photogenerated carriers. The two-dimensional model enables us to reveal limitations related to a decreased efficiency of electric field penetration into the active region of the diode in the case of a sub-micrometer finger spacing. The relationship between the electron and hole drift velocities and the electric field for GaInAs is taken from [8]. It is assumed that surface and volume recombination effects cannot be a controlling factor at short time scales like those considered in this analysis [10]. The photocurrent due to carrier transport is calculated using the Ramo theorem [11]. The analysis is carried out under the assumption that the maximal carrier velocity in GaInAs is equal to 2×10^7 cm/s, which is a conservative estimate for MSM diodes with a contact spacing of 100 nm because of the drift velocity overshoot [5]. This effect should be taken into account in rigorous analysis of drift processes in structures with nanoscale spacings [5, 12]. However, rather good agreement between calculated and experimental values of the speed allows us to apply this model to dynamic analysis of such structures.

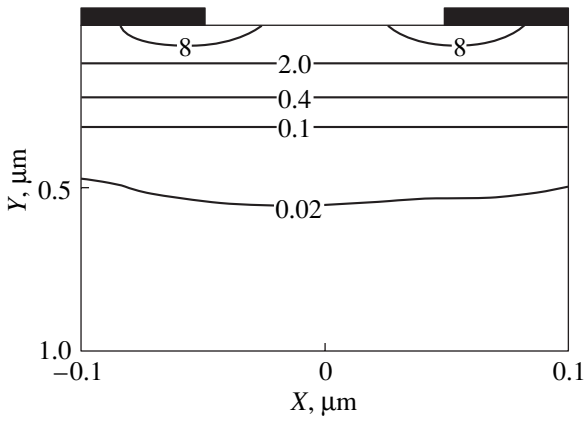

Fig. 1. Electric field distribution in a unit cell of the planar GaInAs MSM diode. The bias voltage across the contacts is 1.5 V (the figures by the curves are given in V/μm).

INTERNAL FIELD AND CARRIER TRANSPORT DYNAMICS

Figure 1 shows the calculated electric field distribution in a unit cell of the MSM photodiode with a finger spacing of 0.1 μm. It is seen that the electric field is relatively high near the surface but decays sharply inward to the diode. In particular, at a bias voltage of 1.5 V, the electric field strength is about 2 V/μm at a depth of 0.1 μm, decreasing 20 times at a depth of 0.3 μm. Such a severe internal field nonuniformity in a small-spacing planar MSM diode affects the rate of spatial separation of the carriers: their drift velocity begins to depend on the electric field strength, with heavier holes moving more slowly than electrons [8]. As a result, the electrons quickly collect at the contacts, since they drift with high velocities both in the high-field region near the surface and in the low-field region in the bulk of the diode. Unlike holes, whose drift velocity drops continuously as the field decreases, the electrons acquire a maximal drift velocity in a relatively low field [8]. Such behavior is due to the specific band structure of GaInAs: namely, intervalley electron transfer from the lower Γ valley of the conduction band to the higher L and X valleys causes a reduction of the electron drift velocity [8]. At the same time, the electric field strength in the active region of the diode is too low for most of holes to reach the saturation velocity; as a result, they move much more slowly. At depths between 0.5 and 1 μm, the electric field is rather weak for electrons as well, so that their drift velocity in this range is also very small. Yet, the electrons leave the active region of the diode (which depends on the penetration depth of the radiation) much faster than the holes. Simulation shows that even 3 ps after all electrons have left the active region, many holes still remain inside the diode, causing an extended "tail" in the impulse response of planar MSM diode and reducing the quantum efficiency (Fig. 2). Thus, problems associated with fabrication of submicrometer MSM diodes are not only the complex technology and difficulties in focusing of incident radiation on small photosensitive areas but also a low effective penetration of the electric field into the active vol-

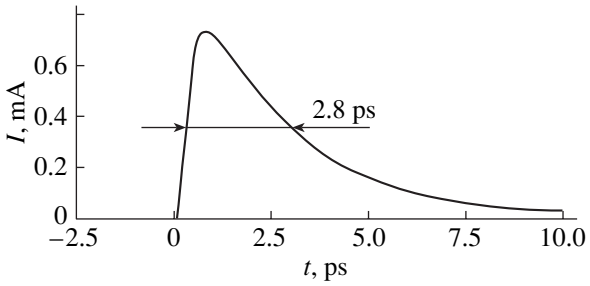

Fig. 2. Impulse response of the planar GaInAs MSM diode to radiation with a wavelength of 750 nm. The finger width and spacing are both of 100 nm; the bias voltage is 1.5 V.

ume of the photodiode. As a result, the drift velocities are far from saturation, are unstable, and depend on the location of carriers.

It should also be noted that the drift path length of photogenerated carriers in submicrometer and nanometer planar MSM structures depends on the penetration depth of incident radiation, rather than by the finger spacing, and is roughly equal to the finger spacing only for those carriers generated near the surface (Fig. 3). The remaining carriers travel much longer distances before they reach the corresponding electrodes. Although the finger spacing is small, the impulse response of the detector slows down because of the slow hole component of the current. This is illustrated in Fig. 2, where the FWHM is equal to 2.8 ps and the decay time of the response (from 90 to 10% of the amplitude) is 5.5 ps.

An increase in the bias voltage improves the situation insignificantly. Although the drift velocity of holes increases with increasing bias, the electron velocity somewhat decreases relative to its peak value [8]. A much higher bias voltage should be applied to compensate for the sharp drop of the field strength in the submicrometer structures and to rise the velocity of most carriers to the saturation value. However, a high voltage applied to the reverse-biased Schottky barrier generates a high electric field at the ends of interdigitated contacts, which causes avalanche breakdown of the junction. For these reasons, photogeneration must occur only in the near-surface region of the semiconductor (i.e., in the high-field region) to take full advantage of the submicrometer-spacing structures.

MSM diodes based on the multilayer semiconductor structures are widely used as detectors of optical radiation at wavelengths between 1.3 and 1.6 μm [13–15]. Usually, a thin layer of a wide-gap semiconductor is sandwiched in the light-absorbing GaInAs layer and Schottky contact metal to reduce the dark current of an MSM diode, which is high because of the low native barrier in the GaInAs-based structures. This additional layer does not absorb long-wave optical radiation, and the resulting heterojunction has an adverse effect, because it suppresses the effective penetration of the electric field into the active GaInAs layer [14]. Our goal

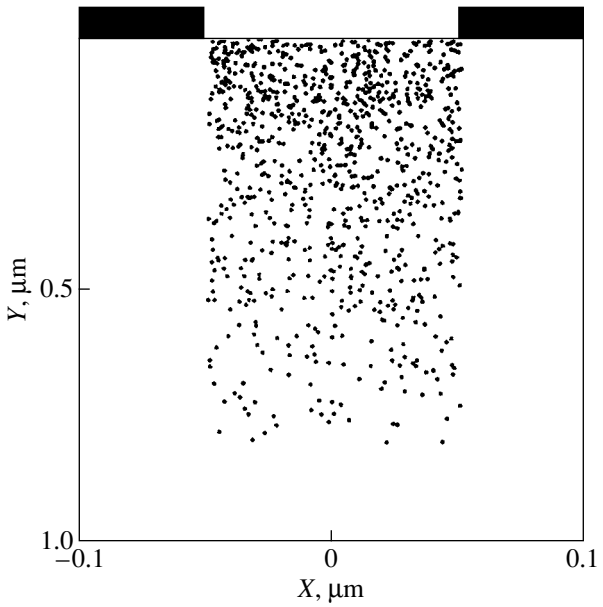

Fig. 3. Distribution of the electrons (holes) in a unit cell of the GaInAs MSM diode at the time of arrival of an optical pulse with a wavelength of 750 nm.

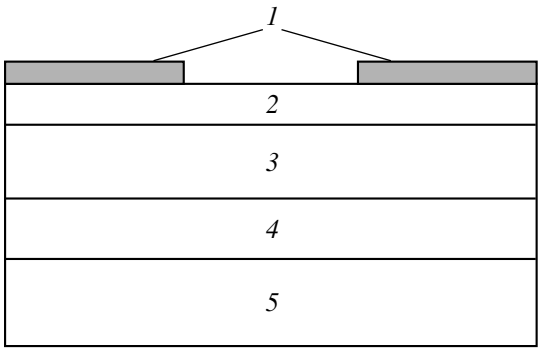

Fig. 4. Cross section of the InP/GaInAs heterojunction photodiode. (*1*) Interdigitated contacts, (*2*) 100-nm-thick InP layer, (*3*) 800-nm-thick GaInAs layer, (*4*) 300-nm-thick InP buffer layer, and (*5*) semi-insulating InP substrate.

was to demonstrate the feasibility of high-speed optical signal detection with a technique that uses an InP/GaInAs heterojunction for effective confinement of carriers generated in the low-field region. The heterostructure of such a photodiode consists of a 800-nm-thick GaInAs layer covered by a 100-nm-thick top InP layer (Fig. 4). Metallic interdigitated contacts are formed on the InP layer. Simulation shows that the presence of the heterojunction, its location, bias voltage, incident radiation density, all to a great extent influence drift of photogenerated carriers. On the one hand, the active InP layer must be as thin as possible to provide the maximal possible rate of carrier extraction; on the other, this layer must be sufficiently thick to absorb most of incident radiation for the detector efficiency to be high. The optical absorption coefficients of

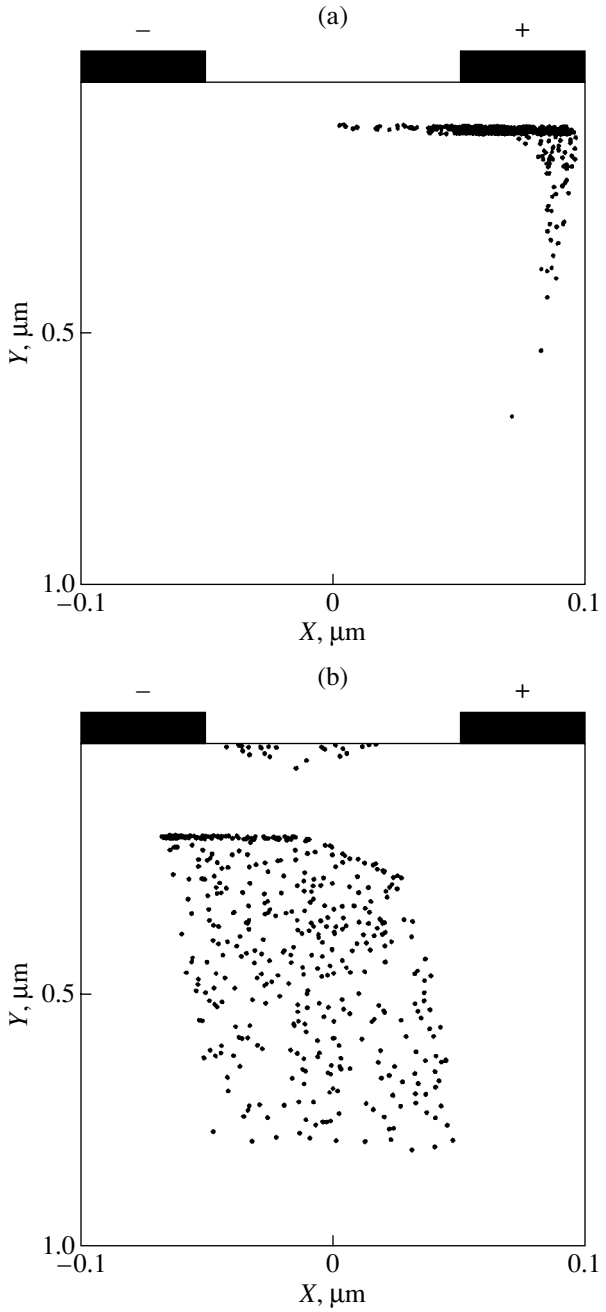

Fig. 5. Distribution of the (a) electrons and (b) holes in the active region of the InP/InGaAs MSM heterojunction photodiode 3 ps after the arrival of an 0.01-pJ optical pulse with a wavelength of 750 nm.

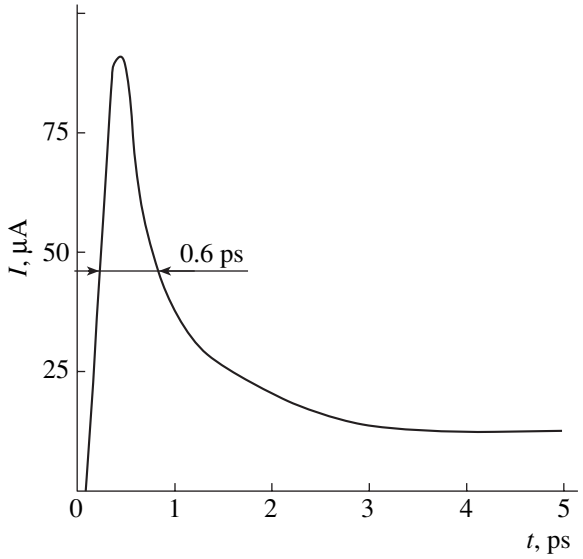

Fig. 6. Impulse response of the MSM heterojunction photodiode to an 0.01-pJ optical pulse with a wavelength of 750 nm. The bias voltage is 1.5 V.

these semiconductors are different [8]. The thickness of the InP layer was taken to be 100 nm. In this case, 30% of radiation at a wavelength of 750 nm incident on the diode is absorbed and; thus, a reasonable tradeoff between the response speed and the internal quantum efficiency of the detector is achieved.

To substantiate the validity of such an approach, we simulated the impulse response of an MSM diode with a InP/GaInAs heterojunction. The presence of the heterojunction shows up as a step in the electric field distribution due to the difference in the band structures of InP and GaInAs: the energy gap of InP is 1.35 eV, whereas that of InGaAs is 0.73 eV. The barrier height between the InP and InGaAs layers is large enough to reduce the drift path length in the MSM heterojunction photodiode and to make it equal to the thickness of the InP layer. The time variation of the distribution of electrons and holes in the active region of the detector illustrates the effect of the heterojunction (Fig. 5). Simulation shows that the heterojunction to a great extent prevents the accumulation of slow carriers generated in the low-field region near the contacts. Indeed, 3 ps after the arrival of the optical pulse, almost all carriers left the InP layer. Only the carriers generated in the upper semiconductor layer collect at the contacts of the MSM diode, providing a very fast detector response (Fig. 6). The photogenerated carriers either concentrate at the interdigitated contacts or recombine in the narrow-gap semiconductor for a time much exceeding the time of transport from the active layer to the contact; in this way, they make a minor contribution to the photocurrent. Carrier trapping by recombination centers in the narrow-gap semiconductor extends the detector bandwidth, since the tail in the photodiode response decreases in this case. However, such an approach imposes certain limitations on the bias voltage of the MSM heterojunction photodiode: under these conditions, the bias voltage must be relatively low in order to reduce the transport of electrons and holes from GaInAs through the heterojunction to the Schottky contacts. At high bias voltages, the blocking action of the heterojunction is less effective.

With such an approach, one can easily shrink the MSM diode active layer and, thus, the drift path length

down to the submicrometer level. Note that the latter parameter depends on the thickness of the InP layer in our case, while in conventional planar MSM diodes, it is related to the finger spacing (i.e., to the resolution of lithographic tools) and to the depth of light penetration into the diode base. Note also that, as the InP layer gets thinner, the diode's capacitance does not increase, but the efficiency slightly drops. However, the response speed improves considerably in this case. Simulation shows that the heterojunction MSM structure enables ultrafast detection of photons with energies exceeding the energy gap of InP. The FWHM value calculated for the response of an MSM heterostructure with an interdigitated contact spacing of 0.1 μm and a contact surface area of 10×10 μm^2 is equal to 0.6 ps (Fig. 6). This is five times shorter than the response of a conventional MSM detector of similar geometry (Fig. 2) and comparable to the response of an MSM diode based on low-temperature GaAs [16, 17]. The improvement of the speed of response of the detector is achieved at a sacrifice in its efficiency. As follows from simulation, the quantum efficiency of the heterojunction MSM photodiode equals 0.1. Such structures are of interest in the case when the speed of response of the detector is of greater importance than its efficiency.

Our calculations are supported by experiments. Earlier, using the electrooptic gating technique, we studied the electrical response of a heterojunction InP/GaInAs MSM diode. When this detector was matched to a coplanar microwave transmission line, the FWHM value was 0.6 ps [18]. However, it should be noted that, in the experiments, the energy of an incident optical pulse was 3–10 pJ. Optical pulses with a high energy may considerably modify the internal electric field [19, 20]. The effect of internal field screening should be taken into account in detailed dynamic analysis of MSM diode structures at high intensities of incident radiation.

CONCLUSIONS

The impulse response of an MSM photodetector to a short light pulse was studied in terms of the distributions of generated carriers and internal electric field. Limitations imposed by scaling down the dimensions of the interdigitated contact system of planar MSM diodes were considered. It was found, in particular, that severe electric field nonuniformity in the active region of submicrometer MSM structures adversely affects the speed of the detector. The heterojunction in the active region of an MSM diode influences drift of carriers photogenerated in the diode and considerably increases the speed of response of an InP/GaInAs MSM diode. Such an approach may be successively used in designing ultra-high-speed optoelectronic devices.

ACKNOWLEDGMENTS

This work was supported in part by the Russian Foundation for Basic Research (grant no. 03-01-00219)

REFERENCES

1. M. Ito and O. Wada, IEEE J. Quantum Electron. **22**, 1073 (1986).
2. D. L. Rogers, J. Lightwave Technol. **9**, 1635 (1991).
3. J. B. D. Soole and H. Schumacher, IEEE J. Quantum Electron. **27**, 737 (1991).
4. S. Y. Chou and M. Y. Liu, IEEE J. Quantum Electron. **28**, 2358 (1992).
5. S. Y. Chou, M. Y. Liu, and P. B. Fisher, Appl. Phys. Lett. **61**, 477 (1992).
6. J. Hugy, Y. Haddab, P. B. Sachot, and M. Ilegems, J. Appl. Phys. **77**, 1785 (1995).
7. S. Averin, R. Sachot, *et al.*, J. Appl. Phys. **80**, 1553 (1996).
8. S. Sze, *Physics of Semiconductor Devices* (Wiley, New York, 1981; Mir, Moscow, 1984).
9. K. Kato, IEEE Trans. Microwave Theory Tech. **47**, 1265 (1999).
10. A. W. Sarto and B. J. Van Zeghbroeck, IEEE J. Quantum Electron. **33**, 2188 (1997).
11. S. Ramo, Proc. IRE **27**, 584 (1939).
12. Yu. Pozhela, *Physics of High-Speed Transistors* (Mokslas, Vil'nyus, 1989) [in Russian].
13. T. Kikuchi, H. Ohno, and H. Hasegava, Electron. Lett. **24**, 1208 (1988).
14. L. Yang, A. S. Sudbo, *et al.*, IEEE Photonics Technol. Lett. **2**, 56 (1990).
15. D. Kuhl, F. Hieronymi, *et al.*, Electron. Lett. **26**, 2107 (1990).
16. Y. J. Chiu, S. B. Flecher, D. Lasaosa, and J. E. Bowers, Appl. Phys. Lett. **71**, 2508 (1997).
17. P. Kordos, A. Foster, M. Marso, and F. Ruders, Electron. Lett. **34**, 119 (1998).
18. S. V. Averin, E. S. von Kamienski, H. G. Roskos, *et al.*, Zh. Tekh. Fiz. **65**, 81 (1995) [Tech. Phys. **40**, 43 (1995)].
19. C. Moglestue, J. Rosenzweig, *et al.*, J. Appl. Phys. **70**, 2435 (1991).
20. S. V. Averin and R. Sachot, Solid-State Electron. **44**, 1627 (2000).

Translated by M. Lebedev

Technical Physics, Vol. 49, No. 6, 2004, pp. 720–727. Translated from Zhurnal Tekhnicheskoĭ Fiziki, Vol. 74, No. 6, 2004, pp. 57–64.

SOLID-STATE ELECTRONICS

Theory of Drift Step-Recovery Diodes

A. S. Kyuregyan

All-Russia Electrotechnical Institute, Moscow, 111250 Russia

e-mail: kyureg@vei.ru

Received October 21, 2003

Abstract—A theory of drift step-recovery diodes as current interrupters in inductive-storage generators is elaborated. The theory includes the nonlinear dependence of the base resistance and barrier capacitance on the current passing through the diodes. Simple relationships are obtained for the diode parameters (the thickness and doping level of the base, the charge of nonequilibrium holes extracted from the base for the time T_B of high-reverse-conductivity phase, and the surface area and number m of series-connected diodes) and parameters of the loop (the capacitance and inductance of the energy storage and the initial voltage U_{C0} across the capacitance) that provide the generation of a voltage pulse with a desired rise time t_B and amplitude U_m on the load. For a given diode efficiency k, the maximal values of the overvoltage factor U_m/U_{C0} and pulse sharpening coefficient T_B/t_B are shown to depend on a factor proportional to $k^\omega(1-k)E_B/E_\mathrm{s}$, where $\omega = 0.27$ (for U_m/U_{C0}) or -0.3 (for T_B/t_B); E_B is the breakdown field; $E_\mathrm{s} = v_\mathrm{s}/\mu$; and v_s and μ are, respectively, the saturated drift velocity and mobility of holes in weak fields. The maximum rate of rise of voltage obtainable with a single-diode ($m = 1$) structure equals $0.3v_\mathrm{s}E_B$. The characteristics of the Si and 4H–SiC diodes are compared. Numerical simulation of the recovery process substantiates the theory. © *2004 MAIK "Nauka/Interperiodica".*

INTRODUCTION

Silicon drift step-recovery diodes (DSRDs) have been used to advantage as current interrupters in inductive-storage nanosecond pulsers for more than 20 years [1, 2]. The operation of such interrupters is based on the effect of "hard" recovery of the blocking capacity of the diodes, which was qualitatively described in the 1960s [3]. Conditions under which this effect shows up most vividly were first established in [4] and then were repeatedly refined [1, 2, 5–7]. However, a quantitative theory of DSRD operation is still lacking. The only theoretical description known thus far [5], first, considers only the final stage of fast current interruption and, second, applies to only inductance-free loops, while current interruption in high-inductance loops is of most practical interest. The problem has become still more topical after the recently discovered effect of subnanosecond current interruption by GaAs [8, 9] and SiC [10, 11] diodes. The lack of a reliable theory makes it impossible to either adequately design the device[1] or access the potential of new materials for current interrupters. This paper is an attempt to solve this problem.

1. PROBLEM DEFINITION

The equivalent circuit of a loop where the current is to be interrupted is shown in the inset to Fig. 1. It includes the inductance L and capacitor C of energy storage; resistor R_s, which specifies losses in the loop; loading resistor R_l; the nonlinear capacitance C_d/m of the space charge regions (SCRs) of m identical series-connected diodes; and the resistance mr of quasi-neutral regions of the diodes [1, 5]. The recovery process, starting at the time ($t = 0$) the diode current reverses sense, may be divided into three stages [3]. Early in the process, the slightly doped d-thick base regions of the

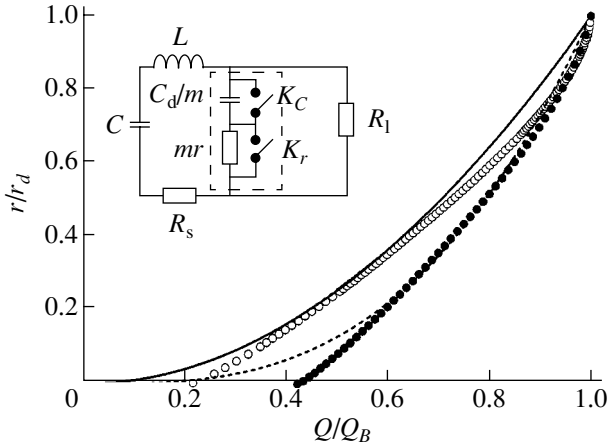

Fig. 1. Resistance of SiC and Si DSRDs vs. the charge extracted at the HRC phase. Symbols (○) and (●) refer to the simulation of the recovery process for SiC and Si devices, respectively. Calculation by formula (4) at $n = 2$ and 3 is shown by the respective solid and dashed curves. The DSRD and loop parameters are listed in the table. The inset shows the equivalent circuit of the loop where fast current interruption by semiconductor diodes takes place.

[1] The problem of designing silicon current interrupters has been solved after long-term laborious semiempirical selection of the parameters of the diodes and conditions for their operation in pulsers.

diodes are filled with a nonequilibrium high-density electron–hole plasma, which has been accumulated for the time of forward current passage. The plasma shunts the capacitances C_d and resistances r; therefore, at this early stage (of duration T_e), both switches in the equivalent circuit are closed. This stage is completed when one or both emitters are recovered and touch the base regions of thicknesses $l_{n,p}$ that are free of the nonequilibrium plasma and have an appreciable resistance (at this time, the switch K_r becomes unclosed). At the second stage, the plasma boundaries approach each other, so that the thicknesses $l_{n,p}$ and the resistances r grow. Of fundamental importance for DSRD operation is correct matching between the parameters of forward and backward current pulses and the diode characteristics. They must be selected such that the plasma boundaries meet in the plane of the p–n junction [1, 2, 7]. Only then does the base remain electroneutral during the second stage and resistance r (hence, losses in the diodes) minimal.

If the plasma regions shrink in this way (we assume that such is indeed the case), the switch K_C breaks at the end of the second stage at a time T_B. From this point on, current passage may be provided only via charging of the diode barrier capacitances C_d and the third stage, fast current interruption, sets in.[2] At the third stage, a voltage pulse with a rise time t_B and amplitude U_m across the load is formed.

The process of recovery depends on many factors (the doping level of the base regions; the emitter efficiency; and the shape, amplitude, and duration of forward and backward current pulses), but the basic governing factor is the difference between the electron, μ_n, and hole, μ_p, mobilities [12]. Since $\mu_n > \mu_p$, l_p grows faster than l_n [3]; therefore, in order for the plasma to be confined in the p–n junction plane, the thickness d_n of the n-base must be smaller than the thickness d_p of the p-base (all other things being equal) [1, 7]. Moreover, in a number of practically important cases where the ratio μ_n/μ_p is high, it may so happen that the p-base breaks free of the plasma almost simultaneously with the recovery of the n^+-emitter or even before [12]. In this case, the diodes of the interrupter must not contain n-type bases. Such a situation arises, in particular, in Si and SiC DSRDs which are considered as an example at the end of the paper. It is this DSRD design ($d_n = 0$, $d_p = d$) that will be considered below under the simplifying assumption that the base is uniformly doped by acceptors with a concentration N.

Our goal is to theoretically calculate the parameters of the interrupter (the thickness d and the doping level N of the base, as well as the surface area S and the number m of the diodes) and of the loop (the inductance L and capacitance C of the energy storage and the initial voltage U_{C0} across the capacitance). Also, it is necessary to estimate the charge Q_p of nonequilibrium holes accumulated in the base for the time of forward current passage, which will provide the formation of a voltage pulse with desired t_B and U_m across the load R_l. As a performance index for the diode, we take the values of the overvoltage factor U_m/U_{C0} and the sharpening coefficient T_B/t_B that are achievable at a given pulser efficiency k. Bearing in mind ultimate values of the DSRD parameters when calculating k, we will take into account losses due to only the recovery process, assuming that other components of the pulser are lossless (i.e., $R_s = 0$).

2. PHASE OF HIGH REVERSE CONDUCTIVITY

At this phase, including the first two stages of recovery, the DSRD resistance mr is much lower than R_l ($mr \ll R_l$) and the time dependence of the charge Q that passed through the loop after the forward current had changed sign is found from the equation

$$L\ddot{Q} + mr\dot{Q} + Q/C = U_{C0} \tag{1}$$

with the initial conditions

$$Q(0) = 0, \quad \dot{Q}(0) = 0, \tag{2}$$

The problem lies in the fact that the functional $r(Q, \dot{Q})$ depends, in general, on many factors [3, 6] and can be found with a sufficient accuracy only in one case, namely, if the concentration p of nonequilibrium holes in the plasma region is x independent, $T_e \ll T_B$, and the thickness λ of the plasma region is much smaller than d ($\lambda \ll d$). In this case, l_p is proportional to Q almost throughout the high-reverse-conductivity (HRC) phase; so, we have

$$r = r_d \frac{Q}{Q_B} f(J), \tag{3}$$

where $J = \dot{Q}$ is the current in the loop, $Q_B = Q(T_B)$, $r_d = d/q\mu_p NS(1 - \eta)$ is the base resistance at the time $t = T_B$, $\eta = J_B/qv_sNS$, $J_B = \dot{Q}(T_B)$ is the current being interrupted, q is the elementary charge, and v_s is the saturated drift velocity of electrons.

If, at the HRC stage, charge losses due to recombination in the base regions and emitter nonideality may be neglected, $Q_B = Q_p$. The dimensionless function $f(J)$ is defined by the dependence of the drift velocity v of the holes on the field strength E. If this dependence is approximated as $v(E) = v_s \dfrac{E}{E + E_s}$, where $E_s = v_s/\mu_p$, we get

$$f(J) = \frac{1 - \eta}{1 - \eta J/J_B}.$$

[2] Other situation is observed in SOS diodes [1, 2], where slow interruption of a very-high-density current proceeds well before plasma extraction.

The conditions given above under which formula (3) is valid are not necessarily met. It is evident, however, that r grows with Q supralinearly and (provided that the base remains quasi-electroneutral) tends toward r_d at $t \longrightarrow T_B$. Numerical simulation of DSRD recovery under various conditions has shown that the approximation

$$r = r_d\left(\frac{Q}{Q_B}\right)^n \tag{4}$$

with $2 \le n \le 3$ gives a reasonable accuracy (Fig. 1). In subsequent estimations, we will use the value $n = 2.5$. Phenomenological formula (4) does not embody the current dependence of r, $r \propto f(J)$ in explicit form, since, when the diode operates in the high-efficiency regime, the inequality $\eta \ll 1$ is usually fulfilled (see Section 4) and a small (no greater than the error of approximation) difference between $f(J)$ and unity may be neglected.

Using (4) and introducing new variables

$$Y = \left(\frac{Q_B m^2 r_d^2}{U_{C0} L}\right)^{1/(2n+1)} \frac{Q}{Q_B},$$

$$\tau = \left(\frac{U_{C0} L}{Q_B m^2 r_d^2}\right)^{n/(2n+1)} \frac{m r_d}{L} t,$$

one can easily reduce Eq. (1) and initial conditions (2) to the form

$$\frac{d^2Y}{d\tau^2} + Y^n \frac{dY}{d\tau} + \xi Y = 1, \tag{5}$$

$$Y(0) = 0, \quad dY(0)/d\tau = 0, \tag{6}$$

where $\xi = (Q_B m^2 r_d^2 / U_{C0} L)^{2n/(2n+1)} L / m^2 r_d^2 C$.

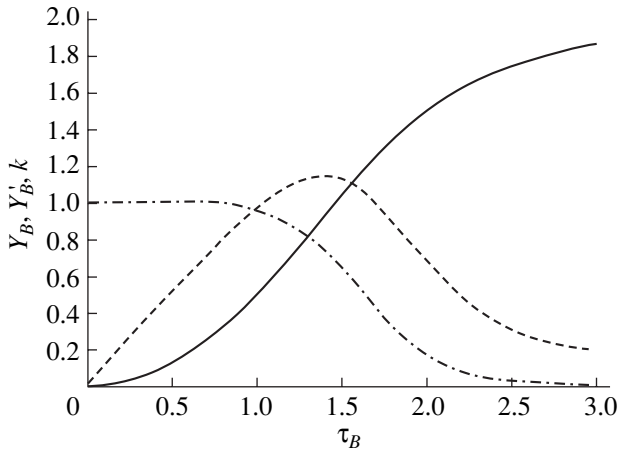

Fig. 2. Dimensionless charge (continuous curve), current (dashed curve), and efficiency (dash-and-dot curve) vs. the dimensionless duration of the HRC phase at $n = 2.5$ and $\xi = 0.1$.

Since the HRC phase is completed at the time $\tau = \tau_B$, which is found from the condition $Q = Q_B$, we have $Y_B \equiv Y(\tau_B) = (Q_B m^2 r_d^2 / U_{C0} L)^{1/(2n+1)}$ and $\xi Y_B = Q_B / C U_{C0}$. To reach the current interruption phase, the initial charge CU_{C0} on the capacitance must exceed Q_B; therefore, $Y_B \le 1/\xi$.

Desired relationships between T_B, C, U_{C0}, Q_B, and k for given r_d, J_B, and L (it will be shown in the next section that these three parameters depend on the voltage pulse parameters and load) can be derived parametrically through solutions $Y_B = Y(\tau_B)$ and $Y'_B = dY(\tau_B)/d\tau$ to Eq. (5), which contains only one undefined parameter ζ:

$$T_B = \tau_B Y_B^n L / m r_d, \tag{7}$$

$$C = L Y_B^{2n} / m^2 r_d^2 \xi, \tag{8}$$

$$U_{C0} = J_B m r_d / Y'_B Y_B^n, \tag{9}$$

$$Q_B = J_B L Y_B^{(n+1)} / m r_d Y'_B, \tag{10}$$

$$k = Y'^2_B / Y_B (2 - \xi Y_B). \tag{11}$$

At the time of interruption, the voltage $U_{CB} = U_C(T_B)$ across the capacitance C is

$$U_{CB} = U_{C0}(1 - \xi Y_B). \tag{12}$$

In the important limiting case $\xi \longrightarrow 0$ (or $C \longrightarrow \infty$, which is the same), we obtain the first integral of Eq. (5):

$$Y' + \frac{Y^{n+1}}{n+1} = \tau. \tag{13}$$

For $n = 1$, the substitution $Y = 2u'/u$ reduces (13) to the known Airy equation. Its solution satisfying initial conditions (6) can be represented through the Kummer degenerate hypergeometric functions $M(a, b, z)$ [12]:

$$Y(\tau) = \frac{\tau^2}{2} \frac{M(7/6, 7/3, 2\sqrt{2}\tau^{3/2}/3)}{M(1/6, 1/3, 2\sqrt{2}\tau^{3/2}/3)}. \tag{14}$$

At other values of ξ and n, the solution to Eq. (5) is not reduced to known special function and can be derived only by numerical integration, which is today a routine procedure. An example of such a solution that will be used below is shown in Fig. 2.

3. STAGE OF FAST CURRENT INTERRUPTION

It can be shown that, at this stage (both switches in the equivalent circuit are broken), the time variation of the charge Q_d on the capacitances is described by the

equation

$$\frac{d}{dt}\left[\left(1+\frac{mr}{R_\mathrm{l}}\right)\frac{dQ_\mathrm{d}}{dt}\right] + \left[\frac{m}{R_\mathrm{l}C_\mathrm{d}(Q_\mathrm{d})}+\frac{mr}{L}\left(1+\frac{R_\mathrm{s}}{R_\mathrm{l}}\right)+\frac{R_\mathrm{s}}{dt}\right]\frac{dQ_\mathrm{d}}{dt} + \frac{1}{L}\left[\left(1+\frac{R_\mathrm{s}}{R_\mathrm{l}}\right)m\int_{Q_0}^{Q_\mathrm{d}}\frac{dQ_\mathrm{d}}{C_\mathrm{d}(Q_\mathrm{d})}-U_C\right] = 0. \quad (15)$$

Here, the dependences $C_\mathrm{d}(Q_\mathrm{d})$ and $r(Q_\mathrm{d}, \dot{Q}_\mathrm{d})$ are arbitrary if the bias current in the quasi-neutral diode regions is much lower than the conduction current and $\eta < 1$. This inequality is needed for the SCR be localized in the diode areas where free charge carriers are totally absent [5]. Equation (15) with the initial conditions

$$Q_\mathrm{d}(0) = Q_0, \quad dQ_\mathrm{d}(0)/dt = J_B \quad (16)$$

(in this section, the zero time is the time of onset of the current interruption stage) describes all possible scenarios of fast current interruption by the diodes with an arbitrary doping profile. In the general case, this equation is hard to analyze. However, the problem is greatly simplified under the assumptions made above. For the case under consideration (the uniformly doped *p*-base), we have

$$C_\mathrm{d}(Q_\mathrm{d}) = q\varepsilon N S^2 Q_\mathrm{d}^{-1}, \quad (17)$$

where ε is the permittivity of the semiconductor, and $r = r_\mathrm{d} f(J)$, as was shown in [5]. The voltage U_C may be considered constant and equal to U_{CB} by virtue of the inequality $t_B \ll T_B$. The condition that the base remains quasi-neutral up to completion of the HRC phase means that $Q_\mathrm{d}(0) = 0$. Then, putting $R_\mathrm{s} = 0$ (see Section 1) and introducing new variables

$$Z = \frac{2mLQ_\mathrm{d}}{q\varepsilon N S^2 R_\mathrm{l}^2(1+\chi)}, \quad \theta = \frac{R_\mathrm{l}t}{2L}, \quad (18)$$

we can recast Eq. (15) and initial conditions (16) as

$$\frac{d^2Z}{d\theta^2}+\left(Z+\frac{2\chi}{1+\chi}\right)\frac{dZ}{d\theta}+Z^2-Z_C^2 = 0, \quad (19)$$

$$Z(0) = 0, \quad \frac{dZ(0)}{d\theta} = \psi \equiv \frac{4J_B L^2 m}{q\varepsilon N S^2 R_\mathrm{l}^3(1+\chi)}, \quad (20)$$

where

$$\chi = mr_\mathrm{d}/R_\mathrm{l},$$

$$Z_C = \frac{2L}{SR^2(1+\chi)}\sqrt{\frac{2mU_{CB}}{q\varepsilon N}}.$$

When deriving (19), we also assumed that the resistance r is constant and equal to its maximal value r_d throughout the current interruption stage (actually, $r = r_\mathrm{d}$ only at the beginning of interruption, when $J = J_B$; subsequently, the current through the diode decreases and $r < r_\mathrm{d}$). This assumption helps us to make the upper-bound estimate of how losses in the diode influence the current interruption dynamics. Such an estimate is necessary, because early in the process the derivative $dZ/d\theta$ is maximal and $Z \ll 2\chi/(1+\chi)$ for any finite r (see (20)), so that it is unclear *a priori* whether the latter circumstance is significant. The estimation will be performed below; for the moment, we will consider the current interruption process without allowance for losses. Analytical solutions to (19) at $\chi = 0$ may be obtained in two limiting cases.

Under the open-circuit conditions ($R_\mathrm{l} \longrightarrow \infty$), we disregard the second term in (19) and obtain a solution in parametric form:

$$\theta = \sqrt{\frac{3}{2Z_\mathrm{m}}}\int_0^u\left[1-\frac{Z_C^2}{Z_\mathrm{m}^2}(1-u)-u^3\right]^{-1/2}du, \quad Z = Z_\mathrm{m}u, \quad (21)$$

where $Z_m = \max Z$ is a positive root of the equation

$$\frac{2}{3}Z_\mathrm{m}^3 = \psi^2 + 2Z_C^2 Z_\mathrm{m}. \quad (22)$$

The charge on the diodes (and the voltage across the load) reaches a maximum at $u = 1$; therefore, for $U_{CB} = 0$, the dimensionless leading edge duration θ_B, pulse duration θ_pul,[3] and pulse amplitude Z_m are calculated from the respective formulas

$$\theta_B = \frac{1}{3}\left(\frac{3}{2\psi}\right)^{1/3}B\left(\frac{1}{2},\frac{1}{3}\right) \approx 1.61\psi^{-1/3}, \quad \theta_\mathrm{pul} = 2\theta_B, \quad Z_B = \left(\frac{3}{2}\psi^2\right)^{1/3}, \quad (23)$$

where $B(x, y)$ is the beta function [13].

It is easy to check that $Z_C^2/Z_\mathrm{m}^2 = U_{CB}/U_\mathrm{m}$; therefore, at high overvoltage factors (when $U_{CB} < U_{C0} \ll U_\mathrm{m}$), which alone are of applied interest, corrections to U_{CB} making it nonzero must be negligible. In fact, using (21) and (22), one can show in a first approximation that the relative increment of Z_m equals U_{CB}/U_m, while θ_B decreases but much more slowly (roughly by a factor of 20 for $\psi = 3$).

In the current generator regime ($L \longrightarrow \infty$), the third and fourth terms in (19) may be neglected and we obtain the solution in explicit form:

$$Z = \sqrt{2\psi}\tanh\left(\theta\sqrt{\frac{\psi}{2}}\right); \quad (24)$$

[3] It is assumed that the pulse is terminated when the voltage across the SCRs of the diodes changes sign. Thereafter, a formal solution to Eqs. (15) or (19) is obviously physically meaningless.

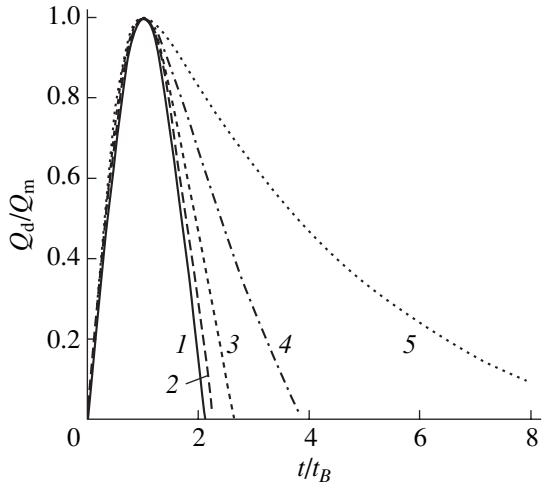

Fig. 3. Time dependences of the charge on the diodes that are obtained by numerically solving Eq. (5) at $\chi = 0$, $U_{CB} = 0$, and $\psi =$ (*1*) 0.01, (*2*) 0.1, (*3*) 1.0, (*4*) 10, and (*5*) 100.

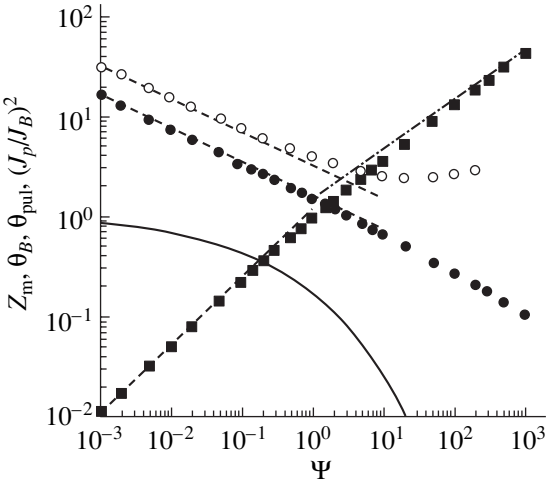

Fig. 4. Dimensionless (square) amplitude Z_m, leading edge time (black circle) θ_B, (○) pulse duration t_{pul}, and the fraction of the energy $J^2(t_{pul})/J_B^2$ that is left in the inductance by the end of the pulse (continuous curve) vs. the parameter ψ at $\chi = 0$ and $U_{CB} = 0$. The dashed and dash-and-dot curves show the results of calculation by formulas (23) and (25) for the limiting cases.

hence,

$$Z_m = \sqrt{2\psi}, \tag{25}$$

and the characteristic dimensionless rise time of the voltage across the load equals $\sqrt{2\psi}$. Thus, the parameter U_{CB} does not influence the pulse parameters in this case; accordingly, the approximation $U_{CB} = 0$ may be used to calculate Z_m and θ_B.

The results of numerical solution of Eq. (19) for $\chi = 0$, $U_{CB} = 0$, and different ψ are shown in Fig. 3, and the ψ dependences of Z_m, θ_B, and θ_{pul} are given in Fig. 4. As was expected, the analytical and numerical calculations coincide at small (open-circuit conditions) and large (current generator regime) ψ. For intermediate values of ψ, the curves $Z_m(\psi)$ and $\theta_B(\psi)$ can be approximated by the power functions

$$\theta_B = a\psi^{-\alpha}, \quad Z_m = b\psi^{\beta}. \tag{26}$$

In particular, in the interval $0.1 < \psi < 10$, approximation (26) provides an accuracy of 1% or higher when $a = 1.45$, $\alpha = 0.36$, $b = 0.88$, and $\beta = 0.60$.

Now we can evaluate the loop parameters L and J_B, as well as the diode parameters m, S, N, and d_p, that will provide the generation of a voltage pulse with given U_m and t_B across the load R_l. Since for the diode with a uniformly doped base $N = mQ_m^2/2q\varepsilon S^2U_m$ and the SCR thickness $w = \varepsilon S/C_d$, one easily finds that

$$L = \frac{R_l t_B}{2a}\psi^{\alpha}, \quad J_B = \frac{2U_m}{b^2 R_l}\psi^{(1-2\beta)}, \tag{27}$$

$$m = \frac{2aU_m}{b\eta v_s E_B t_B}\psi^{(1-\alpha-\beta)}, \quad S = \frac{2U_m t_B}{ab\varepsilon E_B R_l}\psi^{(\alpha-\beta)},$$
$$d = \frac{b}{a}\eta v_s t_B \psi^{(\alpha+\beta-1)}, \quad N = \frac{a\varepsilon E_B}{b\eta q v_s t_B}\psi^{(1-\alpha-\beta)}. \tag{28}$$

When deriving (27) and (28), we used formulas (17), (18), (20), and (26) and assumed that, at the time $t = t_B$, the maximal field strength in the SCR, $Q_d/\varepsilon S$, reaches the breakdown value E_B and the SCR occupies the entire base (i.e., that the SCR thickness $w = d$).

From (27) and (28), we derive a formula for the base resistance:

$$mr_d = b^2 \frac{\eta}{1-\eta} R_l \frac{E_s}{E_B}\psi^{(2\beta-1)}; \tag{29}$$

hence, $\chi \le \eta E_s/(1-\eta)E_B$ for the typical case $\psi \approx 3$ (see below). In most semiconductors, $E_s \le 0.1E_B$ [14]; therefore, $\chi \le 0.1$ even at $\eta < 1/2$. At such χ, the amplitude and duration of the pulse decrease by less than 2 and 0.5%, respectively, as follows from the numerical solution of Eq. (19). This validates the use of the approximation $\chi = 0$ in describing the current interruption process and deriving formulas (27) and (28).

Strictly speaking, the breakdown field E_B in (27)–(29), which depends, although slightly, on the doping profile, is undefined. In our case, this dependence may be approximated by the power law: $E_B = \tilde{E}(N/\tilde{N})^{\gamma}$, where $\tilde{E}$, $\tilde{N}$, and γ are material constants [14, 15].

It is easy to see that this dependence is taken into account if

$$E_B = \tilde{E}\left[\frac{\psi^{(1-\alpha-\beta)}}{\eta}\frac{a\varepsilon\tilde{E}}{bq\tilde{N}v_s t_m}\right]^{\gamma/(1-\gamma)} \quad (30)$$

is substituted for E_B.

4. ULTIMATE VALUES OF THE DIODE PARAMETERS

From formulas (7)–(12) and (27)–(30), one can calculate all the parameters of the diodes and loop that provide desired characteristics of the pulser; however, these formulas involve four undefined parameters (ζ, τ_B, ψ, and η). The definition of these parameters calls for special consideration.

(i) As was noted in Section 1, the quality of the pulser is characterized by the overvoltage factor U_m/U_{C0} and sharpening coefficient T_B/t_B. Expressions for these parameters are easy to derive from (9), (10), and (27)–(29):

$$\frac{U_m}{U_{C0}} = Y_B^n Y_B' \frac{1-\eta}{\eta}\frac{E_B}{2E_s}, \quad (31)$$

$$\frac{T_B}{t_B} = Y_B^n \tau_B \frac{\psi^{(1+\alpha-2\beta)}}{ab^2}\frac{1-\eta}{\eta}\frac{E_B}{2E_s}. \quad (32)$$

Numerical integration of Eq. (5) shows that both quantities decrease monotonically with increasing ξ at any constant ψ, η, and k. Therefore, it is desirable to take ξ as small as possible, all other things being equal. The value of ξ depends (see (8)) on the capacitance C of the capacitor that can be achieved when the voltage across the capacitor exceeds U_{C0} and the stray inductance is below L.

(ii) As the dimensionless duration τ_B of the HRC phase increases, the efficiency k decreases monotonically (Fig. 2); therefore, specifying this most important parameter of the pulser, one uniquely specifies (at a given ξ) the value of τ_B. When selecting k, one should bear in mind that both the overvoltage factor and the sharpening coefficient decrease rapidly with increasing k. For the limiting case $\xi = 0$ and $n = 2$ and 3, the normalized dependences (Fig. 5) of the quality indices are governed by the factors $Y_B^n Y_B'$ and $Y_B^n \tau_B$. These factors can be approximated by the function

$$F(k) = Ak^{\omega}(1-k). \quad (33)$$

For $n = 2.5$, the error of this approximation in the interval $0.1 < k < 0.95$ is within 5% at $A = 4$ and $\omega = 0.27$ (for the sharpening coefficient) or $\omega = -0.3$ (for the overvoltage factor). Function (33) also provides a good fit to the k dependence of the factor $Y_B^{(n+1)}/Y_B'$ (according to (10), this factor defines the charge Q_B extracted at the HRC phase) if one puts $A = 2$ and $\omega = -0.72$ at $n = 2.5$.

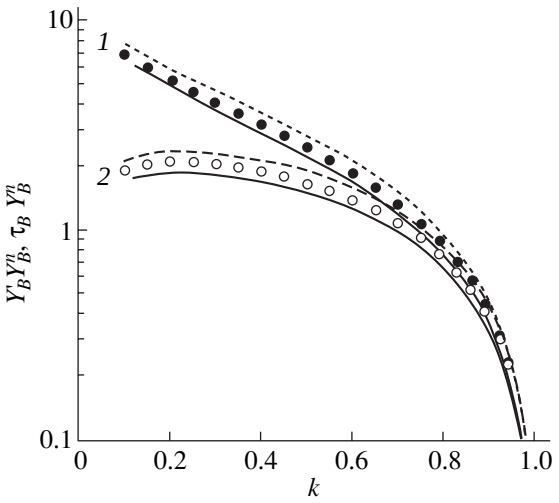

Fig. 5. Normalized (*1*) sharpening coefficient and (*2*) overvoltage factor vs. the efficiency k for $\chi = 0$ and $n = 2$ (continuous curve) and 3 (dotted curve). Symbols, approximation by formula (33) for $n = 2.5$.

(iii) The parameter ψ characterizes pulser–load matching: as ψ grows, the fraction of the energy that remains in the inductance by the time t_{pul} of pulse termination (this fraction equals $J^2(t_{pul})/J_B^2$ decreases and tends toward zero at $\psi \longrightarrow \infty$ (Fig. 4). Therein lies the radical difference of a loop with the nonlinear capacitance C_d/m, which varies according to (17), from a normal linear loop, for which "exact matching" is known to take place at a finite value of $R_l = 0.5\sqrt{L/C}$. Such a situation may also occur in the case under consideration: the singular point ($Z = Z_C$, $dZ/d\theta = 0$) of Eq. (19) is a stable node; that is, the diode current decays aperiodically if $Z_C \geq 8$ (in dimension form, $R_l \leq 0.5\sqrt{L/C_d(U_C)}$). In this case, however, if $U_m/U_{C0} \gg 1$, the Z_C-related parameter

$$\psi = \left(\frac{Z_C}{b}\sqrt{\frac{U_m}{U_C}}\right)^{1/\beta} \gg 1$$

and the leading-to-trailing edge time ratio $(t_{pul} - t_B)/t_B$ grow sharply, as follows from (27) and (28) (Figs. 3, 4). Because of this, when selecting the value of ψ, one should keep in mind the shape of the pulse. For most applications, the value $\psi = 3$ seems reasonable. At this value, more than 90% of the energy stored in the inductance is dissipated by the load for the pulse time and the trailing edge time exceeds t_B insignificantly.

(iv) The parameter η characterizes the pulser qualitatively in accordance with formulas (31) and (32). Basically, decreasing η one may obtain the overvoltage factor and sharpening coefficient as high as desired even if $k \longrightarrow 1$. In this case, however, both the number

Parameters of the *p*-type base semiconductor and loop

	Si	4H–SiC
$\varepsilon/\varepsilon_0$	11.8	10.0
v_s, cm/s	8.5×10^6	8.0×10^6
E_s, V/cm	1.9×10^4	8.0×10^4
$\tilde{E}$, V/cm	4.0×10^5	2.6×10^6
γ	0.18	0.16
$\tilde{N}$, cm^{-3}	10^{16}	
J_B, A	103.7	
L, nH	25.61	
C, nF	367.0	
U_{C0}, V	82.2	
T_B, ns	50.0	
η	0.282	0.443
m	13	1
E_B, V/cm	2.75×10^5	2.43×10^6
S, cm^2	0.217	0.028
N, cm^{-3}	1.24×10^{15}	6.53×10^{15}
d, μm	14.0	20.6
mr_d, Ω	1.26	

m of diodes in the interrupter and the mean concentration $\sqrt{\tilde{p}_m}$ of nonequilibrium holes in the base grow:

$$\bar{p}_m \geq \frac{Q_B}{qSd} = \frac{1-\eta}{\eta^2}\frac{\varepsilon E_B^2}{2q v_s t_B E_s}\frac{a}{b^4}\psi^{(3-\alpha-4\beta)}\frac{Y_B^{(n+1)}}{Y_B'}. \quad (34)$$

As a result, the injection capacity of the emitters

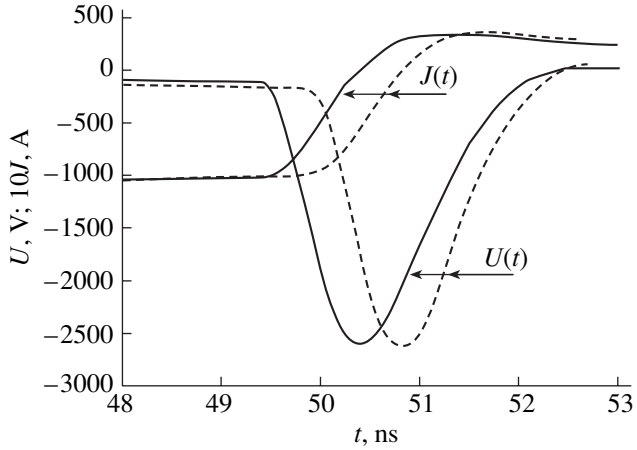

Fig. 6. Time variation of the voltage and current passing through the Si (dashed lines) and SiC (continuous curves) DSRDs that is obtained by numerical simulation of current interruption. The diode and loop parameters are listed in the table.

decreases and the charge losses ΔQ at the stage of forward current passage and the HRC phase grow. At the same time, the scatter in the value of ΔQ must be much less than $Q_B t_B/T_B$; otherwise, the recovery of all m diodes of the interrupter becomes asynchronous. When the sharpening coefficient is high, this condition imposes very stringent requirements on the reproducibility of the surface area and parameters of the diodes, which sometimes cannot be satisfied.

Two features of the results discussed above are noteworthy. First, for given ξ, k, ψ, and η, the quality indices of DSRDs are independent of the pulse parameters: they depend only on the single parameter of the semiconductor, namely, on the ratio between the breakdown field strength E_B and the field E_s at which the curve $v_s(E)$ tends to saturate. Hence, the ratio E_B/E_s may serve to estimate whether a material is a candidate for DSRD technology. In these terms, silicon is "worse" than 4H-SiC roughly twofold (see table). However, this drawback can be compensated for by taking smaller values of η, as exemplified below.

Second, from the formula for m (see (28)), one can find the ultimate rate of rise of the voltage achievable with a one-diode ($m = 1$) interrupter:

$$\max\left(\frac{U_m}{t_B}\right)_{m=1} = \frac{b}{2a}\psi^{(\alpha+\beta-1)} v_s E_B \approx 0.3 v_s E_B. \quad (35)$$

This quantity also depends on the material parameters alone. For silicon DSRDs, the ultimate rate of rise of the voltage equals roughly to 6.4×10^{11} V/cm; for SiC devices, it is almost ten times higher. A further increase in the rate of rise is only possible through an increase in the number of diodes in the interrupter. However, the number of diodes may be raised as long as the current interruption process in all of them occurs simultaneously. In silicon DSRDs, the relative charge losses $\Delta Q/Q_B$ are relatively low, so that synchronization presents no problem [5]. In DSRDs made of wide-gap semiconductors with a high dielectric strength, the mean concentration $\bar{p}_m$ of nonequilibrium carriers in the base (see (34)) may exceed the concentration of charged impurities in the emitters, even if the dopant concentration in them is high, because of high donor or acceptor ionization energies. This results in a severe degradation of the emitter efficiency and drastically increases the charge losses ($\Delta Q \approx Q_B$). Accordingly, requirements for the uniformity and reproducibility of the emitter parameters become still more stringent. In view of the aforesaid, the fabrication of multielement SiC interrupters seems problematic.

By way of example, let us estimate the parameters of the Si and 4H–SiC DSRDs and loops that generate a voltage pulse of amplitude $U_m = 2.5$ kV and a leading pulse time $t_B = 1.0$ ns across a loading resistance $R_l = 50\ \Omega$. We put $\psi = 3$, $\xi = 0.1$, and $k = 0.5$. The parame-

ters of the semiconductors[4] used in calculations and the results of calculations are listed in the table. It is seen that identical characteristics of the pulser are obtained with one SiC diode and 13 Si diodes whose surface area is 7.7 times larger. With the same thickness of the chips, the overall amount of silicon turned out to be 100(!) times greater. Yet, it remains unclear whether even such a great difference in material consumption will compensate a high price of the SiC devices.

To verify our simple theory, we performed numerical simulation of current interruption by silicon and silicon carbide DSRDs with the parameters listed in the table. The diodes were n^+–p–p^+ epitaxial structures with a step doping profile. The emitter thickness was taken to be 10 μm; the concentration of donors and acceptors in the emitters, 2×10^{19} cm^{-3}; and the carrier lifetime in the base, 10 μs. The last two values are as yet unattainable for SiC: we just consider the perfect material in order to access its potentialities. At the stage of direct pumping, a sinusoidal current pulse of width 300 ns was applied to the diodes. The pulse amplitude was taken in such a way that the charge Q_p calculated by formula (10) was equal to 3.5 μC at the time of current reversal in both cases. The results of simulation performed using the Issledovanie computer program [16–18] are given in Fig. 6. All the preset parameters of the voltage pulse are seen to be provided by the pulser whose parameters were calculated from formulas (7)–(12) and (27)–(32). The losses at the HRC phase were also found to be close to the calculated value $LJ_B^2(k^{-1} - 1)/2$ = 13 mJ. In the SiC device, current interruption was accomplished earlier presumably because of higher charge losses.

Note in conclusion that qualitatively our results apply to more sophisticated DSRDs, e.g., to those with bases of *p*- and *n*-type conductivity and/or to those prepared by diffusion methods (i.e., with highly nonuniformly doped bases). In any case, the indices of material suitability for DSRD technology are the quantities E_B/E_s and v_sE_B. Also, all the relationships between the parameters of the pulse, loop, and current-interrupting diodes remain valid, although the values of the coefficients *a*, *b*, α, β, etc., may change. The only exception is formula (28) for the acceptor concentration, which becomes meaningless when the base is doped nonuniformly. DSRDs with nonuniformly doped bases are of interest, since doping profile optimization is bound to appreciably reduce losses in the diodes and improve the efficiency of the pulser.

[4] The values of E_s and v_s for Si and 4H-SiC were taken from [14] and [16], respectively; the values of $\tilde{E}$, $\tilde{N}$, and γ for both materials, from [15].

ACKNOWLEDGMENTS

The author thanks I.V. Grekov and V.S. Belkin for the fruitful discussions, as well as S.N. Yurkov and T.T. Mnatsakanov for the assistance in interruption simulation.

This work was supported by the Russian Foundation for Basic Research (grant no. 02-02-16496).

REFERENCES

1. I. V. Grekhov, Izv. Akad. Nauk, Énerg., No. 1, 53 (2000).
2. I. V. Grekhov and G. A. Mesyats, IEEE Trans. Plasma Sci. **28**, 1540 (2000).
3. H. Benda and E. Spenke, Proc. IEEE **55**, 1331 (1967).
4. I. V. Grekhov, V. M. Efanov, A. F. Kardo-Sysoev, *et al.*, Pis'ma Zh. Tekh. Fiz. **9**, 435 (1983) [Sov. Tech. Phys. Lett. **9**, 188 (1983)].
5. I. V. Grekhov and V. M. Tuchkevich, *Novel Principles of High Power Switching by Semiconductor Devices* (Nauka, Leningrad, 1988) [in Russian].
6. A. F. Kardo-Sysoev and M. V. Popova, Fiz. Tekh. Poluprovodn. (Leningrad) **25**, 3 (1991) [Sov. Phys. Semicond. **25**, 1 (1991)].
7. A. S. Kyuregyan, RF Patent No. 2197034, Byull. Izobret., No 2 (2003).
8. V. I. Korol'kov, A. V. Rozhkov, and L. A. Petropavlovskaya, Pis'ma Zh. Tekh. Fiz. **27** (17), 46 (2001) [Tech. Phys. Lett. **27**, 731 (2001)].
9. A. V. Rozhkov and V. A. Kozlov, Fiz. Tekh. Poluprovodn. (St. Petersburg) **37**, 1477 (2003) [Semiconductors **37**, 1425 (2003)].
10. I. V. Grekhov, P. A. Ivanov, A. O. Konstantinov, and T. P. Samsonova, Pis'ma Zh. Tekh. Fiz. **28** (13), 24 (2002) [Tech. Phys. Lett. **28**, 544 (2002)].
11. I. V. Grekhov, P. A. Ivanov, D. V. Khristyuk, *et al.*, Solid-State Electron. **47**, 1769 (2003).
12. I. V. Grekhov, A. S. Kyuregyan, T. T. Mnatsakanov, *et al.*, Fiz. Tekh. Poluprovodn. (St. Petersburg) **37**, 1148 (2003) [Semiconductors **37**, 1123 (2003)].
13. M. Abramovitz and I. A. Stegun, *Handbook of Mathematical Functions* (Dover, New York, 1971; Nauka, Moscow, 1979).
14. S. Sze, *Physics of Semiconductor Devices* (Wiley, New York, 1981; Mir, Moscow, 1984), Vol. 1.
15. A. S. Kyuregyan and S. N. Yurkov, Fiz. Tekh. Poluprovodn. (Leningrad) **23**, 1819 (1989) [Sov. Phys. Semicond. **23**, 1126 (1989)].
16. M. Hjelm, H.-E. Nilsson, A. Martinez, *et al.*, J. Appl. Phys. **93**, 1099 (2003).
17. T. T. Mnatsakanov, I. L. Rostovtsev, and N. I. Philatov, Solid-State Electron. **30**, 579 (1987).
18. M. E. Levinstein, T. T. Mnatsakanov, P. A. Ivanov, *et al.*, Electron. Lett. **36**, 1241 (2000).

Translated by V. Isaakyan

Technical Physics, Vol. 49, No. 6, 2004, pp. 728–732. Translated from Zhurnal Tekhnicheskoĭ Fiziki, Vol. 74, No. 6, 2004, pp. 65–69.

OPTICS,
QUANTUM ELECTRONICS

Optical Vidicon Based on a Layered Semiconductor Structure: Image Reading and Storage

G. G. Kozlov[1], Yu. K. Dolgikh[1], Yu. P. Efimov[1], S. A. Eliseev[1], V. V. Ovsyankin[1], and V. V. Petrov[2]

[1] *Vavilov State Optical Institute, All-Russia Research Center, Birzhevaya liniya 12, St. Petersburg, 199034 Russia*
[2] *Fock Institute of Physics (Petrodvorets Branch), St. Petersburg State University, Petrodvorets, 198904 Russia*
e-mail: gkozlov@photonics.phys.spbu.ru

Received May 7, 2003; in final form, September 11, 2003

Abstract—A simple device for image scanning and storage based on a semiconductor structure is proposed. The scanning and storage involve laser-beam reading. A video signal is represented by the photoelectromotive force generated by the structure. Simple experiments demonstrating that the structure proposed works as a vidicon and a storage device capable of the data storage for at least two hours are presented. A physical interpretation of the effects observed is proposed. © *2004 MAIK "Nauka/Interperiodica".*

DEVICE CHARACTERIZATION

The purpose of this work is to describe a device for image scanning similar to a TV vidicon, in which an optical beam is used instead of the electron beam. Figure 1 shows the scheme of the device. Two dielectric layers *1* and *2* are deposited on a conducting substrate *3*, so that the band gap of layer *2* is narrower than that of layer *1*. A transparent conducting layer *0* (transparent electrode) is deposited on the wideband-gap layer *1*. This structure is series connected to a load resistor *R* and a power supply (Fig. 1). The wideband-gap layer *1* and the narrowband-gap layer *2* are transparent and absorbing, respectively, in the spectral interval of the image projected on the structure from the side of the transparent electrode. The photoconductivity distribution emerging in the narrowband-gap layer *2* reproduces the distribution of dark and light spots in the image (Fig. 1). The image does not affect the conductivity of layer *1* that is transparent to the image. Therefore, this layer retains the isolating properties, and the current in the circuit is absent. We illuminate the structure using a tightly focused beam, whose wavelength is short enough to induce the photoconduction in the wideband-gap layer *1*. A small conducting region *4* appears at the point of the beam incidence in layer *1*. The resulting current in the circuit depends on the conductivity of layer *2* related to the local brightness of the image. If we scan the short-wavelength beam over the surface of the structure, the video signal at the resistor *R* corresponds to the image. For this reason, the short-wavelength beam is referred to as the reading beam. Apparently, the reading beam penetrates inside layer *2* and affects its conductivity, which gives rise to a background photocurrent for even absolutely black fragments of the image. To suppress this effect, one can choose a strongly absorbing material for layer *1*. Then, the reading beam induces photoconduction in layer *1* and slightly affects the conduction of layer *2*. The absorbing properties of layer *2* must ensure a complete absorption of the reading beam at distances shorter than the length of this layer. The device under consideration can be called an optical vidicon. Note that one can detect a video signal measuring the photoconductivity of a single layer in the presence of the image projected on it. In this case, the variation in the photocurrent upon scanning is related to the nonlinear dependence of the photoconductivity on the intensity of light.

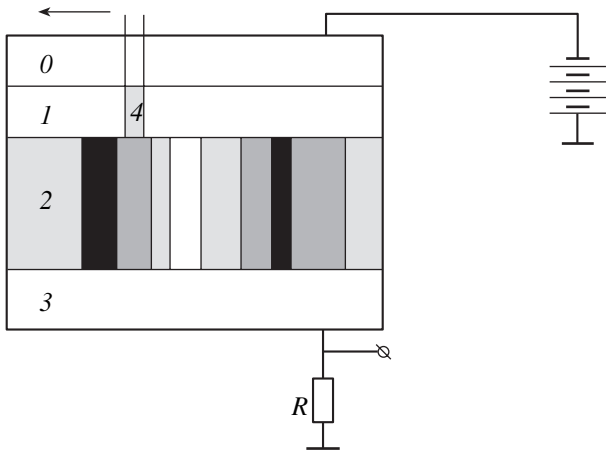

Fig. 1. Schematic circuit of the optical vidicon: *0* transparent conducting layer, *1* wideband-gap dielectric layer, *2* narrowband-gap dielectric layer nontransparent for the image (dark and light stripes show the brightness distribution and the corresponding distribution of the photoconductivity), *3* conducting substrate, and *4* conducting region (created by a short-wavelength reading beam) that closes circuit.

1063-7842/04/4906-0728$26.00 © 2004 MAIK "Nauka/Interperiodica"

EXPERIMENTAL ILLUSTRATION

To roughly test the results of the above analysis, we perform an experiment, whose scheme is shown in Fig. 2. The specific scheme of the aforementioned device is presented in the inset to Fig. 2. A water layer represents the transparent electrode *0* (see notation for Fig. 1). An epitaxial $Al_{0.5}Ga_{0.5}As$ layer (the band gap is about 1.9 eV) with a thickness of 3 μm and a semi-insulating GaAs substrate with a thickness of 300 μm serve as wideband-gap layer *1* and narrowband-gap layer *2*, respectively. A water electrode is used as the conducting substrate *3*. The reading beam is the focused beam of a helium–neon laser incident on the device *3* (Fig. 2) after passing through a deflecting system consisting of a mirror *1* connected to a loudspeaker diaphragm. The vibrations of the diaphragm lead to the reading beam motion along a line segment in the plane of the device *3*. The image represents a light spot created by the focused beam of a neodymium laser (1.06 μm) in the plane of the device *3*. Using mirror *2*, we can place the light spot at the trajectory of the reading beam. In this case, current pulses are generated in the circuit. Note that in spite of the fact that GaAs is transparent for the radiation of neodymium laser, the photoconduction in this material emerges owing to impurities and intrinsic defects.

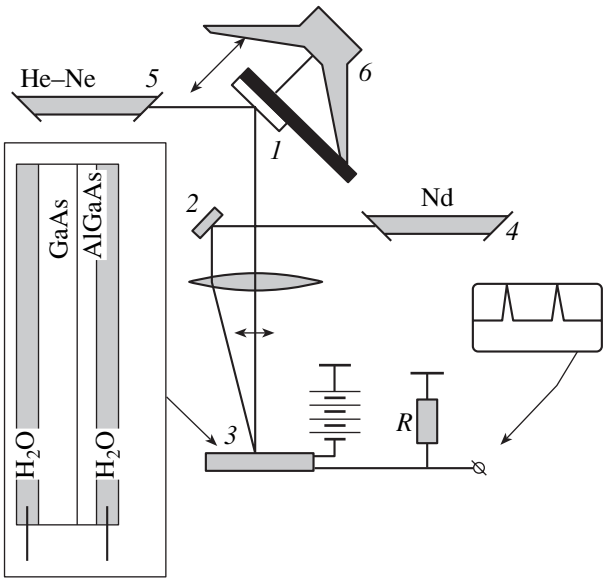

Fig. 2. Demonstration setup. The inset shows the scheme of vidicon *3*. He–Ne laser *5* is the source of the reading beam. Scanning mirror *1* is mounted on a loudspeaker *6*. A light spot of the neodymium laser *4* serves as the image. The spot can be placed on the scanning line of the reading beam with the aid of mirror *2*.

This simple experiment only illustrates the general principles for the operation of an optical vidicon. Below, we demonstrate that the proposed scenario of the generation of current in a system of two layers is inaccurate and qualitative. If the layers are relatively thin, we cannot represent them as a composite resistor, since the motion of charges in the layers is rather complex. On the other hand, we can expect that the spatial resolution of the optical vidicon will increase with the decrease in the layer thickness.

Below, we describe experiments with thin layers and present their qualitative interpretation.

EXPERIMENTS WITH THIN LAYERS

For the further experiments, we employ the following structure. A $Ga_{0.7}Al_{0.3}As$ layer with a thickness of 1 μm (wideband-gap layer *1* in Fig. 1) is grown on a GaAs layer with the same thickness (narrowband-gap layer *2*) that is grown, in turn, using molecular beam epitaxy on an *n*-doped ($\sim 10^{18}$ cm^{-3}) GaAs substrate (conducting substrate *3*). The layers are directly grown on the *n*-GaAs substrate in the absence of a decoupling superlattice at a temperature of 600°C. We sputter a transparent conducting layer of tin oxide SnO (conducting electrode *0*) on top of the epitaxial layers. The first test experiments demonstrate that the illumination of such a structure induces an electromotive force (EMF), and that an additional external source connected to the circuit does not give rise to significant effects. For this reason, we do not use the external source in the further experiments and measure the photoelectromotive force (PEMF) at various illumination conditions. Experiments are carried out at room temperature. The structure is illuminated from the side of the transparent electrode. Below, we present the experimental results obtained. The qualitative interpretation is presented in the next section.

(A) Measurement of the PEMF Spectrum

The radiation of an incandescent lamp modulated at a frequency of about 30 Hz is spectrally filtered by a monochromator. This radiation is incident on the transparent electrode of the structure connected to a 500-kΩ resistor. The PEMF signal from this resistor is recorded as a function of the incident wavelength (Fig. 3a). Then, we additionally illuminate the structure using a cw He–Ne laser, whose intensity is attenuated to about 100 μW/cm^2, and record the PEMF spectrum (the variation in PEMF related to the modulated nonmonochromatic light) (Fig. 3b). It is seen that in the absence of He–Ne laser illumination, PEMF sharply decreases and changes sign at wavelengths greater than 700 nm (corresponding to $Ga_{0.7}Al_{0.3}As$ band gap) and virtually vanishes at wavelengths greater than 870 nm (GaAs band gap at room temperature). In the presence of the He–Ne laser illumination, the PEMF signal increases in the range 700–870 nm. At wavelengths less than 700 nm, the signs of the PEMFs at the transparent electrode and substrate are negative and positive, respectively. Note that the sign of PEMF at the substrate changes in the interval 700–870 nm.

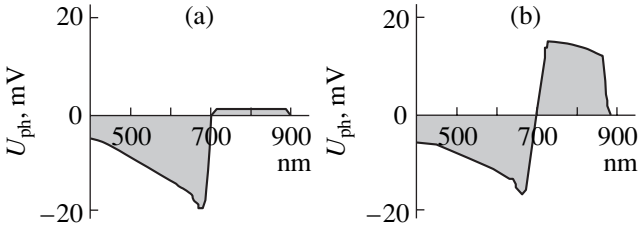

Fig. 3. Spectral curves of PEMF U_{ph} (a) in the absence and (b) in the presence of the He–Ne laser illumination.

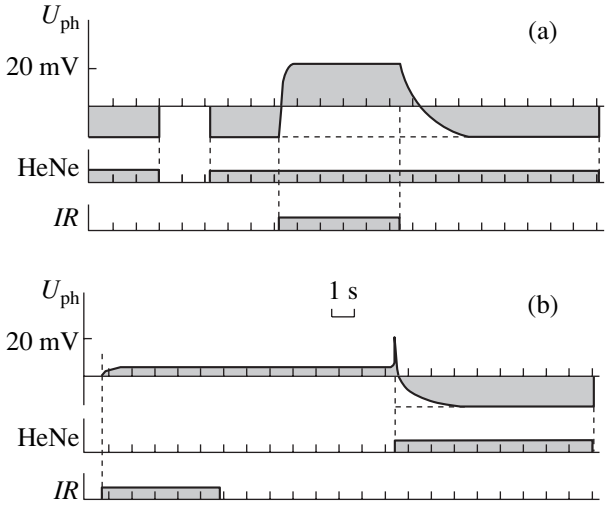

Fig. 4. PEMF kinetics in the presence of IR and He–Ne laser illumination: U_{ph} is PEMF, HeNe is the He–Ne laser illumination, IR is the IR illumination.

(B) PEMF Measurements in the Presence of IR and He–Ne Laser Radiation

In the first experiment, we preliminarily illuminate the structure using a He–Ne laser (the power is about 50 μW at a spot area of about 0.5 cm^2) and detect a negative PEMF at the transparent electrode and a positive PEMF at the substrate. Then, we add IR illumination created by an incandescent lamp with a filter transparent at wavelengths greater than 900 nm. PEMF changes sign, so that the positive sign corresponds to the transparent electrode. After switching off the IR illumination, PEMF slowly (in 1–2 s) returns to the initial level corresponding to the He–Ne laser illumination (Fig. 4a). The recovery time increases with the decrease in the He–Ne laser intensity.

In the second experiment, we switch on the IR illumination for a time of about 5 s in the absence of He–Ne laser radiation. The corresponding photoresponse is relatively low (Fig. 4b). Then, we switch off the IR illumination, switch on the He–Ne laser with a delay of 3–5 s, and observe the time dynamics of PEMF. PEMF is qualitatively the same as in the previous experiment: a positive voltage at the transparent electrode decreases, the PEMF passes zero and returns to the level corresponding to the He–Ne laser illumination (Fig. 4b). Thus, the IR illumination generates a long-lived electric field inside the structure that is destroyed by the radiation of He–Ne laser. The sign of this field is opposite to the sign of the field related to the PEMF induced by the radiation of He–Ne laser.

(C) Experiments on Image Scanning and Storage

The first experiment from section (B) shows that one can employ the structure under study for image scanning using the aforementioned scheme. It follows from the PEMF spectra (Fig. 3) that in the wavelength interval 700–870 nm, the He–Ne laser illumination makes it possible to reveal the corresponding PEMF. In the experiment on image scanning, we use the scheme shown in Fig. 2 without the power supply and the neodymium laser. The incandescent lamp filament is imaged in the plane of the structure by a lens. When the beam of He–Ne laser crosses the filament image, a PEMF pulse is generated at the load resistor owing to the joint action of the image and the reading beam of He–Ne laser.

The second experiment points to the possibility of image storage. We record an image in the following way. In the absence of the radiation of He–Ne laser, we project the filament image through the same IR filter as in the second experiment. Then, we switch off the lamp and store the structure in darkness during a certain time. After that, we read the image using the radiation of He–Ne laser. At the moments when the beam passes the place where the filament was imaged, we observe PEMF pulses at the load resistor. The pulse duration is 1–2 s (the higher the intensity of the reading He–Ne laser, the shorter the pulse). These experiments show that if the structure is not exposed to light after recording and prior to reading, an image can be stored for at least 1–2 h.

QUALITATIVE INTERPRETATION

(A) Interpretation of the Experimental Spectra of PEMF

We start from interpreting PEMF in the long-wavelength (700–900 nm) range (Fig. 3). In our opinion, the reason for PEMF in this spectral range is the Dember effect [1]. The essence of the effect is as follows. Assume that the energy of a photon incident on the surface of a semiconductor is greater than the band gap, and the absorption length L of this light is much less than the thickness of the semiconductor. Thus, light absorbed in a layer with a thickness of about L generates a large number of electron–hole pairs. Electrons and holes diffuse into the depth of the semiconductor. If the diffusion coefficients (or mobilities) of electrons and holes are different, the particles diffuse at different rates, and the resulting charge separation gives rise to an electric field and the corresponding EMF. The appearance of such EMF is known as the Dember

effect. The greater the difference between the diffusion coefficients of electrons and holes, the greater the Dember EMF. This EMF vanishes when the diffusion coefficients are equal.

In the structure under study, the $Ga_{0.7}Al_{0.3}As$ layer becomes transparent at wavelengths greater than 700 nm. Electron–hole pairs are created and the Dember EMF is generated only in the GaAs layer. It is known that the electron mobility in GaAs is greater than the hole mobility. Therefore, electrons diffuse to the depth faster than holes, and the GaAs layer appears to be positively charged at the interface with the $Ga_{0.7}Al_{0.3}As$ layer, which is in agreement with the experimental results (Fig. 3a). At wavelengths greater than 870 nm (GaAs band gap at room temperature), electron–hole pairs are not created in the layers under consideration and the Dember EMF is absent.

A relatively low signal at wavelengths greater than 700 nm (Fig. 3a) can be interpreted in the following way. The necessary conditions for the current in the external circuit (measured current) are the existence of the internal fields in the structure and the presence of carriers in all layers of the structure. At wavelengths shorter than 700 nm ($Ga_{0.7}Al_{0.3}As$ band gap), the carriers are photoexcited electron–hole pairs in the $Ga_{0.7}Al_{0.3}As$ and GaAs layers. At wavelengths greater than 700 nm, electron–hole pairs are not created in the $Ga_{0.7}Al_{0.3}As$ layer. Electrons and holes from the GaAs layer cannot penetrate inside the $Ga_{0.7}Al_{0.3}As$ layer owing to a barrier at the interface of the layers that depends on the difference of the $Ga_{0.7}Al_{0.3}As$ and GaAs band gaps. Thus, the $Ga_{0.7}Al_{0.3}As$ layer becomes insulating, and the signal current sharply decreases. The illumination with the cw short-wavelength radiation of He–Ne laser leads to the recovery of the $Ga_{0.7}Al_{0.3}As$ layer conductance and the corresponding increase in the signal (Fig. 3b).

It is still unclear what the mechanism is for the PEMF generation at wavelengths shorter than 700 nm. In this spectral range, the $Ga_{0.7}Al_{0.3}As$ layer is nontransparent, and the incident light is predominantly absorbed in this layer. Therefore, we can assume that PEMF is related to the internal fields generated in the $Ga_{0.7}Al_{0.3}As$ layer or at the interface with the GaAs layer. The Dember effect can hardly be the reason for the PEMF in this spectral range, since to interpret the PEMF sign change, we must assume that the electron mobility in the $Ga_{0.7}Al_{0.3}As$ layer is less than the hole mobility, which is almost improbable. We can assume that in this spectral range, PEMF is related to a possible internal field of the space charge at the $Ga_{0.7}Al_{0.3}As$–GaAs heteroboundary emerging owing to an uncontrolled doping of layers (this field exists in the absence of light). The sign of the corresponding potential barrier (Fig. 5) can be such that the heteroboundary works as a photodiode generating EMF, whose minus is applied from the side of the transparent electrode in accordance with the experimental results. At wavelengths greater than 700 nm, this EMF is suppressed by the Dember effect in the GaAs layer that increases in this spectral range, since the $Ga_{0.7}Al_{0.3}As$ layer becomes transparent and the intensity of light in the GaAs layer increases.

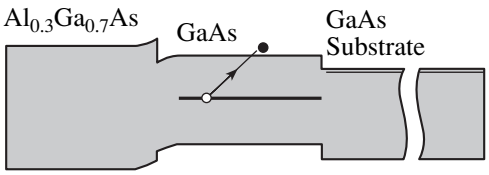

Fig. 5. Qualitative scheme of bands in the structure showing the barrier at the interface between the epitaxial GaAs layer and the doped GaAs substrate resulting from the diffusion of electrons from the *n*-doped substrate to the epitaxial layer; filled deep levels in the GaAs layer; and the motion of photoexcited carriers.

(B) Interpretation of the Experimental Results on PEMF Induced by IR and He–Ne Laser Illumination

In the presence of IR illumination with a photon energy less than the GaAs band gap, PEMF can be related to the excitation of impurities whose levels are lower than the bottom of the GaAs conduction band. The PEMF sign is indicative of the fact that these levels are filled with electrons. The lifetime of carriers at these levels is relatively long, which means that the levels are relatively deep. Consider a scenario when the impurity with such levels is contained in the GaAs layer (Fig. 5). The results of the previous experiment show that a negative voltage appears at the transparent electrode in the presence of the He–Ne laser radiation. The radiation of He–Ne laser weakly affects the GaAs layer owing to the absorption in the $Ga_{0.7}Al_{0.3}As$ layer and the intrinsic absorption of the GaAs layer, where the depth corresponding to an *e*-fold decrease in the intensity is about 0.25 μm. Therefore, we can assume that the effect of the He–Ne laser radiation on the impurity in the GaAs layer is strongly suppressed. On the contrary, IR radiation easily penetrates inside this layer and excites the deep impurity in the GaAs layer. The excitation of this impurity leads to the electron transitions from the deep levels in GaAs to the conduction band. Then, electrons predominantly move to the right-hand side to the depth of the structure, since the barrier related to the difference between the $Ga_{0.7}Al_{0.3}As$ and GaAs band gaps represents an obstacle for the motion to the left-hand side (Fig. 5). Thus, the GaAs layer acquires a positive charge, and the sign of the corresponding contribution of PEMF is opposite to the sign of the contribution of the $Ga_{0.7}Al_{0.3}As$ layer. At a sufficiently high intensity of IR radiation, the sign of the total PEMF at the structure can change, which is in agreement with the experimental data.

A gradual discharge of the deep impurity in the GaAs layer starts after switching off the IR illumina-

tion. The levels of this impurity depleted by the IR radiation are populated by electrons from the conduction band of the GaAs layer that appear owing to the He–Ne laser illumination (or illumination with any other light source with a relatively short wavelength). Therefore, the discharge time of the deep impurity in the GaAs layer depends on the He–Ne laser intensity (the discharge time increases with decreasing intensity), which is in agreement with the experimental results. Experiments on the image storage prove that in the absence of light, the discharge time of the centers can be as long as a few hours or even greater.

For the second experiment described in subsection (B) of the previous section, the scenario is as follows. At the first stage (IR illumination), the excitation of the deep impurity in the GaAs layer takes place, and the internal field appears. The absence of a significant current in the circuit is related to the absence of carriers (free electrons or holes). The radiation of He–Ne laser generates the carriers and gives rise to the current, whose direction depends on the sign of the total PEMF that is the same as in the previous case. The discharge dynamics of the deep levels is also the same.

What is the reason that we do not observe PEMF related to the presence of the deep levels in the GaAs layer in the spectral measurements? Recall that PEMF virtually vanishes in the presence of illumination at a wavelength greater than 870 nm (Fig. 3). It follows from the aforesaid that even in the case of the He–Ne laser illumination the discharge time of deep levels is a few seconds, whereas the modulation period of light is 1/30 s. Hence, the PEMF signal of the deep levels is strongly suppressed.

(C) Interpretation of the Experimental Results on Image Scanning and Storage

We can easily interpret the results obtained based on the above analysis. For example, in the storage experiment, the IR image of the lamp filament induces deep charged centers and the local electric field at the places where the image brightness is relatively high. If the structure is stored in darkness, the centers discharge very slowly owing to a large depth, a low probability of population by the conduction band electrons, and a low amount of electrons in the conduction band (the sample is stored in darkness). The reading beam of a He–Ne laser locally generates free carriers. If this beam is incident on an area with the internal electric field, we observe current in the circuit of the structure. As was mentioned, the corresponding increase in the discharge rate of the impurities makes the reading procedure destructive.

Finally note that we present a few hypotheses, which must be verified in additional experiments, rather than a comprehensive interpretation of the experimental results. The main purpose of this work is to describe experiments on image scanning and storage using the simple semiconductor structure.

REFERENCES

1. R. A. Smith, *Semiconductors* (Cambridge University Press, Cambridge, 1959; Mir, Moscow, 1982).

Translated by A. Chikishev

Technical Physics, Vol. 49, No. 6, 2004, pp. 733–738. Translated from Zhurnal Tekhnicheskoĭ Fiziki, Vol. 74, No. 6, 2004, pp. 70–76.

OPTICS, QUANTUM ELECTRONICS

Theoretical Simulation of the Dead Zone in Hologram Recording on Photopolymerizable Materials

R. S. Akopyan, A. V. Galstyan, and T. V. Galstyan

Yerevan State University, ul. A. Manukyana 1, Yerevan, 375049 Armenia

Center of Optics, Photonics, and Lasers, Lavalle University, Quebec, G1K 7P4 Canada

e-mail: rhakob@www.physdep.r.am

Received July 18, 2003

Abstract—Recording of a diffraction grating in a photopolymerizable material in the presence of a liquid crystal is studied theoretically in terms of the polymerization equation with allowance for diffusion. A model explaining the occurrence of recording delay time (dead zone) by the presence of oxygen or other impurities that prevent the formation of free radicals is put forward. The dead zone duration versus the writing radiation intensity is derived. © *2004 MAIK "Nauka/Interperiodica".*

INTRODUCTION

In recent years, photopolymers have been viewed as promising materials for optical data writing in the near-IR range [1–9]. Of special interest are polymers with dispersed liquid crystals (PDLCs) [7, 10, 11]. These materials, combining the mechanical properties of polymers and electrically controlled anisotropy of liquid crystals (LCs), offer a number of advantages over other recording media, such as photographic films, photoresistors, gelatin, etc. One basic advantage is the possibility of real-time monitoring of hologram recording. The anisotropic properties of LC molecules embedded in the polymeric matrix make it possible to control the parameters of diffraction gratings by application of electrostatic fields, which change the orientation of LC molecules [12, 13]. In addition, the characteristics of diffraction grating recorded in PDLCs are temperature-controllable [7], since the refractive index of LCs depends strongly on temperature. Note that there are many publications concerning another no less promising recording composition: photoconductor + LC [14–16].

However, there are a number of as yet unclear effects attendant on hologram recording, such as delay time of polymerization (dead zone), the dependence of the diffraction efficiency on the radiation intensity preceding polymerization, etc. [2, 6, 17].

In this work, we consider a polymer–monomer–LC–impurity (oxygen) four-component composition, where oxygen serves as a polymerization inhibitor. A cuvette with this composition is illuminated by the interference pattern of two coherent waves (beams). During polymerization, the third (probing) beam tests the diffraction efficiency of a holographic grating being recorded. In more illuminated areas, the monomer polymerizes and its concentration decreases. Simultaneously, the monomer diffuses from less to more illuminated areas. Thus, diffusion fluxes arise and the density (hence, the refractive index) of the final polymer is modulated. The solution of the diffusion equation of polymerization with two components, polymer and monomer, has been considered in [18, 19]. However, experiments show that, during polymerization, the spatial modulation of the density, as well as of the diffraction efficiency, starts increasing only after preliminary illumination of the monomer solution. The time interval within which the solution is illuminated by periodically modulated light but the diffraction efficiency does not grow (i.e., polymerization is absent) is called the dead zone. In this paper, we suggest a model for explaining the dead zone effect. In terms of this model, impurity molecules (oxygen in our case) inhibit polymerization early in the process. Polymerization starts when the impurity concentration drops below a certain critical value.

DIFFUSION MODEL

To prepare PDLC compositions, the LC must be readily soluble in the initial monomer. However, because of phase separation between the LC and polymerizing monomer, the latter displaces the former from areas of polymerization. Since the LC does not take part in the polymerization process and has a minor effect on the polymer's final distribution, its concentration does not enter into the diffusion equation. If the LC concentration is low, as in PDLCs, the monomer and LC may occupy the same volume, since they are miscible with each other. However, the polymer and LC cannot occupy the same volume at any concentration of the latter because of phase separation. Since the LC mobility is much higher than the mobility of the polymer, the polymer displaces the LC from the space of polymerization, with the polymer distribution remaining unchanged.

1063-7842/04/4906-0733$26.00

Consider the equation of polymerization due to periodically modulated light with allowance for diffusion. Let $U(\mathbf{r}, t)$ and $N(\mathbf{r}, t)$ be the monomer and polymer concentrations, respectively. It is assumed that the polymer concentration grows in proportion to the monomer concentration:

$$\partial N(\mathbf{r}, t)/\partial t = F(\mathbf{r}, t)U(\mathbf{r}, t), \quad (1)$$

where $F(\mathbf{r}, t)$ is the proportionality coefficient (the so-called local order of polymerization).

The space–time variation of the monomer concentration is described by the standard diffusion equation with an extra term on the right, which takes into account a polymerization-related decrease in the monomer concentration:

$$\frac{\partial U(\mathbf{r}, t)}{\partial t} + \nabla \cdot \mathbf{j}(\mathbf{r}, t) = -\frac{\partial N(\mathbf{r}, t)}{\partial t}. \quad (2)$$

Here,

$$\mathbf{j}(\mathbf{r}, t) = -D(\mathbf{r}, t)\nabla U(\mathbf{r}, t) \quad (3)$$

is the monomer diffusion flux density and $D(\mathbf{r}, t)$ is the local diffusion coefficient.

In recording conventional holograms, the cuvette is illuminated by the interference pattern of two plane coherent symmetrically incident waves (beams). The light distribution in this case is periodic and is described by the expression

$$I(x) = I_0(1 + V\cos(Kx)),$$

where I_0 is the mean radiation intensity, V is the depth of modulation, $K = 2\pi/\Lambda$, $\Lambda = (\lambda/2)\sin(\alpha/2)$ is the modulation period, and α is the angle between the beams. The x axis is directed along the line of intersection between the plane of beam incidence and the PDLC film plane.

The function $F(x, t)$ can be represented as a product of time- and space-dependent parts:

$$F(x, t) = F_0(t)(1 + V\cos(Kx)). \quad (4)$$

Note that oxygen inhibits the polymerization process. Activated dye molecules react with oxygen, and the polymerization reaction cannot proceed if the oxygen concentration is high. To elucidate the influence of oxygen, let us turn to the basic scheme of photopolymerization:

$$\begin{gathered} h\nu + \mathrm{PI} \longrightarrow \mathrm{PI}^* \quad (\mathrm{PI}\text{ stands for photoinitiatir}), \\ \mathrm{PI}^* + \mathrm{M} \longrightarrow \mathrm{A} + \mathrm{R}^* \quad (\mathrm{M}, \text{monomer}), \\ \mathrm{R}^* + \mathrm{M} \longrightarrow \mathrm{R}_1^* \\ (\mathrm{R}_i^*\ (i = 1, 2, \ldots),\ \text{radical with } i \text{ bonds}), \\ \mathrm{R}_1^* + \mathrm{M} \longrightarrow \mathrm{R}_2^* \quad \text{etc.} \end{gathered} \quad (5)$$

It is significant that the photoinitiator takes part in the reaction only once. Then, it turns into the product A. The oxygen present in the solution may, at the early stage, deactivate the photoinitiator (i.e., carry it from the excited triplet state into the ground state). In this case, the formation of radicals ceases and the chain reaction is terminated [17]:

$$\mathrm{PI}^* + \mathrm{O}_2 \longrightarrow \mathrm{A} + \mathrm{O}_2^* \longrightarrow \text{chain termination}.$$

If, however, the photoinitiator concentration is sufficiently high, radicals will form in a certain amount. These radicals will also combine with the oxygen, giving rise to the peroxidation reaction:

$$\mathrm{R}^\cdot + \mathrm{O}_2 \longrightarrow \mathrm{RO}_2^\cdot,$$

$$\mathrm{R}_i\mathrm{O}_2^\cdot + \mathrm{R}_j\mathrm{O}_2^\cdot \longrightarrow \text{chain termination},$$

$$\mathrm{R}_i\mathrm{O}_2^\cdot + \mathrm{R}_j^* \longrightarrow \text{chain termination}.$$

Each of the above polymerization or polymerization termination mechanisms has a certain probability. If the total probability of chain termination is higher than the probability of polymerization (i.e., the total polymerization reaction coefficient is smaller than unity), the polymerization reaction decays. If the probability of polymerization is higher than the chain termination probability, the total polymerization coefficient exceeds unity. This means that the rate of radical production by illumination is greater than the rate of radical loss due to the presence of oxygen or other impurities.

Thus, whether the photopolymerization reaction will work or not depends on the concentrations of the monomer, photoinitiator (dye), and oxygen. It follows from the aforesaid that the photoinitiator concentration must exceed a certain critical value. With this condition satisfied, the polymerization process is independent of the dye concentration. Therefore, we will assume that the dye concentration is sufficiently high. Then, the result of the reaction depends on the monomer-to-oxygen concentration ratio. The same to a great extent is true for oxygen. As long as the oxygen concentration exceeds a certain value, polymerization does not occur; that is, the order of polymerization $F_0(t) = 0$. As soon as the oxygen concentration drops below this value, the usual polymerization process begins. Let us find the function $F_0(t)$ in explicit form. It depends on a number of parameters, such as the initial oxygen and monomer concentrations, illumination intensity, etc. Since oxygen causes dye losses, the critical oxygen concentration above which the reaction stops is found from the condition that the concentration of oxygen molecules equals a certain monomer concentration. With this in mind, we write $F_0(t)$ as an explicit function of the oxygen concentration and initial monomer concentration:

$$F_0(t) = f_0\theta\left(\frac{U^0}{i_d} - \rho(t)\right), \quad (6)$$

where $\rho(t)$ is the oxygen concentration, θ is a step function, $f_0 = kI_0$, k is a constant, and U_0 is the initial monomer concentration. The quantity i_d indicates how many times the oxygen concentration must be below the monomer concentration, and the ratio U^0/i_d is the threshold oxygen concentration below which the process goes (this parameter will be called the dark threshold).

The subsequent description of the oxygen concentration evolution is based on a series of assumptions. Since the diffusion coefficient of gaseous oxygen is high, the oxygen concentration remains uniform upon illumination of periodically modulated light. The amount of oxygen decreases with illumination time, the decrease being directly proportional to the amount of oxygen. The oxygen–dye reaction yields an inert product, which subsequently does not influence the polymerization process. The differential equation for the oxygen concentration has the form

$$\frac{d\rho(t)}{dt} = -\beta\rho(t), \tag{7}$$

where β is the proportionality coefficient, which is a function of light intensity, type and activity of the dye, temperature, etc.

The solution to this equation has the form $\rho(t) = \rho_0\exp(-\beta t)$, where ρ_0 is the initial oxygen concentration. Eventually, the local order of polymerization will take the form

$$F_0(t) = f_0\theta\left(\frac{U^0}{i_d} - \rho_0\exp(-\beta t)\right). \tag{8}$$

The spatial dependence of the functions $U(\mathbf{r}, t)$ and $N(\mathbf{r}, t)$ is reduced to the 1D dependence of the x coordinate, since the light intensity varies only along the x axis. Substituting Eqs. (1), (3), and (8) into (2) yields the set of equations

$$\begin{aligned}\frac{\partial U(x,t)}{\partial t} &= \frac{\partial}{\partial x}\left[D(x,t)\frac{\partial U(x,t)}{\partial x}\right] \\ &- f_0\theta\left(\frac{U^0}{i_d} - \rho_0\exp(-\beta t)\right)(1 + V\cos(Kx))U(x,t),\end{aligned} \tag{9}$$

$$\begin{aligned}\frac{\partial N(x,t)}{\partial t} &= f_0\theta\left(\frac{U^0}{i_d} - \rho_0\exp(-\beta t)\right) \\ &\times (1 + V\cos(Kx))U(x,t).\end{aligned} \tag{10}$$

The initial condition for diffusion equation (9) can be written as $U(x, 0) = U^0$. The solution to Eq. (9) can be represented as a Fourier series. In view of the fact that polymerization is initiated by the sinusoidal light field and diffusion nonlinearities are neglected, the function $U(x, t)$ (and $N(x, t)$) is periodic and odd in t; consequently, the Fourier expansion of this function involves only cosine terms:

$$U(x, t) = \sum_{i=0}^{\infty} U_i(t)\cos(iKx). \tag{11}$$

Similarly, the Fourier expansion of the diffusion coefficient $D(x, t)$ is

$$D(x, t) = \sum_{i=0}^{\infty} D_i(t)\cos(iKx). \tag{12}$$

Hereafter, the Fourier coefficients $D_i(t)$ are called diffusion coefficients of order i. Substituting (8), (11), and (12) into (9) yields

$$\begin{aligned}&\sum_{i=0}^{\infty}\frac{dU_i(t)}{dt}\cos(iKx) \\ &= \left[\sum_{i,j=0}^{\infty} ijK^2 D_i(t)U_j(t)\sin(iKx)\sin(jKx)\right] \\ &+ \sum_{i,j=0}^{\infty}(iK)^2 D_j(t)\cos(jKx)U_i(t)\cos(iKx) \\ &- f_0\left(\frac{U^0}{i_d} - \rho_0\exp(-\beta t)\right)(1 + V\cos(Kx)) \\ &\times\sum_{i=0}^{\infty} U_i(t)\cos(iKx).\end{aligned} \tag{13}$$

Expanding Eq. (13) termwise and performing appropriate transformations [18], we arrive at a set of differential equations for the Fourier components of the monomer concentration. Fourth- and higher order harmonics are neglected, since the related correction is $\sim 10^6$ times smaller than the third- and lower order components. In Fourier expansion (12), it is reasonable to leave only two first terms. Such an approach, being invalid only if diffusion nonlinearities are included, means in effect that the diffusion coefficient varies exactly as does the polymerizing light intensity:

$$D(x, t) = D_0(t) + D_1(t)\cos(Kx). \tag{14}$$

The diffusion coefficient decreases with polymerization time, since the penetrability of the diffusant drops as polymerization proceeds. Then, according to [18], the Fourier components are given by

$$\begin{aligned}D_0(t) &= \frac{1}{2}[D_{\max}(t) + D_{\min}(t)] \\ &= D_{\text{in}}\exp(-\mu F_0 t)\cosh(\alpha F_0 V t),\end{aligned} \tag{15}$$

$$\begin{aligned}D_1(t) &= \frac{1}{2}[D_{\min}(t) - D_{\max}(t)] \\ &= -D_{\text{in}}\exp(-\mu F_0 t)\sinh(\alpha F_0 V t),\end{aligned} \tag{16}$$

where D_{in} is the initial diffusion coefficient and μ is the exponential decrease constant.

Substituting (15) and (16) into the equations for the Fourier components of the monomer concentration and introducing the variable $\xi = f_0 t$ according to [18], we get

$$\frac{dU_0(\xi)}{d\xi} = -H(\xi)U_0(\xi) - \frac{1}{2}H(\xi)VU_1(\xi), \quad (17)$$

$$\frac{dU_1(\xi)}{d\xi} = -H(\xi)VU_0(\xi) - [H(\xi) + R\exp(-\mu\xi)\cosh(\mu V\xi)]U_1(\xi) - \left[\frac{1}{2}H(\xi)V - R\exp(-\mu\xi)\sinh(\mu V\xi)\right]U_2(\xi), \quad (18)$$

$$\frac{dU_2(\xi)}{d\xi} = -\left[\frac{1}{2}H(\xi)V - R\exp(-\mu\xi)\sinh(\mu V\xi)\right]U_1(\xi) - [H(\xi) + 4R\exp(-\mu\xi)\cosh(\mu V\xi)]U_2(\xi) - \left[\frac{1}{2}H(\xi)V - 3R\exp(-\mu\xi)\sinh(\mu V\xi)\right]U_3(\xi), \quad (19)$$

where $R = (D_{in}K^2)/f_0$, $H(\xi) = \theta(U^0/i_d - \rho_0\exp(-(\beta\xi)/f_0))$.

At a time ξ, the polymer concentration is given by

$$N(x, \xi) = \int_0^\xi F(x, \xi')U(x, \xi')d\xi'. \quad (20)$$

Let us substitute (4), (8), and (11) into Eq. (20) and represent $N(x, \xi)$ as a sum of its harmonics. In terms of diffraction, we are interested in only two initial terms. First, higher harmonics in the expansion of $N(x, \xi)$ are small; second, the Bragg angles for gratings with periods $2K$, $3K$, etc., differ from the Bragg angle for a grating with a period K [20] and, additionally, higher order gratings drop out of monitoring. Therefore,

$$N(x, t) = N_0(t) + N_1(t)\cos(Kx). \quad (21)$$

For the Fourier components, we have

$$N_0(\xi) = \int_0^\xi \theta\left(\frac{U^0}{i_d} - \rho_0\exp\left(-\frac{\beta}{f_0}\xi'\right)\right) \times \left[U_0(\xi') + \frac{1}{2}VU_1(\xi')\right]d\xi', \quad (22)$$

$$N_1(\xi) = \int_0^\xi \theta\left(\frac{U^0}{i_d} - \rho_0\exp\left(-\frac{\beta}{f_0}\xi'\right)\right) \times \left[VU_0(\xi') + U_1(\xi') + \frac{1}{2}VU_2(\xi')\right]d\xi'. \quad (23)$$

Consider now the LC distribution. We have noted that the polymer and LC phases are separated (the polymer displaces the LC from an area of polymerization, since the latter has a higher mobility). Next, we mentioned that the polymer (liquid crystal) concentration in illuminated areas is higher (lower) than in the dark. Let $L(x, t)$ be the LC concentration and $c = L_0/N_0$ be the ratio between the LC and polymer mean concentrations. In a first approximation, we may assume that the modulating concentration of the LC is c times lower than the modulating polymer concentration ($c = L_1/N_1$), much as the LC mean concentration is c times lower than the polymer mean concentration. Hence, the LC concentration at a time ξ and at a point x can be written as

$$L(x, \xi) = I_0 - I_1\cos(Kx) = \frac{N_1}{c} - \frac{N_2}{c}\cos(Kx). \quad (24)$$

Knowing the polymer, monomer, and LC concentrations, one can find the refractive index distribution. According to the Lorentz–Lorenz formula, the refractive index of a medium depends on its density, molar weight, and molar refractive index:

$$\frac{n^2 - 1}{n^2 + 2} = \frac{\varphi}{M}n_{mol}, \quad (25)$$

where φ is the density, M is the molar weight, and n_{mol} is the molar refractive index.

According to [19], formula (25) yields

$$n_1 \sim U_1\frac{n_m^2 - 1}{n_m^2 + 2} + N_1\frac{n_p^2 - 1}{n_p^2 + 2} - L_1\frac{n_{LC}^2 - 1}{n_{LC}^2 + 2} = U_1\frac{n_m^2 - 1}{n_m^2 + 2} + N_1\left(\frac{n_p^2 - 1}{n_p^2 + 2} - c\frac{n_{LC}^2 - 1}{n_{LC}^2 + 2}\right), \quad (26)$$

where n_1 is the modulating refractive index, n_m is the refractive index of the monomer, n_p is the refractive index of the polymer, and n_{LC} is the refractive index of the liquid crystal. The latter parameter is obviously anisotropic and depends on the incident light polarization.

Let us find the orientation of LC molecules. We set diffusion fluxes along the x axis during polymerization. It is known that LC molecules are extremely sensitive to hydrodynamic flows, and most of them are aligned with the flow direction, producing an anisotropic LC lattice, with the crystal director being aligned with the x direction [21]. Thus, if the incident light polarization is normal to the plane of incidence (s polarization), the LC permittivity $\varepsilon_\perp$ will be independent of the angle of incidence. If the light is polarized in the plane of incidence (p polarization), the LC permittivity $\varepsilon_\parallel$ depends on the angle of incidence: $\varepsilon^{-1}\varepsilon_\perp\varepsilon_\parallel = \varepsilon_\parallel\sin^2\theta + \varepsilon_\perp\cos^2\theta$, where θ is the angle between the light propagation direction and normal to the surface.

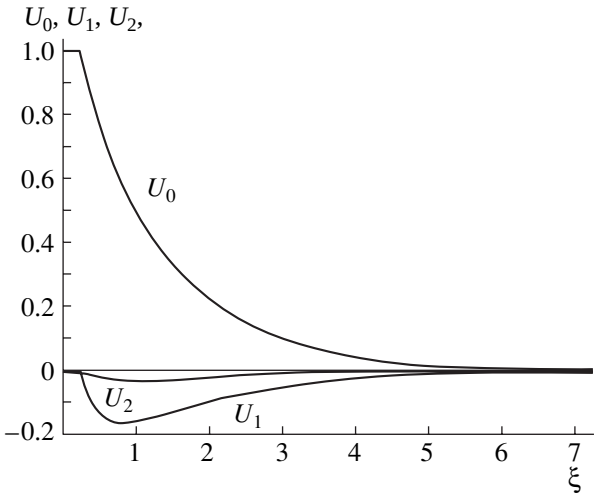

Fig. 1. Fourier components $U_0(\xi)$, $U_1(\xi)$, and $U_2(\xi)$ for $V = 1$, $\beta = 10$, $R = 5$, $\rho_0 = 1$, $i_d = 10$, and $U_0 = 100$.

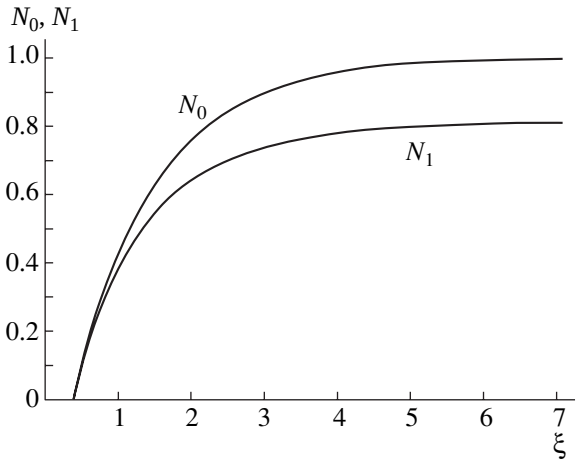

Fig. 2. Fourier components $N_0(\xi)$ and $N_1(\xi)$ of the polymer concentration for $V = 1$, $\beta = 10$, $R = 5$, $\rho_0 = 1$, $i_d = 10$, and $U_0 = 100$.

RESULTS AND DISCUSSION

Numerically solving Eqs. (17)–(19), (22), and (23) with the use of the Mathematica 4.0 computer program, we obtained the Fourier components of the monomer concentration $U(\mathbf{r}, t)$ and polymer concentration $N(\mathbf{r}, t)$. Figure 1 shows the curves for the Fourier components $U_0(\xi)$, $U_1(\xi)$, and $U_2(\xi)$ for $V = 1$, $\beta = 10$, $R = 5$, $\rho_0 = 1$, and $i_d = 10$ (it is assumed that the concentration of oxygen or other inhibitors must be one order of magnitude lower than the initial monomer concentration in order for the reaction to be initiated). Figure 2 shows the Fourier components for the polymer concentration. From formula (24), we find the LC concentration distribution, i.e., the Fourier components L_0 and L_1. Using formula (26), we find the modulating value of the refractive index for the PDLC composition. According to the Kogelnik theory of coupled waves [20], the diffraction efficiency of a holographic grating can be estimated by the formula

$$\eta = \sin^2\left(\frac{\pi\Delta n d}{\lambda\cos\theta}\right), \qquad (27)$$

where d is the grating thickness, λ is the light wavelength, Δn is the modulating value of the refractive index, and θ is the Bragg angle.

Montemezzani and Zgonik [22] generalized the theory of coupled waves for the anisotropic case. For incidence at the Bragg angle, the value of Δn is easy to calculate for specific polarization. In our case, all the parameters, except for Δn, are time-invariable; therefore, we can construct (accurate to a constant) the evolution of the diffraction efficiency during polymerization. The related curve constructed up to a constant normalized to unity is given in Fig. 3. It is seen that the diffraction efficiency starts growing after preliminary illumination of the monomer solution for a time.

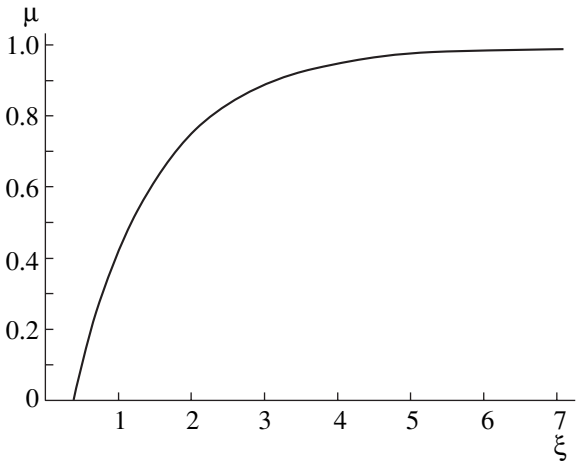

Fig. 3. Diffraction efficiency vs. ξ during polymerization up to a constant normalized to unity.

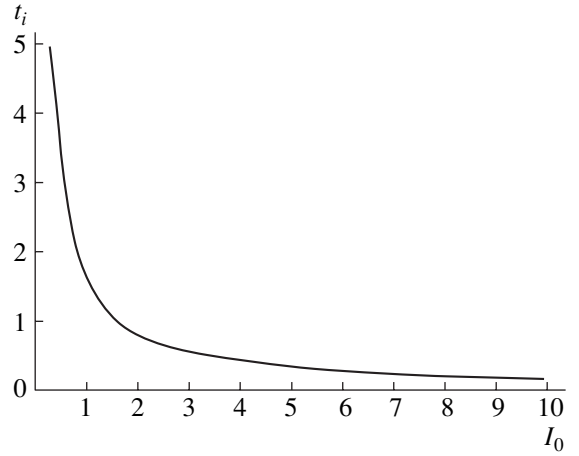

Fig. 4. Dead zone duration t_1 vs. mean intensity of the polymerizing light I_0 for $k' = 1$, $\rho_0 = 1$, $i_d = 10$, and $U_0 = 100$.

Consider the dependence of the dead zone duration (recording delay time) on the light intensity. The time t_i of onset of polymerization can be found from the expression

$$\frac{U^0}{i_d} - \rho_0 \exp(-\beta t_i) = 0. \quad (28)$$

If the concentration of a photoinitiator is sufficiently high, each photon is certain to activate one its molecule, which causes deactivation of one oxygen molecule. Since the light intensity is proportional to the photon density, the coefficient β is proportional to the mean radiation intensity: $\beta = k'I_0$, where k' is a constant factor. Since the diffusion coefficient of oxygen is high, it does not respond to light modulation. Solving Eq. (28) for t_i gives

$$t_i = -\frac{\ln(U^0/(i_d\rho_0))}{k'I_0}. \quad (29)$$

Figure 4 plots the dead zone duration versus the mean intensity of the polymerizing light. When the intensity is zero, the process obviously is not initiated; when the intensity is very high, the dead zone duration tends toward zero. Note in conclusion that the curves in Figs. 3 and 4 are in qualitative agreement with available experimental data (see, e.g., [2, 6, 17]).

CONCLUSIONS

We suggest a model that explains the dead zone effect. It is assumed that diffusion nonlinearities are absent and the polymerization coefficient is proportional to the intensity of the light incident on the polymer. The photopolymerization scheme is as follows: the dye absorbs a photon and is activated, this activity is transferred to the monomer, and the chain polymerization reaction starts. The dead zone arises when the medium contains oxygen, which combines with excited dye molecules, suppressing the activation of the monomer. After the oxygen concentration decreases, the dye activates the monomer, initiating the reaction. In terms of this model, we calculated the dead zone duration as a function of the writing radiation intensity. The results obtained with this model are in good agreement with experimental data [2, 6, 17].

ACKNOWLEDGMENTS

This work was partially supported by the CRDF (grant no. AR2-2302-UE-02).

REFERENCES

1. P. Pilot, Y. Boiko, and T. V. Galstian, Proc. SPIE **3635**, 143 (1999).
2. I. Banyasz, Opt. Commun. **181**, 215 (2000).
3. P. Pilot and T. V. Galstain, in *Proceedings of the International Conference on Applications of Photonic Technology ICAPT-2000, Quebec, 2000*; Proc. SPIE **4987**, 1302 (2000).
4. F. Bouguin and T. V. Galstian, Proc. SPIE **4342**, 492 (2001).
5. T. Galstian and A. Tork, U.S. Patent No. 6,398,981 (4 June 2002).
6. P. Nagtegaele and T. V. Galstian, Synth. Met. **127**, 85 (2002).
7. R. Caputo, A. V. Sukhov, C. Umeton, and R. F. Ushakov, Zh. Éksp. Teor. Fiz. **118**, 1474 (2000) [JETP **91**, 1190 (2000)].
8. Yu. N. Denisyuk, N. M. Ganzhermi, and D. F. Chernykh, Pis'ma Zh. Tekh. Fiz. **26** (9), 25 (2000) [Tech. Phys. Lett. **26**, 369 (2000)].
9. N. M. Ganzhermi, Yu. N. Denisyuk, S. P. Konop, and I. A. Maurer, Pis'ma Zh. Tekh. Fiz. **26** (16), 22 (2000) [Tech. Phys. Lett. **26**, 707 (2000)].
10. R. L. Sutherland, V. P. Tondiglia, L. V. Natarajan, *et al.*, Opt. Lett. **20**, 1325 (1995).
11. D. Duca, A. V. Sukhov, and C. Umeton, Liq. Cryst. **26**, 931 (1999).
12. R. L. Sutherland, V. P. Tondiglia, L. V. Natarajan, *et al.*, Appl. Phys. Lett. **64**, 1074 (1994).
13. L. V. Natarajan, R. L. Sutherland, V. P. Tondiglia, *et al.*, J. Nonlinear Opt. Phys. Mater. **5** (5), 89 (1996).
14. N. L. Ivanova, A. N. Chaĭka, and A. P. Onokhov, Pis'ma Zh. Tekh. Fiz. **26** (3), 1 (2000) [Tech. Phys. Lett. **26**, 91 (2000)].
15. A. N. Chaĭka and F. L. Vladimirov, Pis'ma Zh. Tekh. Fiz. **26** (4), 9 (2000) [Tech. Phys. Lett. **26**, 139 (2000)].
16. N. L. Ivanova, A. P. Onokhov, and A. N. Chaĭka, Pis'ma Zh. Tekh. Fiz. **27** (15), 57 (2001) [Tech. Phys. Lett. **27**, 647 (2001)].
17. T. V. Galstian, S. Harbour, and R. S. Akopyan, Opt. Mater. (in press).
18. G. Zhao and P. Moroulis, J. Mod. Opt. **41**, 1929 (1994).
19. I. Aubrecht, M. Miler, and I. Koudela, J. Mod. Opt. **45**, 1465 (1998).
20. H. Kogelnik, Bell Syst. Tech. J. **48**, 2909 (1969).
21. T. V. Galstian, S. Harbour, R. S. Akopyan, *et al.*, J. Opt. Soc. Am. A (in press).
22. G. Montemezzani and M. Zgonik, Phys. Rev. E **55**, 1035 (1997).

Translated by V. Isaakyan

Technical Physics, Vol. 49, No. 6, 2004, pp. 739–744. Translated from Zhurnal Tekhnicheskoĭ Fiziki, Vol. 74, No. 6, 2004, pp. 77–82.

OPTICS, QUANTUM ELECTRONICS

Optical Nonlinearity of Wide-Bandgap Semiconductor and Insulator Nanoparticles in the Visible and Near-Infrared Regions of the Spectrum

O. P. Mikheeva and A. I. Sidorov

Research Institute of Laser Physics, St. Petersburg, 199034 Russia

Received August 4, 2003

Abstract—Experimental results on the interaction of nanosecond optical pulses at the wavelength of 0.53, 0.65, and 1.06 μm with nanoparticles of crystalline materials with a bandgap of 3 to 7 eV are reported. It is shown that the threshold for the nanoparticles to exhibit a nonlinear response can be as low as 0.05 to 0.5 nJ/cm^2 and that the response can manifest itself as limitation of the radiation or as blooming of the medium. A theoretical model is proposed, which associates these effects with single-photon generation of charge carriers from deep impurity levels produced by defects located near the nanoparticle's surface. © *2004 MAIK "Nauka/Interperiodica".*

INTRODUCTION

Heterogeneous media with nanoparticles demonstrating nonlinear optical properties are of interest for designing optical switches and optical controllers in information technologies. Unlike homogeneous media, which exhibit nonlinear optical response mostly due to optically induced changes in the refractive index and attenuation constant, in heterogeneous media, the nonlinear response can also occur due to an induced change in the optical scattering properties. An advantage of heterogeneous media is the possibility of varying their linear and nonlinear optical properties over a wide range by selecting their components and concentration, size, and shape of the nanoparticles. Additional possibilities for controlling the media characteristics appear with the use of structured nanoparticles, in particular, nanoparticles that have a core and shell (shells) with different properties. For example, nanoparticles with a dielectric core and metal shell under plasma resonance conditions locally intensify the field [1, 2], which increases the effective nonlinearity of the medium and lowers the energy threshold above which nonlinear response is observed. In this situation, modulation of a medium's optical properties may occur due to variation in absorption and scattering of light as a result of a shift in frequency of the plasma resonance and a change in its amplitude [3–5]. The low-threshold nonlinear optical response also occurs in media with nanoparticles of wide-bandgap semiconductors, whose shells have deep dopant states [6]. For example, the response of TiO_2 and BN particles to a nanosecond pulse of visible or near-infrared radiation appears at the incident energy density of $Q_0 < 1$ nJ/cm^2 and exhibits itself in limitation of radiation associated with increase in the light scatter [6].

The goal of this work is to experimentally study low-threshold nonlinear optical effects observed in nanoparticles of wide-bandgap semiconductors and insulators (TiO_2, Al_2O_3, MgO, BaO, MgF_2, CaF_2, BaF_2, $CaCO_3$, and BN) and to develop theoretical models that account for these effects.

LINEAR AND NONLINEAR OPTICAL PROPERTIES OF NANOPARTICLES: EXPERIMENTAL RESULTS

In the experiments, we studied crystalline nanoparticles of oxides (TiO_2 (rutile), Al_2O_3, MgO, and BaO) and fluorides (MgF_2, CaF_2, and BaF_2) of metals and also of calcium carbonate ($CaCO_3$) and hexagonal boron nitride (BN). The bandgap E_g of all these materials is wider than 3 eV. Nanoparticles 50–100 nm in size were extracted from commercial or specially prepared powder by elutriation [7]. To do this, we prepared a suspension of the powder in acetone and allowed it to settle for a long time, after which we separated the upper almost transparent layer containing the smallest particles. Subsequently, the acetone was removed through evaporation. Figure 1 shows nanoparticles of TiO_2, separated by this technology, obtained with the help of a transmission electron-beam microscope. The shape of most of the particles resembles a weakly prolate ellipsoid. Particles of other materials had a similar shape except for BN, whose particles had the form of planar flakes with a thickness-to-width ratio of approximately 1:10. As the transparent medium for nanoparticles, we used VM-4 vacuum oil (water white viscous liquid with refractive index of ~1.4). The volume concentration of nanoparticles in the medium varied within 0.05 to 0.5%. The width d of the samples was 6 to 10 mm.

1063-7842/04/4906-0739$26.00 © 2004 MAIK "Nauka/Interperiodica"

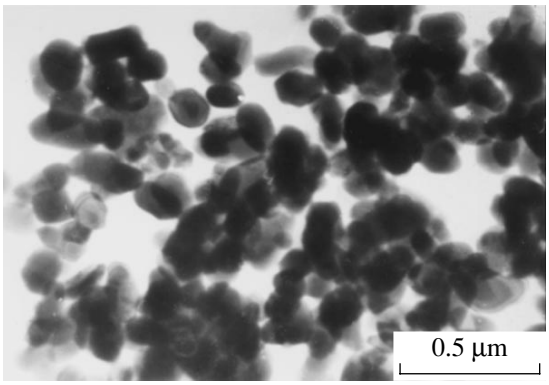

Fig. 1. Image of TiO_2 nanoparticles obtained by an electron-beam microscope.

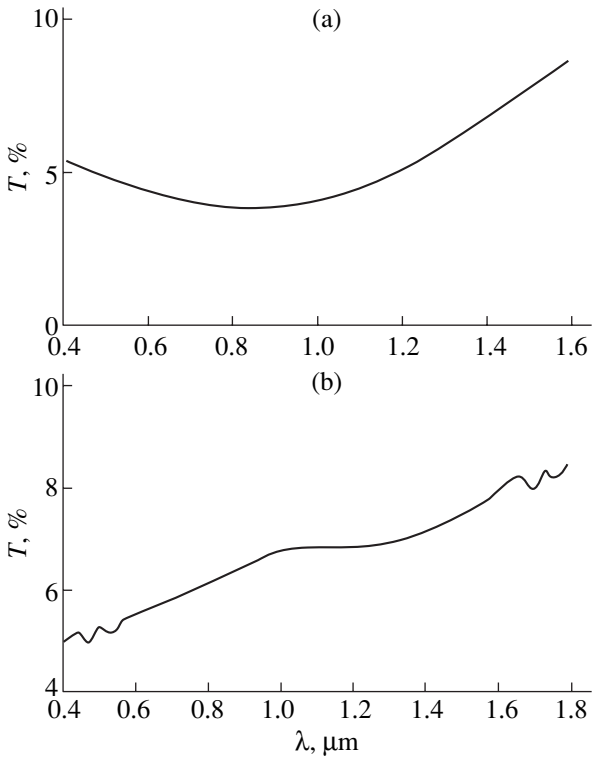

Fig. 2. Transmission spectra of (a) TiO_2 and (b) CaF_2 nanoparticles deposited onto a quartz glass substrate.

As a source of radiation, the experiments used a YAG : Nd laser (λ = 0.53 and 1.06 μm and τ = 10 ns) and an L8331 light-emitting diode (λ = 0.65 μm and τ = 150 ns). In both cases, the light spot on the samples was 6 mm in diameter.

Figure 2 shows transmission spectra of TiO_2 and CaF_2 nanoparticles deposited onto quartz glass substrates. The spectra exhibit wide absorption bands: in the spectrum interval of 0.4 to 1.6 μm for TiO_2 nanoparticles and from 1 to 1.6 μm for CaF_2 nanoparticles. Spectra of pure bulk single crystals of these materials do not have these features. Nanoparticles of other materials studied also exhibit either wide absorption bands or a number of relatively narrow bands in the visible or near-infrared region. For example, BN nanoparticles feature two absorption bands with maxima at λ = 0.75 and 0.9 μm, while a wide absorption band of BaF_2 nanoparticles occupies the 0.5- to 0.95-μm spectrum interval.

Figure 3 shows power density of the transmitted radiation (E_{out}) versus incident power density (E_{in}) obtained experimentally for media with (a) TiO_2 and (b) BaF_2 nanoparticles at λ = 0.53 and 1.06 μm and τ = 10 ns. The samples were 6 mm thick. As is seen from the figure, at low intensities, the transmitted power shows a linear behavior. In the linear region, the transmission coefficient is 50 to 55% at λ = 0.53 μm and 80 to 85% at λ = 1.06 μm. Beginning at a certain threshold power density (E_{thr}), an optical nonlinearity is observed, which manifests itself as limitation of the radiation. For TiO_2, the limitation threshold is 0.15 nJ/cm^2 at λ = 0.53 μm and 0.1 nJ/cm^2 at λ = 1.06 μm. As the incident power increases further, the $E_{out}(E_{in})$ functions become linear again. The nonlinear region is strongly pronounced at λ = 1.06 μm. At 0.53 μm, deviation of $E_{out}(E_{in})$ from a linear function is small. For BaF_2 nanoparticles at λ = 0.53 μm, E_{thr} = 0.1 nJ/cm^2. At λ = 1.16 μm, no optical nonlinearity is observed. The dynamic range of the limited radiation $D = E_{max}/E_{thr}$ (E_{max} is the maximum incident power at which the limitation is still observed) varies for TiO_2 and BaF_2 nanoparticles from 50 to 300.

Similar effects are observed in media with the nanoparticles of the other materials studied (see table). Note that nanoparticles that have no absorption band in the spectrum region above 1 μm do not feature the low-threshold nonlinearity. It should also be noted that refractive indices of all the nanoparticles are higher than the refractive index of the transparent medium, and the bandgap widths of the materials of nanoparticles exceed (in a number of cases, by more than a factor of 2) the photon energy of the incident radiation. The nonlinearity thresholds vary from 0.1 to 0.5 nJ/cm^2, while the limitation dynamic range lies in an interval between 20 and 300.

To increase the dynamic range, one can use multistage or multipass schemes. In an experiment with a two-stage limiter and CaF_2 nanoparticles, the limitation threshold of 0.05 nJ/cm^2 and dynamic range of 10^3 were obtained at a wavelength of 1.06 μm. Each stage had the form of a quartz glass cell with a 10-mm gap thick medium containing the nanoparticles. The distance between the cells was 10 cm. The linear transmission coefficient of each cell at 1.06 μm was 80%.

To check for the effect of the refractive index of nanoparticles on their nonlinear optical properties, we carried out experiments at 0.65 μm (τ = 150 ns) and a pulse repetition rate of 100 Hz. The measurements were averaged over a sequence of 20 pulses. Studied were

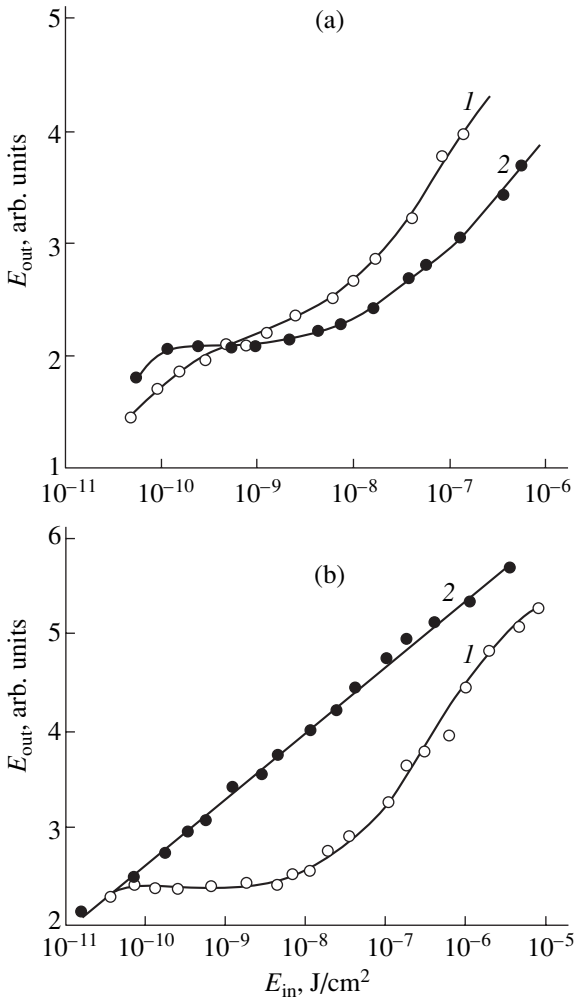

Fig. 3. Power density transmitted through a sample versus incident power density for (a) TiO_2 and (b) BaF_2 nanoparticles at d = 6 mm, τ = 10 ns, and λ = (*1*) 0.53 and (*2*) 1.06 μm.

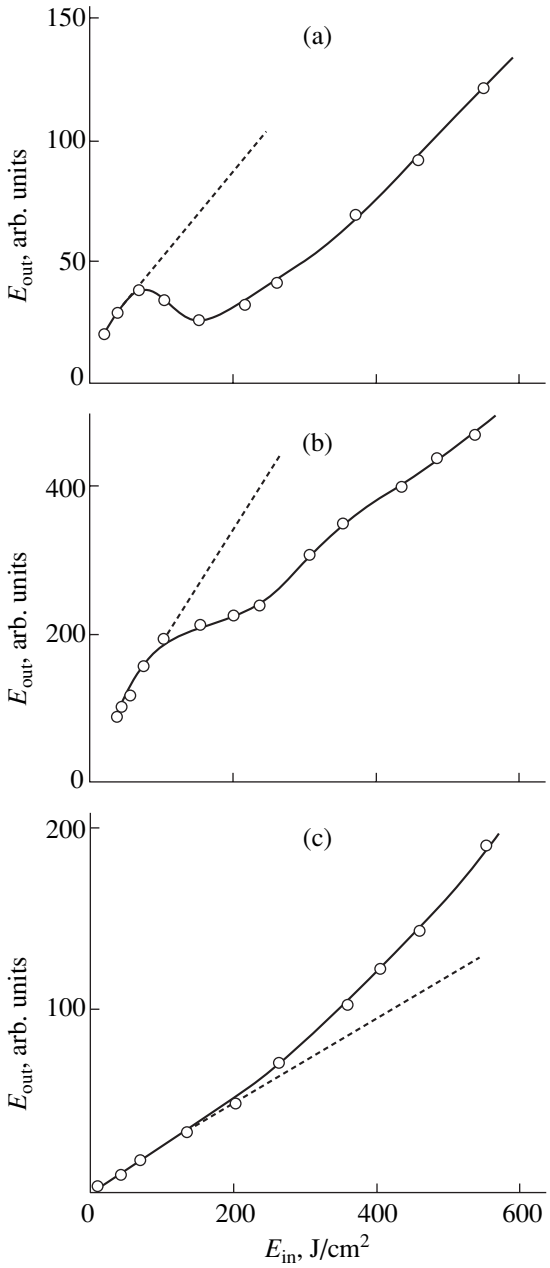

Fig. 4. Power density transmitted through a sample versus incident power at d = 10 mm, τ = 150 ns, and λ = 0.65 μm: (a) TiO_2, (b) CaF_2, and (c) MgF_2.

nanoparticles of TiO_2 (n = 2.55), CaF_2 (n = 1.42), and MgF_2 (n = 1.38) with a 0.1% volume concentration in the medium. Nanoparticles of MgF_2 ($E_g \approx 7$ eV) have an absorption band in the wavelength interval from 0.5 to 1 μm. The samples were 10 mm thick. The experiments have shown that the optical responses of nanoparticles with different refractive indices exposed to radiation differ significantly (Fig. 4). The effect of limitation is only observed in nanoparticles of TiO_2 and CaF_2, whose refractive indices are higher than that of the transparent medium. For TiO_2 nanoparticles, which have a higher refractive index, the limitation effect is more pronounced than for CaF_2 nanoparticles. For MgF_2 nanoparticles, whose refractive index is lower than that of the transparent medium, the optical response manifests itself as an increase in transmittivity with increasing intensity (blooming of the medium). Thresholds of the optical response for the nanoparticles studied ranged from 0.1 to 0.25 nJ/cm^2.

Test experiments aimed to find out the role of the bandgap width of a nanoparticle material in creating the low-threshold nonlinearity used nanoparticles of semiconductor materials with $E_g < 3$ eV: ZnSe (E_g = 2.4 eV), V_2O_5 (E_g = 1.5 eV), and α-Fe_2O_3 (E_g = 1.5 eV). The wavelength of the incident radiation was 0.53 μm. The experiments have shown that media with nanoparticles of these materials do not exhibit the nonlinear response when $E_m < 1$ μJ/cm^2.

Thus, media with nanoparticles of wide-bandgap semiconductors and insulators, being exposed to a

Limitation of visible and near-infrared radiation by nanoparticles of wide-bandgap semiconductors and insulators

Nanoparticle material	E_g, eV	0.53 μm			1.06 μm		
		n	E_{thr}, nJ/cm^2	D	n	E_{thr}, nJ/cm^2	D
TiO_2	3.05	2.65	0.15	50	2.48	0.1	100
Al_2O_3	3.6	1.77	0.25	50	1.75	–	–
MgO	7.3	~1.8	0.1	120	1.72	–	–
BaO	~4.3	2.0	0.5	20	1.9	–	–
BaF_2	~6	1.47	0.1	300	1.47	–	–
CaF_2	~6	1.44	0.1	100	1.42	0.5	30
$CaCO_3$	~5	1.55	0.2	50	1.53	0.5	20
BN	4.8	~2	0.1	100	~2	–	–

nanosecond pulse of visible or near-infrared radiation, show a low-threshold nonlinear optical response with a threshold no higher than 0.5 nJ/cm^2. The nonlinear optical response occurs due to absorption bands, which are present in nanoparticle spectra and are absent in spectra of pure single crystals. Depending on the nanoparticle refractive index, the nonlinear response may manifest itself as a limitation of the radiation or in blooming of the medium.

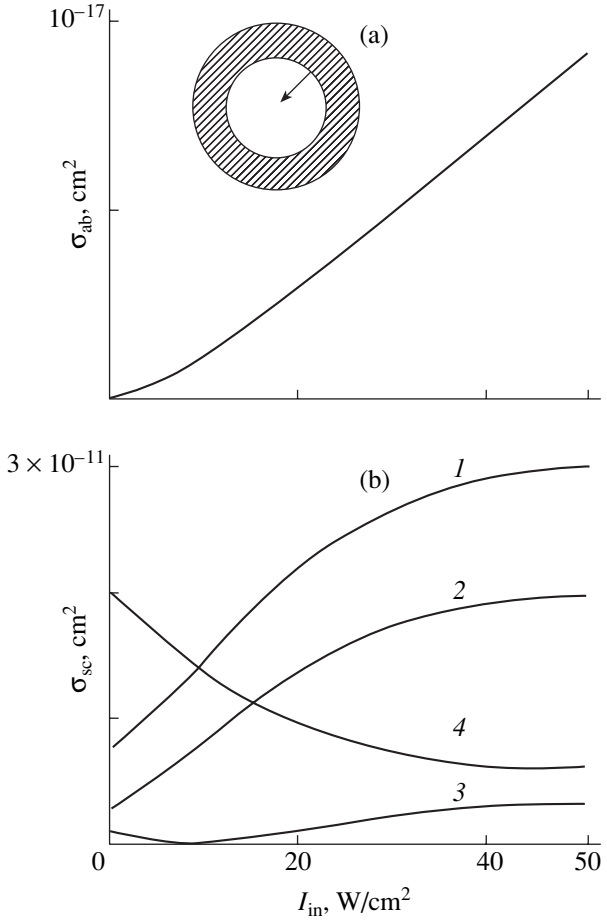

Fig. 5. (a) Absorption and (b) scattering cross sections of a spherical nanoparticle with a dynamic absorbing shell versus intensity of the incident radiation calculated at $n_c = n_s =$ (*1*) 2, (*2*) 1.8, (*3*) 1.5, and (*4*) 1.3; $n_h = 1.5$; and $\tau = 10$ ns. The inset models the nanoparticle.

A MODEL OF LIMITATION OF RADIATION BY NANOPARTICLES OF WIDE-BANDGAP SEMICONDUCTORS AND INSULATORS

The fact that absorption bands appear in a nanoparticle spectrum in the visible and near-infrared regions indicates that deep levels are present in the bandgap of the nanoparticle material, these levels being caused by defects in the crystal structure, because the nanoparticles were produced from pure single crystal materials. We can naturally suppose that the defects concentrate on the surface of nanoparticles. This is associated with methods used to produce the nanoparticles and with properties of the surface, which itself is a single-crystal defect capable of accumulating the defects that diffuse from the bulk of the crystal and which also has its own specific defects that create surface (Tamm's) levels. The wide absorption band observed in the spectra of some nanoparticles indicates that concentration of defects on the surface is very high and they can create an impurity band inside the bandgap. Thus, the nanoparticle structure can be represented as a core consisting of single-crystal material, which features a very low absorption due the large width of the bandgap, and a shell, which contains deep impurity levels. If the photon energy is higher than the energy gap ΔE between the bottom of the conduction band and the impurity level, the photon produces nonequilibrium electrons. The change in concentration of the nonequilibrium carriers adds nonlinear components to the refractive index and absorption coefficient of the nanoparticle's shell. The increase in the carrier concentration in the shell produces a concentration gradient between the shell and core, which initiates carrier diffusion deep into the core. This indicates an increase in the thickness of the layer in which the nonequilibrium charge carriers exist and, therefore, the presence of the nonlinear addition to the refractive index and absorption coefficient. Thus, the model of the limitation process can use nanoparticles of the following structure: a nonabsorbing core and dynamic shell, whose thickness, refractive index, and absorption coefficient depend on the radiation intensity (see the inset to Fig. 5a).

Our numerical simulations used the following assumptions.

The nanoparticles have a spherical shape and consist of a nonabsorbing core and thin defective shell, in which deep impurity levels with $\Delta E < h\nu$ are concentrated. The concentration of defects in the shell is higher than 10^{16} cm^{-3}; i.e., there is no saturation of the

impurity absorption observed at intensities of the incident radiation considered.

Photogeneration of nonequilibrium charge carriers occurs only in the defective shell of a nanoparticle.

Because the shell is thin, we disregard carrier diffusion in the shell itself. Concentration of the nonequilibrium carriers in the dynamic shell and its thickness scale increase linearly with the radiation intensity due to carrier diffusion into the core.

The nonlinear addition to the refractive index is caused by a change in the carrier concentration; the addition to the absorption coefficient, by absorption of the radiation on nonequilibrium carriers.

The absorption and scattering cross sections of a spherical nanoparticle with a shell can be represented as [8]

$$\sigma_a = \frac{8\pi^2\sqrt{\varepsilon_h}r_s^3}{\lambda}\mathrm{IM}(\delta), \quad (1)$$

$$\sigma_s = \frac{128\pi^5\varepsilon_h^2 r_s^6}{3\lambda^4}|\delta|^2. \quad (2)$$

Here, ε_h is the medium's permittivity, r_s is the shell radius, δ is the nanoparticle's polarizability

$$\delta = \frac{\varepsilon_s\varepsilon_a - \varepsilon_h\varepsilon_b}{\varepsilon_s\varepsilon_a + 2\varepsilon_h\varepsilon_b}, \quad (3)$$

$$\varepsilon_a = \varepsilon_c(3-2P) + 2\varepsilon_s P,\ \varepsilon_b = \varepsilon_c + \varepsilon_c(3-P),$$

$$P = 1 - \left(\frac{r_c}{r_s}\right)^3, \quad (4)$$

where ε_c and ε_s are the permittivities of the nanoparticle's core and shell, respectively, and r_c is the radius of the nanoparticle's core.

Calculations were performed at $\lambda = 1.06$ μm, $\tau = 10$ ns, $r_c = 0.05$ μm, and $r_s = 0.05005$ μm. Refractive indices of the nanoparticle's core and shell were $n_c = n_s = 1.3$–2.0, the refractive index of the nonabsorbing medium was $n_h = 1.5$. The equilibrium carrier concentration in the defective shell was 10^7 cm^{-3}. Carrier photogeneration in the defective shell was modeled using the continuity equation for photogeneration and recombination in the presence of impurity absorption [9].

Figure 5 shows the nonlinear additions to the nanoparticle's absorption and scattering cross sections versus the intensity of the incident radiation. Cross sections σ_a and σ_s change with intensity. The function $\sigma_a(I_{in})$ is almost linear except for its initial part. At $n_c > 1.5$, the function $\sigma_s(I_{in})$ is linear in its initial part and saturates at $I_{in} > 30$ W/cm^2 (Fig. 5b, curves *1* and *2*). The effect of saturation is associated with the behavior of function $P(r_c)$ of (4) and exhibits itself when the volume of the nanoparticle's absorbing shell becomes comparable to the core volume. For real nanoparticles, the effect of saturation can also be caused by saturation of the impurity absorption at a small concentration of impurity centers. It is worth noting that, at the nanoparticle radius considered, the scattering cross section is greater by approximately four orders of magnitude than the absorption cross section. Because the extinction coefficient is determined by absorption and scattering,

$$\alpha_{ext} = N(\sigma_a + \sigma_s), \quad (5)$$

where N is the particle concentration, the nonlinear addition to the absorption cross section at the given nanoparticle radius affects the optical properties of nanoparticles insignificantly and variation in the scattering exerts the dominant effect.

Within the approximation of single scattering, the intensity of the radiation that passes through the medium containing nanoparticles is given by the expression

$$I_{out} = I_{in}\exp(-\alpha_{ext}d). \quad (6)$$

Thus, at $n_c > n_h$, the change in the thickness of the nanoparticle's absorbing shell causes an increase in the light scattering and, consequently, limitation of the radiation. The presence of a pronounced threshold in the optical response observed experimentally is due to the exponential intensity behavior of the transmitted radiation versus extinction coefficient (6).

The nanoparticle's refractive index weakly affects the nonlinear addition to the absorption cross section. It only insignificantly changes the slope of the function $\sigma_a(I_{in})$. At the same time, $\sigma_s(I_{in})$ significantly changes with the refractive index (Fig. 5b). At $n_c > n_h$, a decrease in n decreases the scattering cross section and does not affect the behavior of $\sigma_s(I_{in})$ (curves *1* and *2*). At $n_c < n_h$, a minimum appears in $\sigma_s(I_{in})$ (curve *3*). This means that, as the intensity increases, at first the medium blooms and subsequently, limitation of the radiation occurs. The minimum in the characteristic corresponds to a zero value of the real part of the nanoparticle's polarizability. In this situation, the nanoparticle becomes invisible from the viewpoint of light scattering. The case of complete invisibility of a nanoparticle with a shell when the real and imaginary parts of its polarizability are zero is addressed in [8]. At $n_c > n_h$, an increase in the radiation intensity decreases the scattering cross section (curve *4*). Thus, a decrease in the nanoparticle's refractive index decreases the efficiency of limitation of the radiation, while at $n_c < n_h$, the blooming effect is observed in the medium, which is corroborated experimentally (Fig. 4).

The magnitude of the nonlinear addition to the absorption and scattering cross sections for the effects described above is very small. Therefore, a noticeable nonlinear response can only be observed when intrinsic absorption in the nanoparticle's core is very small. This circumstance explains the fact that this optical nonlinearity was not recorded in experiments with nanoparticles of materials whose bandgap is narrower than 3 eV.

In these materials, either their fundamental absorption band itself or its fuzzy edge creates a noticeable absorption in the core. Though the processes described above may evolve in such nanoparticles, the low-threshold nonlinearity cannot be recorded in the presence of absorption in the core. A similar role can be played by impurity absorbing centers in the nanoparticle's core when their concentration is high. The low-threshold nonlinear response can therefore be observed in media with nanoparticles of pure undoped wide-bandgap semiconductors and insulators.

For checking, we also numerically simulated nanoparticles without shells, but with photogeneration of carriers in the entire bulk of the nanoparticle, and nanoparticles with photogeneration of carriers in the shell, but without their diffusion into the bulk of the core. In both cases, our calculations yielded a significant change in the absorption cross section with increasing incident radiation intensity, while the scattering cross section changed by a few fractions of a percent. At the same time, the average magnitude of the nonlinear addition to the absorption cross section for these types of nanoparticles was 3 to 4 orders of magnitude smaller than for nanoparticles with a dynamic absorbing shell, which makes the limiting effect impossible in the range of incident intensities studied.

CONCLUSIONS

The results reported above show that nanoparticles of wide-bandgap semiconductors and insulators can exhibit a low-threshold optical nonlinearity in the visible and near-infrared regions. This nonlinearity is associated with photogeneration of charge carriers from defects near and on the nanoparticle's surface. The condition for the nonlinearity to occur is that absorption in the bulk of the nanoparticle be negligibly small. Depending on values of refractive indices of the nanoparticle and transparent medium in which it resides, the nonlinear response may manifest itself as limitation of the radiation or as blooming of the medium. These effects can be used to develop low-threshold optical switches and limiters with an operation threshold of 0.05 to 0.50 nJ/cm^2.

REFERENCES

1. A. E. Neeves and M. H. Birnboim, J. Opt. Soc. Am. B **6**, 787 (1989).
2. R. D. Averitt, S. L. Westcott, and N. J. Halas, J. Opt. Soc. Am. B **16**, 1824 (1999).
3. R. D. Averitt, S. L. Westcott, and N. J. Halas, J. Opt. Soc. Am. B **16**, 1814 (1999).
4. A. I. Sidorov, Opt. Zh. **70** (2), 9 (2003).
5. O. P. Mikheeva and A. I. Sidorov, Zh. Tekh. Fiz. **73** (5), 75 (2003) [Tech. Phys. **48**, 602 (2003)].
6. A. I. Sidorov, O. P. Mikheeva, and E. B. Shadrin, in *Proceedings of the 11th International Conference on Laser Optics, St. Petersburg, 2003.*
7. E. A. Kolenko, *Technology of Laboratory Experiment: A Handbook* (Politekhnika, St. Petersburg, 1994).
8. C. F. Bohren and D. R. Huffman, *Absorption and Scattering of Light by Small Particles* (Wiley, New York, 1983; Mir, Moscow, 1986).
9. A. I. Sidorov, Opt. Zh. **69** (1), 7 (2002).

Translated by A. Khzmalyan

Technical Physics, Vol. 49, No. 6, 2004, pp. 745–750. Translated from Zhurnal Tekhnicheskoĭ Fiziki, Vol. 74, No. 6, 2004, pp. 83–88.

OPTICS, QUANTUM ELECTRONICS

Diffusionless Motion of High-Absorptivity Domains along the Laser Beam Axis

V. A. Trofimov and Yu. V. Troshchiev

Moscow State University, Vorob'evy Gory, Moscow, 119992 Russia

e-mail: vatro@cs.msu.su

Received October 28, 2002; in final form, October 27, 2003

Abstract—A new mechanism of motion of high-absorptivity domains under the action of Gaussian beams without allowance for diffusion of the material characteristics along the direction of beam propagation is studied by computer simulation. The essence of this mechanism is the dependence of the absorption factor growth rate on the radiation intensity. As a result, high-absorptivity domains may drift from heavily to weakly irradiated regions of the medium. © *2004 MAIK "Nauka/Interperiodica".*

INTRODUCTION

Reliability is known to be a key property of optical data storage and processing devices. Information may be recorded, e.g., by initiation of chemical reactions [1–3], and data processing devices use various bistable circuits (see, e. g. [4–6]). Typical of both processes is the presence of local areas where the material properties differ considerably from those of the environment. These may be high-temperature domains or domains with an enhanced concentration of the chemical reaction product that arise owing to the optical bistability (OB) effect. It is important to study the motion of these domains, the possibility of an additional domain appearing (along with the basic one), and related physical mechanisms.

It is known from available publications that, in optically bistable systems with longitudinal diffusion, domains may move into the bulk of the material as a consequence of beam focusing [5]. In this study, we show that a diffusionless mechanism of domain motion is also a possibility. The term "diffusionless" emphasizes the absence of longitudinal diffusion, while diffusion in the directions perpendicular to the beam axis is taken into consideration. Note also that several types of motion of high-absorptivity domain walls in cavity-free systems without longitudinal diffusion have been already described [7, 8]. For example, when the input intensity grows continuously, the rear domain wall may travel a considerable distance along the medium [4]. If optical radiation has a constant intensity at the entrance to a nonlinear medium, the propagation of the rear domain wall toward the radiation occurs even in the process of domain formation. However, the displacement typically does not exceed several percent of the longitudinal size of the domain being formed. A specific feature of the domain motions that follows from published data is noteworthy: the invariable position of the front domain wall, which is fixed and located near the entrance to a nonlinear medium. Here, we are interested in the possibility of displacing both walls of a high-absorptivity domain by distances on the order of, or larger than, the longitudinal domain size. Such a situation takes place, for example, under the action of a beam with an elliptic profile. The beam may arise when an initially axisymmetric beam interacts with an optical data storage system because of inaccurate focusing onto a given pit or as a result of its propagation through an inhomogeneous medium.

The elliptical profile of optical beams makes it possible to set the bistable dependence, for example, of the temperature of the medium on the beam radius [9]. Bistability arises due to the fact that the variation of the beam intensity and material cooling via transverse heat removal depend on the beam radii in a different manner. As a result, high-temperature (high-concentration) domains are formed not only by the absorption mechanism but also due to the bistable dependence of the material properties on the beam radii. It is important to bear in mind that the light intensities necessary to switch domains from one state to another by the latter mechanism of bistability are lower than those in the case of an axisymmetric beam, when only absorption bistability exists. However, since the heating rate (growth of concentration) depends on the radiation intensity, domain formation due to the ellipticity of the beam usually lags behind domain formation due to nonlinear absorption. Depending on relationships between the beam–medium interaction parameters (ellipticity of the beam profile, beam intensity, time of heat removal, time of change of the concentration, etc.), additional domains may appear both before and after the beam waist [9–11]. In terms of dynamics, the dependence of the rate of domain formation on the beam intensity and the difference in switching intensities in these bistability mechanisms suggest that a considerable displace-

1063-7842/04/4906-0745$26.00

ment of domains is possible. Analysis of this possibility is the aim of this work.

An important point is that our consideration of the particular case of optical radiation–gas interaction does not restrict generality of the results: they are also valid for semiconductors and other media. The basic condition for wide applicability of the results is the nonlinear dependence of the absorption factor on temperature and/or concentration of the product of a certain reaction (for example, polymer reconfiguration reaction), free-carrier concentration in semiconductors, etc. Previously, we studied in detail the formation of multidomain structures in gases [9–11]. Here, interaction of optical radiation with layered and continuous gaseous media is considered.

STATEMENT OF THE PROBLEM

As was mentioned above, we are dealing with interaction between optical radiation and a chemically active medium. Let a reversible chemical reaction $A \rightleftarrows C$ take place, where A is the initial substance and C is the reaction product. We also assume that the optical energy is absorbed by the vibrational levels of the molecules. In a layered medium, the thicknesses of absorbing and transparent layers are denoted as l_a and l_t, respectively. Then, an element of the periodic layered structure has a length $l = l_a + l_t$. Under the assumption that the vibrational levels are nonequidistant and the time of V–V relaxation is much shorter than both the pulse duration and the time of V–T relaxation, the propagation of a Gaussian pulse in the ith layer of the absorbing medium near the beam axis can be described by the following system of dimensionless equations:

$$\begin{gathered}
\frac{\partial E}{\partial t} = q\delta(E)(\sigma_b N + \sigma_f(1-N)) - (E - E_0(T)),\\
\varepsilon\frac{\partial T}{\partial t} = T_E(E - E_0(T)) - \beta(T - T_0),\\
\frac{\partial N}{\partial t} = (1-N)\exp(-T_f/T)\\
- kN\exp(-T_b/T) - D_N(N - N_0),\\
\frac{\partial q_0}{\partial z} + \delta_0\delta(E)(\sigma_b N + \sigma_f(1-N))q_0 = 0, \quad t > 0,\\
l(i-1) \le z \le l(i-1) + l_a,\\
T(z,t) = T_0, \quad q_0(z,t) = q_0(l(i-1) + l_a, t),\\
l(i-1) + l_a < z \le li,
\end{gathered} \tag{1}$$

where

$$\begin{gathered}
q = \frac{q_0}{a_x a_y}, \quad \beta = \beta_0\left(\frac{1}{a_x^2} + \frac{1}{a_y^2}\right),\\
a_r^2 = a_{r0}^2(z^2 + (1 + zF_r)^2), \quad r = 'x', 'y',\\
E_0(T) = \exp(-1/T), \quad \delta(E) = E^n/(1+E)^{n+2}.
\end{gathered} \tag{2}$$

In the transparent layers, the temperature is constant, the absorption is absent and the beam radii vary by the same law as in the absorbing layers. The initial conditions for system (1) have the form

$$\begin{gathered}
q_0(0,t) = q_0(t), \quad q_0|_{z = li} = q_0|_{z = l(i-1) + l_a},\\
i = 1, \ldots, N_l,\\
T|_{t=0} = T_0, \quad E|_{t=0} = E_0(T_0), \quad q_0|_{t=0} = 0,\\
N|_{t=0} = N_0 = 1/(1 + k\exp(-(T_b - T_a)/T_0)).
\end{gathered} \tag{3}$$

These conditions imply that the incident pulse shape is specified by $q_0(t)$ and that the medium is in equilibrium before irradiation. In formulas (1) and (2), $E(z, t)$ is the vibrational energy of a unit gas volume for a given mode, $E_0(t)$ is its equilibrium value at a given translational temperature T, $N \in [0, 1]$ is the concentration of the reaction product normalized to maximum, t is the time normalized to the characteristic time of V–T relaxation, and q is the dimensionless intensity of radiation near the beam axis. Note that, between the active layers, the radiation intensity varies due to diffraction alone. The parameter n specifies the number of a vibrational transition that absorbs the radiation energy. The difference in the populations of levels n and $n + 1$ is defined by the function $\delta(E)$. The parameter T_E takes into account, in particular, the fraction of the absorbed energy that is spent on heating. The coefficient β takes into account the amount of the heat transversely removed into the environment with a temperature T_0, z is the longitudinal coordinate normalized to a given length, δ_0 is the intensity absorption factor over the normalization length, and $q_0(z, t)$ is the peak intensity of the beam. The functions a_x and a_y describe variation of the initial beam radii a_{r0} in the x and y directions as the beam propagates along the z axis. The parameters T_f and T_b have the meaning of the activation energies of the forward and backward chemical reactions, respectively. The parameters σ_f and σ_b ($\sigma_f + \sigma_b = 1$, $\sigma_f > 0$, $\sigma_b > 0$) are the cross sections of absorption by molecules of the reaction product and initial substance, respectively. The coefficient D_N allows for diffusion of the reaction product from the region occupied by the beam (taken to equal to zero). The parameter E_r characterizes beam focusing along the coordinates.

To conclude this section, we note that system (1), which describes interaction between an initially Gaussian beam and a nonlinear medium, is adequate only if the radiation intensity profile does not become "tubu-

lar" (i.e., if the beam has no dip of the intensity at the axis).

SCENARIOS OF THE DOMAIN MOTION

First, note that the following discussion of motion of high-absorptivity domains is based on the above assumption that the initially Gaussian beam does not transform into a tubular beam, which, in turn, becomes Gaussian again due to diffraction. Otherwise, complex diffraction-related processes of generation and collapse of high-absorptivity domains may be observed (as was demonstrated by Vysloukh and Trofimov in [7, 8] and other works).

In domain motion by the diffusionless mechanism, a decrease in the radiation intensity behind a high-absorptivity domain being formed plays a major role. The influence of this factor is twofold. First, absorption of radiation results in the self-action of a domain: the leading (respective to the pulse propagation direction) part of a domain being formed changes the conditions for trailing part formation. Second, these conditions also change when new domains located closer to the entrance section of the medium appear. Evidently, the self-action of a domain persists at all times. When domain formation takes place near the front wall of a vessel or crystal, the rear wall of the domain shifts. If, however, domains form deep in the bulk, the conditions for beam–medium interaction are so that they occupy only a small space of the medium. In both cases, the displacement due to self-action is insignificant.

For high-absorptivity domains to travel a considerable distance, it is necessary that, first, domains located in different sections of the medium form with different rates. This condition is always met. Another necessary condition is the existence of a certain interval along the z axis in a part of which the conditions for switching the medium–beam system from the lower to the upper state are met and, at the same time, the incident intensity is insufficient for such switching to take place throughout this interval. In practice, such a situation arises, for example, under the action of elliptical beams [9, 10]. In this case, additional domains appear at intensities much lower than those in the case of axisymmetric beams, which cause optical absorption bistability. Since the switching rate depends on the radiation intensity, domain formation due to ellipticity occurs at a later time. Therefore, the appearance of such an ellipticity-related domain "in the wake" of a domain that is forming in the region of peak intensity changes the formation conditions of the latter, making it move oppositely to the direction of beam propagation in the absence of longitudinal diffusion. In contrast, if the intensity profile becomes elliptical after the beam has passed through a layer where a domain forms under the action of an axisymmetric beam, another domain, associated with the ellipticity, starts moving because of a change in the intensity induced by the formation of the first domain. Such a motion proceeds in the direction of beam propagation.

COMPUTER EXPERIMENTS

The different scenarios of domain motion are illustrated graphically. The parameter values $T_0 = 0.125$, $T_E = 5$, $\varepsilon = 1$, $T_f = 1$, $T_b = 0.1$, $k = 0.5$, $\sigma_f = 1$, and $\sigma_b = 0$ are the same in all plots.

Note that, under the assumption of fast V–T relaxation (i.e., that only the translational temperature and the concentrations of chemicals change), optical bistability is absent for the values of T_0, T_f, T_b, k, σ_f, and σ_b specified above. Therefore, only bistability due to nonlinear absorption at vibrational transitions is observed under this assumption.

Figure 1 shows that, first, an intense laser beam focused into the bulk of the medium produces a high-concentration domain in the waist region ($t = 40$, 50). As the reaction product concentration at the leading edge of the domain (and in front of it) grows, the domain slightly shifts ($t = 60$, 70). Then, a domain related to beam profile ellipticity originates in the narrowing part of the beam far away from its waist ($t = 80$). This results in the disappearance of the domain that appeared first ($t = 110$). Thus, Fig. 1 illustrates the motion of domains along the z axis: it nucleates at $z = 0.28$, disappears at $z = 0.18$, and eventually forms in the range $z \le 0.1$. We distinguish two stages in domain motion. For $40 \le t \le 70$, the first domain moves, whereas the second domain is as yet unnoticeable, although the reaction product concentration in the region $z \le 0.2$ increases steadily. The reason for the evolution of the first domain is the influence of its front edge on the parts formed earlier. The decrease in the intensity near the beam waist because of absorption in the region in front of the domain plays a minor role: it

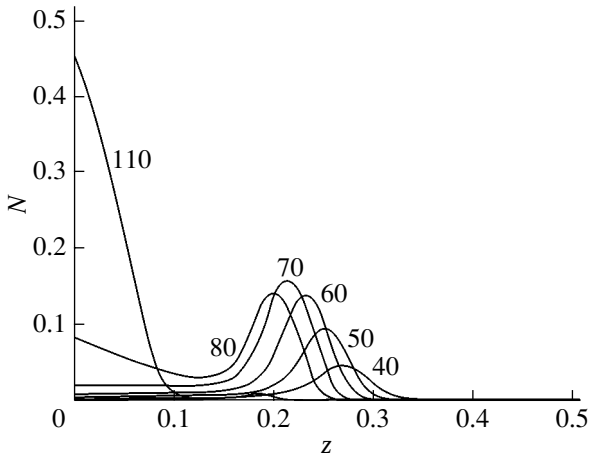

Fig. 1. Motion of a concentration domain in a continuous medium with the parameters $a_{x0} = 0.07$, $a_{y0} = 3.271$, $F_y = 0$, $F_x = -2.5$, $\beta_0 = 0.0006$, and $\delta_0 = 185$. The figures by the curves indicate dimensionless times.

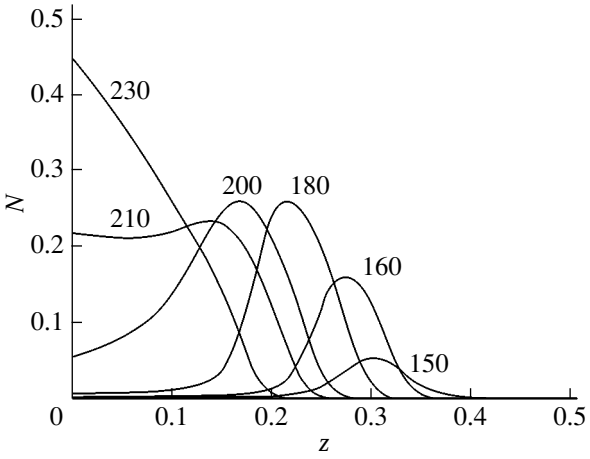

Fig. 2. Motion of a domain in a continuous medium (the moving domain merges with another domain). $q_0 = 0.095$, $a_{x0} = 0.07$, $a_{y0} = 3.271$, $F_y = 0$, $F_x = -2.5$, $\beta_0 = 0.0006$, and $\delta_0 = 100$. The figures by the curves indicate dimensionless times.

merely rises the rate of disappearance of the domain's rear part. For $t = 80$, 110, the domain moves and collapses during the ellipticity-related formation of the second domain.

Consideration of the first stage enables us to suggest the following mechanism of domain motion. During the formation of the domain's leading edge, the beam intensity in the parts that have already formed decreases and these parts disappear. The leading edge forms later on, since the intensity at the site of its formation is lower than in the waist region. As a result, the domain moves opposite the direction of beam propagation in the absence of longitudinal diffusion of the material properties. At the first stage, the second domain is visually almost unnoticeable; nevertheless, it forms and has an effect on the situation.

For other relationship between the parameters of interaction, the domain formed earlier may merge with the following one (Fig. 2) or stop (Fig. 3), having traveled a considerable distance. Figures 3e and 3f illustrate how the rear part of the domain near the waist dis-

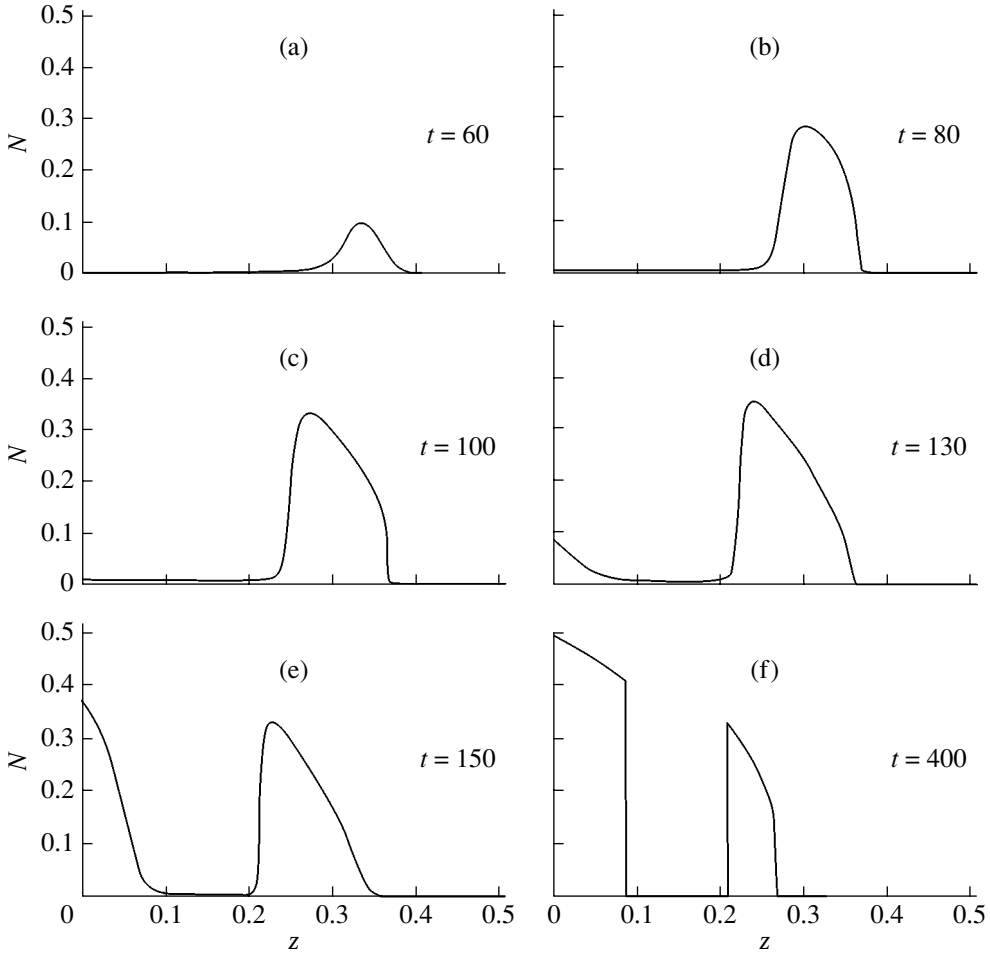

Fig. 3. Motion of a domain in a continuous medium (the moving domain stops). $q_0 = 0.085$, $a_{x0} = 0.07$, $a_{y0} = 3.271$, $F_y = 0$, $F_x = -2.2$, $\beta_0 = 0.0006$, and $\delta_0 = 50$.

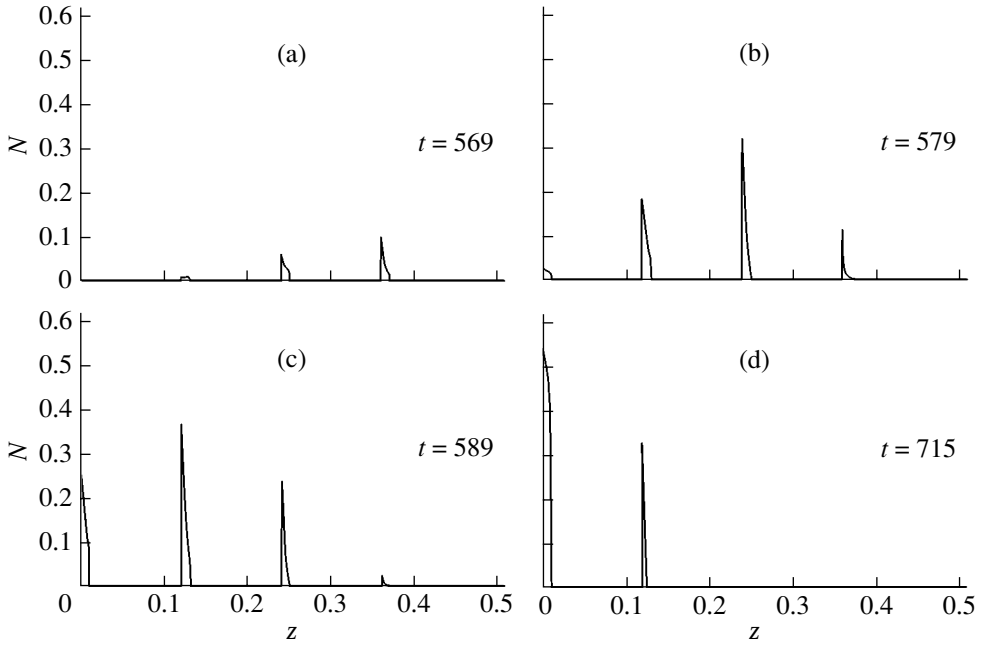

Fig. 4. Motion of a domain in a layered medium. $q_0 = 0.15$, $a_{x0} = 0.07$, $a_{y0} = 3.271$, $F_y = 0$, $F_x = -2.2$, $\beta_0 = 0.0006$, $\delta_0 = 1500$, $l_a = 0.01$, and $l_t = 0.11$.

appears, while its front part near the waist remains almost unchanged, as the domain forms near the material boundary

Of practical interest is application of this mechanism of domain motion to data recording in 3D layered media. By way of example, let us consider the action of optical radiation on a layered medium with the parameters of interaction given in Figs. 2 and 3 (Fig. 4). It follows from Fig. 4 that the early domain made an erroneous record in three layers. From the final pattern (Fig. 4d), it is hard to judge whether a single domain split by a transparent layer as in Fig. 2 was left or the domain stopped as in Fig. 3. However, the record in two layers here is clearly seen. Should the reaction be irreversible, a four-layer record would be observed.

Figure 5a presents another illustration of the domain motion under the action of axisymmetric laser beams. A dynamic two-domain structure may also arise as a result of a decrease in the beam intensity due to absorption (Fig. 5b). The curve at $t = 50$ in Fig. 5b has two peaks: near the boundary and in the bulk of the

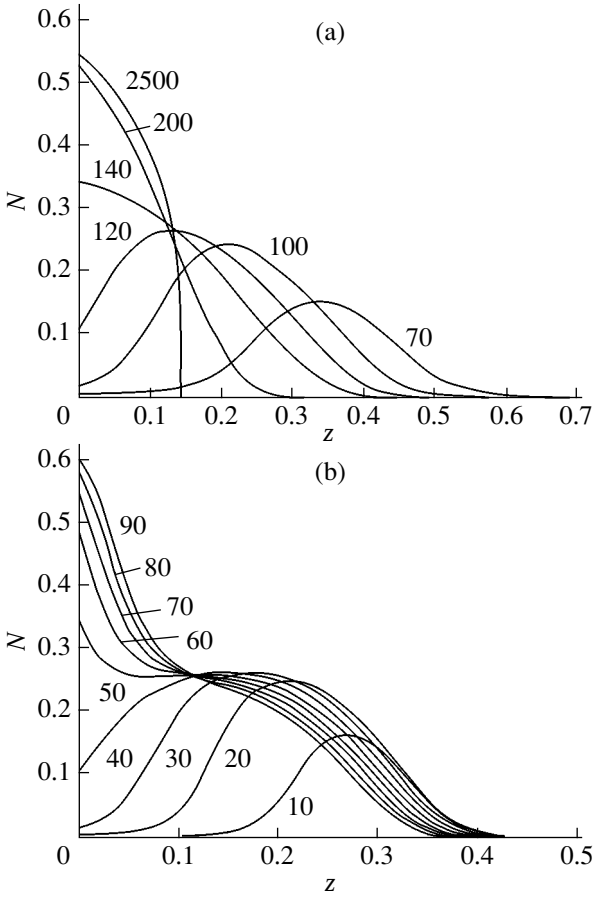

Fig. 5. (a) Motion of a domain under the action of an axisymmetric beam. $q_0 = 0.01$, $a_{x0} = a_{y0} = 0.2$, $F_x = F_y = -1$, $\beta_0 = 0.001$, $\delta_0 = 150$ (the figures by the curves indicate dimensionless times). (b) The dynamic two-domain structure formed under the action of an axisymmetric beam; $q_0 = 0.1$, $a_x = a_y = 0.5$, $F_x = F_y = -2.5$, $\beta_0 = 0.0006$, and $\delta_0 = 500$ (the figures by the curves indicate dimensionless times).

medium. However, realization of the domain motion under the action of axisymmetric beams requires that the conditions of switching to the upper state be met within most part of the medium and the absorption factor be high. These conditions are obviously interrelated and imply that, if the absorption is low, the longitudinal size of the domain is much smaller than the linear size of a medium where it arises.

CONCLUSIONS

The results presented above substantiate a diffusionless mechanism of high-absorptivity domain motion that is distinct from the known mechanisms related to longitudinal diffusion of the material properties or diffraction of the beam. The new mechanism is based on the fact that different parts of a domain are formed with unequal rates. This effect is typical of optically bistable absorbing systems and takes place when the length of domain formation region exceeds the longitudinal size of a domain produced by an axisymmetric beam. Such a situation is most likely to occur in 3D optical memory devices subjected to elliptical beams. In this case, the intensity profile retains ellipticity both in front of and behind the beam waist. Accordingly, additional domains that satisfy the condition for high-absorptivity domain motion may appear in both regions. Similar effects may be favored by the dependence of the *V–T* relaxation time on the vibrational energy of molecules. It is important that the domain motion thus induced proceeds for a much shorter time in comparison with the case considered above, since the conduction-related change in the translational temperature takes a time appreciably exceeding the characteristic time of vibrational energy variation.

Similar effects may be observed in semiconductor memory devices if the relaxation time of free charge carriers as a function of the carrier concentration is taken into account. Therefore, the results of this work are useful for a variety of applications.

REFERENCES

1. S. S. Chesnokov, V. P. Kandidov, and N. I. Koroteev, Proc. SPIE **3733** (1999).
2. P. M. Rentzepis, U.S. Patent No. 5268862 (1993).
3. A. S. Dvornikov, I. Cokgor, F. McCormic, *et al.*, Opt. Commun. **128**, 205 (1996).
4. H. M. Gibbs, *Optical Bistability: Controlling Light with Light* (Academic Press, New York, 1985; Mir, Moscow, 1988).
5. N. N. Rozanov, *Optical Bistability and Hysteresis in Distributed Nonlinear Systems* (Nauka, Moscow, 1997) [in Russian].
6. R. V. Bunkin, N. A. Kirichenko, and B. S. Luk'yanchuk, Izv. Akad. Nauk SSSR, Ser. Fiz. **46**, 1150 (1982).
7. A. V. Vysloukh and V. A. Trofimov, Pis'ma Zh. Tekh. Fiz. **26** (3), 60 (2000) [Tech. Phys. Lett. **26**, 119 (2000)].
8. A. V. Vysloukh and V. A. Trofimov, Opt. Spektrosk. **88**, 802 (2000) [Opt. Spectrosc. **88**, 725 (2000)].
9. V. A. Trofimov, Yu. V. Troshchiev, and O. A. Gunaze, Khim. Fiz. **19** (7), 14 (2000).
10. V. A. Trofimov and Yu. V. Troshchiev, Opt. Spektrosk. **91**, 283 (2001) [Opt. Spectrosc. **91**, 262 (2001)].
11. V. A. Trofimov and Yu. V. Troshchiev, Opt. Spektrosk. **92**, 315 (2002) [Opt. Spectrosc. **92**, 280 (2002)].

Translated by A. Sidorova

Technical Physics, Vol. 49, No. 6, 2004, pp. 751–757. Translated from Zhurnal Tekhnicheskoĭ Fiziki, Vol. 74, No. 6, 2004, pp. 89–95.

RADIOPHYSICS

Ferromagnetic Resonance and Antiresonance in Lanthanum–Yttrium Manganite Powder

A. B. Rinkevich*, A. P. Nossov*, V. G. Vasil'ev, and E. V. Vladimirova****

** Institute of Metal Physics, Ural Division, Russian Academy of Sciences, ul. S. Kovalevskoĭ 18, Yekaterinburg, 620219 Russia*

e-mail: nossov@imp.uran.ru

*** Institute of Solid-State Chemistry, Ural Division, Russian Academy of Sciences, Pervomaĭskaya ul. 91, Yekaterinburg, 620219 Russia*

Received July 21, 2003; in final form, October 20, 2003

Abstract—Absorption of centimeter waves in $La_{0.6}Y_{0.07}Ba_{0.33}MnO_3$ manganite powder is studied under the conditions of ferromagnetic resonance and antiresonance. It is found that interaction between different components of the microwave fields and the manganite distorts the shape of resonance lines and changes the resonance-to-antiresonance amplitude ratio. In the range of ferromagnetic resonance fields, great (up to 25 times) changes in the transmitted microwave power are observed. © *2004 MAIK "Nauka/Interperiodica".*

INTRODUCTION

Investigation of the properties of ultradisperse materials has become an expanding area of exploration in the physics of condensed matter. The dynamic permeability of small metal particles has been the subject of extensive experimental and theoretical research (see, e.g., [1]). The permeability of submicron one-domain spherical particles was studied in [2], where the unusual frequency dependence of its imaginary part (several, instead of one, narrow peaks) was revealed. In the same work, the permeability versus the size of conductive particles was studied. Exchange resonance modes of ultrasmall ferromagnetic spherical bodies were theoretically investigated in [3]. The effect of dipole–dipole interaction on the magnetic properties of ultrathin ferromagnetic particles was touched upon in [4], where the temperature dependence of the susceptibility of an ensemble of particles cooled with and without a magnetic field applied was simulated by the Monte Carlo method. A method of calculating the dynamic susceptibility of one-domain particles with cubic anisotropy was developed in [5]. An algorithm for calculating the relaxation time and frequency dependence of the imaginary part of the susceptibility was suggested, and factors responsible for the peaks in the loss spectrum were considered.

In recent years, the emphasis has been on ferromagnetic resonance in sets of ultrafine particles. It has been shown that, as the particle size grows, the field of resonance decreases because of a change in the effective field, while the resonance linewidth varies insignificantly [6]. The effective field approximation yields reasonable results for the resonance field and linewidth, as demonstrated by numerical calculations for an ensemble of particles [7]. Experimental study of ferromagnetic resonance (FMR) in γ-Fe_2O_3 particles was undertaken in [8]. The authors of [8] took the dependences of the resonance field and linewidth on the particle size and measured the anisotropy of the resonance field for an ensemble of particles frozen under a permanent magnetic field. The conclusion was drawn that surface magnetic anisotropy exists in that given system. It was also shown that this anisotropy is biaxial and the constant of surface magnetic anisotropy was calculated based on data obtained [9]. Ferromagnetic resonance for a single micrometer-size particle was considered in [10].

Lanthanum manganites have recently attracted much attention owing to the colossal magnetoresistance effect. These are complex perovskite-like oxides [11]. Their electromagnetic properties exhibit a number of intriguing features. First, polycrystalline manganites have a granular structure, the conductivity of the intragranular material differing drastically from that of the intergranular space and of grain boundaries [12]. Second, the manganites demonstrate the metal–insulator phase transition and its temperature is close to the Curie point T_C. Third, along with FMR, ferromagnetic antiresonance (FMAR) is observed in the metallic conduction range [13]. To date, a great number of studies have been devoted to FMR and FMAR in manganites [14–16]. Using the FMR technique, the authors of [17] studied the magnetic uniformity of $La_{2/3}Ba_{1/3}MnO_3$ manganite in a wide temperature range, including the Curie point. FMR measurements were made on both bulk samples and films. In this work, we are dealing with manganite powders.

It was shown [18] that the FMAR amplitude in $La_{0.7}Ca_{0.3}MnO_3$ powder drops sharply as the particle size increases. At the present time, the main object of research is FMR manganite powders where the condi-

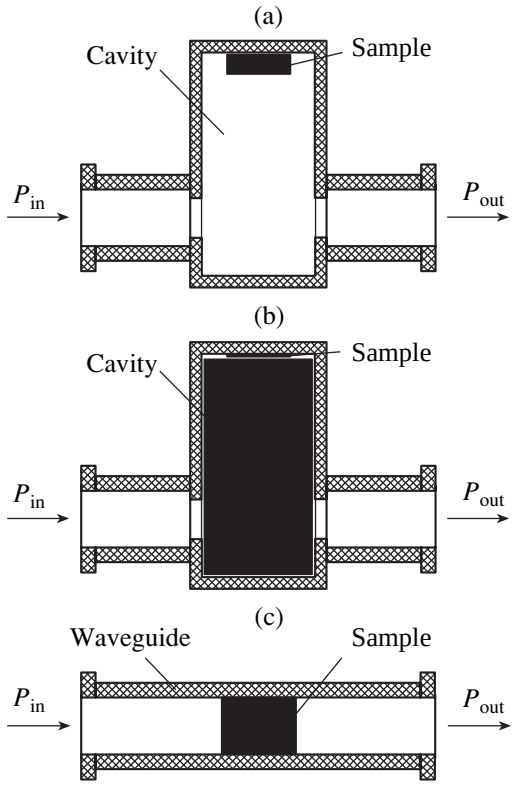

Fig. 1. Microwave measurements: (a) bulk sample in a resonant cavity, (b) composite sample in a resonant cavity, and (c) composite sample in a waveguide.

tion $d < \delta$ is fulfilled, where d is the mean grain size and δ is the skin depth. With this condition met, the influence of the skin effect is insufficient. For $La_{0.5}Pb_{0.5}MnO_3$ manganite with several-micron-size grains, it was demonstrated that an asymmetric FMR line is observed below the Curie point, whereas a more symmetric and narrower EPR line appears above the Curie point [19]. In highly doped manganites, the resonance line above the Curie temperature was studied in [19, 20] by invoking the concept of charge carriers localized near phase or structure inhomogeneities [11]. The study of FMR in $La_{2/3}Sr_{1/3}MnO_3$ powder with 0.1- to 0.2-μm grains at a microwave frequency of 344 GHz detected only a symmetric FMR resonance line. In the sample with 1- to 2 μm grains, this line is highly asymmetric and includes both FMR and FMAR components [21]. Estimates based on these measurements gave microwave conductivity values several hundreds of times lower than dc conductivities.

Resonance frequencies of cavity modes

Mode	E_{010}	H_{210}	E_{110} (H_{010})	E_{111} (H_{011})
f_{calc}, GHz	7.41	9.41	11.26	11.72
f_0, GHz	7.47	9.38	10.62	

In this work, we study FMR and FMAR in moderately doped $La_{0.6}Y_{0.07}Ba_{0.33}MnO_3$ manganite powder under the condition that the skin depth is comparable to, or exceeds, the grain size (≈10 μm or less). In the absence of a magnetic field, the particles consist of several magnetic domains. We suppose that such conditions are the most appropriate for comparing the intensities and shapes of the resonance and antiresonance lines in bulk samples and powders. Also, these conditions may reveal the difference in efficiency of interaction between various components of the microwave field and the magnetic moments of the particles (earlier, this interaction was considered only in bulk polycrystals [16]). We report results on the electromagnetic power absorption in resonant cavities at different oscillation modes for powders and bulk polycrystals of $La_{0.6}Y_{0.07}Ba_{0.33}MnO_3$ manganite. In the powder samples, the transmission coefficient was measured with the technique used in [13].

EXPERIMENTAL

Ferromagnetic resonance and ferromagnetic antiresonance in bulk samples and powders were studied with three techniques. First, we investigated bulk samples measuring $10.5 \times 6.7 \times 4.5$ mm, $2.6 \times 6.7 \times 1$ mm, and $4 \times 1 \times 1$ mm. The sample was placed near the end face of a cylindrical resonant cavity inserted in cascade into the microwave transmission line (Fig. 1a). An input power P_{in} was applied to the entrance of the measuring cell and an output power P_{out} is extracted from the exit of the cell to the transmission line. The magnitude of the transmission coefficient $A = A_{out}(H)/A_{in}$ as a function of the magnetic field strength H was measured (A_{in} and A_{out} are the respective oscillation amplitudes at the input and output of the cavity). The measurements were performed at several cavity modes in the frequency interval f = 7.4–10.7 GHz. Note that an external magnetic field was directed along the larger side of the sample in all our experiments. Then, the bulk sample was powdered and the powder was embedded in a paraffin matrix to prepare a composite. After molten paraffin had been cooled, the composite was placed in the cylindrical cavity, entirely filling it (Fig. 1b). In the second technique, we also measured the transmission coefficient A as a function of the external magnetic field at several oscillation modes. Here, the cylindrical cavity was 32 mm in diameter and 48 mm high. The table lists the calculated, f_{calc}, and measured, f_0, values of the resonance frequencies of several modes.

In the third measuring technique, the composite ($La_{0.6}Y_{0.07}Ba_{0.33}MnO_3$ powder + paraffin) was placed in a 28.5×12.6-mm waveguide in such a way that it completely occupied the cross section of the waveguide and its length along the waveguide axis was 40 mm (Fig. 1c). An external magnetic field was directed normally to the wavevector of the electromagnetic wave in the microwave transmission line.

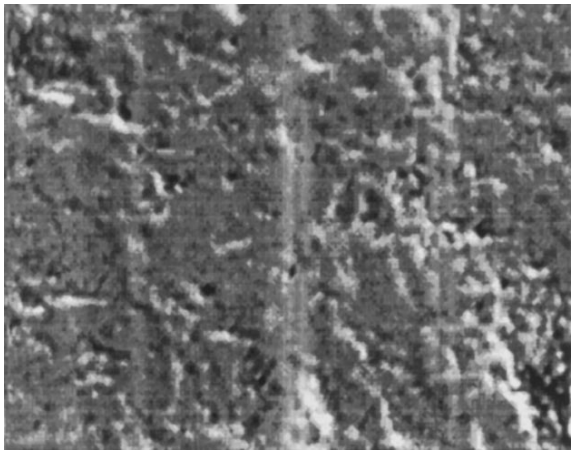

Fig. 2. Electron micrograph taken from the surface of the bulk polycrystal. ×800.

The fields in which the transmission coefficient magnitude reaches a maximum and minimum were taken as the resonance and antiresonance fields, respectively. The measurements were made in a magnetic field of up to 10 kOe at room temperature. The accuracy of measurement of the magnetic field strength was ±3%.

The initial powder of rated composition $La_{0.6}Y_{0.07}Ba_{0.33}MnO_3$ was prepared by codeposition from melt [22]. Then, bulk samples of the polycrystalline manganite were made by isostatic pressing. The samples were annealed in oxygen flow at 1200°C for 6 h. The density of the samples were 40% of the density measured by the X-ray method. In the electron micrograph taken from the surface of the bulk sample (Fig. 2), pores and voids are distinctly seen. After microwave measurements, the bulk samples were subjected to dry grinding in a ball mill using Al_2O_3 balls. The density of the material thus obtained was 78% of the X-ray value. Grain-size analysis of the powders was accomplished with an ANALIZETTE laser diffraction analyzer (FRISCH Co.) with an accuracy of 0.002 μm. It was found that 82% of the grains were from 5 to 10 μm in size; 17%, from 3 to 5 μm; and 3%, less than 3 μm. The increased density of the powder compared with the density of the initial bulk sample is probably due to a reduction of the void content. For the bulk samples, the Curie point was 342 K and the resistivity, 1.6 Ω cm. The skin layer estimated for the unit relative permeability was found to be 0.62 mm at a frequency of 10 GHz.

RESULTS AND DISCUSSION

Consider first the results for the bulk samples. The field dependence of the transmission coefficient magnitude for the samples placed in the resonant cavity is shown in Fig. 3. In Fig. 3a, the sample measures 10 × 6.7 × 4.5 mm; that is, the associated dimension far exceeds the skin depth δ. As the external field strength

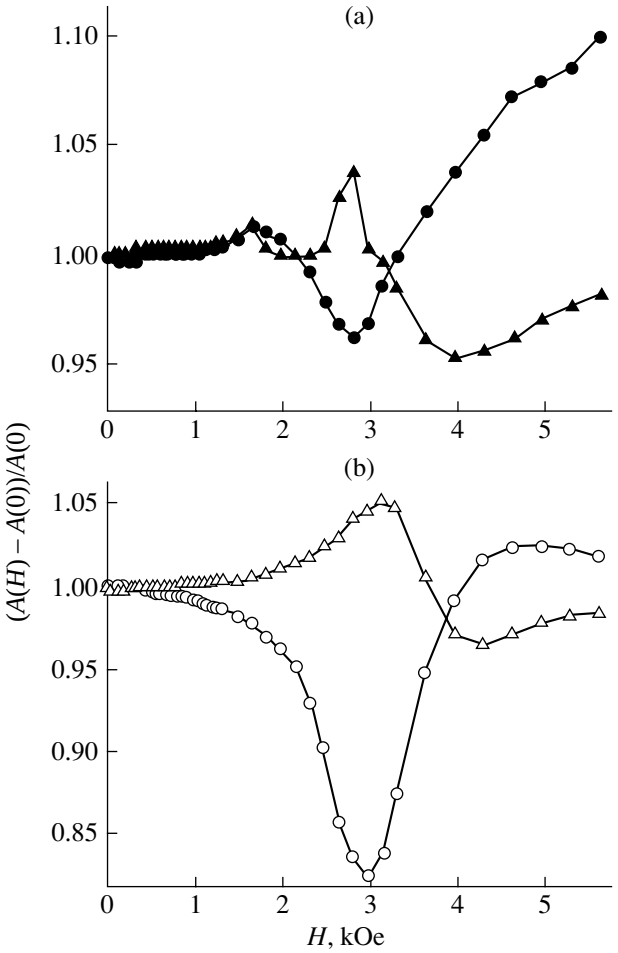

Fig. 3. Relative variation of the amplitude of the signal transmitted through the cavity with the bulk polycrystalline sample inside vs. the magnetic field. The sample dimensions are (a) 10.5 × 6.7 × 4.5 and (b) 12.6 × 6.6 × 1 mm. (●) 7.48, (▲) 10.62, (○) 9.38, and (△) 10.61 GHz.

H grows, the transmission coefficient first reaches a maximum associated with FMAR and then a minimum due to electromagnetic wave absorption under the FMR condition [14]. Figure 3a shows the results for two modes: E_{010} (f = 7.48 GHz) and E_{110} (f = 10.62 GHz). The mode E_{110} is degenerate: its resonance frequency coincides with that of the mode H_{010}. It seems that mode degeneracy affects the field dependence $A(H)$: the maximum narrows, while the minimum broadens. For the 12.6 × 6.6 × 1-mm sample, the results of measurement are shown in Fig. 3b. Here, the skin layer is comparable to one of the dimensions. The dependence obtained at f = 10.61 GHz (the same degenerate modes E_{010} and H_{010} of the cavity) shows a maximum (FMAR) and a minimum (FMR). At the same time, the dependence taken at the lower frequency f = 9.38 GHz (the mode H_{210}) has only a distinct minimum without signs of a maximum.

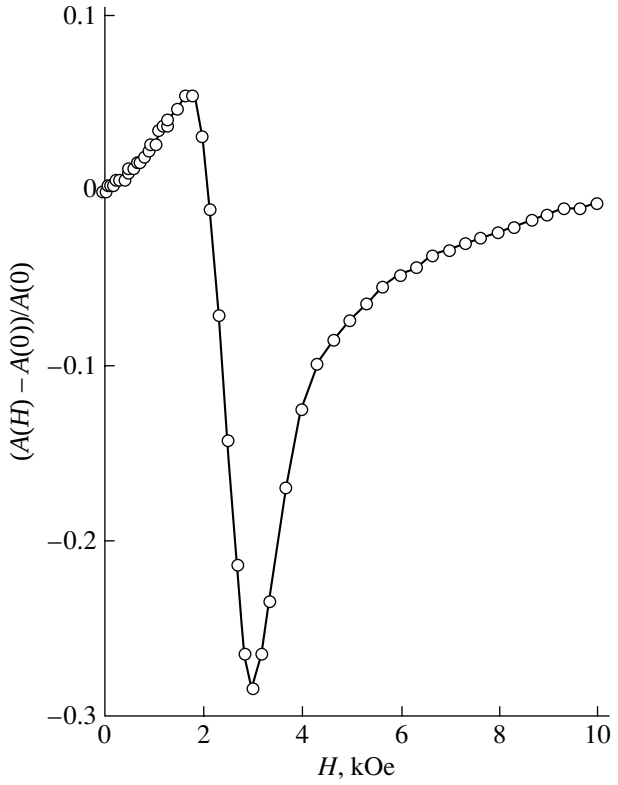

Fig. 4. Relative variation of the amplitude of the signal transmitted through the cavity with the bulk $4 \times 1 \times 1$-mm polycrystalline sample inside vs. the magnetic field.

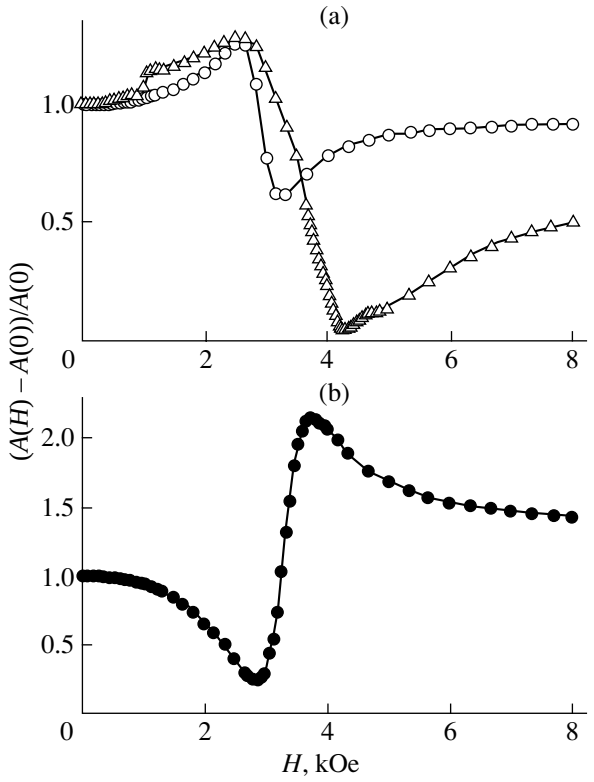

Fig. 5. Relative variation of the amplitude of the signal transmitted through the cavity with the composite sample inside vs. the magnetic field. (○) 8.20, (△) 10.40, and (●) 8.02 GHz.

The absence of antiresonance at the lower frequency may be explained by two reasons. First, the FMAR cutoff frequency is found from the relationship $\omega_{AR,\ min} = \gamma 4\pi M$, where γ is the gyromagnetic ratio and M is the magnetization. This relationship follows from the conventional relationship $\omega_{AR} = \gamma B_0$, where B_0 is the induction for the sample face magnetized tangentially [23]. Estimates made in [24] and measurements made on similar samples [16] showed that FMAR is bound to be observed and was actually observed even at a still lower frequency, 7.4 GHz. The measurements [16] were made for the mode E_{010}. The other possible reason is that one of the sample dimensions is comparable to the skin depth. Therefore, it is reasonable to compare the above results with those obtained for manganite powders, where the grain size is much smaller than δ, and with those measured on rodlike samples where two dimensions are comparable to the skin depth. The related results for the $4 \times 1 \times 1$-mm sample and mode E_{010} (f = 7.47 GHz) are given in Fig. 4. Here, both FMR and FMAR lines are distinctly seen. It than becomes evident that detailed theoretical analysis of how the electric and magnetic field components interact with the magnetic fields of cavity modes with allowance for spin pinning is necessary to elucidate these anomalies.

Figure 5 shows the results obtained for the composite placed in the cavity. At high frequencies of 8.19 and 10.43 GHz, the usual pattern is observed: as the field strength H rises, the transmitted signal amplitude A first reaches a maximum (FMAR) and then a minimum (FMR). For the frequency f = 8.02 GHz, the run of the curve is different. The resonance frequencies of the cavity with the composite inside are difficult to assign to any of the cavity modes, since the permittivity of the composite is not known exactly. Taking for paraffin $\varepsilon \approx 2.05$, we find that the frequency f = 8.02 GHz corresponds most probably to the degenerate modes E_{111} and H_{011}. The field configurations of these modes differ greatly (Fig. 6); therefore, one may assume that simultaneous excitation of these modes and the interference of their fields affect the field dependence at 8.02 GHz.

For applications, the wide variation of the microwave signal is of interest. For example, Fig. 5 shows that the transmitted signal amplitude at 10.43 GHz and H = 4.2 kOe is only 4% of the zero-field amplitude under the FMR condition. In the interval between 3 and 4 kOe, the mean value of the derivative $dA(H)/dH$ is roughly –0.11%/Oe.

The FMR and FMAR conditions were also studied by the technique used in [13]. A 4-cm-long part of the waveguide was filled with the composite, and the field

dependence of the transmitted signal amplitude was measured (Fig. 7). Here, the relative variation of the transmitted signal is noticeably smaller than in the measurements performed in the cavity (see above). The minima in these dependences are related to electromagnetic wave absorption under the FMR conditions. In this case, the transmission coefficient depends on two factors. The first is the composite-to-waveguide impedance ratio $Z(\omega, H)/Z_{10}(\omega)$ at the mode H_{10}. The difference between the impedances causes reflections from the sample boundaries. The second factor is wave attenuation due to absorption. In the FMR case, the field-dependent real part $\mu'(H)$ of the permeability changes sign, passing through zero at the point of FMR, whereas the imaginary part μ'' of the permeability has a minimum under the same conditions. The non-Hermitean imaginary part of the permeability tensor is responsible for electromagnetic wave absorption. Therefore, under the FMR condition, the transmitted signal amplitude goes through a minimum when the signal passes through both the cavity and the waveguide.

Under the FMAR condition, $\mu'(H)$ also changes sign but, in this case, at a small μ'' away from its peak. In this case, the absolute value of the transmission is bound to have a maximum. This maximum is really observed when the sample is in the cavity. It may also be observed when the sample is in the waveguide provided that the length of the sample is much greater than the skin depth, $L \gg \delta$. The classical skin depth is given by $\delta = c(2\pi\omega\mu'\sigma)^{-1/2}$. Our composite has an extremely low conductivity σ, so that the inverse inequality $L \ll \delta$ is valid. The attenuation in the sample is proportional to $\exp(-L/\delta)$. In spite of the significant change in δ under the FMAR condition, the transmitted signal amplitude changes insignificantly.

Figure 8 shows the field dependences of the resonance and antiresonance frequencies, as well as of the FMR linewidth, for the powders. The dependences are nearly linear, with the straight line fitting the data points for the linewidth passing through the origin. If the magnetic field is aligned with one of the axes of a bulk ellipsoidal homogeneous sample, the resonance frequency can be found from the formula [23]

$$\omega^2 = \gamma^2[H - (N_Z - N_X)M_0][H + (N_Y - N_Z)M_0], \quad (1)$$

where M_0 is the saturation magnetization (M_0 = 39 emu/g in our case) and N_X, N_Y, and N_Z are the diagonal elements of the demagnifying factor tensor.

For one-domain particles, the field dependence of the resonance frequency is also almost linear; however, the approximation does not pass through the origin [25], determining the least possible frequency of uniform precession. In our particles of about 5 μm in size, which consisted of several domains at $H = 0$, this feature, typical of ultrafine particles, was not observed.

In the earlier studies of bulk polycrystals of the same composition [16, 24], it was noted that the porosity

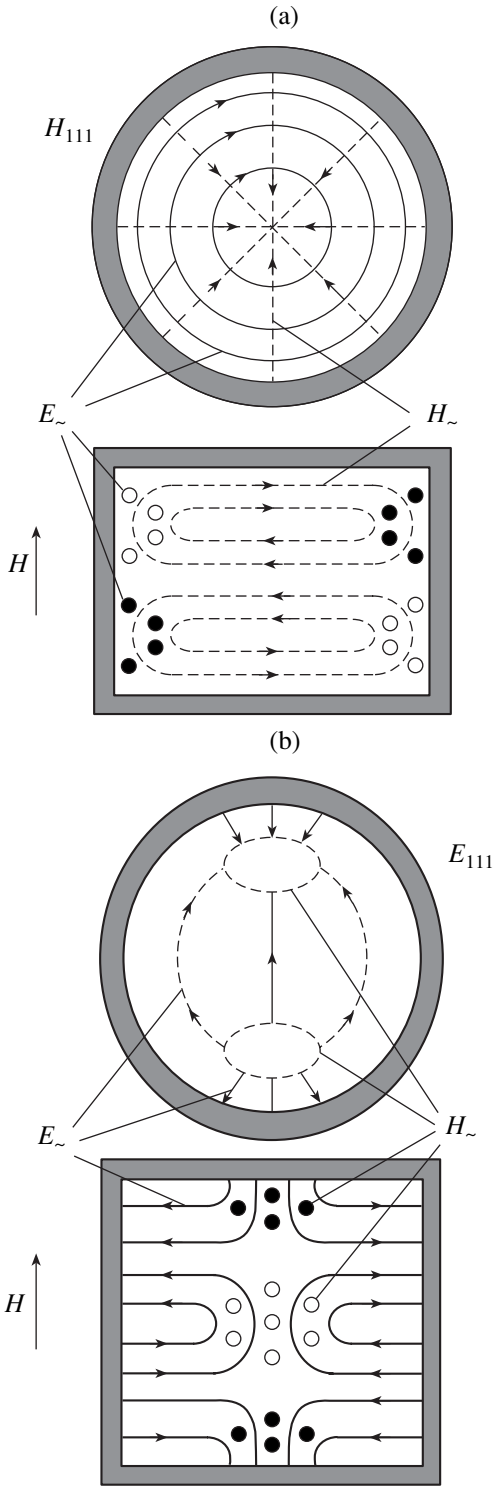

Fig. 6. Microwave field configurations for (a) the mode H_{011} and (b) the mode E_{111} of the cylindrical cavity.

makes a major contribution to the FMR linewidth. This contribution can be estimated from the relationship

$$\Delta H_v = 4\pi M_0 v, \quad (2)$$

where v is the porosity [23].

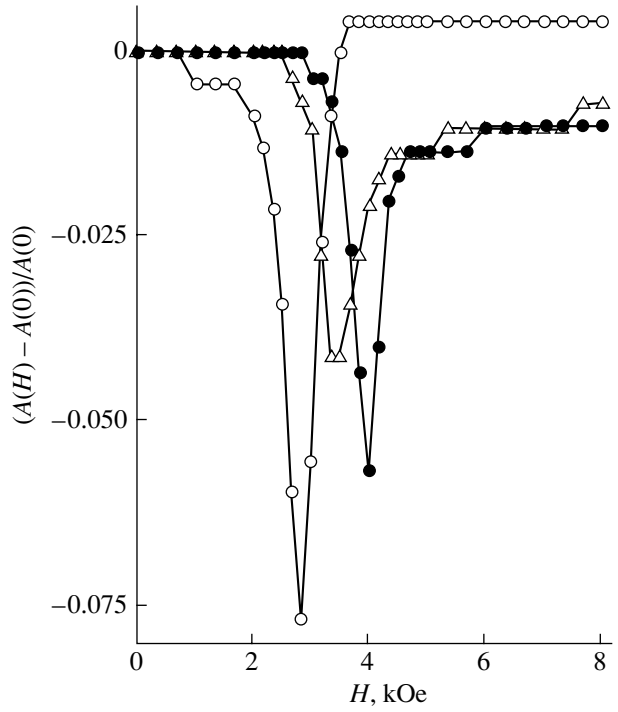

Fig. 7. Relative variation of the amplitude of the signal transmitted through the waveguide with the composite sample inside vs. the magnetic field. (○) 7.50, (△) 8.50, and (●) 10.65 GHz.

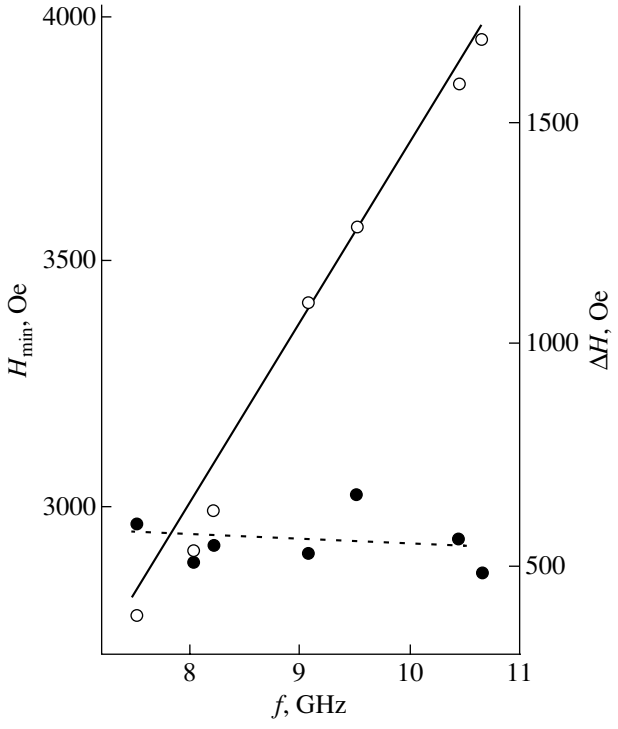

Fig. 8. Frequency dependence of the (○) FMR field H_{min} and (●) FMR linewidth ΔH for the waveguide with the composite sample inside.

For the samples whose density equals 40% of the X-ray value, ΔH_v is estimated as 1.0 kOe. The full FMR linewidth measured in the bulk samples ranged from 1.1 and 1.2 kOe. Clearly, the linewidth depends almost exclusively on the porosity. The density of the powdered manganite was raised to 78% of the X-ray value. Accordingly, the contribution of the porosity was expected to decrease to ~0.4 kOe (that is, the FMR linewidth was expected to narrow appreciably), which was the case, as follows from Fig. 8, where this value equals 0.5–0.6 kOe.

CONCLUSIONS

Absorption and transmission of electromagnetic waves in a composite material consisting of $La_{0.6}Y_{0.07}Ba_{0.33}MnO_3$ manganite powder and paraffin are studied. When placed in a cylindrical resonant cavity, the composite exhibits ferromagnetic resonance and ferromagnetic antiresonance. The former significantly affects the amplitude of the transmitted signal: at f = 10.43 GHz, the resonance amplitude is as low as 4% of the amplitude at H = 0. Such a strong dependence makes it possible to use lanthanum manganite–based composite powders in controllable microwave electronics.

The transmitted signal amplitude does not show ferromagnetic antiresonance when the composite manganite sample is placed in a waveguide. This is because the skin depth in the poorly conducting composite is much smaller than in the bulk polycrystal.

ACKNOWLEDGMENTS

This work was supported by the Russian Foundation for Basic Research and the program “Quantum Macrophysics” of the Presidium of the Russian Academy of Sciences.

REFERENCES

1. J. L. Dorman, D. Fiorani, and E. Tronc, Adv. Chem. Phys. **98**, 283 (1997).
2. G. Viau, F. Fiévet-Vincent, F. Fiévet, *et al.*, J. Appl. Phys. **81**, 2749 (1997).
3. A. J. Aharoni, Appl. Phys. **69**, 7762 (1991).
4. J. Garsia-Otero, M. Porto, J. Rivas, *et al.*, Phys. Rev. Lett. **84**, 167 (2000).
5. Yu. P. Kalmykov and S. V. Titov, Zh. Éksp. Teor. Fiz. **115**, 101 (1999) [JETP **88**, 58 (1999)].
6. U. J. Netzelmann, Appl. Phys. **68**, 1800 (1990).
7. A. H. Thomas, R. W. Chantrell, M. El-Hilo, *et al.*, J. Magn. Magn. Mater. **151**, 54 (1995).
8. F. Gaseau, J. C. Bacri, F. Gendron, *et al.*, J. Magn. Magn. Mater. **186**, 175 (1998).
9. V. P. Shilov, J.-C. Bacri, F. Gaseau, *et al.*, J. Appl. Phys. **85**, 6642 (1999).
10. S. Zhang, S. A. Oliver, N. E. Israeloff, *et al.*, J. Appl. Phys. **81**, 4307 (1997).

11. É. L. Nagaev, Usp. Fiz. Nauk **168**, 917 (1998) [Phys. Usp. **41**, 831 (1998)].
12. K. A. Yates, L. F. Cohen, C. Watine, *et al.*, J. Appl. Phys. **88**, 4703 (2000).
13. B. Heinrich and V. F. Meshcheryakov, Pis'ma Zh. Tekh. Fiz. **9**, 618 (1969) [Sov. Tech. Phys. Lett. **9**, 378 (1969)].
14. S. Tyagi, S. Lofland, M. Dominguez, *et al.*, Appl. Phys. Lett. **68**, 2893 (1996).
15. V. V. Srinivasu, S. E. Lofland, and S. M. Bhagat, J. Appl. Phys. **83**, 2866 (1998).
16. A. Rinkevich, A. Nossov, V. Vassiliev, *et al.*, Phys. Status Solidi A **179**, 221 (2000).
17. S. E. Lofland, S. M. Bhagat, H. L. Ju, *et al.*, Phys. Rev. B **52**, 15058 (1995).
18. J. C. Ramachandran, S. M. Bhagat, J. I. Peng, *et al.*, Solid State Commun. **96**, 127 (1995).
19. A. I. Shames, E. Rosenberg, G. Gorodetsky, *et al.*, Solid State Commun. **107** (3), 91 (1998).
20. A. I. Shames, E. Rosenberg, G. Gorodetsky, *et al.*, J. Magn. Magn. Mater. **203**, 259 (1999).
21. M. Respaud, B. Martinez, L. Balcells, *et al.*, J. Magn. Magn. Mater. **203**, 100 (1999).
22. V. G. Vasil'ev, A. A. Ivakin, and A. A. Fotiev, Zh. Neorg. Khim. **39**, 3 (1994).
23. A. G. Gurevich and G. A. Melkov, *Magnetic Oscillations and Waves* (Fizmatlit, Moscow, 1994) [in Russian].
24. A. Nossov, A. Rinkevich, and R. Zainullina, Fiz. Met. Metalloved. **85**, 428 (1998).
25. W. F. Brown, *Micromagnetics* (Interscience, New York, 1963; Nauka, Moscow, 1979).

Translated by V. Isaakyan

Technical Physics, Vol. 49, No. 6, 2004, pp. 758–763. Translated from Zhurnal Tekhnicheskoĭ Fiziki, Vol. 74, No. 6, 2004, pp. 96–101.

SURFACES, ELECTRON AND ION EMISSION

Identification of Complex Field Emission Spectra (Total Electron Energy Distributions) for Cathodes with a Nonuniform Work Function

E. A. Litvinov*, R. R. Mulyukov, L. R. Zubairov**, Yu. M. Yumaguzin***, and V. A. Ivchenko***

** Institute of Electrophysics, Ural Division, Russian Academy of Sciences, ul. Amundsena 106, Yekaterinburg, 620016 Russia*

*** Institute for Metals Superplasticity Problems, Russian Academy of Sciences, ul. Khalturina 39, Ufa, 450001 Bashkortostan, Russia*

e-mail: linar@imsp.da.ru

**** Bashkir State University, ul. Frunze 32, Ufa, 450074 Bashkortostan, Russia*

Received July 28, 2003

Abstract—Nanocrystalline tungsten specimens are examined by the method of transmission electron microscopy, as well as by field-emission and field-ion techniques. The electron energy distributions taken from nanocrystalline tungsten are shown to differ significantly from those taken of the coarse-grain polycrystal. Analysis shows that the differences are associated with a change in the work function when the metal is transferred to the nanocrystalline state. © *2004 MAIK "Nauka/Interperiodica".*

1. INTRODUCTION

The great interest in nanocrystalline (with grains 10 to 100 nm across) materials [1–3] stems from the fact that their physical properties are far different from those of normal coarse-grain polycrystals. This offers considerable scope for production of materials with desired properties. The properties of nanocrystalline materials are due to a large fraction of grain boundaries, which are in a specific nonequilibrium state [3, 4]. Obviously, one may also expect specific features in their electronic structure.

Field emission spectroscopy as a tool for examining nanocrystalline metals was first applied to nickel [5]. Qualitative and quantitative nanocrystallinity-related changes in the electron energy distributions have been detected. It is noteworthy that two types of the electron distributions depending on the emitting area of the tip have been observed. However, the results of [5] are difficult to analyze, because the area of the microstructure that is responsible for the energy spectra (the bulk of a grain or its near-boundary region) remains unclear.

In this work, we examine the micro- and nanostructure of nanocrystalline metal by transmission electron microscopy, as well as by field-emission techniques, and perform a qualitative analysis of the experimental data.

2. EXPERIMENTAL

The material under investigation was 4N-pure tungsten, a refractory material suitable for emission studies. It was transferred to the nanocrystalline state by applying severe plastic deformations (up to a true logarithmic strain $e = 7$) via torsion under quasi-hydrostatic pressure on a Bridgman anvil. The microstructure of the nanocrystalline specimen was examined with a JEM-2000EX transmission electron microscope [6].

Test specimens that were to be examined in a field ion microscope were prepared by electrochemically etching nanocrystalline tungsten rods to produce emitting tips with a radius of curvature of 30–50 nm. The tips were welded to a nickel ear. The field-ion microscope was equipped with a microchannel ion–electron converter, which enhanced the contrast of surface micrographs 10^4 times. Liquid nitrogen ($T = 78$ K) was used as a coolant, and spectral-grade neon served as an image gas.

Emitters certified for field emission investigation had an atomically smooth near-spherical top, which was prepared by *in situ* evaporation of surface atoms. Surface atoms were controllably removed until a grain boundary was visible in the field-ion image.

A tip thus obtained with a grain boundary in the emitting area was placed in a field-emission spectrometer to study the electronic structure of the material. Measurements were performed in an ultrahigh vacuum (the pressure $<10^{-8}$ Pa). The spectrometer consists of a field-emission microscope for continuous monitoring of the emission pattern and an energy dispersive electrostatic analyzer with a resolution of 30 meV or higher [7].

The emission current at the exit from the analyzer was detected with a secondary-emission electron mul-

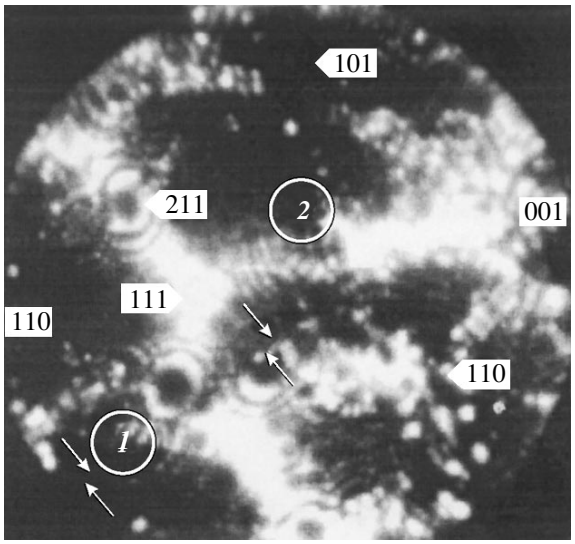

Fig. 1. Field-ion image taken from the nanocrystalline tungsten surface (V = 12 kV) with a grain boundary (indicated by the arrows). Circles *1* and *2* outline surface areas from which the total electron energy distributions shown in Fig. 2 are taken.

tiplier operating in the counting mode. Emission direction selection and tuning to the optical axis of the energy analyzer were accomplished with a special manipulator. The size of an exposed area on the tip surface (≈10 nm) was limited by the size of the hole in the screen (anode). Dedicated software was used to control measurements and data processing with the use of a CAMAC-configured PC. Immediately before measurements, the tip was cleaned by field desorption.

For comparative analysis, measurements were also performed with the tip annealed at 800°C for 20 min by passing the current through the nickel ear.

Deformation working of the tungsten resulted in the homogeneous nanocrystalline structure with a mean grain size of about 100 nm. Tips made of the nanocrystalline tungsten by electrochemical etching had the same structure.

Figure 1 shows the field-ion image of the nanocrystalline tungsten surface with a grain boundary. This image was obtained after 106 atomic layers had been evaporated from the (110) face. The atomic structure of grain boundaries was studied in the course of evaporation of 43 layers. As an object of further field-emission investigation, we used a large-angle boundary (indicated by the arrows in Fig. 1). The structure of this boundary in the bulk was studied by controllable evaporation of surface atoms, and it turned out that it differs from the structure of grain boundaries in plastically undeformed tungsten. According to our estimates based on the field-ion images of different surface areas, the width of an individual grain boundary falls into the interval 0.6–0.8 nm. In undeformed tungsten, this value ranges from 0.3 to 0.4 nm.

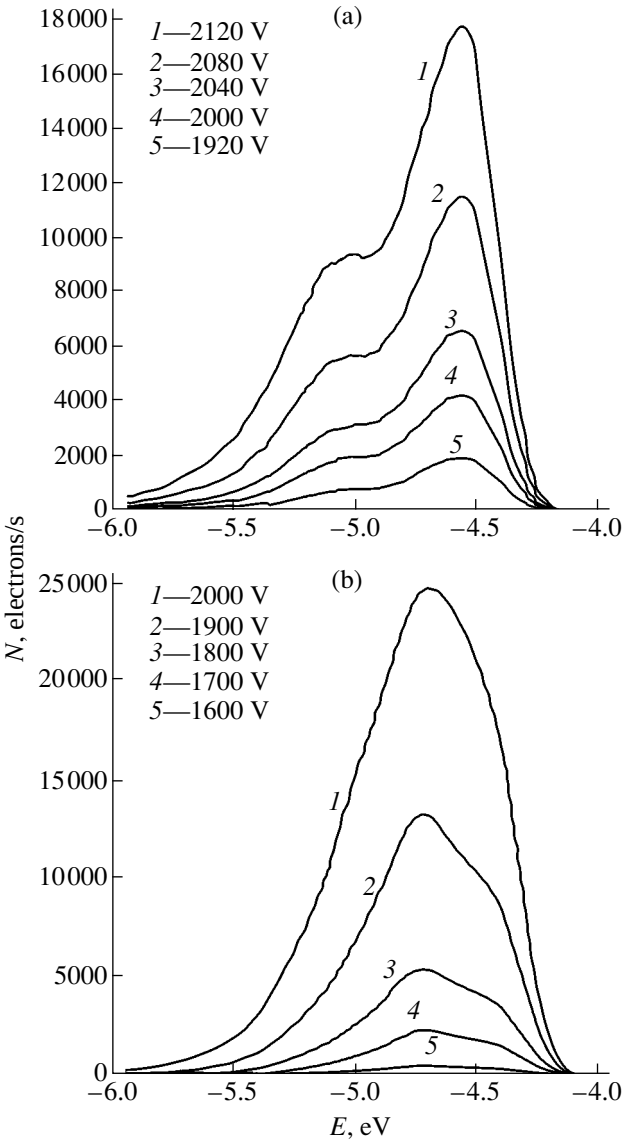

Fig. 2. Total electron energy distributions for different emission voltages. The distributions are taken from different parts of the emission image shown in Fig. 1.

The surface of the tip smoothed in the field-ion microscope to the atomic level was then examined in the field-emission spectrometer. The energy distribution of field-emitted electrons was taken from different areas of the emitting tip surface, which were selected from the emission image. While the resolution of a field-electron image is one order of magnitude poorer than that of a field-ion image, the two images, when combined, allow one to uniquely identify the microstructure of the areas from which the electron energy distributions were taken.

Three typical total electron energy distributions depending on the emitting area on the emitter surface were obtained. The spectra taken from the areas with the grain boundary either exhibit an extra peak in the

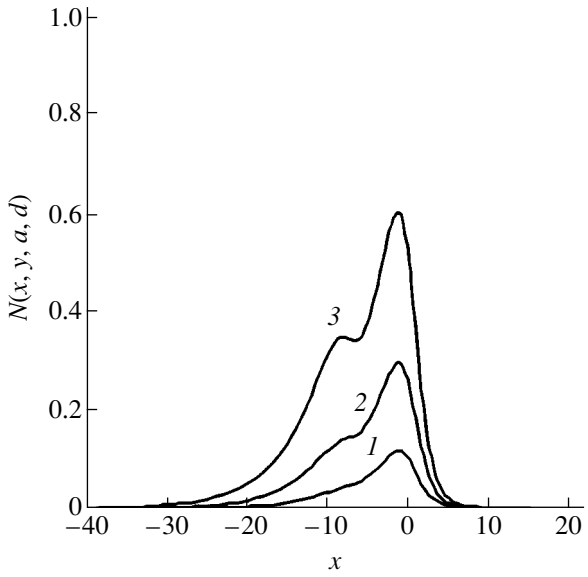

Fig. 3. Set (iv) of the parameters. In set (iii), the parameter a decreases slightly with increasing E. (*1*) $N(x, y_1, a_1, d_1)$, (*2*) $N(x, y_2, a_2, d_2)$, and (*3*) $N(x, y_3, a_3, d_3)$.

low-energy range or have a kink in the high-energy range (Fig. 2). As the emission voltage grows, so does the extra peak (Fig. 2a), while the kink smooths out (Fig. 2b).

In the areas away from the grain boundary, the shape of the distribution is close to that of the normal distribution. However, the FWHM of the related spectrum far exceeds (roughly by 0.4 eV) the FWHM of the conventional spectrum [8] and equals 0.58–0.64 eV.

As was shown previously [9], annealing of nanocrystalline specimens recovers their physical properties and microstructure. In our work, *in situ* annealing at a temperature of 800°C for 20 min resulted in partial recovery of the energy distribution of the electrons emitted. Only one-peak spectra were detected, their FWHM narrowing to 0.45–0.60 eV.

Thus, the energy characteristics of the electrons emitted from the nanocrystalline metal were found to differ substantially from those of the electrons emitted from the coarse-grain polycrystal. This difference may be related to a difference in the material microstructure, particularly, to an increased fraction of grain boundaries, which are in the specific nonequilibrium state. It was shown [10] that grain boundaries have an effective physical width of about 10 nm, which far exceeds their crystallographic width, and atoms within the physical width have a decreased Debye temperature and an increased energy [11]. In general, nanocrystalline material may be viewed as consisting of two, grain and grain-boundary, phases. The former has the properties of normal single crystals or coarse-grain polycrystals. The properties of the latter differ from those of the former, and their values are fixed.

3. TREATMENT OF EXPERIMENTAL DATA

To treat our experimental data, we will proceed as follows. We represent, following [5], the experimental total energy distribution of emitted electrons in the form

$$N = \frac{j}{e} St(x, y), \tag{1}$$

where

$$f(x, y) = \frac{(\exp(x))^y}{1 + \exp(x)}, \tag{2}$$

$$x = \frac{\varepsilon - \varepsilon_F}{kT}, \tag{3}$$

$$y = \frac{T}{2T_i} = \frac{8\pi\sqrt{2m\varphi}\,\eta\left(\frac{\sqrt{e^3E}}{\varphi}\right)}{2ehE} kT. \tag{4}$$

Here, j is the field-emission current density, e is the elementary charge, S is the effective emitting surface area, ε_F is the Fermi energy, k is the Boltzmann constant, T is the absolute temperature, h is the Planck constant, m is the electron mass, φ is the work function, E is the electric field strength, T_i is the inversion temperature, and $\eta(\sqrt{e^3E}/\varphi)$ is a slowly varying function [12].

We assume that, at a grain boundary in the nanocrystalline material, emission takes place from two areas with differing work functions and Fermi energies:

$$\begin{aligned} N = N_1 + N_2 &= \frac{j_1}{e} S_1 f_1(x, y) + \frac{j_2}{e} S_2 f_2(x, y) \\ &= \frac{j_1}{e} S_1 [f_1(x, y) + a f_2(x, y)], \end{aligned} \tag{5}$$

where

$$a = \frac{j_2 S_2}{j_1 S_1}, \tag{6}$$

$$f_1(x, y) = \frac{(\exp(x))^y}{1 + \exp(x)}, \tag{7}$$

$$f_2(x, y) = \frac{(\exp(x - b))^{cy}}{1 + \exp(x - b)}, \tag{8}$$

$$b = \frac{\varepsilon_{F_2} - \varepsilon_{F_1}}{kT} = \frac{\Delta\varepsilon_F}{kT}, \tag{9}$$

$$c = \frac{T_{i_1}}{T_{i_2}} \approx \frac{\sqrt{\varphi_2}}{\sqrt{\varphi_1}}. \tag{10}$$

The values of $\Delta\varepsilon_F$ and $\varphi_2 = \varphi_1 + \Delta\varphi$ will be found in terms of the following model. Conduction electrons

that may be emitted are in a potential well with Coulomb ion–electron interaction:

$$\varphi_{tot} = e^2 n^{1/3}, \quad (11)$$

where φ_{tot} is the total work function in the process of electron emission and n is the concentration of conduction electrons or ions.

The Fermi energy is given by

$$\varepsilon_F = \frac{h^2}{2m}\left(\frac{3}{8\pi}n\right)^{2/3}, \quad (12)$$

and the emission work function is

$$\varphi = \varphi_{tot} - \varepsilon_F. \quad (13)$$

A change in the parameters φ_{tot}, ε_F, and φ is related to a change in the concentration n due to deformation. Then,

$$\Delta\varphi_{tot} = \frac{1}{3}\varphi_{tot}\frac{\Delta n}{n}, \quad (14)$$

$$\Delta\varepsilon_F = \frac{2}{3}\varepsilon_F\frac{\Delta n}{n}, \quad (15)$$

$$\Delta\varphi = \frac{1}{3}(\varphi - \varepsilon_F)\frac{\Delta n}{n}. \quad (16)$$

Without going into the physics of the process, we will study the functions $f_1(x, y)$, $f_2(x, y)$, and $f(x, y) = f_1 + af_2$ formally under certain assumptions concerning φ, ε_F, and Δn.

(i) Let $\varphi - \varepsilon_F < 0$ and $\Delta n > 0$; then, $\Delta\varepsilon_F > 0$, $\Delta\varphi < 0$, a increases with increasing electric field strength E, $b > 0$, and $c \le 1$. For $y = 0.2$, $a = 0.9$, $b = 4.5$, and $c = 0.9$, the functions $f_1(x)$ and $f_2(x)$ are comparable in amplitude, $f_2(x)$ is shifted to the right along the energy scale, and the sum $f_1(x) + af_2(x)$ yields a right-hand broadening (the right-hand hump in Fig. 2b). The contributions of the areas with lower and higher work functions are comparable to each other.

(ii) $\varphi - \varepsilon_F < 0$, $\Delta n < 0$, $\Delta\varepsilon_F < 0$, $\Delta\varphi > 0$, a decreases with increasing electric field strength E, $b < 0$, and $c \ge 1$. For $y = 0.2$, $a = 0.3$, $b = 0.9$, and $c = 1.1$, the function $f_2(x)$ is shifted to the left, and the sum $f_1(x) + af_2(x)$ yields an extra left-hand peak (Fig. 2a). The area with a higher work function makes a small contribution.

(iii) $\varphi - \varepsilon_F > 0$, $\Delta n > 0$, $\Delta\varepsilon_F > 0$, $\Delta\varphi > 0$, a decreases with increasing E, $b > 0$, and $c \ge 1$. For $y = 0.2$, $a = 0.9$, $b = 4.5$, and $c = 1.01$, the contributions from the areas with lower and higher work functions are comparable to each other, and the sum yields a right-hand broadening (Fig. 2b).

(iv) $\varphi - \varepsilon_F > 0$, $\Delta n < 0$, $\Delta\varepsilon_F < 0$, $\Delta\varphi < 0$, a increases with increasing E, $b < 0$, and $c \le 1$. For $y = 0.2$, $a = 0.3$, $b = 8$, and $c = 0.9$, the contribution of the area with a lower work function is small. The sum $f_1 + af_2$ yields an additional left-hand peak (Fig. 2a).

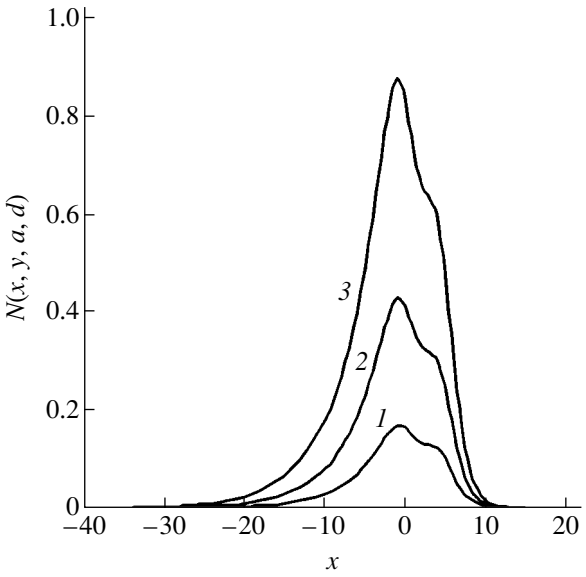

Fig. 4. Calculation results. (*1*) $N(x, y_1, a_1, d_1)$, (*2*) $N(x, y_2, a_2, d_2)$, and (*3*) $N(x, y_3, a_3, d_3)$.

Experiment shows that, as E grows, the left-hand peak becomes more pronounced, a grows slightly, and the factor $d = (j_1/e)S_1$ grows significantly:

$$y_1 = 0.22, \quad y_2 = 0.21, \quad y_3 = 0.2,$$
$$a_1 = 0.1, \quad a_2 = 0.2, \quad a_3 = 0.3, \quad b = -8,$$
$$c = 0.9, \quad d_1 = 0.2, \quad d_2 = 0.5, \quad d_3 = 1,$$

$$f_1(x, y_1) = \frac{(\exp(x))^{y_1}}{1 + \exp(x)}, \quad f_1(x, y_2) = \frac{(\exp(x))^{y_2}}{1 + \exp(x)},$$

$$f_1(x, y_3) = \frac{(\exp(x))^{y_3}}{1 + \exp(x)},$$

$$f_2(x, y_1) = \frac{(\exp(x-b))^{cy_1}}{1 + \exp(x-b)},$$

$$f_2(x, y_2) = \frac{(\exp(x-b))^{cy_2}}{1 + \exp(x-b)},$$

$$f_2(x, y_3) = \frac{(\exp(x-b))^{cy_3}}{1 + \exp(x-b)},$$

$$N_1(x, y_1, a_1, d_1) = (f_1(x, y_1) + a_1 f_2(x, y_1))d_1,$$
$$N_2(x, y_2, a_2, d_2) = (f_1(x, y_2) + a_2 f_2(x, y_2))d_2,$$
$$N_3(x, y_3, a_3, d_3) = (f_1(x, y_3) + a_3 f_2(x, y_3))d_3;$$

$$y_1 = 0.22, \quad y_2 = 0.21, \quad y_3 = 0.2,$$
$$a_1 = 0.97, \quad a_2 = 0.95, \quad a_3 = 0.93, \quad b = 5,$$
$$c = 1.01, \quad d_1 = 0.2, \quad d_2 = 0.5, \quad d_3 = 1,$$

$$f_1(x, y_1) = \frac{(\exp(x))^{y_1}}{1 + \exp(x)}, \quad f_1(x, y_2) = \frac{(\exp(x))^{y_2}}{1 + \exp(x)},$$

$$f_1(x, y_3) = \frac{(\exp(x))^{y_3}}{1 + \exp(x)},$$

$$f_2(x, y_1) = \frac{(\exp(x-b))^{cy_1}}{1 + \exp(x-b)},$$

$$f_2(x, y_2) = \frac{(\exp(x-b))^{cy_2}}{1 + \exp(x-b)},$$

$$f_2(x, y_3) = \frac{(\exp(x-b))^{cy_3}}{1 + \exp(x-b)},$$

$$N_1(x, y_1, a_1, d_1) = (f_1(x, y_1) + a_1 f_2(x, y_1))d_1,$$

$$N_2(x, y_2, a_2, d_2) = (f_1(x, y_2) + a_2 f_2(x, y_2))d_2,$$

$$N_3(x, y_3, a_3, d_3) = (f_1(x, y_3) + a_3 f_2(x, y_3))d_3.$$

According to definition, the parameters *y*, *a*, and *d* might be taken as function of *E*. However, such an approach seems unreasonable, since the local work function and possible *E* dependences of S_1 and S_2 are unknown. The data listed above are obtained from the numerical experiment aimed at finding a set of parameters that adequately characterize the physical experiment.

The numerical data suggest that set (iv) is the most adequate. This set corresponds to the grain boundary. At a small distance from the boundary, the right-hand kink, corresponding to set (iii), appears. Sets (iii) and (iv) meet the condition $\varphi - \varepsilon_F > 0$. As follows from [13], the emission work function of tungsten is $\varphi = 4.52$ eV, $\varphi_{tot} = (12.5 - 10.35)$ eV, $n = 1.05 \times 10^{23}$ cm^{-3}, and $\varphi - \varepsilon_F < 0$. Thus, the isotropic model for work function comes into conflict with experimental data. The contradiction can be removed as follows. Suppose that deformation resulting in the nanocrystalline structure causes the concentration to vary only in a certain crystallographic direction:

$$(\Delta n)^{1/3} = \Delta n_z, \tag{17}$$

where n_z is the linear concentration.

Then,

$$\varphi_{tot} = e^2 n_z, \tag{18}$$

$$\varepsilon_F = \frac{h^2}{2m}\left(\frac{3}{8\pi} n_x n_y n_z\right)^{2/3}. \tag{19}$$

Next,

$$\Delta\varphi_{tot} = \varphi_{tot}\frac{\Delta n_z}{n_z}, \tag{20}$$

$$\Delta\varepsilon_F = \frac{2}{3}\varepsilon_F\frac{\Delta n_z}{n_z}, \tag{21}$$

$$\Delta\varphi = \left(\varphi + \frac{1}{3}\varepsilon_F\right)\frac{\Delta n_z}{n_z}. \tag{22}$$

Relationship (22) meets cases (iii) and (iv). It should be noted that expressions (17)–(22) clearly, while not rigorously, demonstrate the effect of this anisotropy on the work function. A correct model of this effect should be elaborated [14].

The question may arise as to whether it is possible to speak of electron emission from different Fermi levels when emitting metal areas are in electric contact. In our opinion, one may draw on the concept of "spots," which assumes that the work function is nonuniformly distributed over an emitting surface and depends on an external electric field [15]. Next, the work function has the irreversible component, which is related to Joule dissipation of surface currents (these current generate the image force potential) [15]. An emitting surface is not equipotential, but nonuniformities do not affect the integral emission characteristics. We estimate the spot field at a level of $E \le 10^5$ V/cm. External fields used in practice are evidently higher. This validates the above reasoning. An electron leaving a certain area of an emitting surface is either accelerated or decelerated by the contact potential difference, then it is accelerated by the external field, and finally again decelerated to the initial energy to satisfy spectrum recording conditions. Thus, prior to detection, electrons emitted from different areas gain different energies, which reflects on the spectrum and can be characterized as above.

The conclusions that can be drawn from our analysis are as follows. In the nanocrystalline material, current filaments with a decreased (grain boundaries) and increased (regions at a small distance from grain boundaries) work function arise. Such a pattern forms when deformation changes the packaging density in different crystallographic planes. Our investigation opens up the way to searching for materials where this effect shows is more pronounced, making them promising for efficient emitting arrays.

The investigation technique suggested in this work may be helpful in studying the electronic properties of novel materials.

ACKNOWLEDGMENTS

This work was supported by the Russian Foundation for Basic Research (grant nos. 02-02-96415, 02-02-17509, 03-02-16560, and 02-01-97924) and the program "Fundamental Problems in Physics and Chemistry of Nanodimensional Systems and Nanomaterials (Russian Academy of Sciences).

REFERENCES

1. I. D. Morokhov, L. I. Trusov, and V. I. Lapovok, *Physical Phenomena in Ultradispersive Media* (Nauka, Moscow, 1984) [in Russian].
2. R. Birringer and H. Gleiter, *Encyclopedia of Materials Science and Engineering*, Ed. by R. W. Cahn (Pergamon, Oxford, 1988), Vol. 1.
3. A. A. Nazarov and R. R. Mulyukov, *Handbook of Nanoscience, Engineering and Technology*, Ed. by W. Goddard, D. Brenner, S. Lyshevsk, and G. Iafrate (CRC, Boca Raton, 2002).
4. O. A. Kaĭbyshev and R. Z. Valiev, *Grain Boundaries and Properties of Metals* (Metallurgiya, Moscow, 1987) [in Russian].
5. L. R. Zubairov, E. A. Litvinov, R. R. Mulyukov, *et al.*, Dokl. Akad. Nauk **372**, 319 (2000) [Dokl. Phys. **45**, 198 (2000)].
6. N. I. Noskova, E. G. Volkova, R. R. Mulyukov, *et al.*, in *Proceedings of the International Conference "Current Status of Theory and Practice of Superplasticity in Materials," 2000*, pp. 167–173.
7. R. Z. Bakhtizin, V. M. Lobanov, and Yu. M. Yumaguzin, Prib. Tekh. Éksp., No. 4, 247 (1987).
8. A. Modinos, *Field, Thermionic and Secondary Electron Emission Spectroscopy* (Plenum, New York, 1984; Nauka, Moscow, 1990).
9. R. R. Mulyukov and M. D. Starostenkov, Acta Metall. Sin. **13**, 301 (2000).
10. V. A. Shabashov, V. V. Ovchinnikov, R. R. Mulyukov, *et al.*, Nanostruct. Mater. **11**, 1017 (1999).
11. R. R. Mulyukov, Metalloved. Term. Obrab. Met., No. 8, 34 (1998).
12. M. I. Elinson and G. F. Vasil'ev, *Field Electron Emission* (GIFML, Moscow, 1958) [in Russian].
13. V. L. Granovskiĭ, *Electric Current in Gas*, Vol. 1: *Fundamentals of Gas Electrodynamics* (Nauka, Moscow, 1952) [in Russian].
14. V. S. Fomenko, *Emission Properties of Materials: A Handbook* (Naukova Dumka, Kiev, 1981) [in Russian].
15. L. N. Dobretsov and M. V. Gomoyunova, *Emission Electronics* (Nauka, Moscow, 1966) [in Russian].

Translated by V. Isaakyan

Technical Physics, Vol. 49, No. 6, 2004, pp. 764–769. Translated from Zhurnal Tekhnicheskoĭ Fiziki, Vol. 74, No. 6, 2004, pp. 102–108.

SURFACES, ELECTRON AND ION EMISSION

Effect of a Pulsed Magnetic Field on the Nonlinear Dynamics of Vortexlike Domain Walls in Magnetic Films

B. N. Filippov, L. G. Korzunin, and F. A. Kassan-Ogly

Institute of Metal Physics, Ural Division, Russian Academy of Sciences, ul. S. Kovalevskoĭ 18, Yekaterinburg, 620219 Russia

e-mail: filbor@imp.uran.ru

Received September 22, 2003

Abstract—The Landau–Lifshitz equation is numerically solved to study the nonlinear dynamic behavior of domain walls with the 2D vortexlike magnetization distribution in magnetically uniaxial films that have in-plane anisotropy and are exposed to a pulsed magnetic field. It is shown that a pulsed magnetic field H_p may induce transitions between various steady wall motions that differ in magnetization distribution. Solitary rectangular pulses, as well as a regular train of rectangular pulses, may be used to control the period of nonlinear dynamic transformations of the wall internal structure and the related period of variation of the wall velocity. © *2004 MAIK "Nauka/Interperiodica".*

INTRODUCTION

Asymmetric domain walls (DWs) featuring the vortexlike magnetization distribution are known to form in magnetically uniaxial film with the easy magnetic axis parallel to their surface [1–3], as well as in films with cubic anisotropy [4, 5]. Studies indicate that such a structure is present in a wide range of film thicknesses and magnetic parameters. The vortexlike structure of DWs in magnetic films seems more realistic than the structure of simple Bloch walls, since the former makes it possible to completely close the magnetic flux in the sample. To date, a series of experimental data indicating the presence of such walls have been obtained [4–8].

Under dynamic conditions, a vortexlike DW behaves as a topological soliton with intrinsic degrees of freedom. In higher-than-critical (H_c) constant magnetic fields aligned with the easy magnetic axis (EMA), the motion of DWs causes the dynamic reconfiguration of their internal structure, which, in turn, causes the oscillatory behavior of the DW velocity in time. Such behavior has been predicted in [8], and the discovery of this effect is certainly a great stride forward in the physics of nonlinear phenomena.

Deep insight into the nonlinear dynamics of DWs is necessary for an understanding of the genesis of practically important magnetic properties, such as electromagnetic loss, noise intensity, magnetization reversal time, etc. Estimation of these parameters based on the early idea of Bloch walls is currently inadequate. It has been shown in particular [9] that, if the vortexlike structure of DWs is taken into account, the effective mass of the walls differs by two orders of magnitude from the estimate based on the 1D magnetization distribution (Bloch walls). To date, much progress has been made toward understanding the nonlinear dynamics of DWs with the asymmetric vortexlike structure [9–13]. However, the motion of DWs was considered only in constant external magnetic fields.

From the practical standpoint, nonlinear dynamics of the walls in pulsed magnetic fields is of greater interest. Under dynamic conditions, one can estimate, e.g., the parameters of pulsed magnetization reversal or the dynamic properties of sensing heads.

These studies will undeniably discover new physical effects of practical value.

To date, papers considering the effect of a pulsed magnetic field on the nonlinear dynamics of vortexlike DWs and on the nonlinear dynamic reconfiguration of their internal structure in magnetic films are lacking. This work is an attempt to fill this gap.

PROBLEM DEFINITION AND SOLUTION METHODS

Consider a magnetically uniaxial film of thickness b whose surface is parallel to the plane xz and the EMA is aligned with the z axis (Fig. 1). Let the film have two domains with magnetizations $\pm\mathbf{M}_s$ directed along $+z(-z)$ at $x > a/2$ ($x < -a/2$). We assume that the DW is located in a volume V of rectangular cross section D in the xz plane and has a dimension a along the x axis. Let the magnetization in D be $\mathbf{M} = \mathbf{M}(x, y)$; that is, we are dealing with a 2D model of magnetization distribution.

The nonlinear dynamics of the DW was studied by numerically solving the Landau–Lifshitz equation

$$(1 + \alpha^2)\frac{\partial \mathbf{u}}{\partial \tau} = -[\mathbf{u} \times \mathbf{h}_{\text{eff}}] - \alpha[\mathbf{u} \times [\mathbf{u} \times \mathbf{h}_{\text{eff}}]], \quad (1)$$

where $\tau = \gamma M_s t$; γ is the gyromagnetic ratio; t is the real

time; α is the Gilbert damping parameter; and

$$\mathbf{h}_{\text{eff}} = \mathbf{h}_e + \mathbf{h}^{(m)} - k_{\text{A}}(\mathbf{u}\cdot\mathbf{c})\mathbf{c} + \mathbf{h}, \quad (2)$$

is the effective dimensionless field with

$$\mathbf{h}_e = \frac{\partial^2\mathbf{u}}{\partial\xi^2} + \frac{\partial^2\mathbf{u}}{\partial\eta^2},\ \mathbf{h}^{(m)} = \mathbf{H}^{(m)}/M_{\text{s}},$$

$$\mathbf{h} = \mathbf{H}/M_{\text{s}},\ \ \mathbf{u} = \mathbf{M}/M_{\text{s}},$$

$$k_{\text{A}} = 2K/M_{\text{s}},\ \xi = x/b_0,\ \eta = y/b_0,\ b_0 = (A/M_{\text{s}}^2)^{1/2}.$$

Here, K is the constant of uniaxial magnetic anisotropy, $M_{\text{s}} = |\mathbf{M}_{\text{s}}|$ is the saturation magnetization, A is the exchange interaction parameter, $\mathbf{H}^{(m)}$ is the field strength determined from the equations of magnetostatics, and $\mathbf{c}$ is the unit vector along the anisotropy axis. Equation (1) was solved subject to the boundary conditions [10, 11]

$$\left[\mathbf{u}\times\frac{\partial\mathbf{u}}{\partial x}\right]\Bigg|_{y=\pm b/2} = 0, \quad (3)$$

$$u_z|_{x=\pm a/2} = \pm 1;\ u_x|_{x=\pm a/2} = u_y|_{x=\pm a/2} = 0. \quad (4)$$

The domain of calculation D is covered by a fine-mesh rectangular grid so that the volume V is partitioned into parallelepipeds extending along the z axis with their side walls running parallel to the planes xz and yz. The meshes are assumed to be macroscopic but small enough, so that the direction u may be considered constant at any point of each of the parallelepipeds. Also, $\mathbf{u}$ = const along the z axis (the model is two-dimensional). The orientation of $\mathbf{u}$ in D changes from mesh to mesh (for details, see [9–11]). When solving the equation, we used the predictor–corrector method [14]. At the time $\tau = 0$, the initial distribution of $\mathbf{u}_0$ is set by numerically minimizing the DW energy functional, which involves the exchange, magnetically anisotropic, and dipole–dipole (in a continuum approximation) components [10–13]. At the first stage, the iterative term $\mathbf{u}_{n+1}$ is given by the formula (predictor)

$$\mathbf{u}^*_{n+1} = \mathbf{u}_n + \Delta\tau\mathbf{f}(\tau_n, \mathbf{u}_n), \quad (5)$$

where

$$\mathbf{f}(\tau_n, \mathbf{u}_n) = -\frac{1}{1+\alpha^2}$$

$$\times([\mathbf{u}_n\mathbf{h}_{\text{eff}}\cdot(\mathbf{u}_n)] + \alpha[\mathbf{u}_n\times[\mathbf{u}_n\times\mathbf{h}_{\text{eff}}]]).$$

At the second stage, the final form of $\mathbf{u}_{n+1}$ is found (corrector):

$$\mathbf{u}_{n+1} = \mathbf{u}_n + \Delta\tau\mathbf{f}(\tau_n, \mathbf{u}^*_{n+1}). \quad (6)$$

The time step $\Delta\tau$ is taken to be variable, and the maximal angle of rotation of the vector $\mathbf{M}$ in the meshes is limited by a certain small value.

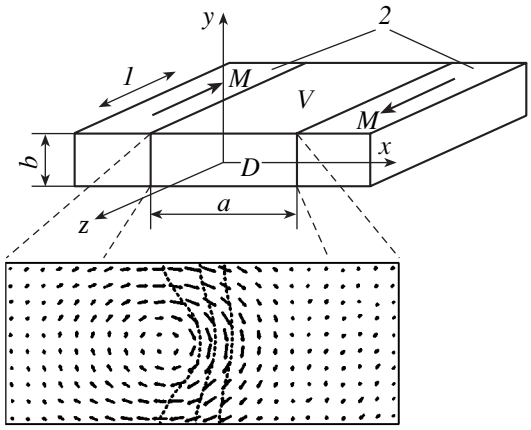

Fig. 1. Problem geometry and equilibrium configuration of a vortexlike asymmetric Bloch wall (the film thickness is 0.05 μm). The arrows indicate the projections of the relative magnetization $\mathbf{u}$ onto the plane xy. (*1*) EMA and (*2*) domains.

The application of random perturbations of any amplitude at any time t, as well as the possibility of starting from any configuration of $\mathbf{M}$, allows us to judge the stability of solutions obtained.

In order that the wall does not appear at the boundary of the volume V, allowance for a shift of this volume as the wall moves is provided. Simultaneously, the movement of the DW central line, where $u_x^4 + u_y^4$ reaches a maximum, is traced.

The above procedure, which allows for the determination of the initial distribution of $\mathbf{u}$, rapidly gives stable solutions. As the initial configuration, we always took the configuration of $\mathbf{M}$ shown in Fig. 1 (a DW with such a magnetization distribution is called an asymmetric Bloch wall). Grids with different numbers of meshes and different ratios a/b were used. The maximal number of meshes were 90×30, and the ratio a/b was varied in the interval $1 \le a/b \le 6$.

Figure 1 shows the distribution of $\mathbf{u}$ in the plane xy, which is perpendicular to the surface of the film and EMA. The vortexlike magnetization distribution is observed. In going from one domain to the other, the z component of $\mathbf{u}$ also changes. At the central (dashed) line $y = y_0(x)$, $u_z = 0$ (the DW center). Thus, the position x of the DC center depends on the depth. It is the asymmetry of this line about the y axis that gives grounds to call this wall asymmetric. Two other lines are lines u_z = const between which the direction of $\mathbf{u}$ changes by approximately 60°.

The basic parameters of the films were $A = 10^{-6}$ erg/cm, $K = 10^{-3}$ erg/cm^3, and $M_{\text{s}} = 800$ G. These values are typical of Permalloy films.

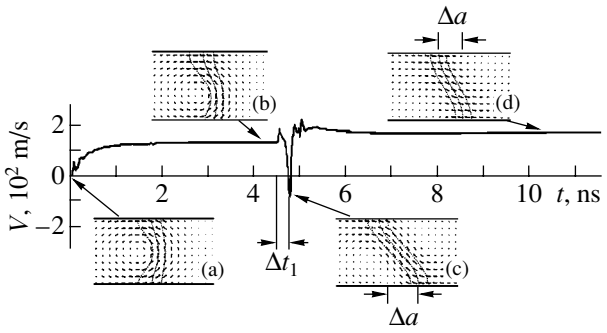

Fig. 2. The time dependence of the wall velocity averaged over the film thickness (continuous curve) and (a–d) instantaneous wall configurations, which illustrate the nonlinear dynamic reconfiguration of the wall at the pulse width $\Delta t_1 = \Delta t_m$ in the 0.05-μm-thick films with $\alpha = 0.1$.

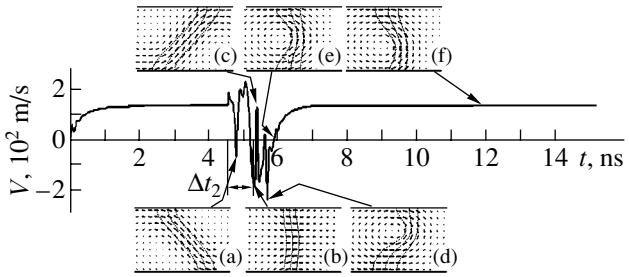

Fig. 3. The same as in Fig. 2 for the pulse width $\Delta t_2 = \Delta t_M$.

RESULTS AND DISCUSSION

We studied the dynamic behavior of DWs subjected to both solitary magnetic pulses of amplitude H_p and a regular (periodic) train of pulses. The pulsed magnetic field was applied along the EMA (the *z* axis). Two situations were considered: (i) the pulsed field is imposed on a constant magnetic field *H*, which is above or below H_c) and is also aligned with the *z* axis, and (ii) $H = 0$. Films under study had different thicknesses, magnetic parameters, and damping parameters.

As was mentioned above, at fields somewhat higher than H_c, the wall moves in such a way that its internal structure and velocity vary periodically [9, 10]. It is significant that two, rather than one, types of motion take place at $H < H_c$. They differ in internal dynamic structure of the wall. For $H < H_0$, the structure is similar to that shown in Fig. 1 but the vortex shifts toward one of the film surfaces. For $H_0 < H < H_c$, the dynamic structure of the wall is an asymmetric Néel structure (see [2] and the discussion which follows). That is, the field H_0 is the field of wall reconfiguration. Then, it might be expected that the behavior of the wall will considerably depend on whether or not the total field $H_t = H + H_p$ exceeds H_c, even if $H < H_c$.

We will concentrate on the most interesting situations, which arise when (i) $H < H_c$ but $H_t > H_c$ and (ii) $H > H_c$.

Consider case (i). Figures 2 and 3 demonstrate the time variation of the film-thickness-averaged velocity of the wall for two different pulse durations Δt_1 and Δt_2 and the respective instantaneous magnetization configurations. Either of the pulses was applied after the steady (i.e., uniform) motion of the wall in the field $H =$ 90 Oe has been established. The fixed distribution of **M** in the wall moving with a certain constant velocity will be called the steady state of the wall.

Seemingly, after the action of the pulse, the structure of the wall must relax to the initial steady state shown in Fig. 2b. Actually, however, this takes place only under certain conditions (see below). Figures 2 and 3 describe a more intriguing situation. Specifically, it is distinctly seen that, first, the transition to the steady motion depends on the pulse duration and, second, the final state (the magnetization distribution after the pulse-induced transient is completed) also depends on the pulse duration. Thus, transitions from one steady state to another are observed. During these transitions, the considerable nonlinear dynamic reconfiguration of the internal structure of the walls occurs. Consider this point in greater detail. When an external magnetic field ($H = 90$ Oe) is applied upon the completion of the short (about 0.18 ns) transient associated with the shift of the intrawall vortex toward the lower surface of the film (transition $2a \longrightarrow 2b$), the steady motion of the wall with a velocity roughly equal to 155 m/s is established (Figs. 2, 3). Then, after the application of a rectangular pulse with an amplitude $H_p = 90$ Oe and duration $\Delta t_1 =$ 0.25 ns, the vortex continues moving to the lower surface and the wall reconfigures into an asymmetric Néel wall as shown in Fig. 2c. At this step, the velocity of the wall turns out to be the lowest and the swing Δa of its central line (the distance between the projections of the extreme points onto any of the film surface), the largest. If the pulse is switched off at this time (the width Δt_1 corresponding to this time will be referred to as minimal and designated by Δt_m), the swing Δa, along with the velocity, starts oscillating. A new steady state of the wall with the structure shown in Fig. 2d ($\Delta a_1 < \Delta a$) is gradually established. In this new state, the velocity of the wall is other than that of the wall with the structure shown in Fig. 2b.

If a pulse of amplitude $H_p = 90$ Oe and duration $\Delta t_2 = 0.65$ ns is applied after the steady motion of the wall with the structure shown in Fig. 2b has been reached, the dynamic reconfiguration of the internal structure proceeds in a different manner. After the pulse has been switched on, the wall turns into an asymmetric Néel wall (Fig. 3a), as in the previous case. When the pulse is switched off, the wall structure becomes similar to the structure of a normal Néel wall (Fig. 3b). The corresponding value of Δt_2 is designated by Δt_M. This is

the minimal value for Δt_2 and, at the same time, the maximal value for Δt_1. According to Fig. 3, the wall experiences profound reconfiguration: the structure shown in Fig. 3b turns into the structure shown in Fig. 3c. The latter also represents an asymmetric Néel wall but with opposite chirality and an opposite slope of the central line. Near the upper surface of the film, an asymmetric vortex originates. Its chirality is opposite to the chirality of the initial asymmetric vortex (Fig. 2b), and the wall turns into an asymmetric Bloch wall with a vortex shifted toward the upper surface of the film (Fig. 3d). Finally, as this vortex moves through the center of the film (Fig. 3e) toward the lower surface, the wall switches to the steady state (Fig. 3f), with its structure differing from the initial structure (Fig. 2b) in chirality. Thus, here, unlike the previous case, after the pulse has been switched off, the wall structure relaxes via a series of complex nonlinear dynamic transformations of the intrawall magnetization distribution.

The reason for such a difference in the relaxation of the wall structure after application of short and long pulses is associated with the mechanism of DW motion, which was elucidated in [9, 15]. According to the works cited, the motion arises only when the resultant magnetization ΔM_x normal to the wall surface appears or, in terms of 1D Bloch walls, when the magnetization starts deflecting (on average over the thickness) from the plane of the wall. For $H > H_c$, these partial deflections are nonstationary (because of violation of the torque balance [9, 15, 16]), and the magnetization **M** starts precessing about the EMA. Accordingly, ΔM_x starts oscillating, causing the dynamic reconfiguration of the wall (for details, see [9–13]). It follows from the aforesaid that, if ΔM_x does not reach its maximal value $(\Delta M_x)_{max}$ (certainly, this value is always lower than the saturation induction) after the pulse has been switched off, the magnetization will relax to the last steady state. If the pulse is switched off after $(\Delta M_x)_{max}$ has been reached, the magnetization will continue precessing until the wall passes into the nearest steady state via a series of transformations. The magnetization configuration corresponding to the maximal value of ΔM_x is shown in Fig. 3b. Note that this configuration is unsteady. Only asymmetric Bloch walls (specifically, those where vortices have different chirality and are shifted toward any of the film surfaces) and asymmetric Néel walls (also with different chirality and different slopes of the wall central line in the general case) are steady. This statement, however, is true if $H = 0$. Otherwise, only the configuration depicted in Fig. 3a is steady, while the configuration in Fig. 3c is not (for the given (parallel to the z axis) field direction). The latter will be steady in the field **H** of opposite polarity. Thus, it turns out, in particular, that the internal structure of DWs may be controlled by application of short magnetic pulses. This opens up possibilities for new designs of magnetic storages. In the case considered, three stable magnetic states can be provided. The first is the initial state shown in Fig. 2b, which is established after the application of the magnetic field and completion of the transients. Here, the intrawall vortex is shifted toward the lower surface of the film and the magnetization chirality corresponds to the counterclockwise rotation of **M**. If the pulse applied is Δt_1 long, the wall reconfigures into the structure shown in Fig. 2d. Walls with such a distribution of **M** are called asymmetric Néel walls [2]. One can recognize the transformation of an asymmetric Bloch wall into an asymmetric Néel wall, e.g., by a change in the velocity. It is seen that the velocity of the latter is higher. In our specific case, the difference is small, 16%. However, this difference will increase if the field $H = H_1$, in which the wall moves steadily before the application of the pulse, is decreased below the field $H = H_2$, in which the wall moves steadily after the termination of the pulse.

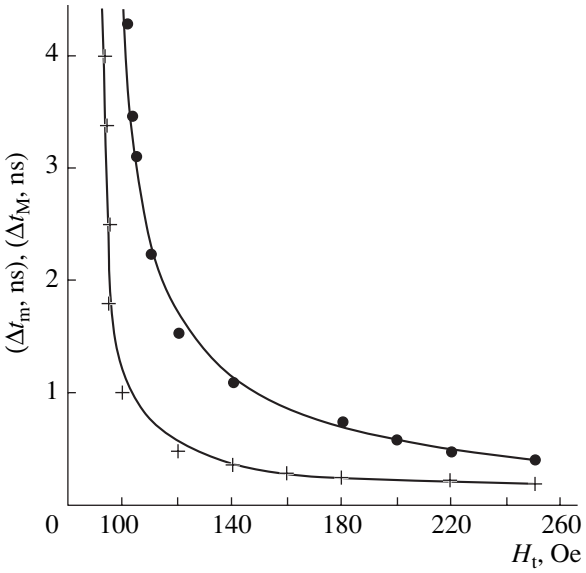

Fig. 4. Minimal pulse widths (+) Δt_m and (●) Δt_M vs. the total magnetic field H_t. The symbols are numerical experiment data. The continuous curves are drawn for clarity. The films have the same parameters as in the previous figures.

According to Fig. 3, after the termination of a pulse Δt_2 long, the initial asymmetric Bloch wall reconfigures into another asymmetric Bloch wall but with opposite chirality. These two walls may be discriminated by applying a low external field $H_x < H_a$ (H_a is the anisotropy field) along the direction of wall motion. In fields H_x directed oppositely, vortices tend toward opposite surfaces. For a given H_p and given parameters of the film, the pulse duration Δt_1 must satisfy the condition $\Delta t_m \le \Delta t_1 \le \Delta t_M$ and the duration Δt_2, the condition $\Delta t_M \le \Delta t_2 \le \Delta t_m + T/2$, where T is the period of dynamic reconfiguration of the wall at $H = 180$ Oe (see the explanation above). The minimal pulse durations Δt_m (for Δt_1) and Δt_M (for Δt_2) are related to the times the field H_p is switched off, i.e., to the occurrence of the configurations shown in Fig. 3a and 3b, respectively.

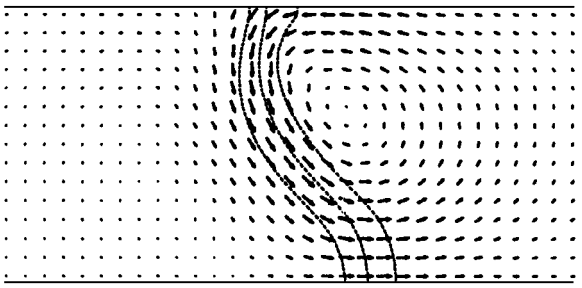

Fig. 5. Wall steady configuration appearing in the 0.1-μm-thick films with $\alpha = 0.001$.

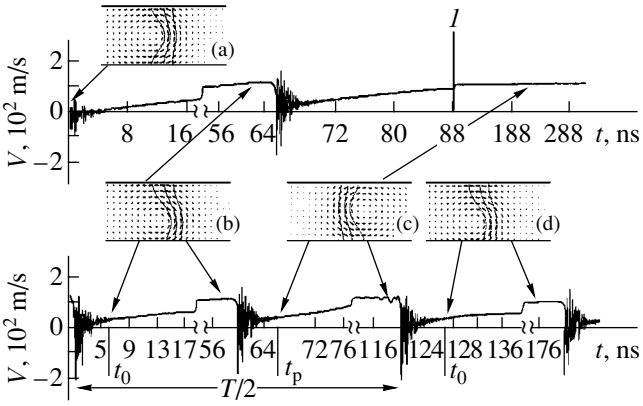

Fig. 6. Time dependence of the film-thickness-averaged wall velocity (continuous curves: the upper curve, no pulsed field; the lower curve, pulsed field of amplitude H_p = 0.5 Oe). (a–d) Instantaneous wall configurations in the 0.1-μm-thick films with $\alpha = 0.001$. The constant field H = 1 Oe. Change of scale is marked by *1*.

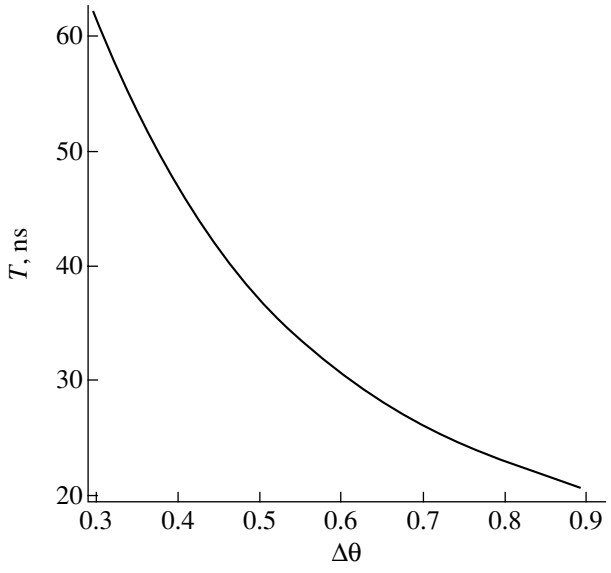

Fig. 7. Period of wall dynamic reconfiguration vs. the relative pulse width. The pulsed field of amplitude H_p = 20 Oe and frequency 5×10^9 s^{-1}. The parameters of the films are the same as in Fig. 6.

The time of application of the pulse H_p is quite immaterial. Figures 2 and 3 corresponds to the pulse durations Δt_m and Δt_M. As follows from Fig. 4, the higher H_t, the smaller these durations. In addition, they depend heavily on the magnetic parameters and film thickness.

Note first of all that numerical experiments were carried out for damping coefficients $\alpha = 0.001$–0.1. At low α (say 0.01 or 0.001), the situation remains basically the same. However, long-term velocity oscillations [10] are observed during the establishment of the steady states both before and after the application of the pulse. Radical changes arise when the film thickness or saturation induction is varied. If, for example, the basic thickness of the film is varied in the interval 0.04–0.065 μm, the pattern described above remains qualitatively the same. For $b > 0.065$ μm, two of the three states (asymmetric Bloch walls with opposite chiralities) remain the same, while the third one changes markedly: its asymmetry has opposite sign compared with the initial asymmetry (cf. Fig. 5 and Fig. 2a). Moreover, in this case, the state corresponding to an asymmetric Néel wall (Fig. 2d) cannot be established at all (Fig. 2d). The same is true for the case when the saturation induction $B_s = 4\pi M_s$ is varied. For B_s = 0.5–1.4 T, the situation corresponds to Figs. 2 and 3. However, when B_s = 1.4 T, one of the states is a DW with the structure shown in Fig. 5 instead of an asymmetric Néel wall. At high inductions and large thicknesses, the difference in the dynamic states of the wall is due to a reduction of stray fields, as was shown in [11, 12].

This study, as well as the previous data [11, 12], indicate that the duration or period (if $H > H_c$) of the dynamic transformations of the wall structure depend primarily on the time of establishment of the wall configurations, for example, that shown in Fig. 3b. This suggests that the period of dynamic intrawall transformations can be controlled by applying relatively short magnetic pulses ($\Delta t < T$) at certain time instants. Moreover, in such a pulsed field, motion of the wall and, hence, dynamic transformations of its structure may take place in subcritical fields H. This makes it possible to control the wall velocity without changing the film parameters.

By way of example, Fig. 6 demonstrates the near-periodic behavior of the wall velocity in the 0.1-μm-thick film with a damping parameter of 0.001. For H = 1 Oe and $H_p = 0$, upon completion of the transient (lasting about 120 ns), the wall with the configuration of **M** shown in Fig. 6c moves with a constant velocity of about 230 m/s (the upper curve in Fig. 6). If 60-ns-long pulses of amplitude H_p = 0.5 Oe are now periodically imposed on the field H at times t_p corresponding to the onset of the structure shown in Fig. 6c and then are switched off for 60 ns at times t_0 corresponding to the onset of the structure shown in Fig. 6b and 6d, the behavior of the velocity becomes almost periodic with a period T equaling 120 ns. Such periodicity is associated with $b \longrightarrow c \longrightarrow d$ periodic reconfiguration of the

wall. When the pulsed field amplitude grows, the period T decreases. Similarly, the period T decreases as the relative width $\Delta\theta = (\Delta t)_p/(\Delta t)_{per}$ of the pulse increases (here, $(\Delta t)_p$ is the absolute pulse width and $(\Delta t)_{per}$ is the sum of the on and off times of the pulse, i.e., the pulse period).

Using a pulsed field, one may also control the wall motion parameters in the case $H_p > H_c$ (at $H = 0$). We recall that, if a constant field $H > H_c$ is applied instead of H_p, the motion of the wall is accompanied by the nonlinear dynamic transformation of its internal structure and the velocity of the wall oscillates [9]. The same effect may be achieved in a pulsed field of different durations. However, the process in this case will be near-periodic if the field H_p differs considerably from H_c and grows with decreasing $\Delta\theta$. In addition, in a constant field H whose amplitude equals the peak field H_p, it is desirable that $(\Delta t)_{per}$ be shorter than, or close to, T. Then, the period of the near-periodic process of nonlinear intrawall transformation will vary with $(\Delta t)_p$. Figure 7 shows the variation of the dynamic transformation period in the field of amplitude $H_p = 20$ Oe and frequency $1/(\Delta t)_p = 5 \times 10^{-9}$ s^{-1} in the film with the basic parameters and $\alpha = 0.001$. It is seen that the wall transformation (velocity oscillation) period varies substantially with the relative pulse width. Hence, one can control the translational velocity of the wall by applying pulsed fields.

Finally, applying a pulsed field at certain times, one can retard the dynamic transformation of the walls and thereby rise their translational velocity.

CONCLUSIONS

(i) Using a pulsed magnetic field, one may control the transitions between various steady regimes of DW motion, which is induced by a constant magnetic field.

(ii) Relaxation of the wall velocity and structure to a new steady state depends heavily on the pulse width. The minimal width of the pulse varies in proportion to the pulse amplitude. Relaxation is accomplished via profound nonlinear dynamic transformations of the wall internal structure. Such behavior is associated with the gyroscopic properties of the elementary magnetic moments constituting the wall.

(iii) Application of magnetic pulses makes it possible to eliminate a dynamic reconfiguration delay in fields lower than the critical field H_c and favors unsteady periodic motion of the walls. For $H < H_c$, the pulsed field may alter the wall dynamic reconfiguration period. The period decreases with increasing pulse width.

Thus, it appears that a pulsed magnetic field allows for effective control of the nonlinear dynamics of DWs moving in a constant magnetic field.

ACKNOWLEDGMENTS

This work was partially supported by the Russian Foundation for Basic Research (grant no. 02-02-16443).

REFERENCES

1. A. E. La Bonte, J. Appl. Phys. **40**, 2450 (1969).
2. A. Hubert, Phys. Status Solidi A **32**, 519 (1969).
3. B. N. Filippov and L. G. Korzunin, IEEE Trans. Magn. **29**, 2563 (1993).
4. S. Tsukahara and H. Kavakatsu, J. Phys. Soc. Jpn. **32**, 1493 (1972).
5. J. N. Chapman, G. R. Morrison, J. P. Jacubovics, *et al.*, J. Magn. Magn. Mater. **49**, 277 (1985).
6. T. Suzuki, K. Suzuki, and Y. Igarashi, Jpn. J. Appl. Phys. **15**, 707 (1976).
7. M. R. Sheinfein, J. Unguris, R. J. Celotta, *et al.*, Phys. Rev. Lett. **63**, 668 (1989).
8. M. R. Sheinfein, J. Unguris, J. L. Blue, *et al.*, Phys. Rev. B **43**, 3395 (1991).
9. S. W. Yuan and H. N. Bertram, Phys. Rev. B **44**, 12395 (1991).
10. B. N. Filippov, L. G. Korzunin, and F. A. Kassan-Ogly, Phys. Rev. B **64**, 104412 (2001).
11. B. N. Filippov and L. G. Korzunin, Zh. Éksp. Teor. Fiz. **121**, 372 (2002) [JETP **94**, 315 (2002)].
12. B. N. Filippov, L. G. Korzunin, and F. A. Kassan-Ogly, Solid State Commun. **121**, 55 (2002).
13. B. N. Filippov, Fiz. Nizk. Temp. **28** (10), 3 (2002) [Low Temp. Phys. **28**, 707 (2002)].
14. G. I. Marchuk, *Methods of Numerical Mathematics*, 2nd ed. (Springer, New York, 1975; Nauka, Moscow, 1980).
15. N. L. Shryer and L. R. Walker, J. Appl. Phys. **45**, 5406 (1974).
16. B. N. Filippov and A. P. Tankeev, *Dynamic Effects in Ferromagnets with Domain Structure* (Nauka, Moscow, 1987) [in Russian].

Translated by V. Isaakyan

Technical Physics, Vol. 49, No. 6, 2004, pp. 770–774. Translated from Zhurnal Tekhnicheskoĭ Fiziki, Vol. 74, No. 6, 2004, pp. 109–113.

SURFACES, ELECTRON AND ION EMISSION

Effect of Laser Erosion on the Copper and Zinc Concentrations in the Surface Layer of Brass

A. I. Boriskin, V. M. Eremenko, P. A. Pavlenko, A. N. Skripchenko, and S. N. Khomenko

Institute of Applied Physics, National Academy of Sciences of Ukraine, Sumy, 40030 Ukraine
e-mail: ipfmail@ipfcentr.sumy.ua

Received September 22, 2003

Abstract—A REMMA 102 scanning electron microscope equipped with semiconductor and wave spectrometers is applied to measure the copper and zinc concentrations in the surface layers of an M161 brass sample and the same sample subjected to a focused laser radiation. The results are compared with the results obtained with an MS3101 laser mass spectrometer having a laser–plasma ion source. The laser-assisted erosion of the surface layer in the brass is shown to significantly change the copper and zinc concentrations. It is found that, when the craters produced by laser pulses on the initial surface do not overlap, the copper and zinc contents in the laser-induced plasma correspond to their contents in the sample. *© 2004 MAIK "Nauka/Interperiodica".*

INTRODUCTION

In the stage of atomization, a focused Q-switched laser pulse affects atoms or molecules that are tightly bound in solids and transforms them into a gas phase (atomic vapor). In the second phase of the laser pulse, the atomic vapor is ionized to form a plasma bunch, which expands in a vacuum under pressure. The compositions of the vapor and the plasma ion component can differ from the elemental composition of a target because of different degrees of atomization and ionization of different elements. Discrimination can appear in the stages of melting, boiling, drop formation, liquid-phase diffusion, ionization, and so on. These processes were studied in many experimental and theoretical works [1]. However, the behavior of the surface subjected to a focused pulsed radiation was beyond the scope of these works. It is assumed that, due to different degrees of evaporation of elements, the surface erosion layer is enriched in nonvolatile and depleted of volatile elements until equilibrium in this process is achieved [1]. This behavior can cause additional discrimination in the methods that apply interaction of laser radiation with solids. This discrimination can mainly lead to a change in the surface composition of a specimen and, hence, to an increase in the discrepancy between the composition of the initial specimen and the composition of the products of evaporation and ionization from the irradiated surface. For example, a focused laser radiation is often used in laser mass spectrometry to preliminarily clean the surface of a specimen to be analyzed. Moreover, when irradiated, a specimen is scanned in laser mass spectrometry with photographic recording. In this case, the choice of a scanning mode and the effect of erosion of a specimen on its composition are very important.

EXPERIMENTAL

We studied the copper and zinc concentrations in the surface layer of M161 brass repeatedly subjected to a focused laser irradiation. The atomic masses of copper and zinc are similar; therefore, the effect of apparatus on their relative sensitivity coefficients is minimum [1]. Moreover, the standard concentrations of the ^{64}Zn and ^{65}Cu isotopes are virtually the same. As will be shown below, this fact significantly simplifies examination of the surface with a mass spectrometer having a laser–plasma ion source. Experiments were performed on a REMMA 102 scanning electron microscope equipped with semiconductor and wave spectrometers and on an MS3101 laser mass spectrometer with photographic recording (both devices are produced at the AO SELMI, Sumy, Ukraine). Erosion craters on the polished surfaces of two M161 standard brass specimens were produced by the focused radiation of an LTI 215 light emitter in the ion source of the laser mass spectrometer. The radiation wave was 1.064 μm, and the laser pulse duration was ~10^{-8} s. The angles between the laser radiation and the normal to the specimen surfaces were 30° and 60°. The specimen, irradiated at an angle of 30°, was analyzed on the REMMA 102 device, and the specimen irradiated at an angle of 60°, on the MS3101. Figure 1 shows the places analyzed with the REMMA 102. In each place, five analyses in different sites were performed. To decrease the error, measurements were carried out in the integrated mode by scanning an electron probe across a 0.3×0.3-mm area for the energy dispersive spectrometer and a 0.1×0.1-mm area for the wave spectrometer. The results were processed on a computer, and, as a standard, we used the M164 standard brass specimen, whose composition is close to that of the M161 brass specimen. The REMMA 102 scanning electron microscope operated under the same condi-

1063-7842/04/4906-0770$26.00 © 2004 MAIK "Nauka/Interperiodica"

tions in all irradiated places. The energy dispersive spectrometer had a probe current of 3 nA and operated at an accelerating voltage of 20 kV and a counting time of 200 s. The accelerating voltage of the wave spectrometer was 20 kV, the probe current was 10 nA, and the counting time was 100 s. Using the MS3101 laser mass spectrometer, we detected the ionic component of the laser plasma for the initial and eroded surfaces as the ratio of the ion mass to the ion charge at a photodetector. When measuring the initial and eroded surfaces with MS3101, we recorded mass spectra on the same photographic film, which allowed us to eliminate the effect of the development of films on the results. The speed of the table with a specimen and the laser frequency were chosen for both surfaces so that to avoid crater overlapping. The conditions of laser operation (the pumping voltage, frequency, and delay time) were the same during measurements. As analytical lines, we used the spectral lines of the ^{64}Zn and ^{65}Cu isotopes. As noted above, their isotope concentrations are virtually the same ($C^{64}\mathrm{Zn}/C^{65}\mathrm{Cu} = 0.998$). For data processing, we used lines of the ^{64}Zn and ^{65}Cu isotopes recorded at the same exposure time. Exposure times were chosen so that the analytical lines $^{64}Zn^{+}$, $^{64}Zn^{2+}$, $^{64}Zn^{3+}$, $^{65}Cu^{+}$, $^{65}Cu^{2+}$, and $^{65}Cu^{3+}$ were located in the linear region of the photodetector. This approach allowed us to significantly improve the measurement accuracy. The analytical lines were processed with an MD 100 microdensitometer (Carl Zeiss, Jena, Germany) and an AIS computer-assisted specter meter [3, 4]. The areas of the recorded lines were taken to be the measures of analytical signals. One photographic film was used to detect four measurements from different sites of the initial and eroded surfaces for ions with different charges.

RESULTS AND DISCUSSION

Table 1 gives the results for the initial surface ($m1, \ldots, m5$) and the eroded surface ($c1, \ldots, c5$) obtained with the energy dispersive spectrometer. Here, C is the element concentration, %; t is the Student criterion; s is the standard deviation; γ is the number of degrees of freedom; and P is the probability [5]. The concentrations on the eroded and initial surfaces were processed statistically [5]. As a result, for each set of Cu and Zn concentrations, we determined the relative systematic error $\tilde{\Delta}$, the relative standard deviation $\tilde{\sigma}(\dot{\Delta})$, and the confidence bounds for $C_{\min}$ and $C_{\max}$ at a 1% significance level and a 0.99 confidence level. As is seen, all experimental results fall within these boundaries. The ratios of the average copper and zinc concentrations on the eroded surface to these values on the initial surface are 1.11 and 0.826, respectively. Such a significant discrepancy can be caused by two factors: discrimination processes during irradiation and the scatter of the experimental data. The Student criterion t was applied to check the hypothesis that two independent partial small sets of the experimental data belong

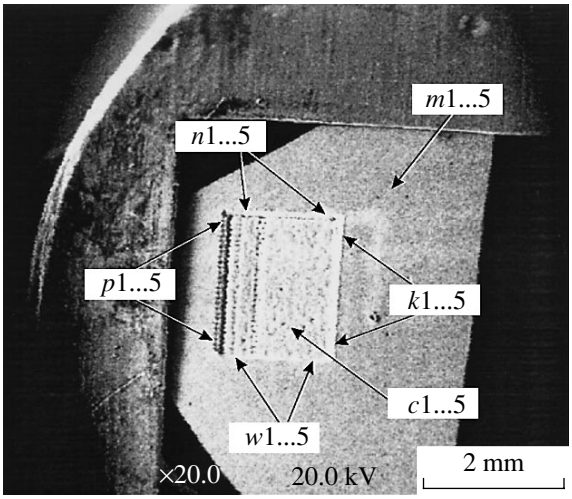

Fig. 1. Specimen.

to the same normally distributed population [5]. Analysis of the experimental data according to [5] showed that the two independent sets $Cc1, \ldots, Cc5$ and $Cm1, \ldots, Cm5$ do not belong to the same normally distributed general set, since the Student coefficients that characterize the normalized deviations of the average values of the partial sets from the average value of the normal general set are $t_{c,m} = 12.01$ for Cu and $t_{c,m} = 11.97$ for Zn. This means that, at a degree of freedom $\gamma = 8$ for both partial sets, this Student coefficient t gives $P < 0.001$, which means that $t < t_{c,m} = 11.97$ in less than one

Table 1

Eroded surface			Initial surface		
parameter	Cu	Zn	parameter	Cu	Zn
$C\,c1$, %	66.01	31.143	$C\,m1$, %	59.02	38.38
$C\,c2$, %	66.39	30.89	$C\,m2$, %	59.46	37.21
$C\,c3$, %	65.93	31.33	$C\,m3$, %	59.7	37.55
$C\,c4$, %	66.59	30.82	$C\,m4$, %	60.86	37.07
$C\,c5$, %	66.84	30.37	$C\,m5$, %	60.08	36.76
$\bar{C}\ c$, %	66.35	30.91	$\bar{C}\ m$, %	59.8	37.39
C_{sec}, %	59.5	37.65	C_{sec}, %	59.5	37.65
$\tilde{\Delta}$, %	11.51	–17.9	$\tilde{\Delta}$, %	0.545	–0.681
$\tilde{\sigma}(\dot{\Delta})$, %	0.579	1.17	$\tilde{\sigma}(\dot{\Delta})$, %	1.16	1.65
s_c	0.384	0.364	s_m	0.695	0.62
$t_c(P_{0.01}, \gamma = 4)$	4.6	4.6	$t_m(P_{0.01}, \gamma = 4)$	4.6	4.6
$C_{\min}$, %	65.56	30.16	$C_{\min}$, %	58.37	36.11
$C_{\max}$, %	67.14	31.66	$C_{\max}$, %	61.23	38.66
$s_{c,m}$	0.862	0.856	$s_{m,c}$	0.862	0.856
$t_{c,m}$	12.01	–11.97	$t_{m,c}$	–12.01	11.97

Table 2

Parameter	Element	Analyses						C_{sec}, %
		c	*m*	*n*	*p*	*w*	*k*	
$\bar{C}$, %	Cu	66.35	59.8	61.26	60.43	62.28	60.94	59.5
	Zn	30.91	37.39	36.18	37.07	35.29	36.59	37.65
$\tilde{\Delta}$, %	Cu	11.51	0.545	2.97	1.57	4.67	2.42	–
	Zn	–17.89	–0.681	–3.91	–1.54	–6.26	–2.81	–
$\tilde{\sigma}(\Delta)$, %	Cu	0.579	1.16	1.21	1.17	2.05	0.837	–
	Zn	1.176	1.65	2.24	2.03	3.87	1.425	–

case per thousand. Therefore, the differences in the copper and zinc concentrations on the eroded and initial surfaces are substantial and cannot be attributed to one general set. In other words, these differences can only be caused by discrimination processes that occur during the irradiation of the specimen surface. The erosion of this surface results in a 6.74% decrease in the Zn concentration and a 6.85% increase in the Cu concentration in the upper layer, which leads to an increase in the relative systematic error $\tilde{\Delta}$ for copper and zinc to ≈11 and ≈18%, respectively. The differences between the copper and zinc concentrations on the initial surface and the corresponding standard values do not exceed 0.3%, and the maximum value of $\tilde{\Delta}$ does not exceed 0.7%. As noted above, the energy dispersive spectrometer of the REMMA 102 was used to perform five analyses in each region at the edges of an erosion zone. The average copper and zinc concentrations in each of the four edges are given in Table 2. The same discrimination is detected at the edges of the erosion zone: a decrease in the Zn concentration and an increase in the Cu concentration. The relative systematic error $\tilde{\Delta}$ varies from 1.54 to 6.24% from region to region. When the focused laser radiation affects a specimen, the condensed phase is sputtered onto the neighboring regions. The sputtering of the condensed phase is nonuniform from the center of interaction, which is clearly visible in Fig. 2. The material is mainly sputtered toward the projection of the laser beam and a certain angle to this direction. Boriskin *et al.* [6] analyzed the composition of the drops sputtered from the radiation zone in an M161 specimen and found that they are depleted of Zn and enriched in Cu. The sputtering of the drops of the condensed phase onto the edges of the erosion zone can cause the discrimination. Moreover, during long-term erosion of a scanned area, copper and zinc selectively evaporate from the surface layer of a specimen. The total effect of these processes can account for the difference between the average concentrations on the eroded

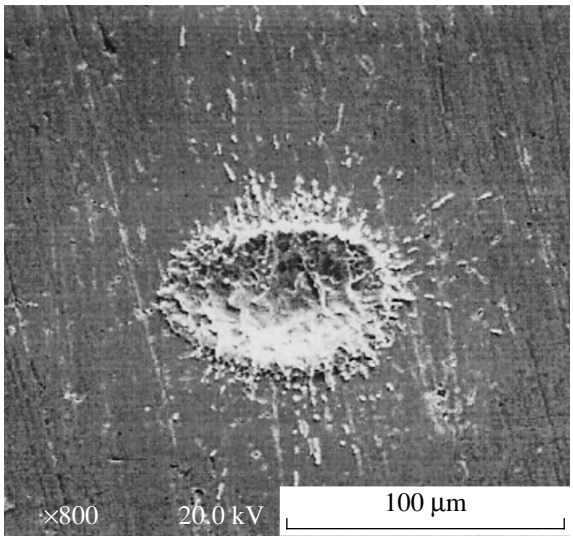

Fig. 2. Crater produced by five laser pulses; the angle between the normal to the specimen surface and the laser beam is 60°.

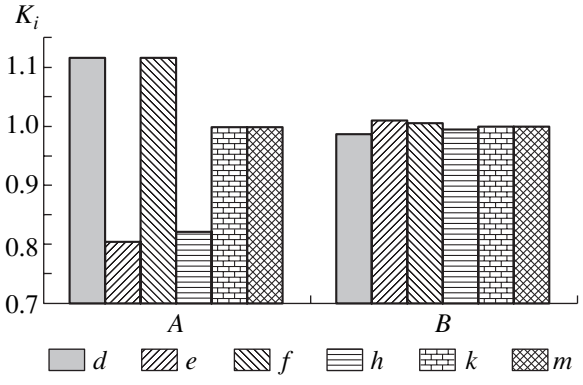

Fig. 3. REMMA 102: (*A*) eroded surface and (*B*) initial surface. K_i is the concentration ratio. The wave spectrometer: (*d*) $\bar{C}_{ch}\mathrm{Cu}/C_{sec}\mathrm{Cu}$ and (*e*) $\bar{C}_{ch}\mathrm{Zn}/C_{sec}\mathrm{Zn}$. The energy dispersive spectrometer: (*f*) $\bar{C}_{ch}\mathrm{Cu}/C_{sec}\mathrm{Cu}$, (*h*) $\bar{C}_{ch}\mathrm{Zn}/C_{sec}\mathrm{Zn}$, (*k*) $C_{sec}\mathrm{Zn}/C_{sec}\mathrm{Zn}$, and (*m*) $C_{sec}\mathrm{Cu}/C_{sec}\mathrm{Cu}$.

Table 3

Initial surface				
Parameter	$As^{64}Zn^{+}/As^{65}Cu^{+}$	$As^{64}Zn^{2+}/As^{65}Cu^{2+}$	$As^{64}Zn^{Z_i\ sum}/As^{65}Cu^{Z_i\ sum}$	$C_{sec}{}^{64}Zn/C_{sec}{}^{65}Cu$
Analysis 1	0.999	0.976	0.996	0.998
Analysis 2	0.984	0.999	0.987	0.998
Analysis 3	1.06	0.947	1.04	0.998
Analysis 4	0.98	0.966	0.976	0.998
$\bar{K}_i$	1.01	0.972	0.998	0.998
$\tilde{\Delta}$, %	0.858	–2.64	–0.012	–
$\tilde{\sigma}(\dot{\Delta})$, %	3.86	2.27	2.68	–
$K_{i\,\min}$	0.945	0.937	0.956	–
$K_{i\,\max}$	1.07	1.01	1.04	–

Table 4

Eroded surface				
Parameter	$As^{64}Zn^{+}/As^{65}Cu^{+}$	$As^{64}Zn^{2+}/As^{65}Cu^{2+}$	$As^{64}Zn^{Z_i\ sum}/As^{65}Cu^{Z_i\ sum}$	$C_{sec}{}^{64}Zn/C_{sec}{}^{65}Cu$
Analysis 1	0.819	0.805	0.818	0.998
Analysis 2	0.871	0.839	0.868	0.998
Analysis 3	0.816	0.806	0.815	0.998
Analysis 4	0.897	0.805	0.889	0.998
$\bar{K}_i$	0.848	0.814	0.845	0.998
$\tilde{\Delta}$, %	–15.07	–18.51	–15.35	–
$\tilde{\sigma}(\dot{\Delta})$, %	4.71	2.05	4.4	–
$K_{i\,\min}$	0.784	0.787	0.786	–
$K_{i\,\max}$	0.912	0.84	0.904	–

surface and the edges of the erosion zone and the average concentrations measured on the initial surface. The specimen was also analyzed with the wave spectrometer; the thus-obtained results are in good agreement with the results obtained with the energy dispersive spectrometer. Some of these results are given in Fig. 3.

After processing the photographic film containing spectra taken from the initial and eroded surfaces with the MS3103 mass spectrometer, we collected a data bank for the analytical signals (As) of the ^{64}Zn and ^{65}Cu isotopes for the ions with the charges $Z = 1$ and 2. As noted above, the analytical signals of the isotopes with the corresponding charge Z for copper and zinc were processed at the same exposure time. Discrimination processes during the surface erosion were estimated as the difference between the ratio of analytical signals $As^{64}Zn^{Z_i}/As^{65}Cu^{Z_i}$ and the ratio of standard concentrations $C_{att}{}^{64}Zn/C_{att}{}^{65}Cu$. In the ideal case (in the absence of discrimination), these values must coincide. The results of measurement with MS3101 for four analyses on the initial and eroded surfaces are given in Tables 3 and 4. The data processing after [5] showed that the two sets of the ratios of analytical signals for the initial and eroded surfaces do not belong to one general set and that their differences are specified by the laser radiation-induced erosion of the surface. The same specific features are seen here, namely, a significant decrease in the Zn concentration and an increase in the Cu concentration. It is interesting to estimate the charge composition of the analytical signals from the initial and eroded surfaces. Table 5 gives the ratios of the analytical signals for the double- and triple-charged ions of the ^{65}Cu and ^{64}Zn isotopes to the corresponding signals of the single-charged ions. These data indicate that the ratios of the analytical signals for the double- and triple-charged ions to the analytical signals of the single-charged ions are the same for Cu and Zn on each surface. However, the yields of the double-charged and triple-charged ions from the initial surface are ≈3.5 and ten times, respectively, greater than the corresponding yields from the eroded surface. This indicates that, although the laser operating conditions are the same, the laser radiation power densities in these two variants are different. As follows from the fact that the yield of the multicharged ions from the radiation zone is higher for the initial surface, the laser radiation power density here is higher than at the eroded surface. The decrease in the power density at the eroded surface can be explained by its roughness, which increases the interaction area of the eroded surface as compared to the initial surface at the same sizes of the radiation spot. Usually, when laser mass spectrometry is applied to calculate the element concentration, the analytical lines of single-charged ions are used. This significantly decreases the data processing time and simplifies the processing. This approach can be grounded if the total contribution of all multicharged ions to an analytical signal is small.

Table 5

Parameter	Eroded surface	Initial surface
$As^{65}Cu^{2+}/As^{65}Cu^{+}$	0.013	0.047
$As^{65}Cu^{3+}/As^{65}Cu^{+}$	2.7×10^{-05}	2.1×10^{-04}
$As^{64}Zn^{2+}/As^{64}Zn^{+}$	0.014	0.046
$As^{64}Zn^{3+}/As^{64}Zn^{+}$	3.1×10^{-05}	2.0×10^{-04}

As is seen from Table 5, this contribution is insignificant and can be neglected at a certain value of the laser radiation power density.

CONCLUSIONS

The study of the eroded surface of the standard M161 specimen has shown that the discrimination of the copper and zinc concentrations is substantial. As a result of laser radiation, the zinc content in the surface layer decreases and the copper content increases. However, the analysis of a similar surface with an MS3101 mass spectrometer under the conditions when craters that are formed by individual laser pulses do not overlap with each other shows no substantial differences in the ratio $As^{64}Zn^{z_i}/As^{65}Cu^{z_i}$ and the standard ratio $C_{att}{}^{64}Zn/C_{att}{}^{65}Cu$. The measurements show that the preliminary erosion of the surface of the standard M161 specimen results in significant changes in the copper and zinc contents in the surface layer. These discrimination changes are caused by different physical properties of the elements that make up the specimen. This finding can be important for not only laser mass spectrometry but also other physical methods where a material is excited by a focused laser radiation. We assume that the discrimination can be decreased by excluding crater overlapping in order that a sample for analysis to be evaporated with a laser pulse from only the initial surface of a material. These conditions can easily be realized by scanning a specimen and choosing its speed of motion along the *x* and *y* coordinates and the laser frequency. However, additional investigations are required to find out whether this assumption is valid for various matrices whose elements have strongly different physical properties. It is also interesting to study the effect of surface erosion on the concentrations of these elements.

REFERENCES

1. G. I. Ramendik, *Elemental Mass-Spectrometric Analysis of Solids* (Khimiya, Moscow, 1993) [in Russian].
2. A. I. Boriskin, P. A. Pavlenko, V. M. Eremenko, *et al.*, Vestn. Sumsk. Gos. Univ., Ser. Fiz., Mat., Mekh., No. 13, 105 (2002).
3. G. I. Ramendik, A. Yu. Khromov, *et al.*, Zh. Anal. Khim. **43**, 224 (1988).
4. G. I. Ramendik, A. Yu. Khromov, V. L. Volkov, *et al.*, Prib. Tekh. Éksp., No. 2, 182 (1986).
5. A. K. Mitropol'skiĭ, *Statistical Calculation Techniques* (GIFML, Moscow, 1961) [in Russian].
6. A. I. Boriskin, O. V. Varakin, V. M. Eremenko, *et al.*, Vestn. Sumsk. Gos. Univ., Ser. Fiz., Mat., Mekh., Nos. 5–6, 124 (2002).

Translated by K. Shakhlevich

Technical Physics, Vol. 49, No. 6, 2004, pp. 775–778. Translated from Zhurnal Tekhnicheskoĭ Fiziki, Vol. 74, No. 6, 2004, pp. 114–117.

EXPERIMENTAL INSTRUMENTS AND TECHNIQUES

Performance of Thermionic Energy Converters with Oxygen-Containing Emitter and Collector

V. P. Kobyakov* and A. G. Kalandarishvili**

** Institute of Structural Macrokinetics and Materials Science, Russian Academy of Sciences, Chernogolovka, Moscow oblast, 142432 Russia*

*** Russian Research Centre Kurchatov Institute, pl. Kurchatova 1, Moscow, 123182 Russia*

Received July 23, 2003

Abstract—The performance of a thermionic converter module with an emitter made of oxygen-containing single-crystalline tungsten and a collector made of oxygen-containing niobium is studied. Both materials are prepared by chemical vapor deposition. Comparison with previous results for similar modules with the collectors made of other materials is carried out. © *2004 MAIK "Nauka/Interperiodica".*

INTRODUCTION

It is known that oxygen introduced into the electrode gap of an arc cesium thermionic converter (TC) through the use of oxygen-containing collector [1–3] or emitter [4] materials considerably improves the TC output. The output characteristics of TC prototypes with the emitter made from oxygen-free single-crystalline CVD tungsten and collector made from oxygen-containing CVD niobium were studied in [3]. It was conjectured that use of an oxygen-containing collector in TCs with the emitter made of oxygen-containing single-crystalline CVD tungsten [4] may raise the TC output power. In this work, we check this assumption by studying the output characteristics of TCs with both the emitter and collector made of oxygen-containing materials. The results obtained here are compared with the performance of TC prototypes with the collector made of polycrystalline tungsten, which does not absorb oxygen from the electrode gap, and with the collector made of Cb = 1 (Nb + 1 wt % Zr) oxygen-free niobium alloy.

EXPERIMENTAL

The objects under study were cylindrical monomodular TC prototypes. The emitters of all the TCs were made by the chloride CVD technique [5], which provides tubular tungsten single crystals faceted by six (110) planes and containing an elevated amount of oxygen (10^{-3}–10^{-2} wt %) in the form of quasi-solid solution. Such emitters show steps and steeply ascending portions on the work function polytherms. In particular, the work function amounts to 5.6–5.7 eV at temperatures above 2000 K [5, 6]. In order for single-crystalline tubes be used in cylindrical TCs, they are spun on a lathe and then electrochemically polished in an alkaline etcher to remove a damaged layer (about 100 μm thick) from the surface. After processing, the work function declines to 5.2 eV.

Also, three-layer cermet collectors for TCs were made by gas-pressure compacting [7, 8] using oxygen-containing (0.76 wt%) CVD niobium [9]. Modules being compared in this work differ only in collector material. The fabrication technology and bench tests are detailed elsewhere. Note only that test conditions were the same as in [3]. The system was evacuated to a residual pressure of 10^{-4} Pa, and cesium vapor was applied to the electrode gap. The performance of the module was optimized by varying the cesium pressure. After the module had operated as a converter for about 100 h, the *I–V* characteristics were taken at different emitter (T_e) and collector (T_c) temperatures. From the envelopes of the *I–V* characteristics, the maximal output power *P* was determined at each temperature.

RESULTS AND DISCUSSION

Figure 1 compares the dependences $P = f(T_e)$ at different collector temperatures for the module with the collector made of oxygen-containing niobium (Fig. 1a) with similar curves for the modules where the collectors are prepared from oxygen-free polycrystalline tungsten (Fig. 1b) [10] and Cb = 1 niobium alloy (Fig. 1c). The run of the curves in Fig. 1 is typical of TCs with emitters made of single-crystalline oxygen-containing tungsten [10]. Namely, starting from a certain (relatively high) temperature, the curves steepen sharply. The fact is that, in this material, the electron work function rises significantly at temperatures from 1700 to 1900 K (depending on experimental conditions) as a result of intense oxygen evolution from the bulk to the surface [4–6]. At a maximal emitter temperature of 2100 K, the output of the module equals 17.5 W/cm^2. It is immediately obvious that the output of the module under study is appreciably lower (roughly by 37%) than that of the module with the polycrystalline tungsten collector, while being much higher

1063-7842/04/4906-0775$26.00 © 2004 MAIK "Nauka/Interperiodica"

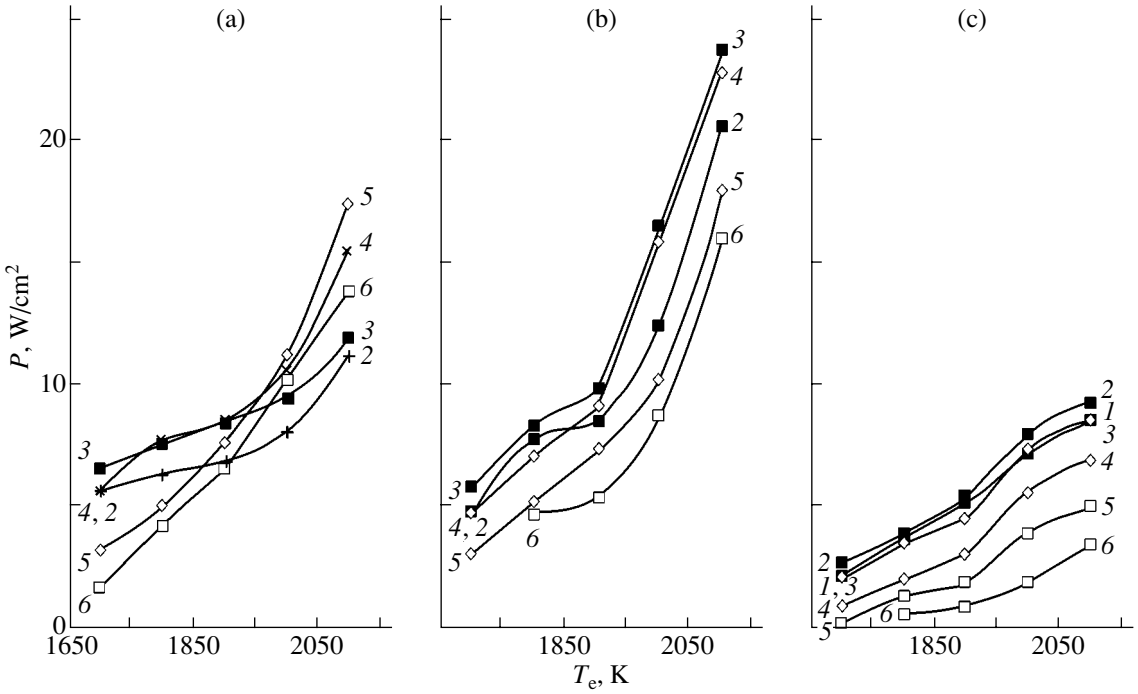

Fig. 1. Curves $P = f(T_e)$ for modules with the collector made of (a) oxygen-containing niobium, (b) oxygen-free polycrystalline tungsten, and (c) Cb = 1 alloy. The collector temperature is (*1*) 800, (*2*) 900, (*3*) 1000, (*4*) 1100, (*5*) 1200, and (*6*) 1300 K.

(by more than 80%) than the output power of the module with the Cb = 1 collector.

Figure 2 shows the dependences $P = f(T_e)$ at different emitter temperatures. In general, they do not differ at all from normal curves of the TC output optimized in terms of the collector temperature and reflect TC operation under conditions when many variables take steady-state values. The increase in the collector optimal temperature in going from the Cb = 1 collector (900 K) to the polycrystalline tungsten collector (1050 K) and then to the oxygen-containing niobium collector (1200 K) catches the eye. In the first case, the optimal collector temperature does not depend on the emitter temperature, whereas in the two others, the optimum temperature shifts toward lower values as the emitter temperature declines. This trend is the most pronounced in Fig. 2a. Note that high collector temperatures are of great importance in terms of the heat removal effectiveness when TCs are designed for space applications. It is also noteworthy that the run of the curves $P = f(T_e)$ in Fig. 1 is naturally related to the collector temperature. The position of the curves relative to the vertical axis correlates with the collector optimal temperature in Fig. 2. However, a number of features deserve attention. In Fig. 1c, all the curves run in a similar manner. Curves *5* and *6* in Figs. 1a and 1b (collector temperatures above 1100 K) run smoothly without inflections. In the case of the oxygen-containing niobium collector, these curves lie below curves *2–4* at low emitter temperatures but then (1900–1950 K) intersect the other curves and reach high power values. For the tungsten collector, curves *5* and *6* go under all others throughout the temperature range. At collector temperatures of 110 K or below, curves *2–4* exhibit more or less distinct inflections.

These features may be related to different amounts of oxygen present in the electrode gap, as well as on the surface and in the bulk of the electrodes of the modules being compared. It can naturally be expected that the total amount of oxygen is the highest when both electrodes are made of oxygen-containing materials. However, oxygen comes to the gap largely from the bulk of the emitter throughout the emitter temperature range. As for the oxygen-containing niobium, intense oxygen evolution from the collector is hardly probable in the collector temperature range used in this work: it was shown [11] that oxygen evolution from this material becomes tangible at temperatures above 1700 K.

In the module with the collector made of Cb = 1 niobium alloy, the amount of oxygen is insignificant. This alloy is an oxygen getter, so that most of the oxygen evolving from the emitter during operation is absorbed by the collector. The only indication that oxygen does evolve from an internal source, which the emitter material is, is the inflection in the curves (Fig. 1c). However, as the emitter temperature is raised within the interval studied, the steady state is established and the output grows smoothly. The position of the curves along the vertical axis in Fig. 1c totally correlates with the distance of one or another point from the peak in Fig. 2c (within the collector temperature interval considered).

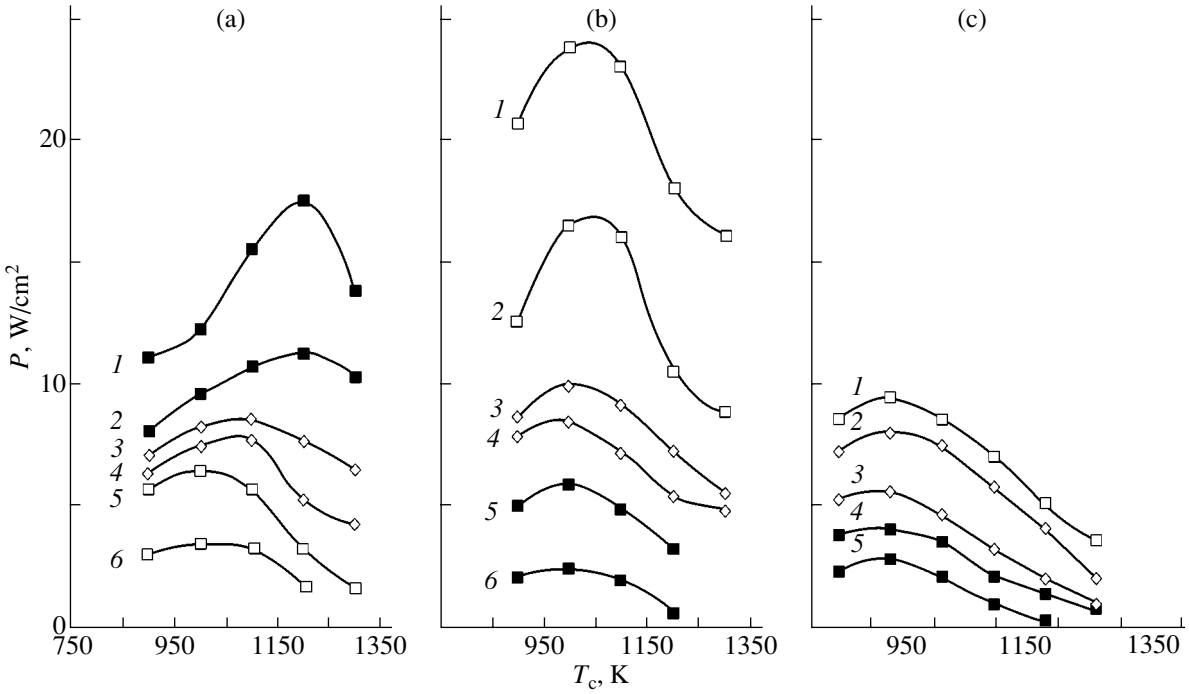

Fig. 2. Curves $P = f(T_c)$ for modules with the collector made of (a) oxygen-containing niobium, (b) oxygen-free polycrystalline tungsten, and (c) Cb = 1 alloy. The emitter temperature is (*1*) 2100, (*2*) 2000, (*3*) 1900, (*4*) 1800, (*5*) 1700, and (*6*) 1600 K.

In this respect, the module with the polycrystalline tungsten collector holds an intermediate position, since tungsten does not dissolve oxygen owing to its electronic configuration [12]. Quasi-solid oxygen–tungsten solutions, from which oxygen may evolve only at high temperatures and with low diffusion rates, can be produced solely by CVD of single-crystalline tungsten under special conditions [4, 5].

In the light of the aforesaid, one could expect that a TC module with an oxygen-containing emitter and collector is more efficient than the module where the collector is a good oxygen adsorbent (Cb = 1 alloy in our case). At the same time, we see that the output parameters of the module with the oxygen-containing emitter and collector are lower than those of the module where the collector is made of the oxygen-free tungsten. Presumably, this is associated with the fact that, in the given collector temperature range, the niobium is still capable of absorbing a part of the oxygen from the emitter. In this case, the oxygen coverage of the emitter decreases and the emissivity and adsorptivity of the emitter surface degrade. At the same time, an increased amount of oxygen on the collector surface raises the related work function and shifts the most efficient operating conditions toward higher collector temperatures as the emitter temperature rises. As a result, when the temperatures of both electrodes are high, the collector contribution become appreciable and curves *5* and *6* in Fig. 1a intersect the others. Simultaneously, however, the situation on the emitter is impaired, which is a more significant factor. Eventually, the output characteristics of the tungsten-collector module turn out to be the highest. At the same time, the module where both electrodes are made of the oxygen-containing materials offers the highest optimal collector temperature, 1200 K.

As was mentioned above, the temperature curves of the output have steps throughout the collector temperature range only in the case of the module where the total amount of oxygen is the lowest (Fig. 1c). This is a sound indication of an internal oxygen source (the oxygen-containing tungsten emitter) present in the system. In the other two cases, where the oxygen content is *a fortiori* higher, steps persist only at low collector temperatures (up to T_c = 1100°C). At higher T_c, the steps smooth out; that is, the steady state on the electrode surface is not reached.

CONCLUSIONS

From our investigation it follows that use of electrodes both made of oxygen-containing materials (tungsten and niobium) is appropriate if a thermionic converter is designed for energy sources that must meet stringent requirements for weight and dimensions even at a sacrifice in the output power. In this case, a high optimal collector temperature (1200 K versus usual 900 K) allows for a substantial reduction of the weight and overall dimensions of a temperature radiator.

If the goal is to achieve the maximal possible output, then, as follows from the data currently available ([10] and this work), the module must have the emitter made of oxygen-containing single-crystalline tungsten and

the collector made of oxygen-free polycrystalline tungsten. Whether oxygen-containing tungsten will be efficient as a collector material remains unclear.

REFERENCES

1. D. M. Ernst, in *IEEE Conference Record of 1970 Thermionic Conversion Specialist Conference: Papers Presented at the 9th Annual Conference, Miami Beach, 1970* (IEEE, New York, 1970), pp. 492–497.
2. J. Dunlay, S. Matsuda, and V. Poirier, in *Proceedings of the 3rd International Conference on Thermionic Electrical Power Generation, Julich, 1972*, Vol. 3, pp. 1085–1090.
3. V. P. Kobyakov and A. G. Kalandarishvili, Zh. Tekh. Fiz. **68** (8), 131 (1998) [Tech. Phys. **43**, 997 (1998)].
4. V. P. Kobyakov, Zh. Tekh. Fiz. **66** (7), 169 (1996) [Tech. Phys. **41**, 726 (1996)].
5. V. P. Kobyakov, Kristallografiya **41**, 552 (1996) [Crystallogr. Rep. **41**, 523 (1996)].
6. V. P. Kobyakov, Zh. Tekh. Fiz. **66** (7), 161 (1996) [Tech. Phys. **41**, 722 (1996)].
7. C. V. Weaver and W. A. Ranken, in *IEEE Conference Record of 1969 Thermionic Conversion Specialist Conference, Carmel, 1969*, pp. 347–354.
8. P. Fiebelmann, Forsch. Geb. Ingenieurwes **38** (5), 133 (1972).
9. V. P. Kobyakov, Neorg. Mater. **38**, 1065 (2002).
10. V. P. Kobyakov and A. G. Kalandarishvili, Zh. Tekh. Fiz. **73** (2), 65 (2003) [Tech. Phys. **48**, 199 (2003)].
11. V. P. Kobyakov and V. N. Taranovskaya, Kristallografiya **44**, 1017 (1999) [Crystallogr. Rep. **44**, 948 (1999)].
12. V. P. Kobyakov and S. A. Zaslavskiĭ, Vysokochist. Veshchestva, No. 5, 75 (1989).

Translated by V. Isaakyan

Technical Physics, Vol. 49, No. 6, 2004, pp. 779–783. Translated from Zhurnal Tekhnicheskoĭ Fiziki, Vol. 74, No. 6, 2004, pp. 118–122.

EXPERIMENTAL INSTRUMENTS AND TECHNIQUES

Experimental Demonstration of the Sensitivity of an Optically Pumped Quantum Magnetometer

E. B. Alexandrov, M. V. Balabas, A. K. Vershovski, and A. S. Pazgalev

Vavilov State Optical Institute, All-Russia Research Center, Birzhevaya Liniya 12, St. Petersburg, 199034 Russia

e-mail: ealex@online.ru

Received November 10, 2003

Abstract—The sensitivity σ of an optically pumped quantum magnetometer is measured directly by comparing the output frequencies of ^{85}Rb and ^{87}Rb magnetometers integrated in a single two-isotope cell. The result $\sigma_{87} = 59.6 \pm 6$ fT Hz$^{-1/2}$ agrees well with the value $\sigma_{87}^{\text{light}} = 53.7 \pm 2$ fT Hz$^{-1/2}$ obtained indirectly by measuring the ratio of the resonance steepness to the shot noise of light. © *2004 MAIK "Nauka/Interperiodica".*

1. INTRODUCTION

In the last few decades, a great step forward has been made in the field of quantum magnetometry [1–4]. New types of optically pumped quantum magnetometers (OPQMs) that demonstrate a low-field short-term sensitivity on the order of several tenths of a femtotesla have been designed [5]. The parameters of conventional OPQMs that operate in the geophysical range of magnetic fields (20–80 μT) have also been improved. The most vivid example is a potassium-vapor OPQM, which combines a sensitivity of 10 fT Hz$^{-1/2}$, a base-line stability of the order of 10 pT, and an absolute accuracy of 0.1 nT [2]. Similarly high sensitivities may be reached in still lower fields (<15 μT) with Cs and Rb magnetometers operating on the unresolved Zeeman structure. Magnetometers with a high sensitivity in this range are needed, for example, for the fundamental experiment on detecting the permanent dipole moment of a neutron [6].

The sensitivity of OPQMs is usually estimated indirectly by measuring the resonance steepness-to-noise ratio [7]. This approach is based on the assumption that a minimal change in the magnetic field detectable by a magnetometer in a given frequency band (for example, 1 Hz) can be expressed as

$$\begin{aligned}\delta B_{\min} &= (1/\gamma)N/(dS/df)|_{f = f_0} \\ &= (1/\gamma)kN/(S/\Gamma).\end{aligned} \quad (1)$$

Here, γ is the gyromagnetic ratio, $f = f_0$ is the magnetic resonance frequency, $k \approx 1$ is the resonance form factor, Γ is the resonance line width, N is the rms noise level measured in the same frequency band, and S is the signal amplitude. The parameters k, S, Γ, and N can be measured directly in experiments; otherwise, the experimentalist can measure the resonance steepness $S' = (dS/df)|_{f = f_0}$ at the center of the resonance line and the noise level away from the resonance and then calculate the sensitivity as $\delta B_{\min} = (1/\gamma)/N/S'$.

The latter approach, however, implies that the OPQM noise is completely determined by the shot noise of light. This, in turn, means that (i) the noise inside and outside the resonance line is the same and (ii) the noise in the closed feedback loop is also defined by the shot noise of light. In other words, this approach implies that atomic fluctuations are negligible compared with the shot noise (which is the case for OPQMs) and that any type of technical noise may be reduced to the shot noise of light.

These assumptions, while quite plausible, have never been substantiated experimentally. Difficulties associated with experiments in this field are the following: to measure the inherent noise of the magnetometer, which is responsible for the ultimate sensitivity, it is necessary to eliminate the contribution of magnetic field variation to the measurand (the frequency of double radiooptical resonance in fields on the order of several femtoteslas). To stabilize the field with such an accuracy is a challenge at least in the geomagnetic range.

Under normal conditions, the noise of the terrestrial magnetic field exceeds the OPQM noise by four or five orders of magnitude. Moreover, the magnetic field gradient variation cannot, as a rule, be suppressed below several hundreds of fT/Hz$^{-1/2}$ per meter.

For many fundamental reasons, the magnetic field variation in a set of Helmholtz rings and/or multilayer magnetic shields is also difficult to suppress below a certain level. It is obvious that any system suppressing magnetic field variations based on readings of a single detector may reduce the variation only to the sensitivity level of this detector and only near its location. Suppression of first- or second-order magnetic field gradients calls for much more sophisticated multidetector equipment. There are also other fundamental limita-

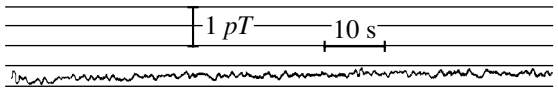

Fig. 1. Magnetic field gradient recorded under ultraquiescent magnetic conditions (Georgina island, Canada) when two potassium OPQMs were compared (the cell volume 1800 cm^3).

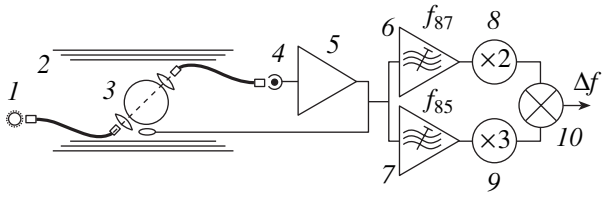

Fig. 2. Schematic of the experimental setup: (*1*) lamp containing the mixture of ^{87}Rb and ^{85}Rb isotopes; (*2*) magnetic shield; (*3*) cell containing the mixture of ^{87}Rb and ^{85}Rb isotopes; (*4*) photodetector; (*5*) wide-band amplifier; (*6, 7*) narrow-band amplifiers tuned to the self-oscillation frequencies of ^{87}Rb and ^{85}Rb, respectively; (*8, 9*) frequency multipliers; and (*10*) balanced mixer. The intermediate and terminal narrow-band amplifiers, microwave lamp-exciting generator, temperature stabilization loops of the lamp and cell, and magnetic field stabilization loops are omitted.

tions, such as thermal current noise in the metallic shield, etc.

Thus, the only way to directly measure the sensitivity of the magnetometer is to compare its readings with those of a device with the same or higher sensitivity provided that a change in the gradient between the locations of two devices does not exceed the sensitivity expected. In the case of OPQMs, this is difficult to accomplish: two similar OPQMs cannot be placed closer than 50 cm, since crosstalk between rf channels may be a problem.

That is why a sensitivity as high as 100 fT $Hz^{-1/2}$ or better calculated from the measured resonance steepness-to-noise ratio is so difficult to demonstrate experimentally (unless the field is ultralow [5]). To our knowledge, the highest OPQM sensitivity 60 fT $Hz^{-1/2}$ in the terrestrial field was demonstrated as a result of cooperation between GEM Systems Co., Inc. (Toronto, Canada) and the authors of this work (Vavilov State Optical Institute, St. Petersburg, Russia). Such a high value was obtained under extremely quiescent magnetic conditions by comparing two potassium OPQMs with a cell volume of 1800 cm^3 (Fig. 1). However, even in this case, the actual relative noise of the two magnetometers was higher than estimated by a factor of 8 to 20. It therefore becomes clear why metrologists and geophysicists are sceptical about high sensitivities thus obtained and continue to insist on direct measurements.

In this work, we report direct measurements of the OPQM sensitivity at a level of several fT $Hz^{-1/2}$ in a finite (nonzero) magnetic field. Our data are in good agreement with those obtained from the resonance steepness-to-shot noise ratio.

2. EXPERIMENTAL

We eliminated the effect of magnetic field gradient variation by integrating two rubidium-isotope magnetometers in a single cell and taking the difference between their readings. The experimental setup is shown in Fig. 2. In a laboratory shield exposed to a field B = 1170 nT, two single-beam self-oscillatory magnetometers were made. They operated on the unresolved structure of lines in the F = 2 state of ^{87}Rb and ^{85}Rb isotopes, were pumped with an rf gas-discharge lamp, had a mutual feedback loop, and shared a cell with walls of diameter 70 mm covered by an antirelaxation coating. The cell contained a drop of a rubidium isotope mixture in the proportion 1 : 1. Pumping was accomplished with circularly polarized light from the ^{87}Rb D_1 and ^{85}Rb D_1 lines of the spectroscopic lamp filled with the same isotope mixture. Near-optimal conditions for self-oscillation at both spectral lines were set by appropriately selecting the signal phase and amplifier gain. The setup was placed in the trilayer magnetic shield, and the signal from one magnetometer was used to stabilize the magnetic field 1170 nT inside the shield.

The use of the mutual cell made it possible to completely eliminate the gradient variation problem, since atoms of both isotopes in the given configuration are subjected to the same field averaged over the cell volume. Such a configuration of the magnetometers cannot provide a record high sensitivity that is comparable, e.g., to the sensitivity of potassium magnetometers (this issue will be touched upon below). Here, we would like to stress that our primary goal was to experimentally check the validity of determining the sensitivity by measuring the steepness-to-noise ratio, rather than to achieve a record high sensitivity.

The gyromagnetic ratios for ^{87}Rb (F = 2) and ^{85}Rb (F = 3) are given by

$$\gamma = \mu_B(g_J - 2Ig_I)/(2I + 1). \quad (2)$$

For ^{85}Rb, I = 5/2, g_J = 2.002331, and $g_I = 0.294745 \times 10^{-3}$; for ^{87}Rb, I = 3/2, g_J = 2.002331, and $g_I = 0.998823 \times 10^{-3}$ [8]. The value of μ_B equals 13.99624624(56) Hz/nT [9]. Then, γ_{85} = 4.667415 Hz/nT and γ_{87} = 6.995795 Hz/nT.

Using the proximity of the ratio γ_{87}/γ_{85} to the rational number 3/2, we devised a simple measuring scheme that effectively suppresses residual magnetic field fluctuations. To this end, the self-oscillation signal from the two isotopes that was detected by the same detector and amplified by the same amplifier was applied to two resonant amplifiers, each separating the self-oscillation

signal at the frequencies f_{85} and f_{87} corresponding to the isotopes. Simultaneously, the self-oscillation signal of ^{85}Rb was used to stabilize the field in the cell volume with a precision reference oscillator. Then, the frequency f_{85} = 5465 Hz was multiplied by three and the frequency f_{87} = 8192 Hz, by two. In this way, the field-to-frequency conversion coefficients became equal to each other up to the contribution from the nuclear magnetic moment $\Delta f_N = 8 \times 10^{-4} f_{85}$. Next, the difference frequency $\Delta f = (3f_{85} - 2f_{87}) = (3\gamma_{85} - 2\gamma_{87})B = \mu_B(3/2 g_1^{87} - 5/2 g_1^{85})B$ = 12.47 Hz was separated with a balanced mixer and measured in the field B = 1170 nT (Δf = 12.47 Hz). The frequency Δf differs from zero only due to the contribution from the nuclear moments (Δf may be slightly different from the above value because of imperfect phase tuning in the self-oscillation circuits), and its dependence on the magnetic field is three orders of magnitude weaker than the field dependence of f_{85} and f_{87}. Thus, the effect of residual magnetic field variation on the difference frequency is suppressed by a factor of 1000 with this measuring scheme. At the same time, crosstalk between the rf channels of the magnetometers is completely eliminated.

To evaluate the suppression of magnetic field fluctuations, we, along with difference frequency measurements, recorded the light intensities at the entrance to and the exit from the cell. In such a way (Fig. 3), we were able to trace the contribution of a frequency shift varying as the light intensity to the output frequency of the magnetometer.

The signal at the difference frequency Δf was recorded with a 14-bit analog-to-digital converter (ADC). The value of Δf averaged over 1 s was calculated from 512 counts by using fast Fourier transformation.

The value of the magnetic field in the shield (B = 1170 nT) was chosen from the following considerations. On the one hand, the field must be taken sufficiently low so that the Zeeman split of the Rb spectrum and the line broadening due to magnetic field nonuniformity in the shield contribute insignificantly to the resonance line width. On the other hand, the measurand Δf, which varies as the magnetic field, must be sufficiently high in order that be measured with a relative accuracy of 10^{-5} for a time of about 1 s. Note that an accuracy of 10^{-5}, with which the difference frequency was measured, corresponds to an accuracy of 10^{-8} in measuring the carrier frequency, since the difference frequency was three orders of magnitude lower than both carriers.

It is significant that, despite both magnetic resonance signals being detected by the same photodetector, the noise levels in the two magnetometers are not mutually correlated. The self-oscillation circuit of either of the magnetometers separates out from the wide-band noise spectrum a narrow spectral band of

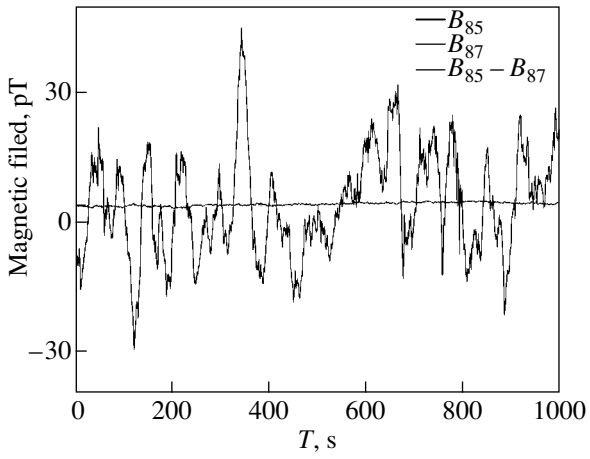

Fig. 3. Magnetic field (B) records in the ^{87}Rb and ^{85}Rb magnetometers and the difference between the records.

width Γ (Γ = 1–4 Hz is the magnetic resonance width) around the resonance frequency f_{85} or f_{87}. Since these frequency bands are 2.7 kHz apart, the shot noise levels in them are mutually independent. However, extra noise is present in each of the channels, because the radiation of one isotope is parasitic for the radiation of the other. In our case, this effect increases the radiation intensity roughly twofold, increasing the rms noise in each of the channels by a factor of $\sqrt{2}$.

The measurements were carried out at a cell temperature of 30°C and a total photocurrent of 21 μA. To eliminate the residual dependence of the self-oscillation frequency on the radiation intensity and cell temperature, we stabilized the temperature of the lamp projection, which contained the drop of the metal, and the cell temperature. The cell temperature was kept constant accurate to 2°C. The dark linewidth was 1 Hz; the operating linewidth, 3.5 Hz (Fig. 4).

A series of difference frequency measurements were made over given times of up to 6000 s, and then the difference frequency variance $\sigma_{\Delta f}$ was estimated. To relate this variance to the variances of the ^{87}Rb and ^{85}Rb channels, we must know the ratio of the channel weights, σ_{87}/σ_{85}, and the inherent noise N_{MS} of the measuring system:

$$\sigma_{\Delta f}^2 = \sigma_{87}^2 + \sigma_{85}^2 + N_{MS}^2. \quad (3)$$

To measure the ratio of the channel weights, we first measured the short-term sensitivity in the broken feedback loop of each of the channel for 1 s. Resonance was excited in a stabilized field, the variance component of the signal was detected with a synchronous detector, and the response of the synchronous detector to a small (compared with the resonance width) frequency offset from the resonance was recorded. In other words, the resonance steepness $S' = \Delta S/\Delta f$ and the noise signal amplitude were measured. The ratio of the variational

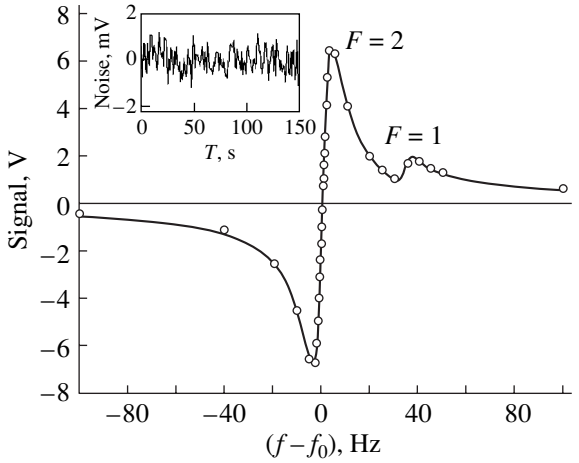

Fig. 4. Resonance line of ^{87}Rb versus the shot noise of the photocurrent (τ = 1 s). Γ(HWHM) = 3.74 Hz, f_0 = 8192 Hz, dS/df = 3.33 V/Hz, $\sigma_{87}^{\text{light}}$ = 21.5 fT s$^{1/2}$ = 53.7 ± 2 fT Hz$^{-1/2}$.

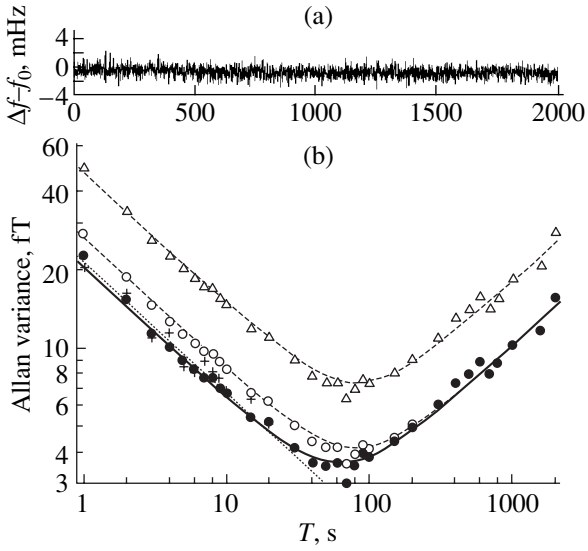

Fig. 5. (a) Record of the difference frequency $\Delta f = (3f_{85} - 2f_{87})$, f_0 = 12.868 Hz; (b) (△) Allan variance of the difference frequency Δf, (○) Allan variance of the frequency f_{87} (including the measuring system noise), (●) Allan variance of the frequency f_{87} (the measuring system noise subtracted), and (+) sensitivity of the ^{87}Rb channel that is found from the resonance steepness-to-shot noise ratio.

sensitivities of the channels was found to be $\delta B_{\min}^{85}/\delta B_{\min}^{87}$ = 1.44 ± 0.08. Since the amplitudes, linewidths, and spectral densities of the noise for both signals turned out to coincide within 5%, one can argue that the ratio of the variational sensitivities is consistent with the theoretical predictions and depends on the difference in the gyromagnetic ratios of the Rb isotopes (γ_{87}/γ_{85} = 1.499).

Using the ratio measured and formula (3), we can relate the difference frequency variance $\sigma_{\Delta f}$ to the frequency variances of the ^{87}Rb and ^{85}Rb channels: $\sigma_{87} = (\sigma_{\Delta f}^2 - N_{\text{MS}}^2)/1.78$ and $\sigma_{85} = (\sigma_{\Delta f}^2 - N_{\text{MS}}^2)/1.26$.

The fluctuations in the frequency synthesizer and frequency meter were measured by application of signals from G3-110 reference frequency generators to their inputs. The sensitivity threshold of the ADC was found to be 20 fT Hz$^{-1/2}$ (including the noise component due to fast Fourier transformation). When estimating the inherent noise of the entire measuring channel, including the frequency synthesizer, by the same method (i.e., by application of the signals from the reference generators instead of the real signal), we faced the problem of the inherent noise of the generators. We were not able to improve the measurement accuracy: this would require reference generators with an inherent noise of lower than 10^{-8} Hz$^{-1/2}$. The value measured with the G3-110, 105 ± 20 fT Hz$^{-1/2}$, should, therefore, be viewed as the upper level of the fluctuations inherent in the measuring scheme (the lower one is thus 20 fT Hz$^{-1/2}$).

We tried to narrow the range of estimates, assuming that, under a constant level of illumination, the inherent noise of a magnetometer is inversely proportional to the resonance steepness (as follows from (1)), while the noise N_{MS} of the measuring system is additive and independent of the resonance parameters. An attempt was made to isolate this resonance-independent component, varying (under constant illumination) the rf field amplitude and tracing the dependence of the resonance steepness S' on the channel noise σ_{87}, measured directly. Approximating this dependence by the model formula $\sigma_{87}(S') = [(A/S')^2 + N_{\text{MS}}^2]^{1/2}$, we obtained N_{MS} = 71 ± 20 fT Hz$^{-1/2}$. Such an estimation is certainly based on the same assumption as the method of finding the sensitivity from the steepness-to-noise ratio. Therefore, this estimate, strictly speaking, may be used if the validity of this method is proved. It will be shown below that this method provides good agreement with experimental data even without taking into account the noise of the measuring system.

An example of calculating the ultimate sensitivity of the magnetometer from the steepness-to-shot noise ratio is given in Fig. 4. Figure 5 shows the results of direct measurements: the time series of the difference frequency and the Allan diagram for the difference frequency Δf. The symbols are data points; the curves approximate the dependence of the noise on the time of measurement.

From Fig. 5, it follows that the sensitivity of our magnetometers depends on the shot noise over averaging times shorter than 50 s. The Allan variance reaches a minimum of ≈4 fT over times of 60 to 100 s and then grows as $T^{1/2}$: $\sigma_{87}^{\text{long}} = (0.33\ \text{fT s}^{1/2})T^{1/2}$.

The Allan variance of the difference frequency Δf in the time interval 1–50 s is $\sigma_{\Delta f} = 118.4 \pm 4$ fT Hz$^{-1/2}$. Converting it to the frequency variance of the ^{87}Rb channel, we get $\sigma_{87} = 66.4 \pm 2$ fT Hz$^{-1/2}$. With regard to our estimate of the noise N_{MS} of the measuring system, the corrected value is $\sigma_{87}^{corr} = 51 \pm 9$ fT Hz$^{-1/2}$. The latter result almost coincides with that given by the steepness-to-noise ratio method: $\sigma_{87}^{light} = 53.7 \pm 2$ fT Hz$^{-1/2}$ (Fig. 4). Thus, the procedure of determining the sensitivity of a magnetometer from the ratio of the resonance steepness to the shot noise of radiation has been substantiated experimentally for the first time.

Note in conclusion that the sensitivity demonstrated in this work is lower than the ultimate value expected for OPQMs. The basic factors limiting the sensitivity in our case are as follows.

(i) The cell used in the experiments was relatively small (180 cm^3) to avoid line broadening due to magnetic field nonuniformity in the shield.

(ii) As was mentioned above, the radiation of one isotope is parasitic for the radiation of the other in a two-isotope configuration. Because of this, the sensitivity was reduced by a factor of $\sqrt{2}$.

(iii) In a two-isotope configuration, the line of one isotope is excessively broadened, since atoms of one isotope experience spin-exchange collisions with atoms of the other isotope.

(iv) In the case of rubidium, the efficiency of optical detection of optical orientation is roughly twice as low as in the case of potassium, because the hyperfine split of the ground and excited states in the former case is much higher.

Our experimental verification of the procedure of finding the sensitivity from the resonance steepness-to-short noise ratio supports its validity at sensitivity levels achieved today. It seems quite possible that new noise sources, for example, the magnetization noise of the working medium, will show up when the noise level is reduced further.

ACKNOWLEDGMENTS

This work was partially supported by the INTAS (project no. 01-0765).

REFERENCES

1. E. B. Aleksandrov, M. V. Balabas, A. É. Ivanov, *et al.*, Opt. Spektrosk. **78**, 325 (1995) [Opt. Spectrosc. **78**, 292 (1995)].
2. E. B. Alexandrov, M. V. Balabas, A. S. Pasgalev, *et al.*, Laser Phys. **6**, 244 (1996).
3. D. Budker, D. F. Kimball, S. M. Rochester, *et al.*, Phys. Rev. A **62**, 043403 (2000).
4. D. Budker, V. Yashchuk, and M. Zolotorev, Phys. Rev. Lett. **81**, 5788 (1998).
5. I. K. Kominis, T. W. Kornack, J. C. Allred, and M. V. Romalis, Nature **422**, 596 (2003).
6. E. Alexandrov, M. Balabas, G. Ban, *et al.*, PSI Sci. Rep. (Paul Sherrer Institute, Villigen, 2002), Vol. 1, pp. 25–26.
7. C. Cohen-Tannoudji, J. DuPont-Roc, S. Haroche, and F. Laloe, Phys. Rev. Lett. **22**, 758 (1969).
8. A. A. Radtsig and B. M. Smirnov, *Reference Data on Atoms, Molecules, and Ions* (Énergoatomizdat, Moscow, 1986; Springer-Verlag, Berlin, 1985).
9. P. J. Mohr and B. N. Taylor, Rev. Mod. Phys. **72**, 351 (2000).

Translated by V. Isaakyan

Technical Physics, Vol. 49, No. 6, 2004, pp. 784–786. Translated from Zhurnal Tekhnicheskoĭ Fiziki, Vol. 74, No. 6, 2004, pp. 123–125.

SHORT COMMUNICATIONS

Photoanisotropic Compositions with an Extended Spectral Range of Anisotropy

S. S. Petrova and V. G. Shaverdova

Institute of Cybernetics, Academy of Sciences of Georgia, Tbilisi, 380086 Georgia

Received July 4, 2003

Abstract—Experimental data for two- and three-component compositions (dyes embedded in gelatinous and polymeric matrices) that are Weigert-sensitive to polarized radiation in a wide spectral range are reported. It is shown that the matrix considerably affects the photoanisotropic properties of the compositions. © *2004 MAIK "Nauka/Interperiodica".*

It is known that polarization holography applications need media that become anisotropic under the action of polarized light—the effect discovered by Weigert in 1919 [1]. In developing a theory of polarization holography, Kakichashvili showed [2] that the holographic medium and the polarized wave field equally take part in imaging. Thus, having an appropriate light-sensitive photoanisotropic medium at hand, one can detect (write) and reproduce all characteristics of an electromagnetic field, including the state of polarization. A variety of light-sensitive media are available today where polarized light induces photophysical and photochemical processes resulting in photoanisotropy and photogyrotropy. Among these media are composite materials consisting of organic dyes embedded in polymeric or gelatinous matrices [3–6].

In organic-dye-based polarization-sensitive media considered previously, photoanisotropic absorption was observed in a relatively narrow range depending on the properties of the dye. It is known that the photochemical behavior of dyes in the free state usually differs greatly from their behavior in mixtures, specifically, the absorption spectra of dyes in mixtures may change. A decrease in the dye absorptivity is sometimes accompanied by a shift or broadening of the absorption peak or by appearance of new absorption bands [7].

It would be natural to assume that the photoanisotropic properties of dye mixtures will be different from those of the dyes incorporated into these mixtures. Based on these assumptions, two- and three-component compositions Weigert-sensitive in the spectral range 400–750 nm have been formulated.

The two-component composition consists of a mordant yellow azo dye, which is Weigert-sensitive to the blue–green spectral range (component A), and a dye from the triphenylmethane group, which is Weigert-sensitive to the red range (component B). The three-component composition also contains a dye from the fuchsin group (component C), which has a maximum absorptivity in the green range. The absorption spectrum of fuchsin has a long-wave peak between 500 and 550 nm [8].

Mordant yellow azo dyes (MYADs) (component A) are Weigert-sensitive to polarized light in the interval 325–550 nm, and their spectral sensitivity is maximal at 420 to 440 nm. They exhibit anisotropic absorption from 350 to 510 nm and photoinduced birefringence throughout the visible range [9]. It is believed that photoinduced anisotropy in mordant dyes is due to conformation *cis*- and *trans*-isomerization.

Triphenylmethane dyes (TPMDs) (component B) are not Weigert-sensitive: even intense radiation from a He–Ne laser (632.8 nm), which is actinic for these dyes, causes uniform bleaching of the region irradiated.

As early as in 1976, it was shown [10] that treatment of TPMD-colored gelatinous layers in aqueous solutions of potassium, sodium, or ammonium bichromate causes a drastic rise in the optical sensitivity of the material and pronounced anisotropy. When TPMD-colored bichromate-tanned gelatin is irradiated by the continuous spectrum of a xenon lamp, the area irradiated by 400- to 550-nm-wavelength radiation blackens uniformly; however, at wavelengths from 550 nm up to the visible range boundary, the color changes nonuniformly. This is because the uniform darkening at 400–550 nm takes place in the bichromate-tanned gelatin itself, while the optically induced anisotropy results from photochemical reactions between chromium compounds and active functional groups of the dye and gelatin [11] (comparison was made with bichromate-tanned dye-free gelatin). In other words, bichromate has the opposite effects on components A and B: it sensitizes component B (and partially component C), while reducing the sensitivity of component A to the polarized light from the short-wave part of the spectrum. Since the MYAD enters into the composition as a basic component (component A), a decrease in its sensitivity, which shows up as uniform blackening, is extremely undesirable. Keeping in mind that the bichromate-tanned gelatin is responsible for the black-

1063-7842/04/4906-0784$26.00

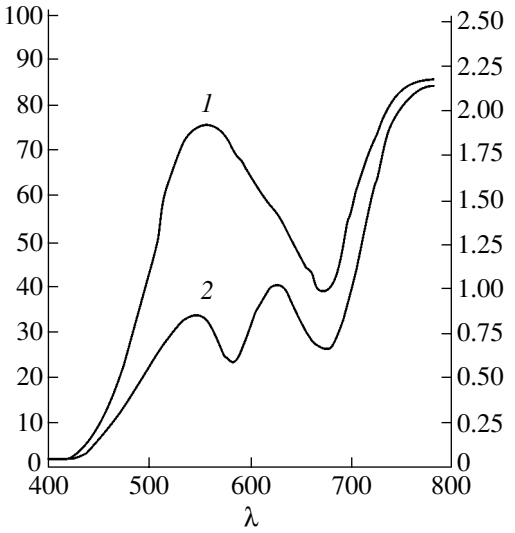

Fig. 1. Transmission curves of the samples: (*1*) two-component and (*2*) three-component composition.

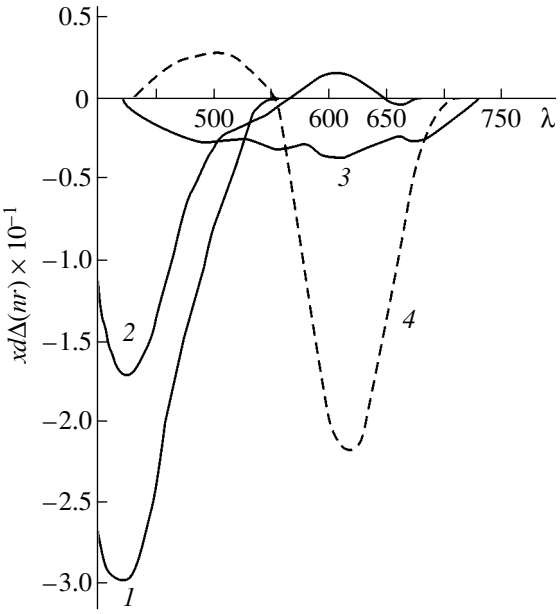

Fig. 2. Spectral dependences of the photoanisotropy for the two-component composition. (*1*) λ = 441.6 nm, *t* = 10 min; (*2*) λ = 514.5 nm, *t* = 30 s; (*3*) λ = 632.8 nm, *t* = 15 min; and (*4*) TPMD (turquoise basic), λ = 632.8 nm, *t* = 15 min.

ening, we carried out additional experiments where other matrices not as sensitive to bichromate were employed. It turned out that a polyvinyl pyrrolidone (PVP) matrix is promising for the multicomponent composition. Irradiation by a He–Cd laser (441.6 nm) does not cause uniform blackening, while leaving all the advantages of component B unchanged. Thus, using PVP as a matrix, we could formulate two- and three-component compositions Weigert-sensitive to basic wavelengths of 441.6, 488.0, 514.5, and 632.8 nm.

The dyes considered in this paper differ in physicochemical properties and mechanisms responsible for anisotropy. Therefore, special techniques are needed to make the most of their photoanisotropic properties. The concentrations of each of the dyes involved were selected empirically, and the component ratio was determined from spectrophotometric measurements.

Figure 1 shows the transmission curves for the two- and three-component compositions. Component A is chrome yellow "K" ($c = 3.28 \times 10^{-2}$ mol/l); component C, fuchsin ($c = 1.33 \times 10^{-2}$ mol/l); the matrix, PVP (5 wt %) and ammonium bichromate (2.5 wt%). The degree of induced anisotropy was measured quantitatively. To this end, the samples were irradiated by light with different wavelengths. The exposures were kept the same (≈48 J/cm^2) by varying the irradiation time (Figs. 2, 3). The anisotropy was measured with a modified SF-10 spectrophotometer. The reference channels of the instrument contained focusing systems and polarizers, which could be tuned parallel and perpendicularly to the plane of polarization of probing light. The focusing systems served to narrow the exit pupil of the measuring beam in order that small areas of the material under test be illuminated. A dial holder allowed us to place the material parallel, perpendicular,

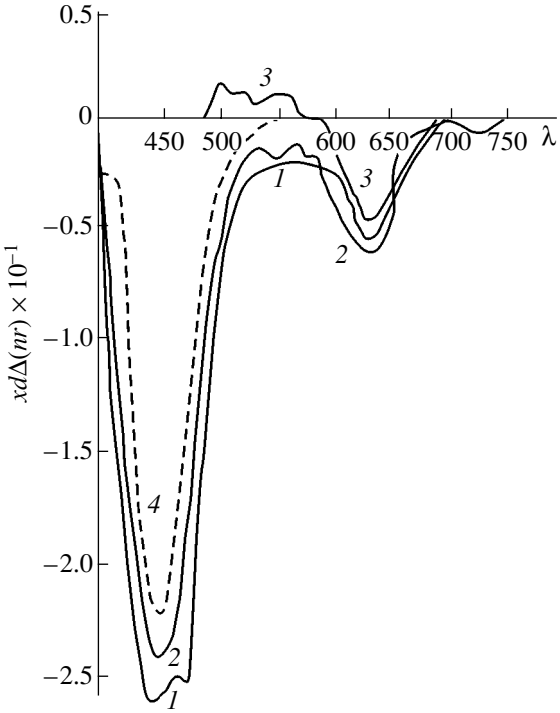

Fig. 3. Spectral dependences of the photoanisotropy for the three-component composition. (*1*) λ = 441.6 nm, *t* = 15 min; (*2*) λ = 514.5 nm, *t* = 30 s; (*3*) λ = 632.8 nm, *t* = 30 min; and (*4*) MYAD (chrome yellow "K"), λ = 441.6 nm, *t* = 15 min.

and at an angle of 45° to the polarization of the actinic radiation.

As follows from Fig. 2 (curve *3*), illumination by the He–Ne laser causes absorption anisotropy throughout the visible range. The sign of the anisotropy does not change. This suggests that the composition responds to the radiation of the laser differently than component B (TPMD) entering into it, for which alternating-sign anisotropy is observed (curve *4*).

Figure 3 shows the absorption anisotropy distributions for the three-component composition. The anisotropy curves taken under irradiation by the He–Cd and Ar lasers (curves *1*–*3*) differ substantially from that obtained for the MYAD (curve *4*). Photoanisotropy arising under irradiation by the He–Cd laser covers the entire visible spectrum, exhibiting two maxima: one in the interval 420–440 nm and the other (long-wave) between 620 and 630 nm. At the same time, for the MYAD, the absorption is anisotropic between 350 and 510 nm. Thus, our experiments lend support to the validity of the assumption that the photoanisotropic properties of the dyes in mixtures and in free state differ.

As follows from the figures, the samples are anisotropic throughout the visible part of the spectrum (400–750 nm) and are Weigert-sensitive to polarized light at different wavelengths (365–632 nm).

Since our multicomponent compositions are Weigert-sensitive in a wide spectral range, they may find application in color Weigert photography, color polarization holography, novel holographic polarization components, etc.

Works are now under way on formulating new compositions. Specifically, new dyes and polymer binders to further sensitize the material are being looked for. Results of these investigations will be reported in subsequent publications.

REFERENCES

1. F. Weigert, Verh. Dtsch. Phys. Ges. **21**, 479 (1919).
2. Sh. D. Kakichashvili, *Polarization Holography* (Nauka, Leningrad, 1989), pp. 10–11 [in Russian].
3. A. Ya. Zheltov, B. I. Stepanov, and V. G. Shaverdova, Zh. Prikl. Spektrosk. **52**, 280 (1990).
4. V. G. Shaverdova, G. A. Kakauridze, and I. A. Shvaitzer, Proc. SPIE **1183**, 253 (1990).
5. V. G. Shaverdova, Izv. Akad. Nauk Gruz. (Matsne) **29** (1–2), 27 (2003).
6. S. S. Petrova, Zh. Tekh. Fiz. **71** (3), 81 (2001) [Tech. Phys. **46**, 351 (2001)].
7. A. N. Terenin, *Photonics of Dye Molecules* (Nauka, Leningrad, 1967), p. 47 [in Russian].
8. G. N. Vinyukova, *Chemistry of Dyes* (Khimiya, Moscow, 1979) [in Russian].
9. Sh. D. Kakichashvili and V. G. Shaverdova, *Photochemical Recording of Holograms* (Leningrad, 1983), pp. 34–40 [in Russian].
10. Sh. D. Kakichashvili and V. G. Shaverdova, Opt. Spektrosk. **41**, 892 (1976) [Opt. Spectrosc. **41**, 525 (1976)].
11. G. N. Nikitina, V. P. Sherstyuk, I. I. Dipung, V. G. Shaverdova, and Sh. D. Kakichashvili, *Fundamentals of Optical Memory and Optical Media* (Leningrad, 1983), No. 14, pp. 56–61 [in Russian].

Translated by V. Isaakyan

Technical Physics, Vol. 49, No. 6, 2004, pp. 787–789. Translated from Zhurnal Tekhnicheskoĭ Fiziki, Vol. 74, No. 6, 2004, pp. 126–128.

SHORT COMMUNICATIONS

On the Properties of Photovoltaic X-ray Detectors Based on GaAs Epitaxial Structures

V. F. Dvoryankin, Yu. M. Dikaev, and A. A. Kudryashov

Institute of Radio Engineering and Electronics, Russian Academy of Sciences (Fryazino Branch), Fryazino, Moscow oblast, 141190 Russia

e-mail: vfd217@ire216.msk.su

Received July 23, 2003

Abstract—Operation of a new photovoltaic detector of X-ray bremsstrahlung based on GaAs epitaxial structures at room temperature without bias is studied. The efficiency of the absorbed energy conversion into short-circuit current is calculated from the measured photoresponses for the photon energies in the range from 12 to 120 keV. In this energy range, the absorption in GaAs is governed by photoelectric effect. The efficiency of the X-ray bremsstrahlung energy conversion in GaAs peaks at 80 keV. It is suggested that the X-ray absorption of a thin 50-μm detector can be enhanced by applying an inclined irradiation scheme. The effect is most pronounced in the region of hard X-rays. © *2004 MAIK "Nauka/Interperiodica"*.

In the previously proposed photovoltaic X-ray detector fabricated on the basis of GaAs epitaxial structures, the collection of photoinduced charge carriers is realized with zero bias voltage at room temperature [1]. The absorption of X-ray photons with energies from 12 to120 keV in GaAs is defined by photovoltaic effect, which results in the photoemission of electrons with the kinetic energy $E_{ph} = E - E_c$, where E is the photon absorption energy and $E_c \approx 12$ keV is the binding energy of electrons at K-shells of Ga and As atoms.

The quantum yield of the internal photoelectric effect can be taken proportional to the electron energy:

$$\eta = kE_{ph}, \quad (1)$$

where k is the efficiency factor of the absorbed energy conversion to photoelectrons, which depends on the properties of the detector material.

This coefficient can be determined experimentally. The amount of X-ray photons absorbed in the active region of the detector is given by the Lambert law [2]:

$$N = N_0[1 - \exp(-\mu d)], \quad (2)$$

where N_0 is the number of X-ray photons falling per unit area of the detector surface, μ is the linear absorption coefficient of the detector material, and d is the photon absorption depth.

The short-circuit current produced by the detector per unit area can be expressed as

$$J = q\eta N = IS, \quad (3)$$

where q is the electron charge, I is the X-ray radiation intensity, and S is the photoresponse of the detector.

From (1)–(3), the dependence of photoresponse on the energy of the X-ray photons can be written in the form

$$S = (kqN_0/I)(E - E_c)[1 - \exp(-\mu d)]. \quad (4)$$

This expression is also valid for the X-ray bremsstrahlung with the efficient energy corresponding to E. The absorption coefficient μ as a function of the X-ray radiation energy for GaAs can be taken from tables [2].

The X-ray sensitivity of this detector ranges from 8 to 120 keV. For the absorption thickness $d = 50$ μm, the short-circuit current peaks at 35 keV; the experimental values of S in this case were obtained in [3]. Using these quantities and formula (4), we calculated (kqN_0/I), which is shown in Fig. 1a. The peak value at $E = 80$ keV corresponds to the most efficient conversion of the photon energy to photocurrent, when the transformation of the initial high-energy electrons into the secondary low-energy electrons occurs with the minimal losses for the "by-product" formation of phonons and plasmons. Under the assumption of monoenergy radiation, the maximum of conversion efficiency in GaAs falls at 60 keV [1]. In our study, we used a mixed X-ray bremsstrahlung beam, where in the beam with the effective photon energy 80 keV the number of photons with $E < 80$ keV is greater than that with $E > 80$ keV. The range from 20 to 60 keV is characterized by a linear dependence, which can be presented in the form

$$(kqN_0/I) = KE, \quad (5)$$

where $K \cong 0.2$ [μA min Gy^{-1} cm^{-2} keV^{-2}] is the proportionality factor.

Substituting (5) into (4), we calculated the dependence $S = S(E)$ within the linear range of the photon energies for various d (Fig. 1b). It is seen that an increase in the absorption layer thickness leads to the

1063-7842/04/4906-0787$26.00

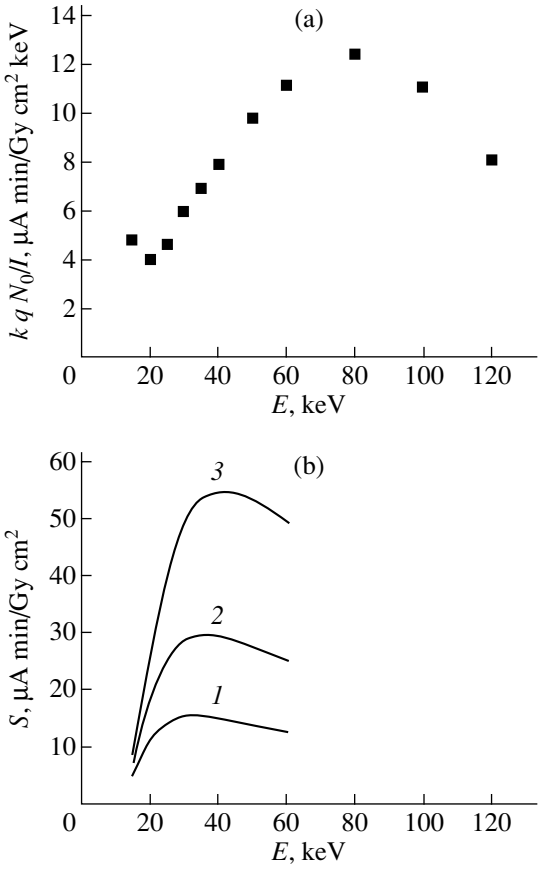

Fig. 1. (a) The efficiency of the energy conversion to photocurrent and (b) the photoresponse of a GaAs detector vs. the effective energy of X-ray radiation for d = (*1*) 25, (*2*) 50, and (*3*) 100 μm.

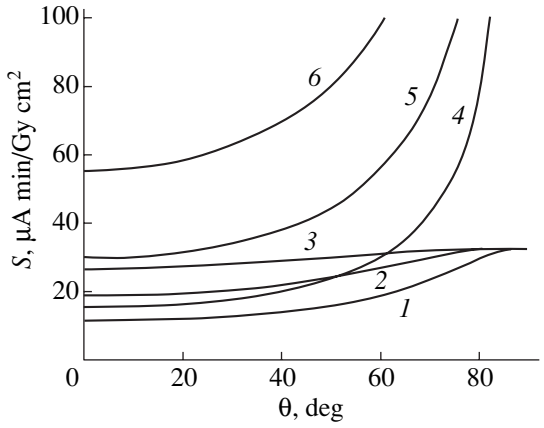

Fig. 2. The photoresponse of a GaAs detector vs. the angle of incidence for the photon energy E = (*1–3*) 20 and (*4–6*) 40 keV and the detector thickness d = (*1*, *4*) 25, (*2*, *5*) 50, and (*3*, *6*) 100 μm.

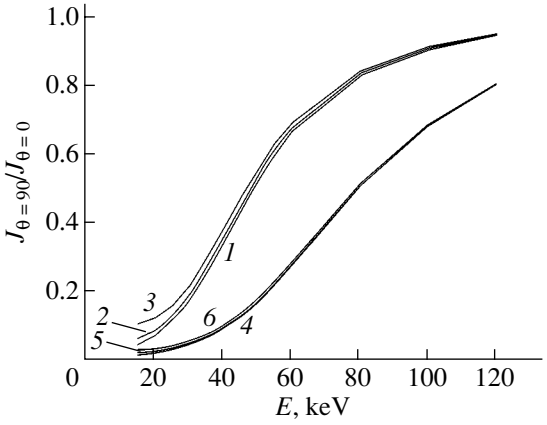

Fig. 3. The photocurrent of end-on-irradiated detector with L = (*1–3*) 1 and (*4–6*) 4 mm and d = (*1*, *4*) 25, (*2*, *5*) 50, and (*3*, *6*) 100 μm.

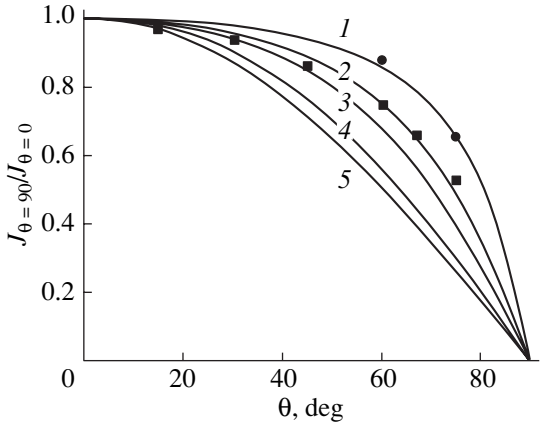

Fig. 4. The detector current vs. the angle of incidence for μd = (*1*) 1/3, (*2*) 2/3, (*3*) 1, (*4*) 2, and (*5*) 4. Squares correspond to E = 23 keV, μ = 130 cm^{-1}, d = 50 μm; circles, to E = 30 keV, μ = 62 cm^{-1}, d = 50 μm.

growth of photoresponse and to a shift of the peak toward harder X-rays.

Photoresponse can be increased by irradiating detector at a sliding angle of incidence. In this case, the effective absorption thickness becomes

$$d_\theta = d/\cos\theta, \qquad (6)$$

where θ is the angle between the incident X-ray beam and the surface normal.

An increase in θ leads to the growth of the photon absorption depth d_θ in the active layer. With the substitution of (6), formula (4) suggests similar behavior of short-circuit photocurrent as that illustrated by curves in Fig. 1b. However, if the linear length L of the detector is limited, the induced photocurrent is proportional to the aperture $L\cos\theta$ and corresponds to the value

$$J_\theta = jL\cos\theta. \qquad (7)$$

It is seen from Fig. 2 that, with a growing angle, the signal drops (according to (7)), whereas the photoresponse grows (according to (4)). By increasing the angle of incidence, the signal from photodetector can be enhanced by several times depending on the photon

energy with the aperture being the same. This effect is appreciable for harder X-rays. Thus, the detector with a thin active layer of photon absorption can be efficient for the detection of harder X-rays, when the response at normal incidence is only weak.

It is interesting to consider the situation when the detector is irradiated end on. In this case, the signal is proportional to the detector aperture d and the absorption layer thickness is defined by the length L. The ratio between the end-on- and the normal-incidence signals is

$$J_{\theta = 90}/J_{\theta = 0} = (d/L)[1 - \exp(-\mu L)]/[1 - \exp(-\mu d)], \quad (8)$$

which tends to $1/(\mu L)$ for a thin ($\mu d \ll 1$) and long ($\mu L \gg 1$) detector and to unity for a detector with low absorption, which takes place in the case of hard X-rays. The dependences of ratio (8) on the photon energy for different detector thickness d are plotted in Fig. 3.

Figure 4 presents the quantities

$$J_\theta/J_{\theta = 0} = \cos\theta[1 - \exp(-\mu d_\theta)]/[1 - \exp(-\mu d)] \quad (9)$$

as a function of the angle of incidence (at $\theta < \arccos(d/L)$. Note that formulas (8) and (9) depend neither on the origin of photoelectrons nor on the quantum yields and are valid within the entire sensitivity range of the detector. Figure 4 also shows the experimental values of photocurrent obtained in a detector with the absorption layer thickness 50 μm under the irradiation by photons of different energies. It is seen that, measuring the angle dependences of the detector signal, one can determine the active absorption layer thickness by choosing a value of d in (9) that yields the closest correlation between calculation and the experiment.

The irradiation of the detectors with a dose of 6000 R did not noticeably deteriorate the sensitivity S, which indicates their applicability for long-term operation.

REFERENCES

1. R. A. Akhmadullin, V. F. Dvoryankin, G. G. Dvoryankina, *et al.*, Pis'ma Zh. Tekh. Fiz. **26** (1), 34 (2002) [Tech. Phys. Lett. **26**, 15 (2002)].
2. O. F. Nemets and Yu. V. Gofman, *A Handbook on Nuclear Physics* (Naukova Dumka, Kiev, 1975) [in Russian].
3. V. F. Dvoryankin, Yu. M. Dikaev, A. A. Kudryashov, *et al.*, Izmer. Tekh. (2003).

Translated by A. Sidorova

Technical Physics, Vol. 49, No. 6, 2004, pp. 790–794. Translated from Zhurnal Tekhnicheskoĭ Fiziki, Vol. 74, No. 6, 2004, pp. 129–133.

SHORT COMMUNICATIONS

Formation of Coniform Microdischarges in KrCl and XeCl Excimer Lamps

M. I. Lomaev*, V. F. Tarasenko*, A. N. Tkachev, D. V. Shitts*, and S. I. Yakovlenko****

** Institute of High-Current Electronics, Siberian Division, Russian Academy of Sciences, Akademicheskiĭ pr. 4, Tomsk, 634055 Russia*

e-mail: vft@loi.hcei.tsc.ru

*** General Physics Institute, Russian Academy of Sciences, ul. Vavilova 38, Moscow, 117942 Russia*

e-mail: syakov@kapella.gpi.ru

Received August 11, 2003

Abstract—The dynamics of formation of the steady-state regime in KrCl and XeCl double-barrier excimer lamps excited by a pulsed-periodic discharge is studied. Diffusive microdischarges in the form of two cones with joint vertices are shown to appear for about 1 s. Over this time interval, the initially volume exciting discharge (within several early pulses) transforms into a spark (immediately before the formation of the coniform microdischarges). It is demonstrated that the spark–diffusive discharge transition may be associated with fast electron generation. © *2004 MAIK "Nauka/Interperiodica".*

INTRODUCTION

At present barrier-discharge-excited sealed off lamps are viewed as the most promising sources of ultraviolet and vacuum ultraviolet. Operation and application of these lamps have been the subject of extensive investigation (see [1, 2] and references therein). Emphasis has been on the discharge and output radiation characteristics under the steady-state operating conditions, when the parameters of exciting and output pulses remain unchanged. However, the dynamics of formation of the steady-state regime (steady discharge) is very complex and has been thus far poorly understood. It was shown [2] that barrier discharge glow in coaxial KrCl and XeCl lamps varies with pulse repetition rate. At low repetition rates (from several hertz to several tens of hertz), a volume discharge is observed. As the repetition rate increases, small-diameter diffusion channels are produced. Subsequently, when the repetition rate reaches ≈1 kHz, the discharge splits into coniform diffusive microdischarges with joint vertices. The number of such microdischarges grows with increasing excitation power (that is, with increasing repetition rate) and eventually they occupy the entire volume of an excimer lamp (the bases of the cones completely cover the surface of the quartz tubes). It should be noted that the average radiation output reaches a maximum at the developed stage of diffusive microdischarges, while the radiation efficiency becomes maximal in the intermediate range of repetition rates (≈1 kHz), where early coniform microdischarges start arising on the background of diffusive cylindrical microdischarges. It was conjectured [3] that fast electrons generated in an enhanced electric field play an important role in formation of diffusive cones.

The aim of this work is to study the dynamics of formation of the barrier discharge steady stage, where the average power of radiation due to KrCl* and XeCl* molecules is the highest, and find reasons behind the formation of coniform microdischarges.

EXPERIMENTAL SETUP AND TECHNIQUES

We experimented with an excimer lamp (for details, see [1, 2]) composed of two coaxial quartz tubes. The outer diameter of the outer tube 2.5 mm thick was 65 mm, and the outer diameter of the inner tube 1.5 mm thick was 43 mm; accordingly, the discharge gap was 8.5 mm long. The length of the excimer lamp was 60 cm. The outer electrode was made of a grid and had a length of 10 or 57 cm. The inner electrode was made of aluminum foil. The inner quartz tube and the inner electrode were cooled by running water. The lamp was excited by pulses of amplitude up to 8 kV, duration ≈1.5 μs, and repetition rate 75 kHz. Under the steady-state conditions, such a pulse rate provided a sufficiently high average output and efficiency for both molecules (35 mW/cm^2 and 11%, respectively, for KrCl* ($\lambda \approx 222$ nm)).

To trace the dynamics of barrier discharge initiation, the lamp was excited by pulse bursts with a variable number of pulses. The pulse burst repetition rate was 1 Hz. The duration of a pulse burst was gradually varied from 10 μs to 0.5 s. Proceeding in this way, we could observe variation of the discharge shape at the time the lamp was switched on. During experiments, we recorded voltage pulses across the lamp, the discharge current, and radiation pulses from exciplex molecules in the UV range. In addition, the discharge was photo-

1063-7842/04/4906-0790$26.00

graphed at different durations of pulse bursts. Prior to experiments, the pressure and composition of the gas mixture were optimized. The best results were obtained in the mixture Kr : $Cl_2 \cong 200 : (1.0–0.5)$ at a pressure of 200 Torr and in the mixture Xe : $Cl_2 \cong 120 : (1.0–0.5)$ at 120 Torr.

EXPERIMENTAL RESULTS

The basic experimental results can be summarized as follows. Within 1 s after excitation, the steady-state operating conditions in the lamp are formed in four steps. At the early stage (0–0.02 ms), a volume discharge is initiated in the electrode gap (Fig. 1a). At the second stage (0.02–0.10 ms), filamentary channels arise on the background of the volume glow (Fig. 1b). Then (0.1–400 ms), the filamentary channels transform into a few bright branched channels of low radiation efficiency (Fig. 1c). At the final (fourth) stage (usually 0.4–1.0 s; Fig. 1d), only coniform microdischarges are observed, the radiation efficiency being several times higher than at the third stage.

The waveforms of radiation, voltage, and current pulses were recorded at each of the stages. When the lamp is switched on by the first pulse, the radiation intensity is the lowest; then, it grows (initial pulses, Fig. 2a). During the first pulse, the voltage across the gap is the highest ($U \approx 8$ kV) and the current is minimal. Subsequently, the current amplitude grows and the voltage drops. At the third stage, the peak radiation power is low and the discharge is contracted (Fig. 2b). At the fourth (steady-state) stage, the radiation pulse amplitude grows severalfold (Fig. 2c) but the voltage across the gap ($U \approx 5.5$ kV) and the discharge current change insignificantly. Figures 1c and 1d show that the appearances of the discharge at the third and fourth stages are much different. Of most interest in these experiments is the fact that the spark turns into the "decontracted" discharge without circulating the working medium and changing its composition. When an exciting pulse burst lasts about 1 s, bright sparks change to coniform microdischarges. It is should be noted that discharge decontraction was observed earlier in pulsed–periodic discharges of transversely pumped flowing CO_2 lasers [4] and longitudinally pumped pulsed–periodic metal-vapor lasers [5]. This effect was explained by variation of the gas mixture composition during laser operation. In our case, the composition of the mixture remained unchanged and all the four stages were reproduced at each excitation of the lamp.

DISCUSSION

In our experiments, the transition of the contracted discharge to the volume (diffusive) form can be explained by fast electron generation. Although generation of runaway electrons in pulsed discharges at elevated pressures had been known for long, runaway electron beams with a current varying from several tens

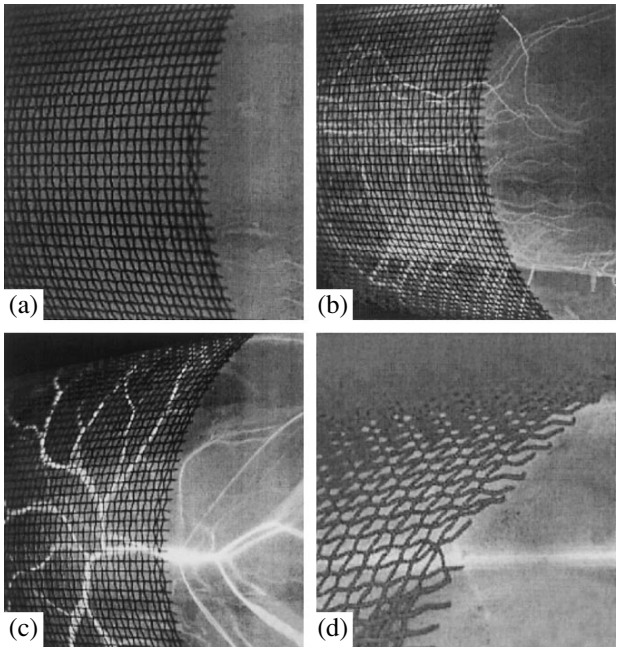

Fig. 1. Discharge glow in the Kr + Cl_2 mixture at stages (a) 1, (b) 2, (c) 3, and (d) 4.

to several hundreds of amperes under atmospheric pressure of air and helium in the discharge gap were produced only in 2003 [6–9].

As follows from the photos, early diffusive discharges appear, as a rule, at the sites of the former branched bright channels. It is clear that, between pulses, the electron concentration is the highest at the area of highest current density during a previous pulse. This area is narrow and long. At its ends, the electric field is enhanced. When a subsequent pulse is applied, fast electrons, which cause volume preionization, are emitted from the conducting area ends, where the potential drop is high (see below). Preionization may take place both throughout the plasma cone and in a smaller volume. In the latter case, the transition region of the diffusive discharge forms, which may serve as a plasma cathode and expand the discharge area [10]. Since a voltage pulse changes polarity when an exciting pulse is applied, both ends of the plasma channel turn into the cones.

It appears that heating of the gas at the sites of highest current density at the third stage favors fast electron generation. Plasma heating may also be a factor at the fourth stage. At this (last) stage, the discharge splits into diffusive coniform microdischarges with joint vertices and brighter filamentary channels distinctly seen at their axes (Fig. 3). During heating, the working medium concentration at the sites of highest current density decreases and the electrons are readily accelerated to high energies. Since the mixture is heated to a steady-state temperature by a large number of pulses, the fourth stage is set with a certain delay. It is worthy

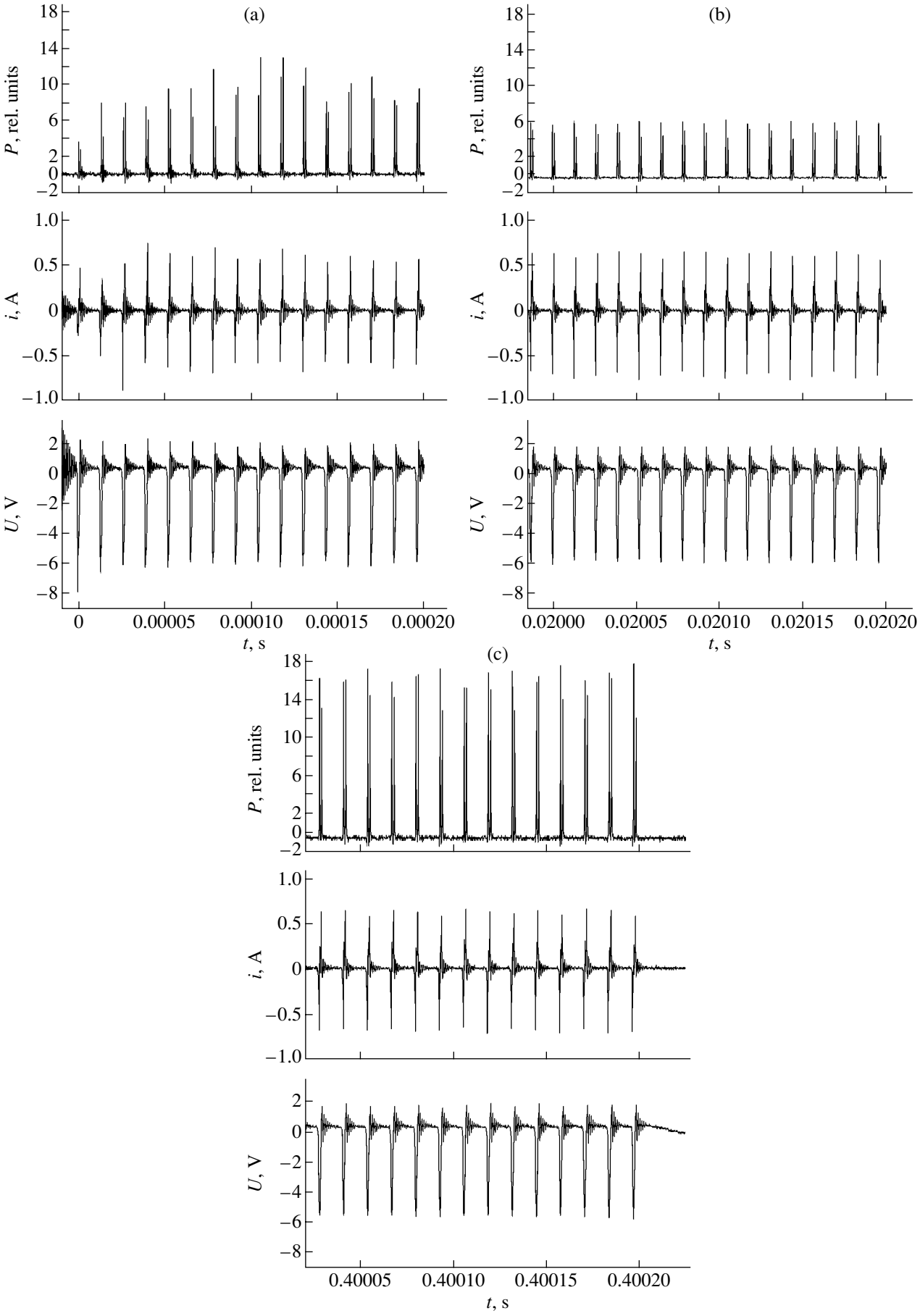
(a)
(b)
(c)
P, rel. units
i, A
U, V
t, s
18
14
10
6
2
0
−2
1.0
0.5
0
−0.5
−1.0
2
0
−2
−4
−6
−8
0
0.00005
0.00010
0.00015
0.00020
0.02000
0.02005
0.02010
0.02015
0.02020
0.40005
0.40010
0.40015
0.40020

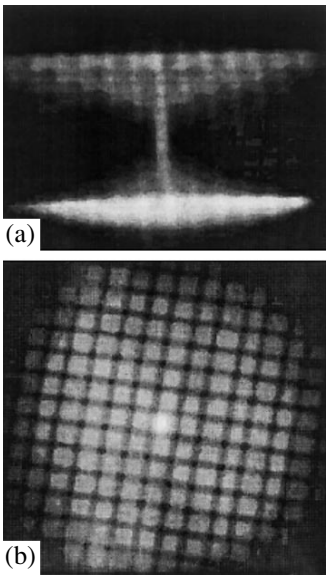

Fig. 3. (a) Side and (b) top views of the diffusive coniform microdischarge in the Xe + Cl_2 mixture at 120 Torr.

to note that, under optimal conditions, diffusive microdischarges usually remain unmoved or move very slowly (by no more than several centimeters per second).

Let us estimate the probability of fast electrons occurring under our conditions. The experiments show that the discharge excited in the lamp is initially more or less homogeneous. After several pulses, thin filaments appear, which subsequently give rise to a smaller number of spark channels with a bright bridge between the barriers. As the number of pulses increases further, the radiation intensity from this bridge in the visible range drops and the bridge expands at the edges with the formation of two cones with joint vertices. Figure 3 demonstrates the top and side views of an individual cone.

As was noted, the spark–cone transition is related to fast electrons emitted from the ends of the plasma bridge. These electrons ionize the surrounding gas and favor the formation of diffusive cones. Generation of fast electrons is due to field enhancement near the ends of the bridge.

To clarify this statement, let us consider the well-known electrostatic problem of potential distribution when the cathode has a conductive tip in the form of an oblong semiellipsoid of revolution whose axis is normal to the planes of the electrodes [11] (Fig. 4a).

The potential distribution has the form

$$\varphi(\xi, \zeta) = -\frac{U_0}{d}x(\xi, \zeta)\left\{1 - \left(\ln\left(\frac{1+\varepsilon}{1-\varepsilon}\right) - 2\varepsilon\right)^{-1} \times \left[\ln\left(\frac{\sqrt{1+\xi/a^2}+\varepsilon}{\sqrt{1-\xi/a^2}-\varepsilon}\right) - \frac{2\varepsilon}{\sqrt{1+\xi/a^2}}\right]\right\}.$$

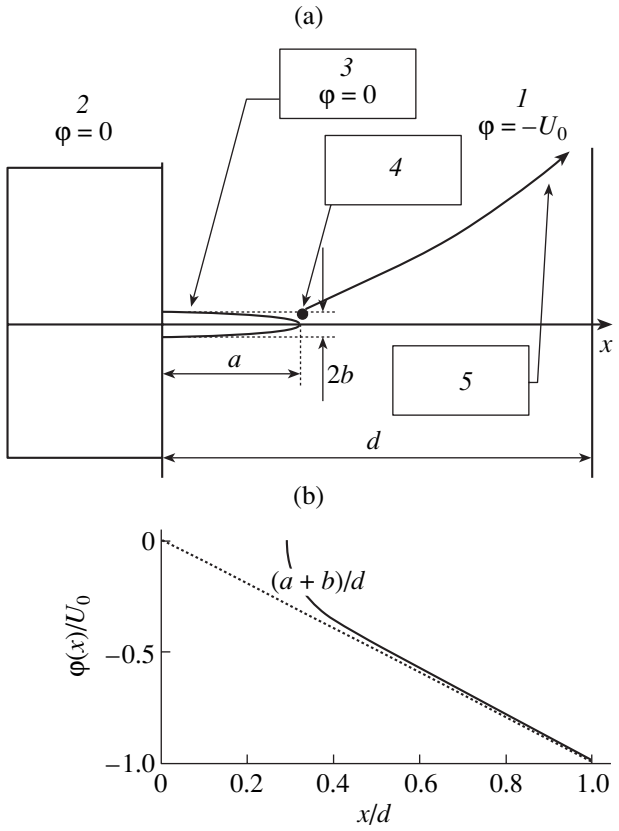

Fig. 4. (a) Geometry of the problem and (b) potential distribution along the x axis, which is an extension of the major axis of the semiellipse. Calculation is made for d = 28 mm, a = 8 mm, and b = 0.7 mm. (*1*) Anode, (*2*) cathode, (*3*) plasma, (*4*) region of electron acceleration, and (*5*) trajectory of an electron emitted.

Here, ξ and ζ are the parabolic coordinates, U_0 is the potential difference between the plane electrodes, $x(\xi, \zeta) = (a/\varepsilon)\sqrt{(1+\xi/a^2)(1+\zeta/a^2)}$ is the coordinate along the field, a and b are the major and minor semiaxex of the ellipse, and $\varepsilon = \sqrt{1-(b/a)^2}$ is the eccentricity. This solution is valid for $d - a \gg b$.

From the exact solution (Fig. 4b), it follows that, near the tip, the potential drops, as was expected, over a distance on the order of the radius of the curvature of the tip (~b). However, the potential drop magnitude depends not on the curvature of the tip but on the tip–cathode distance a: $\varphi(a + b) = -U_0(a + b)/d$. In fact, if the radius of curvature of the tip tends to zero, the field strength become infinite but the potential drop remains finite: $\varphi(a) = -U_0 a/d$. Thus, the value of φ depends on the distance of the tip to the cathode.

The photos show that the channel length exceeds half the electrode (barrier) spacing. We will assume that the electron density in the channel is high, so that the

Fig. 2. Waveforms of radiation, discharge current, and voltage pulses in the Kr + Cl_2 mixture at stages (a) 1 and 2, (b) 3, and (c) 4.

channel behaves as a good conductor. At the same time, the conductivity of the plasma around the channel is assumed to be low. In this case, the potential distribution near the channel is close to that considered in the above model problem.

Having traveled a distance (2–3)*b* from the tip, the electrons emitted acquire an energy of $\approx eU_0/2 \approx 3$ keV and ionize the ambient gas. The cross section of xenon atom ionization by an electron of energy ≈3 keV is $\sigma_1 \approx 0.8 \times 10^{-17}$ cm^2. At a pressure $p = 120$ Torr (the particle concentration is $N = 4 \times 10^{18}$ cm^{-3}), ionization occurs when the electron travels a distance $1/(\sigma_i N) \approx 3 \times 10^{-3}$ cm. Before the electron stops, it will cover a length $eU_0/(2E_i\sigma_i N) \approx 4$ mm. Here, $E_i = 22$ eV is the ionization energy or the energy of electron–ion pair generation. This result is consistent with the size of the cones observed in the experiment.

Having gained a high energy near the tip, the electron follows a curved trajectory. Curvature is a result of scattering and acceleration in an electric field. The direction of the electric field near the tip is such that electron emission into the half-space between the tip and anode is almost isotropic. Scattering events add to electron path divergence. However, the field turns the electrons toward the anode, thereby forming a cone.

Channel formation is usually related to various types of instability [12, 13]. Under normal conditions (in the absence of barriers), an ionized channel moves toward the electrodes by ionizing the near-electrode regions, which causes electrode short-circuit. In our experiments, this effect is prevented by the insulating barrier.

CONCLUSIONS

We studied the dynamics of discharge initiation in KrCl ($\lambda = 222$ nm) and XeCl (308 nm) excimer lamps excited by a barrier discharge. It was shown that the steady stage of the discharge (which appears as a number of coniform microdischarges with joint vertices) is established in four steps with various forms of discharges within a second. Prior to forming the steady (fourth) stage, which shows the highest radiation efficiency, the spark stage (branched bright channels or sparks) is observed. It was demonstrated that fast electrons generated in the discharge gap are responsible for the transition from the spark discharge to the diffusive discharge.

ACKNOWLEDGMENTS

This work was supported by the International Science and Technology Center (project no. 1270).

REFERENCES

1. U. Kogelschatz, Plasma Chem. Plasma Process. **23**, 1 (2003).
2. M. I. Lomaev, V. S. Skakun, A. E. Sosnin, *et al.*, Usp. Fiz. Nauk **173**, 201 (2003).
3. V. F. Tarasenko, D. V. Shitts, and M. V. Lomaev, Izv. Vyssh. Uchebn. Zaved. Fiz. **46** (7), 93 (2003).
4. G. A. Mesyats, V. V. Osipov, and V. F. Tarasenko, *Pulsed Gas Lasers* (Nauka, Moscow, 1991; Opt. Eng., Bellingham, 1995).
5. V. M. Klimkin, Proc. SPIE **4747**, 164 (2002).
6. S. B. Alekseev, V. M. Orlovskiĭ, and V. F. Tarasenko, Pis'ma Zh. Tekh. Fiz. **29** (10), 29 (2003) [Tech. Phys. Lett. **29**, 411 (2003)].
7. S. B. Alekseev, V. M. Orlovskiĭ, V. F. Tarasenko, *et al.*, Pis'ma Zh. Tekh. Fiz. **29** (16), 45 (2003) [Tech. Phys. Lett. **29**, 679 (2003)].
8. V. F. Tarasenko, V. M. Orlovskiĭ, and S. A. Shunaĭlov, Izv. Vyssh. Uchebn. Zaved. Fiz. **46** (3), 94 (2003).
9. V. F. Tarasenko, S. I. Yakovlenko, V. M. Orlovskiĭ, *et al.*, Pis'ma Zh. Éksp. Teor. Fiz. **77**, 737 (2003) [JETP Lett. **77**, 611 (2003)].
10. E. Arnold, M. I. Lomaev, V. S. Skakun, *et al.*, Laser Phys. **12**, 1227 (2002).
11. V. V. Batygin and I. N. Toptygin, *Problems in Electrodynamics* (Fizmatgiz, Moscow, 1962; Academic, London, 1964).
12. Yu. P. Raĭzer, *Modern Physics of Gas Discharge* (Nauka, Moscow, 1980) [in Russian].
13. Yu. P. Raĭzer, *Gas Discharge Physics* (Springer-Verlag, Berlin, 1991; Nauka, Moscow, 1992).

Translated by V. Isaakyan

Technical Physics, Vol. 49, No. 6, 2004, pp. 795–797. Translated from Zhurnal Tekhnicheskoĭ Fiziki, Vol. 74, No. 6, 2004, pp. 134–136.

SHORT COMMUNICATIONS

The Effect of Accelerating Cavity's Transients on the Particle Energy Spread

V. I. Ivannikov *, V. M. Pavlov **, Yu. D. Chernousov *, and I. V. Shebolaev *

** Institute of Chemical Kinetics and Combustion, Siberian Division, Russian Academy of Sciences, Novosibirsk, 630090 Russia*

e-mail: Chern@catalysis.nsk.su

*** Budker Institute of Nuclear Physics, Siberian Division, Russian Academy of Sciences, Novosibirsk, 630090 Russia*

e-mail: Pavlov@inp.nsk.su

Received August 11, 2003

Abstract—An accelerating resonator loaded by current is analyzed based on an equation for normalized amplitude of the oscillations obtained by the method of counterpropagating waves. An expression for the accelerating voltage is derived with allowance for transients observed upon enabling the generator and beam. The effect of transients on the particle energy spread is taken into account. A possibility of stabilizing the beam energy at an arbitrary phase of the generator and without detuning the accelerating resonator in the process of transition to the steady state is demonstrated. © *2004 MAIK "Nauka/Interperiodica".*

Transients in standing-wave accelerating structures (resonators) are one of the causes for the particle energy spread occurring in accelerators excited by pulsed microwave field. The energy spread on the trailing edge of the microwave pulse can easily be eliminated by interrupting the beam injection. A method for eliminating the energy spread on the leading edge of the microwave pulse was addressed in [1]. The method relies on the possibility of interrupting the transient at the moment when the beam is enabled by detuning the cavity's frequency and delaying the beginning of beam injection with respect to the beginning of the microwave pulse.

This work considers another possibility of stabilizing the beam energy on the leading edge of the microwave pulse, which does not require the accelerator to interrupt transients in the resonator.

To evaluate the energy spread due to the transients, it is necessary to take into account that the accelerating resonator is excited by two sources: the external generator and beam. In the steady-state mode, this problem is solved by representing the resonator as an equivalent oscillatory circuit [2]. Transients in the resonators can be better described in terms of the method of counterpropagating waves [3] developed in [4–6]. Below, we use this method to analyze the resonator with the beam operated in various modes.

The method of counterpropagating waves yields the following equation for the normalized complex amplitude of oscillations in the resonator:

$$\frac{dv}{dt} + \left[\frac{\omega_0(1+k)}{2Q_0} + i\Delta\omega\right]v = \sqrt{\frac{\omega_0 k}{Q_0}}a - \alpha I_0, \qquad (1)$$

where ω_0 is resonator's natural frequency, k is the coupling coefficient between the resonator and feeder line, $\Delta\omega$ is the difference between the generator's and resonator's frequencies, Q_0 is the resonator's unloaded Q factor, and a is the normalized amplitude of the wave in the feeder line.

The load due to the current is taken into account by the term αI_0, where I_0 is the complex amplitude of the fundamental harmonic of current and α is the positive real number, which characterizes the effect of current on oscillations in the resonator. The equation implies that the particles are bunched and the bunches follow at a rate equal to the generator's frequency.

The method represents the normalized amplitude of the oscillations as a superposition of amplitudes of counterpropagating waves at the center of the resonator normalized in terms of the condition $|v|^2/2 = W$, where W is the energy stored in the resonator. In the accelerating resonator operated in the fundamental mode E_{010}, the normalized amplitude is in-phase with the accelerating electric field. It is convenient to choose the origin so that I_0 could further be regarded a positive real quantity.

If the frequency of the fundamental harmonic of current equals the resonator's eigenfrequency and the resonator is excited by the beam alone, the following expressions for α and effective voltage U can be obtained:

$$\alpha = \sqrt{\frac{\omega_0 Z_e L}{8Q_0}}, \quad U = \sqrt{\frac{\omega_0 Z_e L}{2Q_0}}|v|. \qquad (2)$$

Relation (2) is derived using definitions of the unloaded Q factor ($Q_0 = \omega_0 W/P_0$) and effective shunting impedance ($Z_e = U^2/(P_0 L)$, where P_0 is the power loss in the walls of the resonator and L is the resonator length) [7].

In a beam grouped into short bunches, all particles acquire the same energy proportional to the accelerating voltage

$$u(t) = \sqrt{\frac{\omega_0 Z_e L}{2Q_0}}\mathrm{Re}\{v(t)\}. \quad (3)$$

For a beam grouped into short bunches, I_0 is twice as high as the average beam current I. Representing a in terms of power P and phase φ of the generator ($a = \sqrt{2P}\exp(i\varphi)$), Eq. (1) can be written as

$$\frac{dv}{dt} + \left[\frac{\omega_0(1+k)}{2Q_0} + i\Delta\omega\right]v = \sqrt{\frac{2\omega_0 P}{Q_0}}[\sqrt{k}\exp(i\varphi) - \beta], \quad (4)$$

where $\beta = [Z_e L I^2/(4P)]^{1/2}$ is the current-load factor (beam current-to-critical current ratio at $k = 1$).

The general solution to Eq. (4) has the form

$$v(t) = v_p + v_d\exp[-(1/\tau + i\Delta\omega)t], \quad (5)$$

where v_p is the normalized amplitude of the steady-state oscillations, v_d is the initial normalized amplitude of the damped natural oscillations, and $\tau = 2Q_0/[\omega_0(1 + k)]$ is the time constant of these oscillations.

Each of the amplitudes v_p and v_d is a sum of two terms, which refer to oscillations excited by the generator and beam.

When $\Delta\omega = 0$, the normalized amplitudes of steady-state oscillations excited, respectively, by the generator and beam are

$$v_g = \frac{2}{1+k}\sqrt{\frac{2Q_0 kP}{\omega_0}}\exp(i\varphi), \quad v_b = -\frac{2\beta}{1+k}\sqrt{\frac{2Q_0 P}{\omega_0}}. \quad (6)$$

Due to their importance in practice, let us consider steady-state oscillations (6) in more detail. By representing the sum of amplitudes in the exponential form, the normalized amplitude of the steady-state oscillations can be written as

$$v_0 = \frac{2}{1+k}\sqrt{\frac{2Q_0 P}{\omega_0}} \times (\sqrt{k - \beta^2\sin^2\psi_0} - \beta\cos\psi_0)\exp(i\psi_0), \quad (7)$$

where ψ_0 is determined from the equality

$$\cos\psi_0 = \frac{\sqrt{k}\cos\varphi - \beta}{(k + \beta^2 - 2\beta\sqrt{k}\cos\varphi)^{1/2}}. \quad (8)$$

When the resonator is loaded by the beam, the phase ψ_0 of the resultant oscillations may significantly differ from the phase of oscillations created by the generator. The resonator gives energy to the beam if $\cos\psi_0 > 0$. This condition is met when $|\varphi| < \varphi_c$, where $\varphi_c = \arccos(\beta k^{-1/2})$ is the critical generator's phase.

According to expression (3), normalized amplitude (7) of the oscillations corresponds to the accelerating voltage

$$u_0 = \frac{2\sqrt{Z_e LP}}{1+k}(\sqrt{k - \beta^2\sin^2\psi_0} - \beta\cos\psi_0)\cos\psi_0. \quad (9)$$

If the quantity $\beta^2\sin^2\psi_0$ in (9) is neglected as being much smaller than k, the following known approximate formula for the accelerating voltage is obtained [8]:

$$u_0 = \frac{2\sqrt{Z_e LkP}\cos\psi_0 - Z_e LI\cos^2\psi_0}{1+k}. \quad (10)$$

At a given ψ_0, accelerating voltage (9) attains its maximum when the resonator's coupling factor takes the optimum value

$$k_{opt} = (1 + 2\beta^2) + 2\beta\sqrt{1+\beta^2}\cos\psi_0. \quad (11)$$

Then the accelerating voltage and efficiency η ($\eta = uI/P$) of the resonator are, respectively,

$$u_m = \frac{\sqrt{Z_e LP}\cos\psi_0}{\sqrt{1+\beta^2} + \beta\cos\psi_0}, \quad \eta_m = \frac{2\beta\cos\psi_0}{\sqrt{1+\beta^2} + \beta\cos\psi_0}. \quad (12)$$

For a superconducting resonator ($Q_0 \longrightarrow \infty$), Z_e tends to infinity; therefore, the resonator's efficiency is determined by the characteristic impedance $\rho_e = Z_e/Q_0$; its coupling to the feeder line, by the external Q factor $Q_e = Q_0/k$. Substituting β written in terms of ρ_e ($\beta = [\rho_e L Q_0 I^2/(4P)]^{1/2}$) into expressions (11) and (12), we obtain at $Q_0 \longrightarrow \infty$ the optimum values of external Q factor, accelerating voltage, and efficiency for the superconducting resonator:

$$Q_s = \frac{2P}{\rho_e LI^2(1+\cos\psi_0)}, \quad u_s = \frac{2P\cos\psi_0}{I(1+\cos\psi_0)}, \quad \eta_s = \frac{2\cos\psi_0}{(1+\cos\psi_0)}. \quad (13)$$

It should be noted that $\eta_s = 1$ is only at $\psi_0 = 0$; therefore, losses due to radiation into the feeder waveguide are absent in this case alone.

To evaluate the energy spread caused by transients on the leading edge of the microwave pulse, it is necessary to calculate v_d, which depends on the initial conditions (making conditions).

If the generator and beam are enabled simultaneously at the moment $t = 0$, $v(0) = 0$. Then $v_d = -v_p$ and the accelerating voltage changes from zero to a steady-state value.

If $\Delta\omega = 0$, and the beam is enabled when oscillations produced by the generator have almost reached their

maximum amplitude, then, taking the beam enabling time as the origin, we obtain the initial condition $V(0) = V_g$. Then $V_d = -V_b$ and the accelerating voltage becomes

$$u(t) = u_0 + \frac{2\beta\sqrt{Z_e LP}}{1+k}\exp(-t/\tau). \quad (14)$$

At the optimum coupling coefficient, the accelerating voltage spread divided by u_m (relative energy spread) is

$$\frac{\Delta u}{u_m} = \frac{\beta}{\sqrt{1+\beta^2}\cos\psi_0}. \quad (15)$$

For example, at $\beta = 0.5$ and $\psi_0 = 30°$, the relative energy spread is 0.51 and, at $\beta = 0.5$ and $\psi_0 = 0$, it equals 0.44.

The energy spread on the leading edge of the microwave pulse can be eliminated by enabling the beam with a certain delay after the generator is switched on. In this case, the condition $V_d = 0$ (interruption of the transient at the moment when the beam is enabled) can be satisfied. This is achieved when the damped natural oscillations excited by the beam and generator are equal in amplitude and are in antiphase. For this situation to occur, the resonator's frequency must differ from the frequency of the generator by a quantity depending on the phase φ of the generator. This possibility is addressed in [1].

Let us consider how oscillations in the resonator tuned exactly to the generator frequency ($\Delta\omega = 0$) come to the steady state. If the beam is enabled at $t = 0$ with a delay t_b after the generator is switched on, $V(0) = V_g(1 - \exp(-t_b/\tau))$. At $t \geq 0$, the initial amplitude of the damped natural oscillations is

$$V_d = -[V_b + V_g\exp(-t_b/\tau)]. \quad (16)$$

The delay t_b can be chosen such that V_d takes a pure imaginary value. Then the accelerating voltage, given by expression (3), is independent of time and equals u_0. Thus, the energy can be stabilized by properly choosing t_b alone. At the optimum coupling coefficient (11), the necessary delay of the beam engagement relative to the microwave pulse is

$$t_0 = \tau\ln\frac{\sqrt{1+\beta^2}\cos\psi_0 + \beta}{\beta}. \quad (17)$$

As follows from expressions (6), when the phase of the generator is $\varphi = 0$, the amplitudes V_g and V_b are real; therefore, the energy can only be stabilized at $V_d = 0$. When $\varphi \neq 0$, V_d can take pure imaginary values. In this case, the transient is not interrupted at the moment the beam is enabled. The phase and amplitude of oscillations in the resonator change so that the two factors compensate for each other and the change in the particle energy is independent of time.

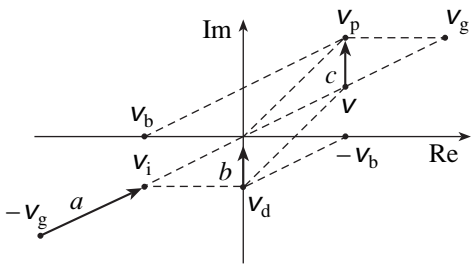

Complex plane of the normalized amplitudes: (*a*) extinction of oscillations produced by the generator before the beam is enabled, (*b*) extinction of the oscillations after the beam is enabled, and (*c*) evolution of the resultant oscillations in the resonator.

The figure gives a graphical interpretation of this effect on the complex plane of normalized oscillation amplitudes. At the moment when the generator is switched on, steady-state oscillations with amplitude V_g and antiphase damped natural oscillations with initial amplitude $-V_g$ build up in the resonator. After a time t_b, when the amplitude of damped oscillations excited by the generator becomes $V_i = -V_g\exp(-t_b/\tau)$, the beam is enabled. Steady-state oscillations with amplitude V_b and damped oscillations with initial amplitude $-V_b$ are excited in addition to those that already exist. The sum of amplitudes of the damped oscillations at this moment is the initial amplitude V_d for the subsequent time moments. The damped oscillations, which have an imaginary amplitude, do not affect the accelerating voltage.

Thus, the general expression for the accelerating voltage obtained in this paper can be used to evaluate the energy spread caused by the transients. It is shown that the energy spread can be eliminated in the process of transition to the steady state.

REFERENCES

1. V. F. Vikulov, V. N. Zavorotylo, V. V. Ruzin, and V. K. Shilov, Zh. Tekh. Fiz. **52**, 2188 (1982) [Sov. Phys. Tech. Phys. **27**, 1345 (1982)].
2. M. M. Karliner, in *Proceedings of the Joint US–CERN–Japan International School on Frontiers of Accelerator Technology, Hayama, 1996*, pp. 418–434.
3. J. L. Altman, *Microwave Circuits* (Van Nostrand, New York, 1964; Mir, Moscow, 1968).
4. S. N. Artemenko, Radiotekh. Élektron. (Moscow) **40**, 1184 (1995).
5. V. I. Ivannikov, Yu. D. Chernousov, and I. V. Shebolaev, Zh. Tekh. Fiz. **66** (5), 162 (1996) [Tech. Phys. **41**, 493 (1996)].
6. V. I. Ivannikov, Yu. D. Chernousov, and I. V. Shebolaev, Radiotekh. Élektron. (Moscow) **45**, 180 (2000).
7. O. S. Milovanov and N. P. Sobenin, *Microwave Engineering* (Atomizdat, Moscow, 1980) [in Russian].
8. A. A. Zavadtsev, B. V. Zverev, and N. P. Sobenin, Zh. Tekh. Fiz. **54**, 82 (1984) [Sov. Phys. Tech. Phys. **29**, 46 (1984)].

Translated by A. Khzmalyan

Technical Physics, Vol. 49, No. 6, 2004, pp. 798–799. Translated from Zhurnal Tekhnicheskoĭ Fiziki, Vol. 74, No. 6, 2004, pp. 137–138.

SHORT COMMUNICATIONS

Green Luminescence in Diffusion-Doped Layers of Zinc Selenide

V. P. Makhniy, M. M. Sletov, and I. V. Tkachenko

Fed'kovich National University, 58001 Chernovtsy, Ukraine

e-mail: oe-dpt@chnu.cv.ua

Received September 29, 2003

Abstract—Diffusion-doped layers with a green emission band dominating in the room-temperature luminescence spectrum are obtained by annealing single-crystal zinc selenide substrates in tellurium and zinc vapors.

It is known that any color sensation can be produced using a proper combination of three monochromatic colors, in the majority of cases—red, green, and blue [1]. Zinc selenide (ZnSe) possessing the direct-gap band structure and the value of $E_g \approx 2.7$ eV at 300 K makes it possible, in principle, to obtain effective luminescence in the entire visible spectral range. At the same time, an analysis of the available published data shows that the samples obtained up to this point emit mainly in the red–orange and blue spectral regions [2–7], except for ZnSe⟨Al⟩ crystals whose luminescence spectrum exhibits a wide yellow–green band [2]. The samples containing copper and oxygen [5], cadmium [6], or alkali elements [7] exhibit a comparatively weak green band along with the red and blue ones. In this study, we report on the observation of a rather intense green luminescence in diffusion-doped ZnSe layers and present the results of investigations of the basic characteristics of this emission.

As initial substrates, we used the plates cut from a ZnSe single crystal grown by the Bridgman method from a stoichiometric melt. At room temperature, the samples possess low electron conductivity ($\sigma_m \approx 10^{-12}\ \Omega^{-1}\ \text{cm}^{-1}$) and the photoluminescence (PL) spectrum shown in the figure. The red band (with a maximum at $\lambda_m \approx 0.64$ μm) is caused by the recombination on donor–acceptor pairs consisting of doubly charged negative vacancies of zinc (V''_{Zn}) and singly charged positive vacancies of selenium ($V^{\bullet}_{\text{Se}}$) [2, 8]. The blue band ($\lambda_m \approx 0.48$ μm) results from the transitions with participation of the levels of interstitial selenium atoms and their vacancies [2, 8].

A diffusion-doped layer was obtained by successive annealing of the initial substrates in saturated Te and Zn vapors. The process was performed in an evacuated (residual pressure, 10^{-4} Torr) and sealed quartz ampule, where a sample and a weighed amount of a doping metal were placed in the opposite ends. As a result of the above operations, the layer formed on the sample surface had a higher electron conductivity ($\sigma_n \approx 10^{-2}\ \Omega^{-1}\ \text{cm}^{-1}$) and a totally different emission spectrum (see figure).

The PL spectrum of the diffusion-doped layer at 300 K displays a single asymmetric wide band characterized by the following properties: (a) the emission intensity I depends linearly on the excitation level L; (b) the peak position corresponds to $\lambda_m \approx 0.52$ μm and is independent of L; and (c) a decrease in the excitation level reduces the fraction of long-wavelength emission and has virtually no effect on the shape of the short-wavelength "wing." The above features are typical of the emitting transitions with the participation of a local center interacting with phonons [9]. This is confirmed by the luminescence spectrum measured in the regime of λ modulation [10], the long-wavelength wing of which has two equidistant ($\hbar\omega_0 \approx 0.02$ eV) bending points in agreement with the *L*O phonon energy in ZnSe crystals [2]. The most probable centers of radia-

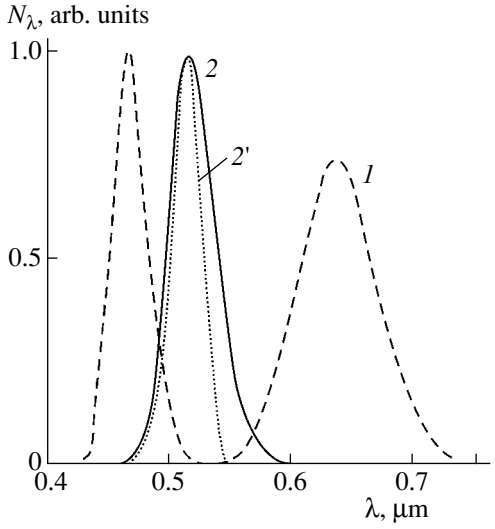

Luminescence spectra of the initial (*1*) and Te- and Zn-doped ZnSe samples (*2* and *2'*, respectively) for two excitation levels: (*1* and *2*) 10^{18}; (*2'*) 10^{16} ph/s.

1063-7842/04/4906-0798$26.00

tive recombination are the neutral vacancies of zinc, whose energy levels lie 0.17–0.20 eV above the top of the valence band [11]. Note that the λ-modulated transmission spectra of the annealed samples contain a singularity in the neighborhood of $\lambda \approx 0.52$ μm, which is absent in the spectra of the initial substrates. Elucidation of the nature of the green emission band calls for a special consideration invoking experimental and theoretical investigations of the mechanisms behind the defect formation in emitting diffusion-doped layers.

Thus, the results presented above convincingly indicate that the obtaining of zinc selenide layers with the dominating green PL band at 300 K is possible. The presence of an isovalent Te impurity makes it possible to hope for high radiation and temperature stability of the parameters of this emission, which is characteristic, for example, of ZnSe crystals doped with Te during growth [12].

REFERENCES

1. A. A. Berg and P. J. Din, *Light Emitting Diodes* (Clarendon, Oxford, 1976; Nauka, Moscow, 1979).
2. D. D. Nedeoglo and A. V. Simashkevich, *Electrical and Luminescence Properties of Zinc Selenide* (Shtiintsa, Kishinev, 1984).
3. N. K. Morozova, V. A. Kuznetsov, V. D. Ryzhikov, *et al*., *Zinc Selenide: Production and Optical Properties* (Nauka, Moscow, 1992).
4. V. I. Gavrilenko, A. M. Grekhov, D. V. Korbutyak, and V. G. Litovchenko, *Optical Properties of Semiconductors: A Handbook* (Naukova Dumka, Kiev, 1987).
5. N. K. Morozova, I. A. Karetnikov, V. V. Blinov, and E. M. Gavrishchuk, Fiz. Tekh. Poluprovodn. (St. Petersburg) **35**, 25 (2001) [Semiconductors **35**, 24 (2001)].
6. M. M. Berezovskiĭ, V. P. Makhniĭ, and M. M. Sletov, Zh. Prikl. Spektrosk. **62** (6), 109 (1995).
7. M. E. Agel'menev, A. N. Georgobiani, Z. P. Ilyukhina, *et al.*, Neorg. Mater. **25**, 731 (1989).
8. V. P. Makhnii, I. V. Malimon, and Yu. Ya. Chaban, Neorg. Mater. **36**, 1301 (2000).
9. V. P. Gribkovskiĭ, *A Theory of Emission and Absorption of Light in Semiconductors* (Nauka i Tekhnika, Minsk, 1975).
10. V. P. Makhniĭ, *Fundamentals and Methods of Modulation Spectroscopy* (Ruta, Chernivtsi, 2001).
11. *Physics of II–VI Compounds*, Ed. by A. N. Georgobiani and M. K. Sheĭnkman (Nauka, Moscow, 1986).
12. V. D. Ryzhikov, *Scintillation Crystals of II–VI Semiconductors: Production, Properties, and Applications* (NIITÉKhM, Moscow, 1999).

Translated by Yu. Vishnyakov

Technical Physics, Vol. 49, No. 6, 2004, pp. 800–803. Translated from Zhurnal Tekhnicheskoĭ Fiziki, Vol. 74, No. 6, 2004, pp. 139–142.

SHORT COMMUNICATIONS

Calculation of the Ion Transverse Velocity Distribution Function under Ion Cyclotron Resonance Heating

A. I. Karchevskiĭ† and E. P. Potanin

Institute of Molecular Physics, Russian Research Centre Kurchatov Institute, pl. Kurchatova 1, Moscow, 123182 Russia

e-mail: potanin@imp.kiae.ru

Received October 20, 2003

Abstract—The ion transverse velocity distribution functions and the fraction η of ions heated above a certain energy W_1 are calculated as applied to the ion cyclotron resonance heating method of isotope separation. It is assumed that the longitudinal ion velocity distribution in a plasma source is nonequilibrium. Under high heating temperatures, the averaged ion transverse velocity distribution becomes essentially nonequilibrium and exhibits two maxima. The ion heating efficiency η is calculated for W_1 = 40 eV and various values of the parameter $p = \lambda/L$, where λ is the wavelength of the electric field of an antenna and L is the heating zone extension. The relative contributions of the time-of-flight and Doppler broadenings are evaluated. © *2004 MAIK "Nauka/Interperiodica".*

INTRODUCTION

The ion cyclotron resonance (ICR) method of isotope separation consists in selective resonance cyclotron heating of target isotope ions in mutually orthogonal variable electric and constant magnetic fields [1–6]. Stable isotopes are today produced by the electromagnetic technique [7] and by using gas centrifuge stages [8]. In the latter case, only isotopes of those elements producing volatile compounds with a sufficiently high vapor pressure at room temperature can be separated. The electromagnetic technique is well developed, but its yield is relatively low. Provision of high ion currents in an electromagnetic separator is a challenge, since the current density is limited by electrostatic repulsion of like-charged particles. The ICR method seems to offer advantages over the electromagnetic technique as applied to metal isotope separation, since virtually no limitations are imposed on the ion fluxes. At the present time, the ICE method is under development.

CALCULATION

The basic components of an ICR separator is a plasma source, which produces an ion flux with a certain distribution of ions over transverse and longitudinal velocities, and an rf antenna, which generates electromagnetic fields in the zone of ICR heating. As the plasma passes through the heating zone, the transverse velocity distribution changes noticeably. A number of ICR separators (see, e.g., [3]) use inductive antennas, which are twisted multiphase cylindrical helices (helical antennas). In the case of a four-phase antenna with the current shifted by π/2 in each subsequent phase, the electric field in the cylindrical heating zone can be represented as a vector rotating with an angular velocity ω and directed along the positive z axis:

$$E_x = E\cos(\omega t - Kz - \varphi), \quad (1)$$

$$E_y = -E\sin(\omega t - Kz - \varphi), \quad (2)$$

where $K = 2\pi/\lambda$ is the wavenumber, E is the electric field amplitude, and φ is the initial phase.

If the effect of plasma particle motion on the vacuum filed of the antenna can be neglected (which is valid when the plasma density is low), expressions (1) and (2) approximate the heating electric field in the plasma over a distance $r \le R/2$, where R is the antenna radius [9].

In the Cartesian system, the equations of motion of singly charged ions with a mass m and charge e in a longitudinal magnetic field B_z imposed on the wave field given by (1) and (2) (the electric field rotates with the angular velocity ω in the same direction as the ions in the magnetic field) can be written as

$$m\frac{dV_x}{dt} = eE\cos(\omega t - KV_z t) + eV_y B_z, \quad (3)$$

$$m\frac{dV_y}{dt} = -eE\sin(\omega t - KV_z t) - eV_x B_z. \quad (4)$$

Here, V_x, V_y, and V_z are the transverse and longitudinal components of the ion velocity.

Let $V_\perp = \sqrt{V_x^2 + V_y^2}$ be the ion transverse velocity magnitude. We consider ICR heating of an ion flux with certain transverse and longitudinal velocity distributions, and our goal is to find the transverse velocity dis-

† Deceased.

tribution function at the exit form the heating zone, which has a finite length L. It is assumed that the transverse velocity distribution at the entrance to the heating zone is Maxwellian:

$$f_{\perp 0}(V_\perp) = \left(\frac{m}{2\pi k T_{0\perp}}\right)\exp\left(-\frac{m}{2kT_{0\perp}}(V_x^2 + V_y^2)\right). \quad (5)$$

First, we will take advantage of the results [9] for the transverse velocity distribution at the exit from the heating zone when the ions have the same longitudinal velocity V_z and their initial transverse velocity distribution is Maxwellian (distribution (5)):

$$f_\perp(V_\perp) = \left(\frac{m}{2\pi k T_{0\perp}}\right) \times \exp\left(-\frac{m}{2kT_{0\perp}}(V_\perp^2 + V_0^2)\right) I_0\left(\frac{mV_0V_\perp}{kT_{0\perp}}\right), \quad (6)$$

where k is the Boltzmann constant, $T_{\perp 0}$ is the initial transverse temperature of the ionic component, and I_0 is the modified zero-order Bessel function.

Under heating, when the transverse energy of the ions far exceeds the initial thermal energy, the parameter V_0 is given by

$$V_0 \cong \frac{2E\omega_0}{B_z(\omega - KV_z - \omega_0)}\sin\left((\omega - KV_z - \omega_0)\frac{L}{2V_z}\right),$$

where ω_0 is the cyclotron frequency of an ion.

Function (6) is normalized to unity. It depends both on the longitudinal velocity V_z of the ion beam and on the heating field frequency ω. Actually, the flux arriving at the heating zone is a superposition of individual fluxes, each having a particular longitudinal velocity V_z. Let the longitudinal velocity distribution function be designated as $f_z(V_z)$. Then, the total distribution function can be represented as the product of two functions:

$$f(V_\perp, V_z) = f_\perp(V_\perp) f_z(V_z). \quad (7)$$

Let us study the heating process using a model non-Maxwellian longitudinal velocity distribution $f_z(V_z)$ at the exit from the plasma source. This distribution is a linear function of the ion velocity when the velocities are low, and it decays exponentially when the velocities are high:

$$f_z(V_z) = \frac{mV_z}{kT_z}\exp\left(-\frac{mV_z^2}{2kT_z}\right), \quad (8)$$

where T_z is the effective longitudinal temperature.

We assume that this function remains invariable over the length of the heating zone and introduce the parameter $p = \lambda/L$, where λ is the wavelength and L is the length of the heating zone. If L is constant, p varies with the wavelength λ and, consequently, with the wavenumber K; conversely, if λ is constant, p varies with the length of the heating zone. The distribution function averaged over longitudinal velocities is defined as

$$F(y) = \bar{f}(y)/\left(\frac{m}{2kT_{0\perp}}\right)^{1/2} = 4\int_0^\infty \exp(-(y^2 + y_0^2 + x^2))I_0(2yy_0)xy\,dx, \quad (9)$$

where

$$y = \frac{V_\perp}{(2kT_{\perp 0}/m)^{1/2}}, \quad x = \frac{V_z}{(2kT_z/m)^{1/2}},$$

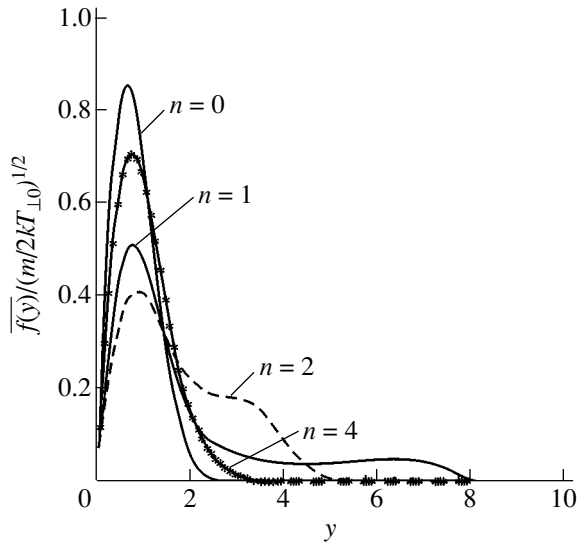

Fig. 1. Transverse velocity distribution functions for p = 0.5, T_z = 10 eV, E = 50 V/m, and different n.

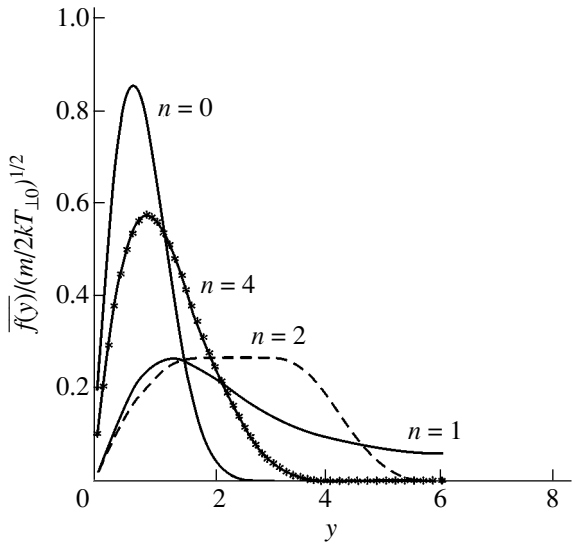

Fig. 2. Transverse velocity distribution functions for p = 1.0, T_z = 10 eV, E = 50 V/m, and different n.

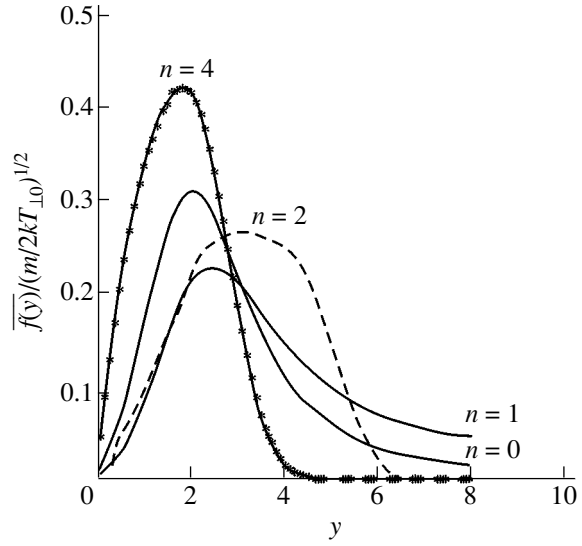

Fig. 3. Transverse velocity distribution functions for p = 2.0, T_z = 10 eV, E = 50 V/m, and different n.

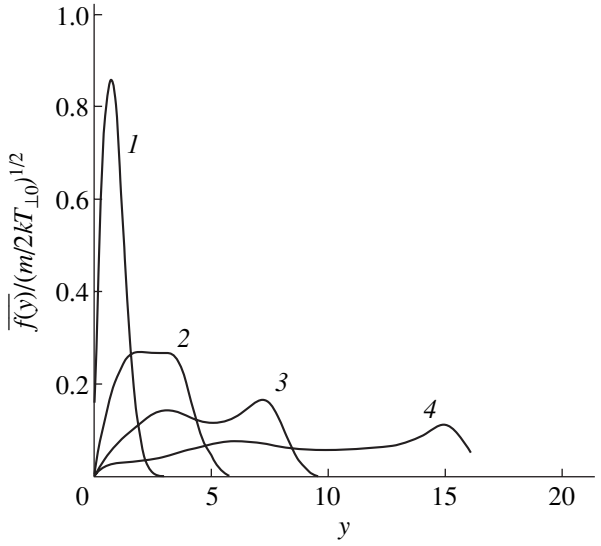

Fig. 4. Transverse velocity distribution functions for p = 1.0, T_z = 10 eV, $T_{\perp 0}$ = 5 eV, and $\omega - \omega_c = KV_{z0}$. E = (*1*) 0, (*2*) 50, (*3*) 100, and (*4*) 200 V/m.

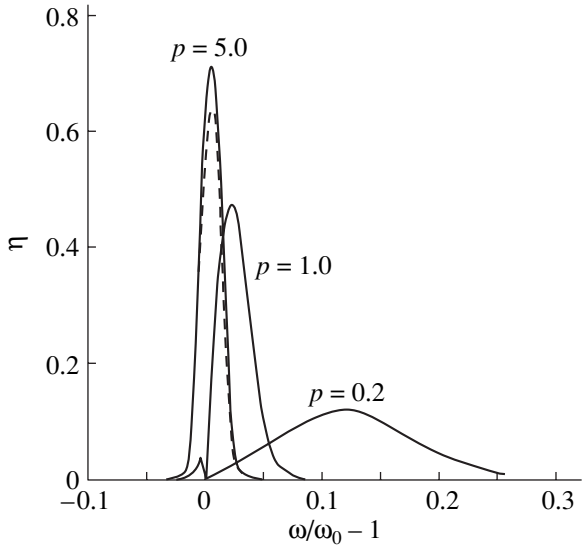

Fig. 5. Heating efficiency η vs. frequency offset $\omega/\omega_0 - 1$ for E = 50 V/m, T_z = 10 eV, W_1 = 40 eV, and different p (n = 2).

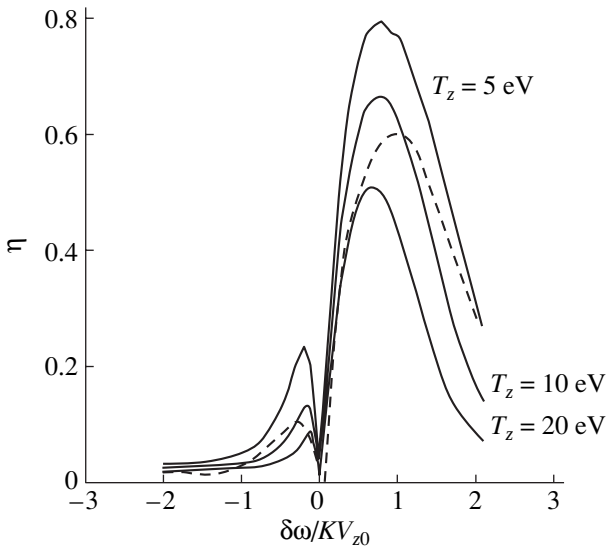

Fig. 6. Heating efficiency η vs. dimensionless frequency offset $\delta\omega/KV_{z0}$ for p = 1, E = 50 V/m, W_1 = 20 eV, and different longitudinal temperatures (n = 2).

$$n_L = \left(\frac{2kT_z}{m}\right)^{1/2}\frac{2}{L\omega_0}, \quad n_E = \frac{2E}{B_z\left(\frac{2kT_{\perp 0}}{m}\right)^{1/2}},$$

$$y_0 = \frac{n_E \sin\left((\Omega - \pi n_L x/p - 1)\frac{1}{n_L x}\right)}{(\Omega - \pi n_L x/p - 1)}.$$

Calculations are performed for a model binary isotope mixture with mass numbers of 6 and 7. Let us introduce the dimensionless parameter n, which characterizes the detuning of the oscillator frequency from the cyclotron frequency of the ions: $n = 2\delta\omega/KV_{z0}$, where $\delta\omega = \omega - \omega_0$ and $V_{z0} = (\pi kT_z/2m)^{1/2}$ is the mean longitudinal velocity of the ions. With the offset parameter n thus defined, exact tuning to the maximal heating temperature ("resonance") in terms of the mean longitudinal velocity corresponds to n = 2. Figures 1–3 show the distribution function $F(y)$ for the variable electric field amplitude E = 50 V/m, longitudinal ion temperature T_z = 10 eV, length of the heating zone L = 0.8 m, and different values of p and n under off-resonance conditions. An increase in p here corresponds to a decrease

in the wavenumber K. Figure 4 plots the distribution function $F(y)$ for different heating field amplitudes E, $T_z = 10$ eV, $T_{\perp 0} = 5$ eV, and $p = 1$ (one-wave antenna) under the resonance conditions in terms of the mean longitudinal ion velocity ($\omega - \omega_0 = KV_{z0}$; i.e., $n = 2$). Curve *1* is plotted for the zero heating field ($E = 0$) and has the Maxwellian form. Curves *2–4* are plotted for $E = 50$, 100, and 200 V/m, respectively. The wide transverse energy range and the presence of two humps at high heating levels are worthy of note. The nonmonotonicity of the transverse velocity distribution, along with heating anisotropy, may cause instabilities. From (5)–(7), one can derive an expression for the fraction η of particles heated to energies above a given energy W_1 ($y_1 = \sqrt{W_1/kT_{0\perp}}$):

$$\eta = 4\int_0^\infty dx \int_{y_1}^\infty xy \exp(-(y^2 + y_0^2 + x^2)) I_0(2yy_0) dy. \quad (10)$$

Figure 5 shows the efficiency η of ion heating for $W_1 = 40$ eV and different values of the parameter $p = \lambda/L$, which characterizes the contributions from the time-of-flight and Doppler broadenings. The length of the heating zone L is set constant, $L = 0.8$ m, so that the parameter p here varies as the wavenumber K.

When p is large (large λ, small K), the time-of-flight broadening prevails. In the case of small p, the Doppler component makes a major contribution. For $p = 5$, the linewidth depends solely on the time-of-flight broadening. The dashed line, constructed for $p = 5$, includes the wavenumber dependence of the electric field amplitude in terms of approximations used in [9]. Figure 6 plots the heating efficiency η against the dimensional detuning $\delta\omega/KV_{z0}$ of the oscillator frequency from the cyclotron frequency for a one-wave antenna ($p = 1$), $E = 50$ V/m, $W_1 = 20$ eV, and different longitudinal temperatures. The dashed line is the result of calculation [9] for $E = 50$ V/m and the longitudinal temperature $T_z = 10$ eV.

ACKNOWLEDGMENTS

The authors thank V.G. Pashkovskiĭ for the assistance in the calculations.

REFERENCES

1. G. A. Askar'yan, V. A. Namiot, and A. A. Rukhadze, Pis'ma Zh. Tekh. Fiz. **1**, 820 (1975) [Sov. Tech. Phys. Lett. **1**, 356 (1975)].
2. J. M. Dawson, H. C. Kim, D. Arnush, *et al.*, Phys. Rev. Lett. **37**, 1547 (1976).
3. A. I. Karchevskiĭ, V. S. Laz'ko, Yu. A. Muromkin, *et al.*, Fiz. Plazmy **19**, 411 (1993) [Plasma Phys. Rep. **19**, 214 (1993)].
4. A. C. La Fontaine and P. Louvet, *Compte rendu des Journees sur les Isotopes Stables* (Saclay, 1993), pp. 332–336.
5. M. I. Belavin, A. B. Zvonkov, and A. V. Timofeev, RF Patent No. 1742900 (5 July 1993).
6. V. I. Volosov, I. A. Kotel'nikov, and S. G. Kuzmin, Fiz. Plazmy **24**, 517 (1998) [Plasma Phys. Rep. **24**, 474 (1998)].
7. R. N. Kuzmin, V. G. Bondarenco, and V. M. Tchesnocov, in *Synthesis and Applications of Isotopically Labelled Compounds*, Ed. by U. Pleiss and R. Voges (Wiley, New York, 2001), Vol. 7, p. 10.
8. E. I. Abbakumov, V. A. Bazhenov, Yu. V. Verbin, *et al.*, At. Energ. **67**, 255 (1989).
9. A. L. Ustinov, Preprint No. 5354/6, IAE (Institute of Atomic Energy, Moscow, 1991).

Translated by V. Isaakyan